Cooling and power systems integrating organic Rankine cycle with chemisorption technologies

Thesis by

Ke Tang

In Partial Fulfilment of the Requirements

for the Degree of

Doctor of Philosophy (PhD)

Sir Joseph Swan Centre for Energy Research

School of Engineering

Newcastle University

Date of Submission:

October 2019

Abstract

Innovative cooling and power systems combining ORC and chemisorption cycles have been studied for the recovery of low-grade heat energy. A comprehensive literature review has been carried out summarising the previous reports with various low-grade heat driven systems, especially the chemisorption refrigeration and ORC technologies with their features, advantages and challenges.

An ORC-Adsorption (ORC-AD) coupling system has been proposed and thermodynamically studied the performance indicators such as net power, refrigeration and thermal efficiency of the system. The results demonstrate that the combination of ORC and chemisorption technology can effectively improve the utilisation of the low-grade heat.

In the study, novel chemisorption adsorbents have been developed by adding carbon-coated Nickel, Aluminium and Iron (Ni@C, Al@C and Fe@C) into the conventional $SrCl_2$-EG and $MnCl_2$-EG. Scanning Electron Microscopy (SEM), and Energy Dispersive X-ray spectroscopy (EDX) have been used to observe the surface morphology of the adsorbents, while the thermal diffusivity and conductivity are tested by Laser Flash Analysis (LFA). It demonstrates a higher thermal conductivity of the novel sorbent. The sorption performance of the prepared sorbents has been tested. The results reveal the developed novel chemisorption composite that utilising Ni@C can effectively decrease cycle time and enhance the overall energy efficiency.

Based on the experimental results, further system evaluation has been conducted by a simulation study. Cogeneration systems including ORC-AD, AD-ORC, ORC-resorption and resorption-ORC have been compared to evaluate different integrated cycles. Results show that AD-ORC and resorption-ORC have potential advantages over ORC-AD and ORC-resorption. Finally, the simulation model using $MnCl_2$-EG-Ni@C as the sorbent has been applied in resorption-ORC, showing a large improvement of the system performance.

Acknowledgement

I would like to present the sincere gratitude to my supervisors Professor Anthony Paul Roskilly, Dr Yiji Lu and Dr Yaodong Wang, for their guidance, help and encourage throughout the whole four years.

Except for the great supervisors, technicians Mr Ian Douglass, Mr Stephen Crosby and Mr Paul Chilton in the lab and other staff Mr Ye Yuan, Dr Zhichao Zhang and Mrs Jan Fairless also receive my sincere appreciations for their continuous support with kindness.

Also, I would like to thank the China Scholarship Council for granting the PhD scholarship under No. 201608060039 and Sir Joseph Swan Centre for Energy Research funding of four years PhD tuition fees. National Natural Science Foundation of China for general program (Grant No. 51606118) and for Innovative Research Groups (Grant No. 51521004), NSFC-RS Joint Project under the grant number No. 5151101443 and IE/151256, Prosperity Outcomes Award 2016 (EP/P511201/1)-Study of carbon based Nanomaterial to Enhance heat transfer and efficiency in Chemisorption Cogeneration system, EPSRC IAA- Study of engine waste heat technologies (EP/K503885/1), IDRIST project (EP/M008088/1), IAA- Study of engine waste heat technologies (EP/K503885/1) and Heat-STRESS (EP/N02155X/1) from EPSRC are also of highly appreciate.

Besides, my friends who deserve thanks include Mr Jian Zhou, Mr Yin Wang, Mr Shi Chen, Mr Zhi Li, Mr Julien Lee, Mr Weidong Lin, Mr Yuhang Zhong, Mr Fanjie Jing and Mr Andy Wang. Study abroad is quite challenging, but there are always kinds of people cheering me up through the rough times.

To my love, Mr Nong You, who has supported and encouraged me during the project period, I wish we will never leave each other.

I am grateful to my family members especially my mother and father, who always inspire me with their positive attitudes in life, even I know you will never read this thesis.

Table of contents

List of figures

List of tables

List of publications

[1] **K. Tang**, Y. Lu, L. Jiang, L. Wang, Y. Wang, A.P. Roskilly, X. Yu, Investigation of thermal characteristics of strontium chloride composite sorbent for sorption refrigeration, Thermal Science and Engineering Progress, 10 (2019) 179-185.

[2] **K. Tang**, Y. Lu, Y. Wang, L. Wang, and A.P. Roskilly, Enhancement of Low Grade Heat driven adsorption by Adding Carbon Coated Ni/Al/Fe into $SrCl_2$-NEG, Conference: IChemE CatSIG event on Novel Catalyst and Reactor Technologies, 11/2018

[3] **K. Tang**, Y. Lu, L. Jiang, A. P. Roskilly, Y. Yuan, and Y. Wang, "Development and testing of novel Chemisorption Composite using SrCl2-NEG adding with Carbon coated Ni and Al," Energy Procedia, vol. 142, pp. 4037-4043, 2017/12/01/ 2017.

[4] L. Jiang, Y. Lu, **K. Tang**, A. P. Roskilly, Y. Wang, Y. Yuan, et al., "Investigation of a novel composite sorbent for improved sorption characteristic," Energy Procedia, vol. 142, pp. 1455-1461, 2017/12/01/ 2017.

[5] L. Jiang, Y. J. Lu, **K. Tang**, Y. D. Wang, R. Wang, A. P. Roskilly, et al., "Investigation on heat and mass transfer performance of novel composite strontium chloride for sorption reactors," Applied Thermal Engineering, vol. 121, pp. 410-418, 7/5/ 2017.

[6] Y. Lu, A. P. Roskilly, **K. Tang**, Y. Wang, L. Jiang, Y. Yuan, et al., "Investigation and performance study of a dual-source chemisorption power generation cycle using scroll expander," Applied Energy, vol. 204, pp. 979-993, 2017/10/15/ 2017.

[7] Q. Wu, Y. Lu, **K. Tang**, Y. Wang, A. P. Roskilly, and H. Zhang, "Experimental Exploration of a Novel Chemisorption Composite of SrCl2-NEG Adding with Carbon Coated Ni," Energy Procedia, vol. 105, pp. 4655-4660, 2017/05/01/ 2017.

[8] Y. Lu, A. P. Roskilly, X. Yu, **K. Tang**, L. Jiang, A. Smallbone, et al., "Parametric study for small scale engine coolant and exhaust heat recovery system using different Organic Rankine cycle layouts," Applied Thermal Engineering, vol. 127, pp. 1252-1266, 2017/12/25/ 2017.

[9] Q. Wu, X. Yu, H. Zhang, **K. Tang**, Y. Lu, Y. Wang, and A.P. Roskilly, Conference: International Workshop on Digital Design and Manufacturing Technologies, 01/2016

[10] L. Jiang, Y. J. Lu, A. P. Roskilly, R. Z. Wang, L. W. Wang, and **K. Tang**, "Exploration of ammonia resorption cycle for power generation by using novel composite sorbent," Applied Energy, vol. 215, pp. 457-467, 2018/04/01/ 2018.

[11] L. Jiang, R. Z. Wang, Y. J. Lu, A. P. Roskilly, L. W. Wang, and **K. Tang**, "Investigation on novel modular sorption thermal cell with improved energy charging and discharging performance," Energy Conversion and Management, vol. 148, pp. 110-119, 2017/09/15/ 2017.

[12] L. Jiang, R. Z. Wang, Y. J. Lu, A. P. Roskilly, L. W. Wang, and **K. Tang**, "Investigation on innovative thermal conductive composite strontium chloride for ammonia sorption refrigeration," International Journal of Refrigeration, vol. 85, pp. 157-166, 2018/01/01/ 2018.

[13] Q. Wu, X. Yu, H. Zhang, Y. Chen, L. Liu, X. Xie, **K. Tang**, Y. Lu, Y. Wang and A.P. Roskilly, Fabrication and Thermal Conductivity Improvement of Novel Composite Adsorbents adding with Nanoparticles, Chinese Journal of Mechanical Engineering, Volume 29, Issue 6, pp 1114–1119, 11/2016

Nomenclature

Acronym	
AC	Activated carbon
AD-ORC	Adsorption-ORC system
Al@C	Carbon Coated Aluminium
BSE	back-scattered electrons
$CaCl_2$-EG	Calcium Chloride-Expanded Graphite
CFCs	Chlorofluorocarbons
CH_4	Methane
CO_2	Carbon dioxides
CO_x	Carbon oxides
DCENG	Disc compacted expanded natural graphite blocks
EDX	Energy Dispersive X-ray spectroscopy
ENG-TSA	Consolidated disk of expanded graphite treated by the Sulfuric Acid
Fe@C	Carbon Coated Iron
FEG	Field emission guns
GE	General Electric
GWP	Global Warming Potential
H_2	Hydrogen
HCFCs	Hydro-chlorofluorocarbons
LGH	Low-grade heat
M_aCl_b	Metal Chlorides
MH_n	Metal Hydrides
Mm	Misch metal
$MnCl_2$-EG	Manganese Chloride-Expanded Graphite
N_2O	Nitrous oxides
NH_3	Ammonia
Ni@C	Carbon Coated Nickel
NIST	National Institute of Standards and Technology
NO_x	Nitrogen oxides
O	Oxygen
ODP	Ozone Depletion Potential
ORC	Organic Rankine Cycle
ORC-AD	ORC-Adsorption system

PCENG	Plate compacted expanded graphite blocks
PM	Particulate matter
PMHs	Porous metal hydrides
SE	Secondary Electrons
SEM	Scanning Electron Microscopy
SO_x	Sulphur oxides
$SrCl_2$ -EG	Strontium Chloride -Expanded Graphite
VOCs	Volatile Organic Compounds

Symbols

A	Cross-sectional area (m^2)
Ar	Arrhenius factor
COP	Coefficient of Performance (%)
C_p	Specific heat capacity ($kJ \cdot kg^{-1} \cdot K^{-1}$)
g	Gravitational acceleration ($m.s^{-2}$)
H	Enthalpy ($J \cdot mol^{-1}$)
h	Height (m)
L	Length (mm)
LMTD	Log mean temperature difference (K)
$\dot{m}$	Mass flow rate (kg/s)
m	Mass (kg)
Mr	Reflects the impact of the vacant sites of the chemical reaction
P	Pressure (kPa)
$\dot{Q}$	Heat consumed or generated in unit time (kW)
Q	Heat (kJ)
R	Natural gas constant ($8.314\ J \cdot mol^{-1} \cdot K^{-1}$)
R_{f_w}	Heat resistance between the thermal fluid and the wall ($m^2 \cdot K^{-1} \cdot W^{-1}$)
R_{w_ad}	Heat resistance between the wall and the adsorbent ($m^2 \cdot K^{-1} \cdot W^{-1}$)
S	Entropy ($kJ \cdot kg^{-1} \cdot K^{-1}$)
SCP	Specific Cooling Power (kW/kg)
t	Time (s)
T	Temperature (K)
V	Volume (m^3)
$\dot{W}$	Work consumed or produced in unit time (kW)

x	Ammonia conversion ratio (%)
X	Mass ratio (%)

Greek letters

α	Thermal diffusivity ($mm^{2}\cdot s^{-1}$)
δ	Thickness (mm)
η	Efficiency (%)
k	Thermal conductivity ($W\cdot m^{-1}\cdot K^{-1}$)
π	Archimedes' constant (3.14)
ρ	Density ($kg\cdot m^{3}$)

Subscripts

th	Thermal
_	Ideal
0	Ambient
½	Half maximum
1	Inlet point of heat source in ORC
15	Inlet point of cold source in ORC
2	Outlet point of heat source in ORC
3	Inlet point of heat source in sorption cycle
4	Outlet point of heat source in sorption cycle
5	Inlet point of evaporator in ORC
5a	Point of saturated liquid phase
6	Outlet point of evaporator in ORC
6a	Point of saturated gas phase
7	Outlet point of expander in ORC
7a	Point of saturated liquid phase
8	Outlet point of condenser in ORC
a	Adsorbent
ad	Adsorption
add	Additives
am	Ammonia
c	Cold source in C_{pc}; Constraining in P_c/T_c
Carnot	Carnot Cycle

cond	Condenser
de	Desorption
e	Electricity
eq	Equilibrium
evap	Evaporation
exe	Exergy
exp	Expander
f	Fluid
fw	Fluid to wall
g	gas
gc	Gas channel
h	heat source
H	High
i	Isentropic
in	Inlet
l	liquid
L	Low
m	Mechanical
net	Net
ORC	ORC
out	Outlet
pump	Pump
ram	Reacted
ref	Refrigeration
sam	Sample
sd	Start desorption
sup	Superheat
w	Working fluid in $\dot{m}_w$ and C_{pw}; Wall in d_{w_in}, $d_{w_}$out, λ_w, and δ_w
waste	Waste

Chapter 1 Introduction

1.1 Background

The contradictions between rapid increasing energy demand and environmental depletion caused by energy consumption are restricting the development of world economy and rising growing global concerns. In recent years, although techniques such as nuclear power and hydropower are rapidly developing, the traditional energy supplies of oil, coal and natural gas still occupy a dominant role in the energy resource structure. The conventional energy supplies generate large amounts of environmental air pollutions such as nitrogen/sulphur/carbon oxides (NO_x/SO_x/CO_x), particulate matter (PM), volatile organic compounds (VOCs), and Green House gases (the most critical emissions including carbon dioxides (CO_2), nitrous oxides (N_2O) and methane (CH_4)) [1].

The challenge to maintain the balance between energy demand and the environment drives scientists to research more on exploiting alternative energy, enhancing energy efficiency and reducing the emissions. Kyoto Protocol announced to cut the greenhouse gases emission by 5.2 % based on statistics in 1990. The effective and efficient use of low-grade thermal energy are promising to improve the existed energy system and reduce the release of CO_2 and alleviate the severe problem of global warming [2].

Low-grade heat refers to the energy that bears in the geotherm, solar power, and industrial waste heat, of which the temperature is lower than 270 ^oC. It is also one kind of inexhaustible renewable energy that can be obtained from solar energy and terrestrial heat. On the other hand, this kind of energy widely exists over chemical plants and power plants but wastes from the conventional techniques. Low-grade thermal energy cannot be directly utilised as conventional energy resources because it is close to the ambient temperature, and the application techniques require more on functional temperature range than old energy consumption methods.

In some circumstances such as in a ship or in a building, it requires the electricity and the cooling at the same time with the easy access to wasted heat. Therefore, by building a cogeneration system driven by low-grade heat (wasted heat), it is possible to comfort the request from the mentioned conditions.

ORC has been widely recognised as one of the most important technologies recovering low-grade heat energy sources [3, 4]. It is based on the principle of Rankine Cycle but using the organic working fluid to convert low-grade heat to power [5]. Lots of studies have been done

relevant to this cycle by experiments or modelling [6, 7]. ORC is a mature technique, which means it is hard to improve the cycle performance.

Apart from ORC, low-grade heat driven sorption system, providing cold to end users, can be used to recover waste heat, promote the utilisation of energy cascade and significantly save energy due to its relatively low driven temperature [8]. Moreover, the sorption technology can also be used in heat pump, heat storage and power generation fields. The adsorption could be divided into two types, chemical and physical adsorption. Focusing on the transformation of the adsorbents, researchers found the employment of mixed physical and chemical adsorbent a superior sorbent as it inherits the high thermal conductivity and the high adsorption amount but without suffering from the swelling problem at the same time. Although some improvements of the sorption working pairs or apparatus have been done, adsorption refrigeration is still in an active researching stage. Other additional materials are attracting interests for its desirable properties on heat and mass transfer. They are explored to be mixed into the composite sorbents with the hope of further improving the sorption performance.

It then comes to the idea of integrating ORC with adsorption technology, as ORC could convert low-grade heat to electricity while chemisorption could produce refrigeration by low-grade thermal energy. The complex coupling system can realise the cascaded utilisation of the energy source and produce multiple productions. Eventually, it would improve the whole energy efficiency, and reduce waste.

1.2 Aim and Objectives

Lots of patents and research reports describe the applications of low-grade thermal energies. However, only few authors have studied the ORC-Sorption coupling systems and comprehensively compared them in detail. The primary goal of the PhD research project is to develop the integrated ORC-chemisorption cogeneration systems recovering the low-grade heat, with the expectation to enhance the overall energy efficiency of the low-grade heat and comfort the conditions requiring electricity and cooling power at the same time. The objectives of the PhD project are:

- Review existing research works covering low-grade heat utilisation technologies, particularly ORC and sorption technologies. The advantages, disadvantages, features, and recent development of mentioned cycles are included.
- Study the thermodynamics of an ORC-Adsorption system to demonstrate that it is potential to realise high-efficiency energy consumption by integrating ORC with sorption technology.

- Develop the novel adsorbents by adding Ni/Al/Fe@C into conventional $SrCl_2$/$MnCl_2$-EG by an innovative methodology proposed by the author and explore their thermal and physical properties.
- Conduct the experimental investigation of the adsorption system in the laboratory using the novel sorbents. Compare and evaluate the adsorption and desorption performance results by several representative performance indicators. Collect the useful data for later simulations of the cogeneration systems.
- Compare and study different cooling and power systems to use the low-grade heat by integrating ORC and chemisorption cycles. Simulate and calculate to assess the behaviours.

1.3 Structure of the thesis

This thesis presents the research in the form and order of:

- Chapter 2: A detailed background study, introducing the technology of thermal driven power generation and refrigeration systems by emphasizing ORC and sorption cycles, evaluating their features, reviewing the reported applications and performance, and concluding the challenges at present to explain the motivation of this PhD project.
- Chapter 3: Study and demonstrate the feasibility of integrating ORC with the adsorption cycle to improve energy efficiency. Analyse the performance of using the integrated system in low-grade heat conversion.
- Chapter 4: Manufacture the conventional composite adsorbents of $SrCl_2$-EG and $MnCl_2$-EG with Ni/Al/Fe@C with a developed methodology. Test the surface morphology of the novel adsorbents to prove that the innovative methodology is useful to improve the uniformity of the sorbent. Test the sorbent thermal diffusivity and conductivity to demonstrate the potential of using the novel sorbents to improve the heat transfer process in sorption performance.
- Chapter 5: Experimental investigation on the prepared adsorbents on a set rig. Compare the sorption behaviours of the sorbents with different additives, for instance, the reaction rate, equilibrium conversion, COP and SCP. Reveal the influence of the carbon coated additives.
- Chapter 6: Simulation study of four different cooling and power models using dimensional data of the adsorption unit in Chapter 5. Compare the influence of integrating ORC with adsorption or resorption cycles in various ways. Use the data of Chapter 5 to fit the adsorption kinetic models of the novel sorbents. Apply the fitted

kinetic models into the superior system. Demonstrate the improvement made by the cogeneration system using the novel sorbents.

- Chapter 7: Results summary and future suggestion.

Chapter 2 Literature review

Substituting the conventional energy sources with low-grade heat presents a great potential tackling the barrier of contradiction between inefficient energy supply and energy consumption [9]. Large amounts of low-grade heat are wasted without systematic and scientific utilisation, which could have practical value instead [10-12]. It is not only crucial to recover low-grade thermal energies, but also essential to enhance the utilisation efficiency.

Chapter 2 reviews the technologies of heat-driven power and cooling systems with a focus on ORC for power generation and sorption for refrigeration to comfort the conditions simultaneously requiring cooling and power. The features of different cycles and previous research experiences are reported. At the end of this chapter, the cogeneration systems integrating Rankine Cycle with sorption technology to utilise low-grade thermal energy are discussed.

2.1 Heat-driven power generation cycles

This section mainly summarises the power generation cycles driven by the heat sources such as Carnot Cycle, Rankine Cycle, and its variations. Various layouts of ORC are reviewed for the power generation systems using the low-grade heat. The advantages and disadvantages are concluded along with the research gaps to clarify the motivation of constructing the cogeneration system.

2.1.1 Carnot Cycle

Carnot Cycle, proposed by Sadi Carnot in 1824, is based on the principle shown in Fig 2.1 (a) [13]. Considered to have no heat losses, Carnot Cycle is constructed by two isothermal and two adiabatic processes. The process 1-2 presents that the steam is heated reversibly and isothermally from saturated liquid to saturated vapour in a boiler. The following process 2-3 shows that the saturated steam is isentropically expanded in a turbine. After that, the vapour is isothermally cooled in the condenser during the process 3-4 and is then isentropically compressed in a compressor to the initial state in the period of process 4-1.

$$\eta_{th,Carnot} = 1 - \frac{T_L}{T_H} \qquad 2.1$$

Equation 2.1 is the thermal efficiency of the Carnot Cycle, where T_L is the controlled temperature of the sink during process 3-4 and T_H is the temperature of the heat source in process 1-2. T_L is limited by the cooling medium such as the atmospheric air or a lake, and T_H is restricted by the maximum temperature that the engine components could withstand.

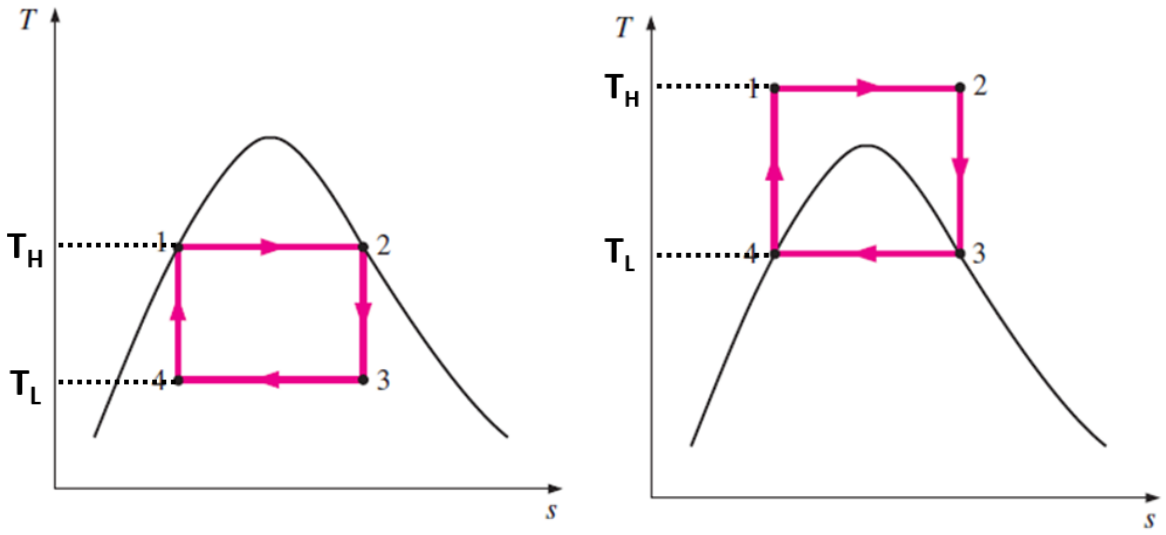

(a) *T-s* diagram of Carnot Cycle A (b) *T-s* diagram of Carnot Cycle B

Figure 2.1 *T-s* diagram of two Carnot vapour cycles [13]

Carnot Cycle relevant to Fig 2.1 (a) has some drawbacks. For example, achieving the reversible isothermal heat transfer requires a very large heat exchanger and a very long working time in the reality. Other issues include that the maximum temperature limits the thermal efficiency of the cycle, and the turbine also has an issue to deal with the impingement from the high moisture steam. Although the latter problem could be potentially eliminated by a working fluid which has a steep saturated vapour line, in process 4-1, it still has other problems on precisely operating a condensation process that ends up with perfect quality at stage 4 or building a compressor that handles two phases. Fig. 2.1. (b) proposed a mode to eliminate some of the mentioned problems by applying a superheating process above the critical point. However, this cycle has other challenges such as the isothermal heat transfer at various temperatures and the isentropic compression to extremely high pressure. Therefore, it is impractical to build the device closely approximating the Carnot cycle.

Carnot Cycle is the most thermally efficient cycle within two operating temperature limits. Moreover, Carnot Cycle is the ideal cycle for heat engines concerning the thermodynamics respects. However, Carnot Cycle would never be built in the reality.

2.1.2 Rankine Cycle and its variations

Recognised as one of the most popular energy conversion systems, Rankine Cycle mainly consists of a pump, a boiler, a turbine and a condenser as shown in Fig. 2.2 (a) [13]. A *T-s* diagram of ORC is presented in Fig 2.2 (b) to explain the working principle of Rankine Cycle.

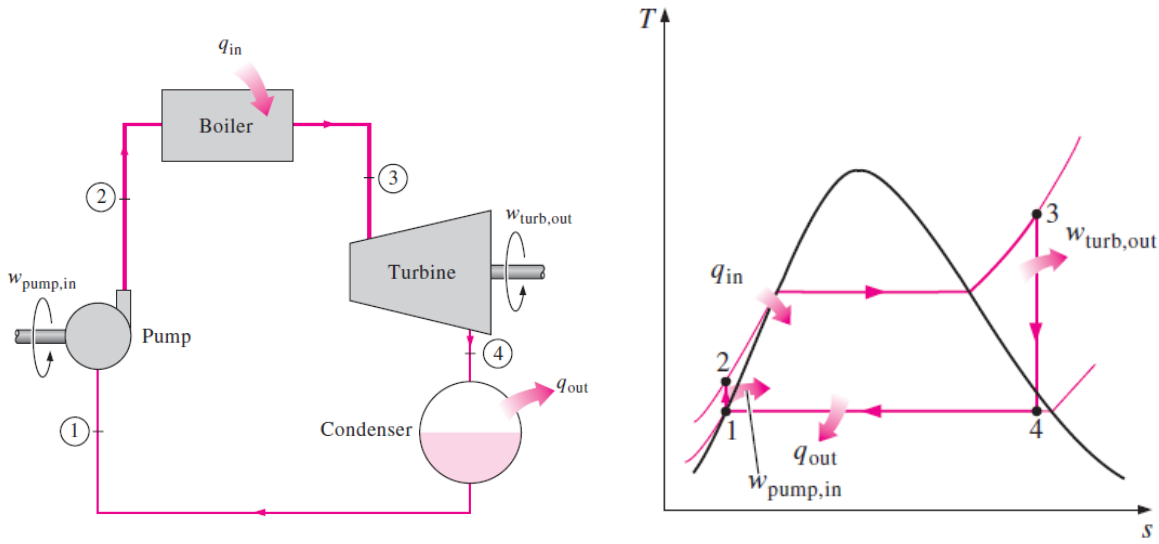

(a) Simple ideal Rankine Cycle (b) *T-s* diagram of a Rankine Cycle

Figure 2.2 Simple ideal Rankine Cycle [13]

The working principle of the cycle is described as follows. The liquid phase water is first pumped to high pressure through the isentropic pump compression from point 1 to point 2 and then flows to the boiler as displayed in Fig. 2.2. In the boiler, it is heated at a constant pressure to evaporate with the provided heat source and this results to the superheated steam at stage 3. The vapour is then isentropically expanded in the turbine with the output during process 3-4. Finally, it is condensed at a fixed pressure to the initial stage of the liquid phase through process 4-1.

However, the Rankine Cycle also suffers from some actual irreversibility, which are caused by the fundamental fluid friction and heat losses when the steam works in the cycle. A pressure pumped higher than required could alleviate the impact of the pressure drop, while a larger heat input could reduce the heat loss. All these result in a lower cycle efficiency than that of the theoretical one.

The advantages of the steam Rankine Cycle are retrieved from the working fluid of water, including its high specific heat capacity and broad ranges of variable working conditions. It is also environmentally friendly and safe to use. However, the cycle requires a very high driven temperature to prevent the exiting of the liquid phase from the boiler. Otherwise, it would gradually damage the blades of the turbine, resulting in both reduces of the device lifetime and efficiency [14]. In conclusion, it is not suitable to use the steam Rankine Cycle recovering the low-grade heat.

Organic Rankine Cycle (ORC)

In a case that an organic working fluid with a lower boiling temperature is applied instead of water to recover low-grade heat from solar ponds, biomass plants or geothermal power, the cycle is named as the Organic Rankine Cycle (ORC), which has been extensively investigated since the 1880s [15].

The ORC progress is intertwined with the formative of the empirical thermodynamics development as Cardwell states in his book [16]. The first commercial application of an organic fluid was the 1853 Du Trembley system, where the combined vapours were applied to ship propulsion [17]. For the following half century, there were very few applications of ORC. In the 1960s, Sundstrand Aviation Corp developed a 600kW ORC using waste heat from two 6600kW diesel generating sets [18]. In the 1970s, General Electric (GE) developed a 3kW ORC for mobile homes. As of 2015, Ormat Technologies Inc., found in 1964, has built more than 3000 ORC units up to 4kW, and approximately 500 modules in the power range of 1-25 MW, totalling more than 2000MW.

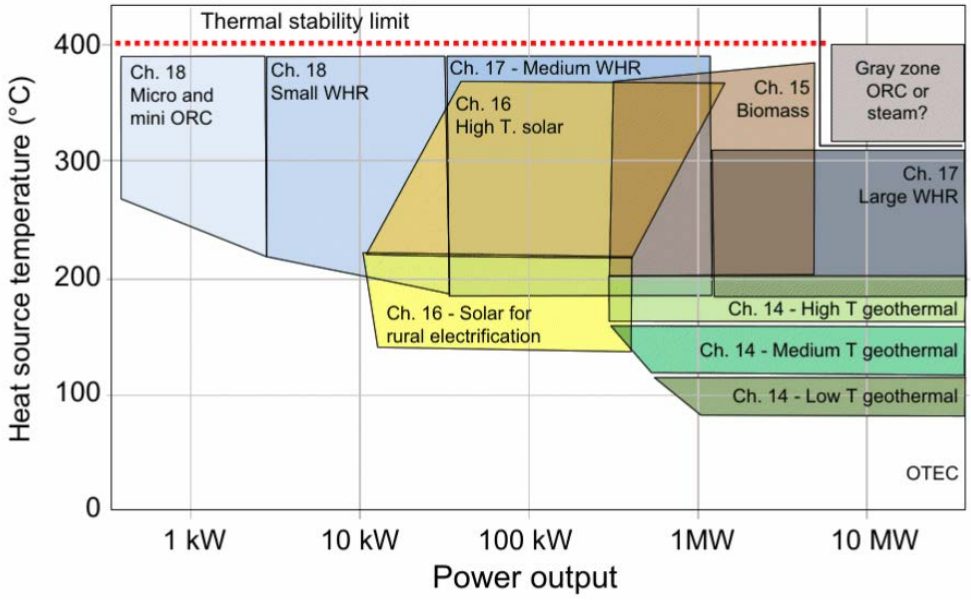

Figure 2.3 A representation of ORC applications fields in the heat source temperature-power output plane [19]

ORCs are the unrivalled technical solutions for generating electricity from low-medium temperature heat sources of limited capacity. The applications among different heat sources are displayed in Fig. 2.3 [19].

The working fluids for the ORC can be categorised as wet, dry and isentropic, according to the fluid state at the exit of the expander. They also have different slopes of the saturation curves as indicated in Fig. 2.4 [20]. The slopes of the wet fluids like R717 are negative on the saturation line, while the dry fluids such as n-pentane have positive slopes. Besides, the fluid

of R134a represents one kind of isentropic working fluids in ORC with vertical/infinite slopes. The wet fluid may need additional superheating process to avoid the wet contents as it is a mixture of both liquid and vapour phases at the exit of the expansion, which leads to the extra costs.

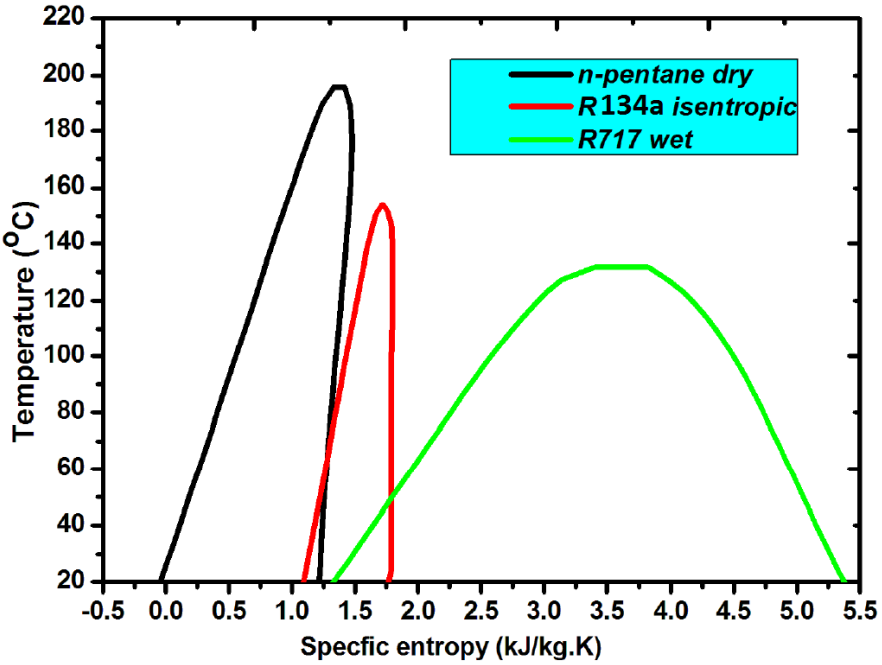

Figure 2.4 Dry, isentropic and wet ORC working fluids [20]

In summary, ORC is one of the most promising technologies to convert low-grade heat into useful power. The background study above presents a desirable working temperature range covering the range of low-grade heat. The working fluid of ORC should have a lower critical temperature than water, which enables the ORC to be driven by the heat source with a relatively low temperature. Moreover, it is suggested to use dry or isentropic working fluids in an ORC in case of the damage to the expansion device.

Kalina Cycle

In 1984, Kalina proposed a cycle named Kalina Cycle as a transformation of the ORC [21], requiring an additional separator as presented in Fig 2.5 [20]. This cycle uses the mixture of ammonia-water as the working fluid, enabling a better exergy utilisation in the condition of various heat source temperature than that of a pure working fluid ORC [22].

The working principle of Kalina Cycle could be described as follows. The ammonia in the binary working fluid initially evaporates, and then water begins the phase change from liquid to vapour during the heating process. The two-step phase change results in a process that is not isothermal or isobaric, and the cooling process follows in a similar way.

Therefore, the overall heat losses in the Kalina Cycle is reduced, and the temperature of the working fluid can be very close to that of the heat source. It also explains the superiority of the Kalina Cycle, considering the features of the ORC [22-24].

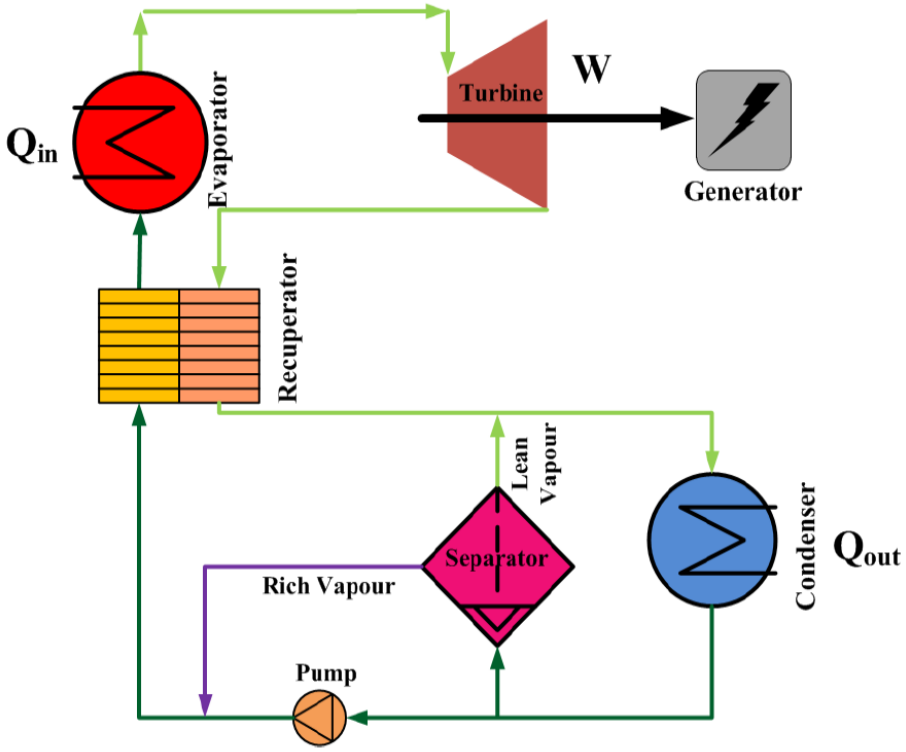

Figure 2.5 Illustration of the Kalina Cycle [20]

Many studies have been done to explore the performance of Kalina Cycle. According to the theoretical analysis in the report, with the 532℃ heat source, the first law efficiency of this cycle is 32.86%, about 20% higher than that of the Rankine Cycle, and the second law efficiency is 70.03%, around 50% higher [21]. In 1999, the Kalina Cycle was commercially constructed for the first time in Husavik, Iceland, using the geothermal energy [25]. It was designed to generate power of 2MW using the heat source of 124℃, remaining the geothermal water at 80℃ for district heating. A thermodynamic analysis was conducted to assess the recovery of the waste heat from two engines, using the Kalina Cycle and ORC to present the comparison [24]. In this study, the ORC fits better in the medium temperature range and requires lower maximum pressure to generate the same power with which the Kalina Cycle supplies.

Through the theoretical and experimental explorations, the Kalina Cycle is proved to be an effective cycle to convert low-grade heat into mechanical power, and it is potential for the Kalina Cycle to recovery broader temperature range by adjusting the concentration of the

working fluid. However, it requires more precise controlling strategies and more components compared to ORC, leading to a higher construction cost and more complex structure.

Goswami Cycle

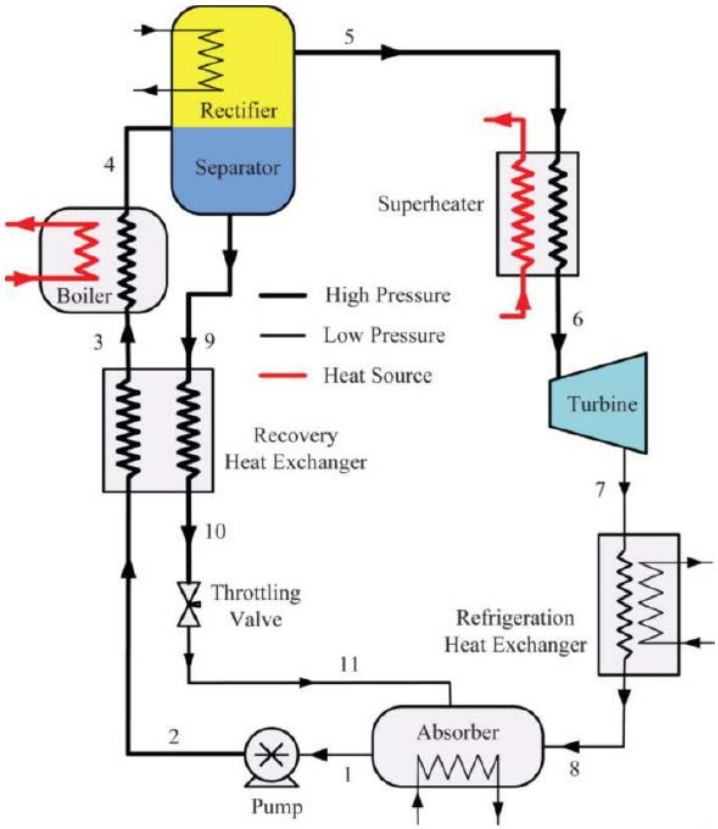

Figure 2.6 Schematic diagram of the Goswami Cycle [26]

Also using the ammonia-water mixture, the Goswami Cycle is a combination of the Rankine Cycle and absorption refrigeration as illustrated in Fig 2.6 [26]. Similar with Kalina Cycle, this cycle takes the same advantages from the binary fluid, but it has an added heat exchanger at the exit of the expander to produce the cold. Goswami Cycle can generate both mechanical power and cooling effect in a loop [27-29]. When the heat source is in the range of 47℃ to 187℃, the absorber achieved its highest exergy, while with a heat source temperature higher than 187℃, the rectifier has a highest exergy loss [30]. At a temperature of 147℃, a maximum value of the second law efficiency was retrieved at 65.8% [28]. However, due to the system design, the Goswami Cycle still has the disadvantages of low refrigeration efficiency, only about 1.2% [30].

From the reviews above, although the Goswami Cycle produces mechanical power and refrigeration simultaneously, the low efficiency of the refrigeration production seriously restrains the technology to be widely applied.

2.1.3 Different layouts of ORC systems

Types of ORC include Basic ORC (BORC), single stage regenerative ORC (SRORC), double stage regenerative ORC (DRORC), reheat ORC (RORC), ORC with recuperator and dual loop ORC (DLORC).

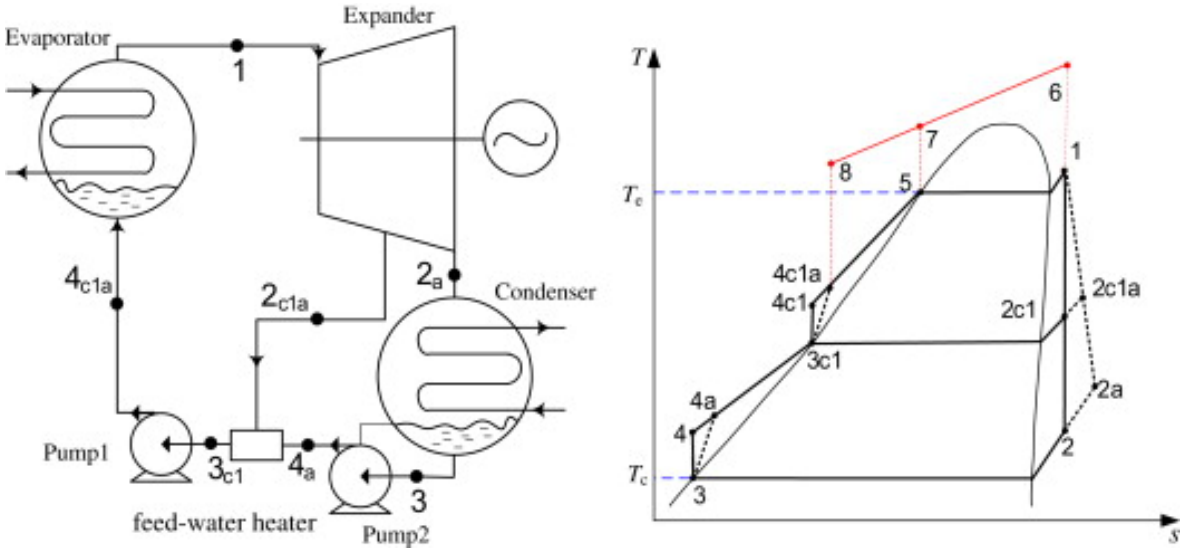

(a) Configuration of the cycle (b) T-s diagram

Figure 2.7 SROC [31]

In SRORC, some fractions of the vapour are leaded into the feedwater heater, when they are between the two stages in the expander as shown in Fig 2.7 [31]. The regenerator reduces the heat consumption of the boiler and thus, it enhances the thermal efficiency [32]. Like SRORC, DRORC in Fig 2.8 has one more extraction in the expander, which improves the thermal efficiency of the system by further deceasing the load of the evaporator [31, 32].

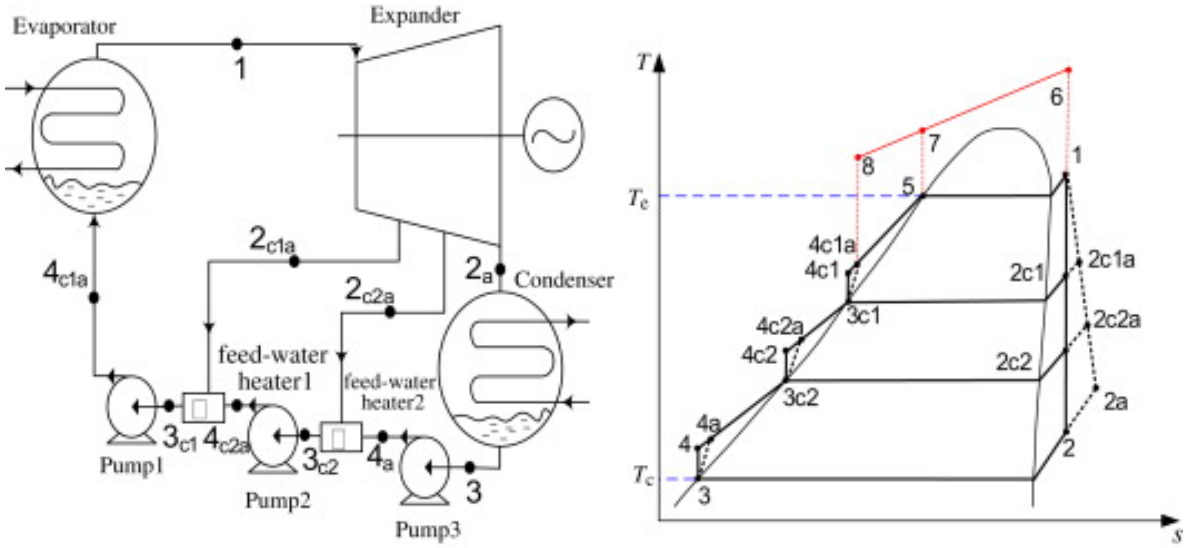

(a) Configuration of the cycle (b) *T-s* diagram

Figure 2.8 DRORC [31]

Fig 2.9 shows the system of RORC [32], in which, the outlet vapour of the first evaporator re-enters the boiler and is reheated to enter the second evaporator. In this way, the moisture of the steam can be eliminated in the final expansion and protect the blades of the expander.

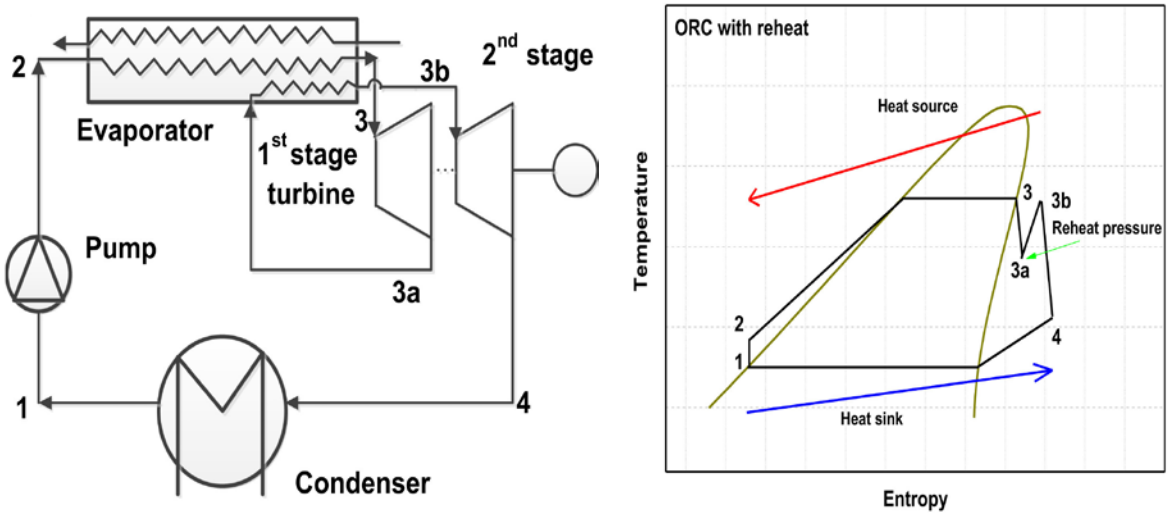

(a) Configuration of the cycle (b) *T-s* diagram

Figure 2.9 RORC [32]

Fig 2.10 presents ORC with an extra recuperator, compared with the BORC [32]. In this system, the working fluid at a high temperature out of turbine enters an internal heat exchanger (IHX) and exchanges the heat with the working fluid at a low temperature out of the pump. Thus, the thermal efficiency is improved by this heat recovery process.

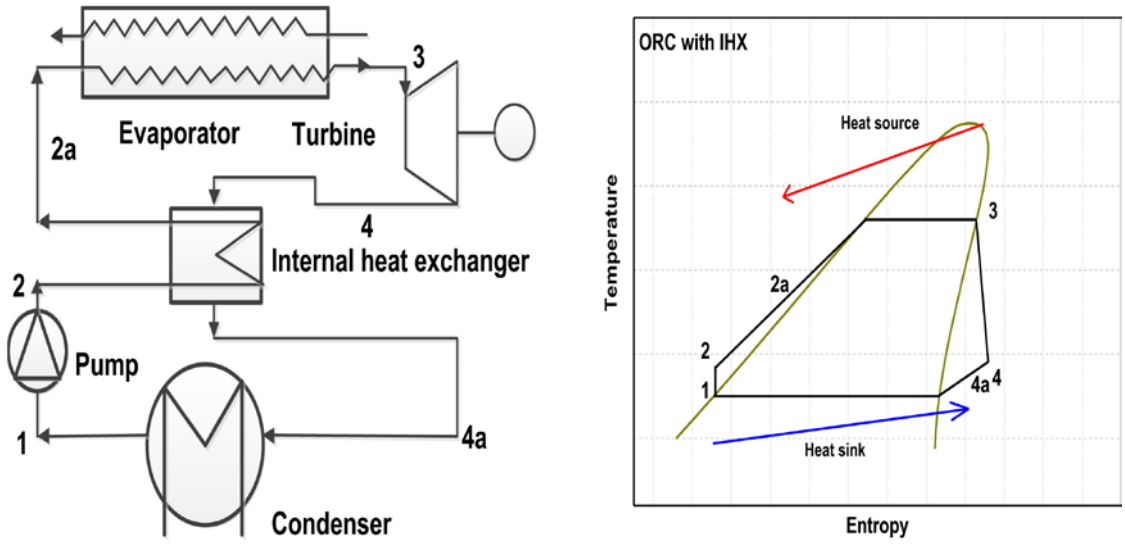

(a) Configuration of the cycle (b) *T-s* diagram

Figure 2.10 ORC with a recuperator [32]

Fig 2.11 is the system of DLORC, in which, the high temperature loop recovers the waste heat of engine exhaust and the low temperature loop uses the heat of the jacket water and the

working fluid in the high temperature loop after expansion [33]. This system is suitable to recover a couple of heat sources at the same time. The overall efficiency of the engine with this cycle is enhanced by nearly 14.4 %, due to the decrease of the heat released to the environment [33].

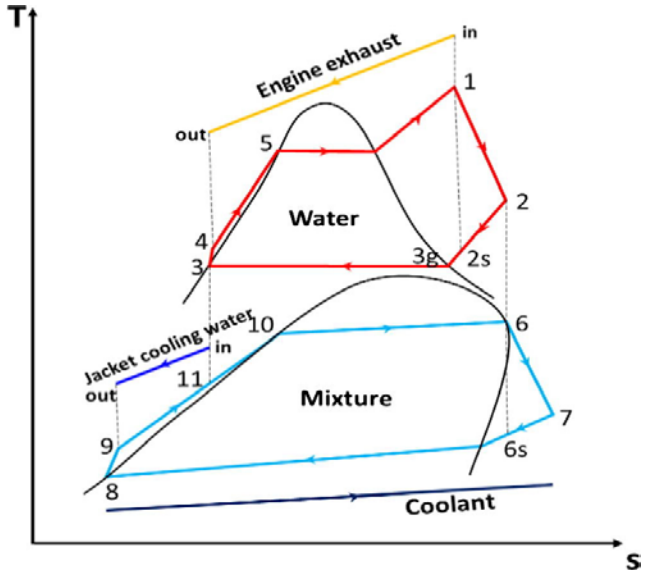

(a) *T-s* diagram of DLORC

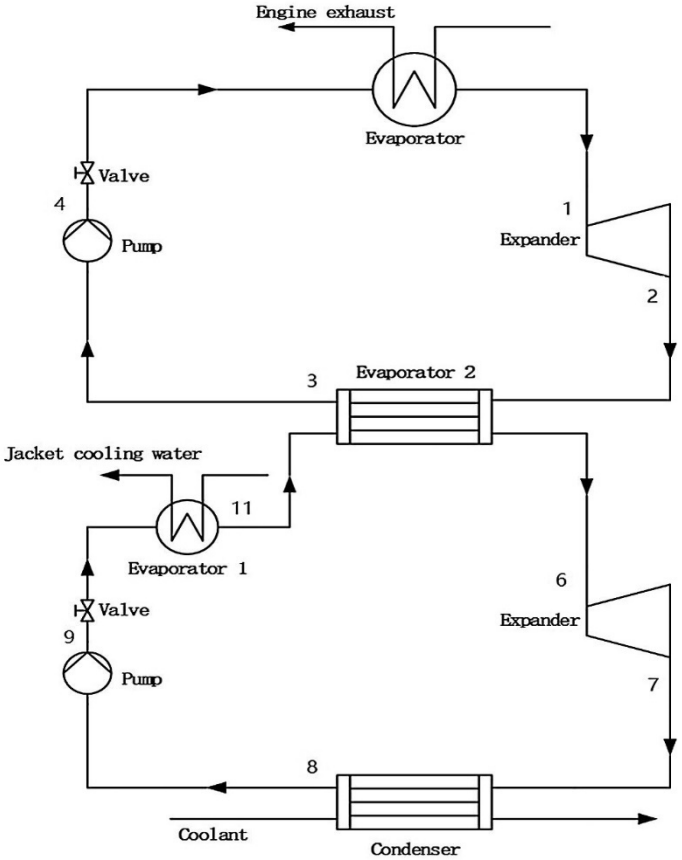

(b) System configuration

Figure 2.11 DLORC [33]

Nazari et al. [34] proposed a combined steam-ORC system for recovering the waste heat of a gas turbine as presented in Fig 2.12. Results showed a maximum exergy efficiency of 57.62 % and a minimum product cost rate of 396.7 $/h.

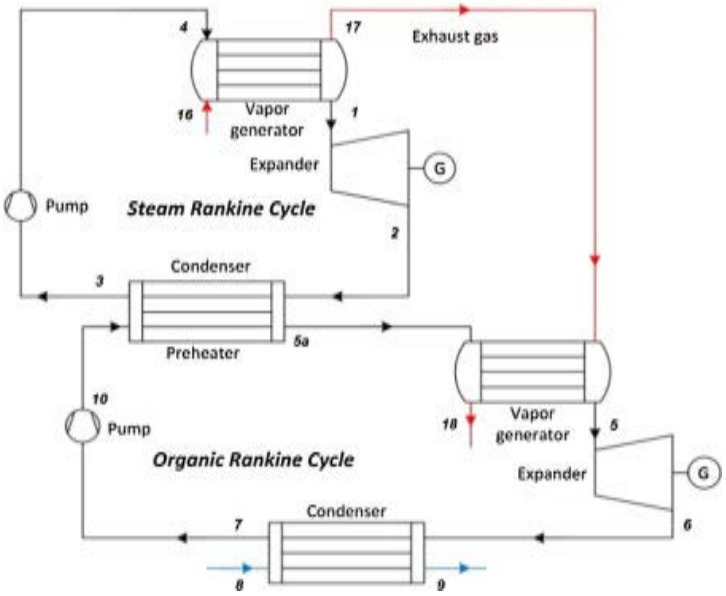

(a) System configuration

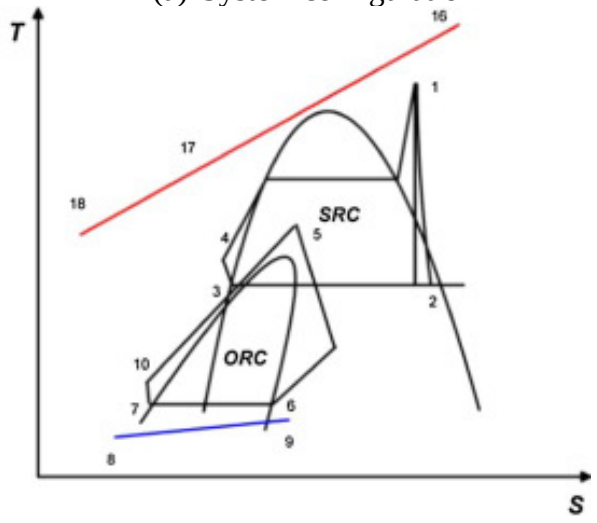

(b) *T-s* diagram

Figure 2.12 Steam-ORC system [34]

Likewise, Shu et al. [35] explored a novel transcritical cascade-ORC system as presented in Fig 2.13, to realise the multi-grade heat recovery for a heavy-duty engine. The waste heat of the engine included the charge air (CA), jacket water (JW), exhaust gas (EG), and exhaust gas recirculation (EGR). The design and arrangement of the heat exchanging processes were based on the heat grade of the various heat sources. The rankings of the alternate fluids based on the performance were: toluene > decane > cyclohexane > D4 and R143a > R125 > R218 > R41, for the high temperature loop and low temperature loop, respectively. The result showed a largest efficiency increment of the original engine up to 16.0%.

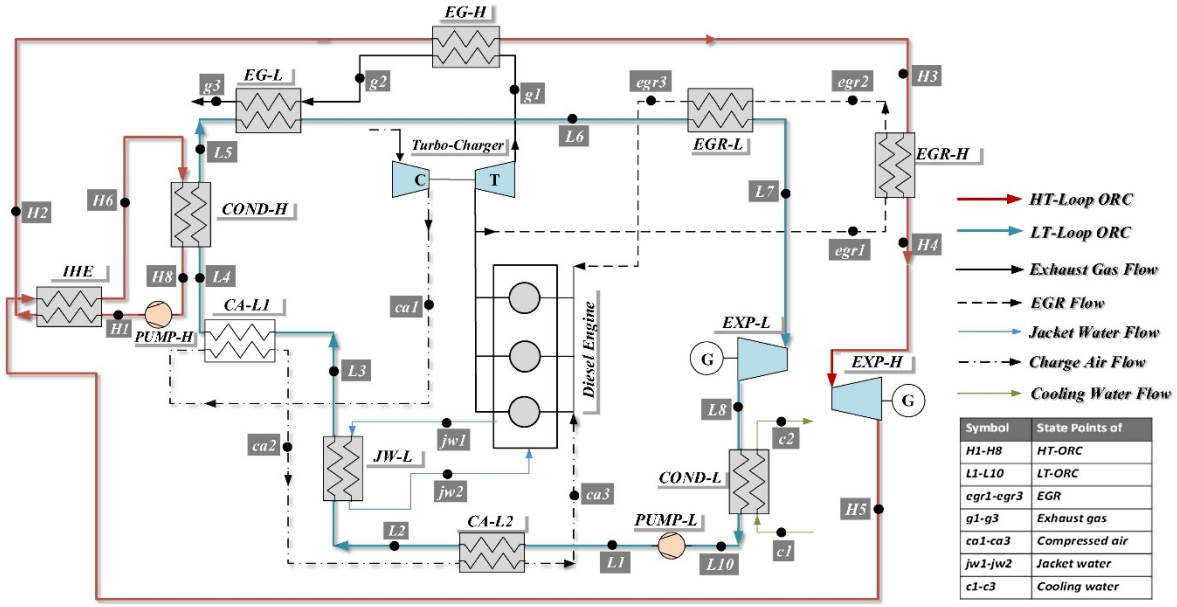

(a) System configuration

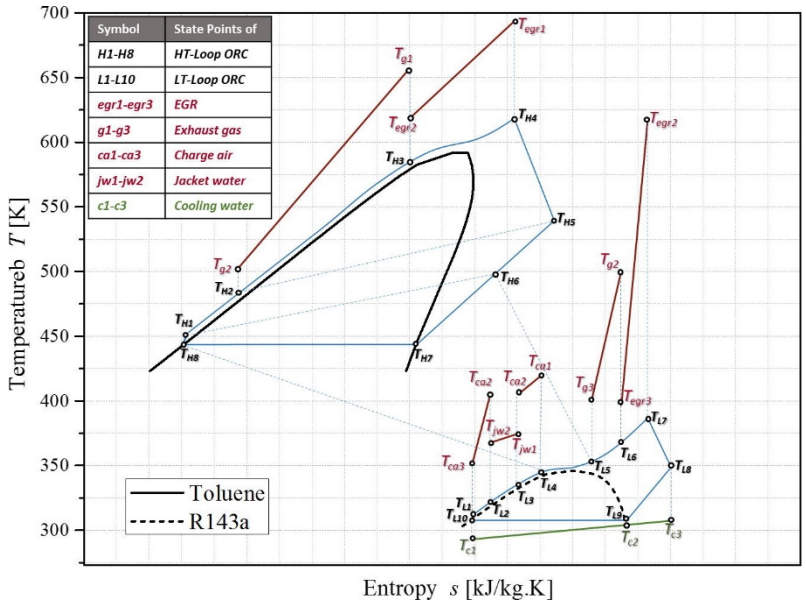

(b) *T*-*s* diagram

Figure 2.13 Transcritical cascade-ORC system [35]

Among these configurations, ORC with IHX and DLORC are preferable. SRORC and DRORC are quite complex in their configurations. The effort to verify the stages of the working fluid and send them to another pump is a relatively high requirement. Moreover, RORC needs to send the expanded working fluid into the evaporator again, costing another expander and special design of the evaporator. Among all configurations of ORC in recent scientific research, ORC with IHX or DLORC are the two superior layouts, as they are amended in a reasonable way and still in a simple structure. For ORC with IHX, it is easy to modify the existed system with simple changes of the pipes and adding one IHX. For DLORC, it makes sense in most cases where two low-grade heat sources are produced.

Except for the system configurations, selecting the working fluid is also a crucial issue in the ORC application field. By comparing the flow rate, pressure ratio, flammability, system efficiency, irreversibility, toxicity, global warming potential (GWP) and ozone depletion potential (ODP), Tchanche et al. [36] evaluated 20 different working fluids for the solar ORC from their thermodynamic and environmental characteristics. Chen at al. [23] assessed 35 various fluids on a supercritical Rankin Cycle and an ORC to find out the influence of their properties such as the density, specific heat, latent heat and the effectiveness of superheating. A study of the fluid selection for a geothermal ORC system was based on the exergy analysis, which indicated that the working fluid with a high critical temperature, for example, isopentane, is more favourable in series circuits [37]. When a heat source is under 450 K or in parallel circuits, however, the working fluid with a low critical temperature is more suitable, such as R227a. An investigation on a small scale solar ORC system indicated that R600 and R600a are the optimal working fluids among the six candidates, in the temperature range 70℃ to 120℃, by the first and second law analysis [14]. Wei et al. [38] studied the performance of ORC using R245fa as the working fluid and hot gas as the heat source. The result discovered that the net power and the efficiency of the cycle could deteriorate with a high ambient temperature.

Although it is worthy of applying ORC into the low-grade heat conversion field, the potential enhancement of this single technology is limited by its long research history and the mature development condition. Integrating ORC with other available thermal cycles attracts increasing interests from scientists who dedicate themselves to seek solutions for the low-grade heat efficiency.

2.2 Heat-driven solid-gas sorption refrigeration

Despite the application of low-grade heat on power generation field, refrigeration is another kind of possible conversion for low-grade heat.

Solid-gas sorption refrigeration systems, producing cold for end users by reusing industrial waste heat, solar energy, soil heat, emissions from engine and other kinds of low-grade thermal energy. They have been wide-ranged advanced for controlling the environment degradation and developing cascaded utilization of heat in the past few decades [39-46]. Moreover, solid gas sorption is considered to have more advantages than conventional refrigeration systems. It can be driven by low-grade heat, applying environmentally friendly refrigerants like water, methanol, ammonia, and hydrogen, and therefore, it possesses more possibilities on energy saving and causes zero ozone depletion potential (ODP) as well as zero global warming potential (GWP) [47].

Except for the solid-gas sorption technologies, the liquid-gas absorption is also one type of the refrigeration systems but has some challenges for application. For example, the liquid-gas absorption takes a narrower working temperature range along with the problem of the corrosion on the device or the crystallisation of the solution.

Besides, solid-gas systems have many advantages to be applied in low-grade heat conversion. For instance, they are extremely simple, reliable and flexible as they do not virtually have the moving components, so they are suitable for more locations. For instance, they can work for ice-making or air-conditioning on a fishing boat or automobile by using waste gases from the engine [48]. Moreover, for a larger scale like space heating and cooling of a building, thermal lift and deep-freezing, the solid-gas sorption refrigeration is also capable.

The principle of the solid-gas sorption will be explained in Section 2.2. Besides, the adsorption mechanism and thermodynamic characteristics of physical, chemical and composite adsorption will be introduced. At the end of Section 2.2, the previous explorations of the sorbent material will be reported.

2.2.1 The principle of the solid-gas sorption

The basic sorption refrigeration system consists of the adsorption bed and the condenser/evaporator, as the schematic diagram shows in Fig. 2.14 [49].

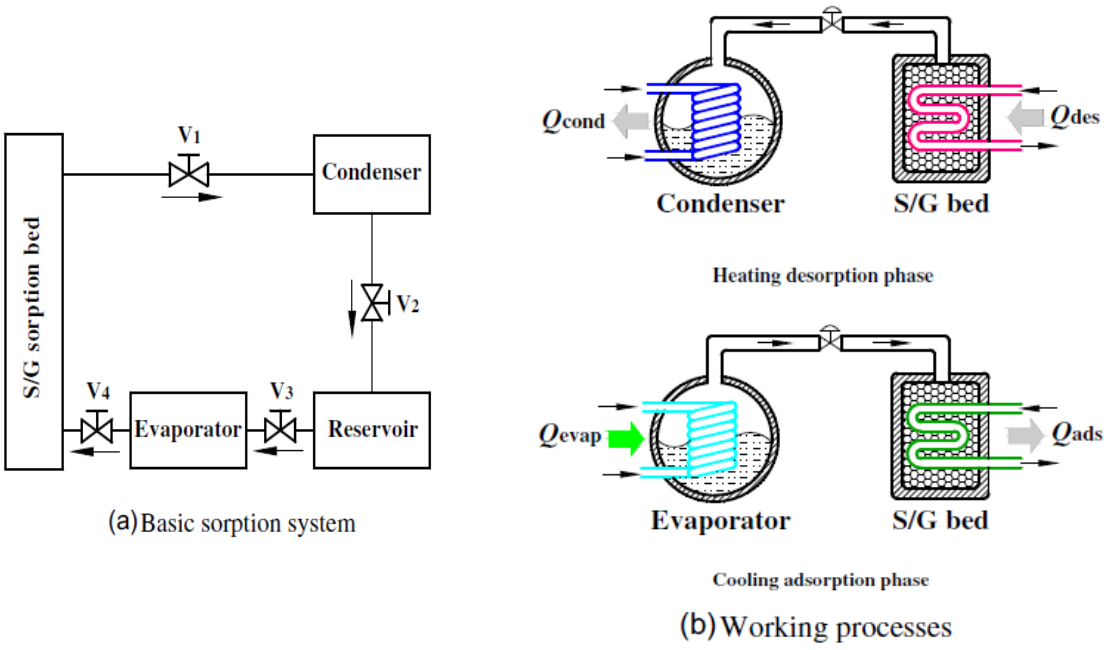

Figure 2.14 Schematic diagram of the basic solid-gas sorption refrigeration cycle [50]

The basic solid-gas sorption has two main working processes: heating-desorption and cooling-adsorption. At the stage of decomposition, the sorbent bed is heated to desorb the gas,

which would be condensed into the liquid phase in the condenser. This process releases the condensation heat to the ambient and stores the liquid refrigerant. At the stage of synthesis, the adsorbent in the reaction bed adsorbs the gas, causing the evaporation on the other side. The condenser in the last process thus works as an evaporator instead during this period, producing the cooling effect because of the latent heat. In this process, the adsorption heat is also retrieved from the reaction bed.

There are three most considered refrigerants in the adsorption system, including water, ammonia and methanol. The selection of the refrigerants is decided by different applications such as the temperature range and power output. Table 2.1 lists their physical properties [20]. The comparison of these three most popular refrigerants is listed in Table 2.2 [20].

Refrigerant	Chemical formula	Boiling point (°C)	Relative molecular weight (g/mol)	Latent heat of vaporization L (kJ/kg)	Standard density (kg/m^3)	ρL (MJ/m^3)
Water	H_2O	100	18	2258	958	2163
Ammonia	NH_3	-33.3	17	1368	681	932
Methanol	CH_3OH	64.7	32	1102	791	872

Table 2.1 Physical properties of the most common refrigerants [20]

Water is generally regarded as one ideal refrigerant for its high latent heat and non-toxic. It works with zeolite or silica gel. Nevertheless, water is not suitable for a condition where the temperature is lower than zero Celcius. When the evaporating pressure is low, the mass transfer is limited. Thus, it slows the reaction speed and leads to low specific cooling power (SCP).

Ammonia is also a kind of common refrigerant. It has a faster adsorption process than that of water or methanol due to the high evaporating pressure (around 8 bars at 30°C). Besides, ammonia is friendly to the environment. However, the latent heat of ammonia is nearly half of that of water. Moreover, by the method of the secured gas tightness, the drawback of irritation, when high concentration ammonia is exposed to the ambient, could be solved.

Methanol is the third refrigerant mentioned in Table 2.1 [20]. It has the excellent property for the physical adsorption systems as its one of the smallest and simplest organic molecules.

However, it is unstable at a temperature that is higher than 120℃, and it reacts with copper at a high temperature.

	Water	Ammonia	Methanol
Advantages	Safe and no-toxic; Non-pollution; Compatible with copper; Highest latent heat	Natural refrigerant; Non-pollution; High evaporating pressure; High latent heat; Good heat stability	Low refrigeration temperature (ice-making)
Disadvantages	Not suitable for the temperature lower than 0 ℃; Low evaporating pressure	Incompatible with copper; Flammable in a specific concentration; Toxicity; Blasting danger in air	Toxic; Inflammable; Low evaporating temperature (lower than 1atm); Incompatible with copper under high temperature; Instable at temperature higher than 120 ℃; Low evaporating pressure
Common adsorbents	Zeolite Silica gel	Activated carbon Metal chlorides	Activated carbon Zeolite

Table 2.2 Comparison between water, ammonia and methanol [20]

The performance of the sorption technology is mainly decided by three aspects: the sorption working pair [51-61], heat and mass transfer in the adsorbent bed [62-66], and the thermodynamic cycle of the sorption [67-72]. The working pairs of the gas-solid sorption will be introduced in Section 2.2.2.

The improvement of the solid-gas sorption system could be made by the modification of the heat exchanger, as the heating-desorption and cooling-adsorption process are always accompanied with huge amounts of heat rejected or absorbed [73, 74]. It determines the

research desire to optimise the heat and mass transfer in the reactor-heat exchanger. One common method is to enlarge the surface area of the heat exchanger. Several categories of heat exchangers have been studied: finned-tube heat exchanger [75], fixed heat exchanger [62], fluidised heat exchanger [76], spiral plate heat exchanger [77], multi-compartment heat exchanger [78], and so on. Moreover, to advance the heat transfer between the adsorption bed and the thermal fluids, the heat-pipe thermal controls were proposed and researched to be integrated with solid-gas sorption refrigerators [79-82]. Some representatives include the conventional thermosiphon heat-pipe thermal control [83], split heat-pipe thermal control [84], double heat-pipe thermal control [85], gravity heat-pipe thermal control [86], sorption heat-pipe thermal control [79], ejector heat-pipe thermal control with falling film evaporation [87]. This development resulted in smaller heat exchanger areas with high heat transfer coefficients, which enables the high flexibility for the heat exchanger to be implemented in solid-gas reactors. Thus, the heat-pipe control proves itself to be an effective thermal control technology to enhance the heat exchanger, and also advances the reliability of machines on the solid-gas sorption refrigeration aspect [83].

Besides, many researchers have started the exploration work of the thermodynamic cycle to enhance the sorption technology since the 1980s. The primary intermittent thermodynamic cycle was widely utilised in the single-bed solid sorption at the initial stage. In the single-bed sorption, the sorption bed is connected to a condenser and an evaporator alternatively due to a different process. The nature drawback of the intermittent working leads to discontinuous cold production. Two-bed sorption refrigeration systems, therefore, provide one solution to overcome this obvious disadvantage by interchanging the operating modes of two sorption beds in one cycle to produce cooling continuously. Other advanced cycles like heat recovery sorption cycle, mass recovery sorption cycle, mass and heat recovery sorption cycle, double/multi-effect sorption cycle, combined double-way sorption cycle, double-effect and double-way sorption cycle, two/multi-stage sorption cycle were also proposed and investigated with the intention to improve the solid-gas sorption refrigeration performance [88, 89].

The coefficient of performance (COP) is a key parameter to assess the working performance of a sorption refrigeration cycle. It can be defined as Equation 2.4. According to the equation, COP grows with the increase of the evaporated mass of the refrigerant Δx_{evap}, or the decrease of the heat consumption $\sum mC_p\Delta T$. Therefore, three types of the sorption refrigeration cycles were developed: reducing the heat consumption by heat recovery process, improving the

cycled refrigerant mass by mass recovery process, and widening the temperature range by lowering the regeneration temperature of the adsorbents.

$$COP = \frac{Q_{cold}}{Q_{in}} = \frac{H_{evap} \cdot \Delta x_{evap}}{H_{de} \cdot \Delta x_{de} + \sum mC_p \Delta T} \quad 2.2$$

Fig. 2.15 is the classification of the different solid-gas sorption refrigeration cycles [50].

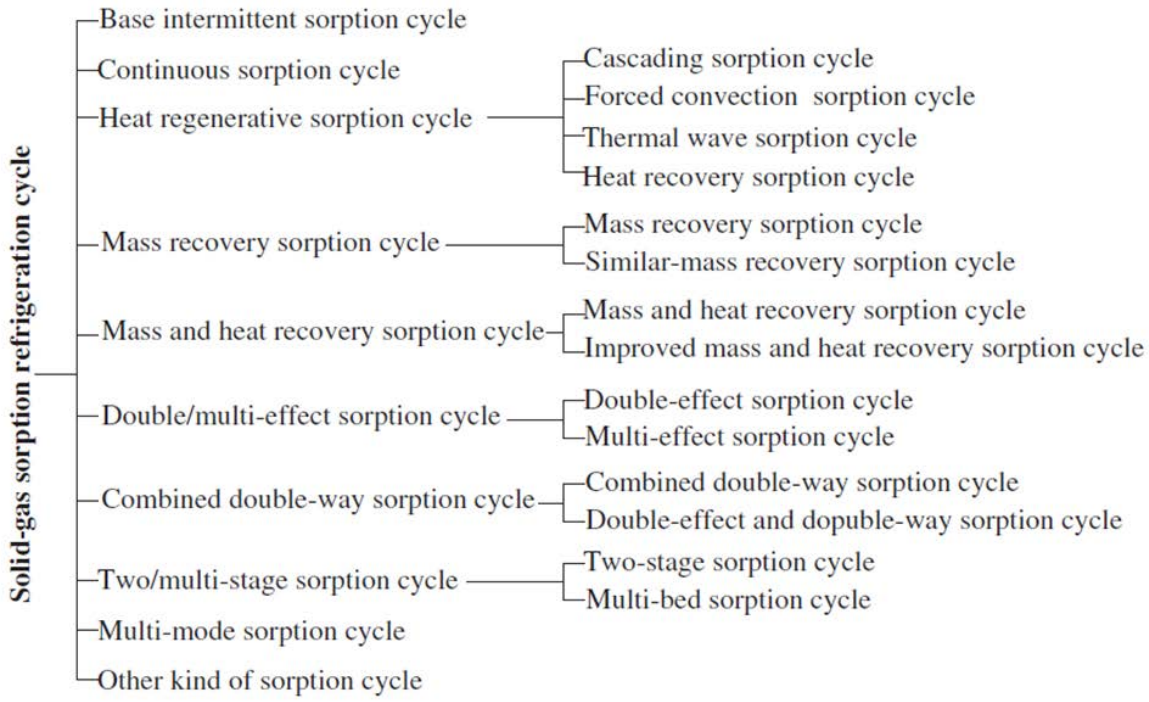

Figure 2.15 Classification of different solid-gas sorption refrigeration cycles [50]

2.2.2 Physical, chemical and composite sorption

Regarding the driven force during the adsorption process, the solid-gas sorption can be classified into two categories: physical sorption and thermochemical sorption [90].

Physical sorption

Physical sorption occurs on the surface of sorbent and is not relative with the solid skeleton itself. The principle of the physical sorption is based on the Van der Waals force between the sorbent and the refrigerant, as shown in Fig. 2.16 [50]. For the physical sorption process, the adsorption heat is nearly equal to the condensation heat.

Solid-gas physical sorption cycle is a bivariant process. It works ranging from the 0% equilibrium line to the 100% equilibrium line during both heating and cooling phases. Furthermore, the working temperature and pressure of the physical sorption are not of one variable functional equation and the processes can occur whenever the operating temperature

and working pressure are within the working region (0% equilibrium line to 100% equilibrium line). Theoretically, the sorption capacity of the adsorbent in the physical sorption is decided by both the temperature and pressure variables.

The activated carbon (AC), zeolite, silica gel and the graphite are common adsorbents in the physical adsorption area.

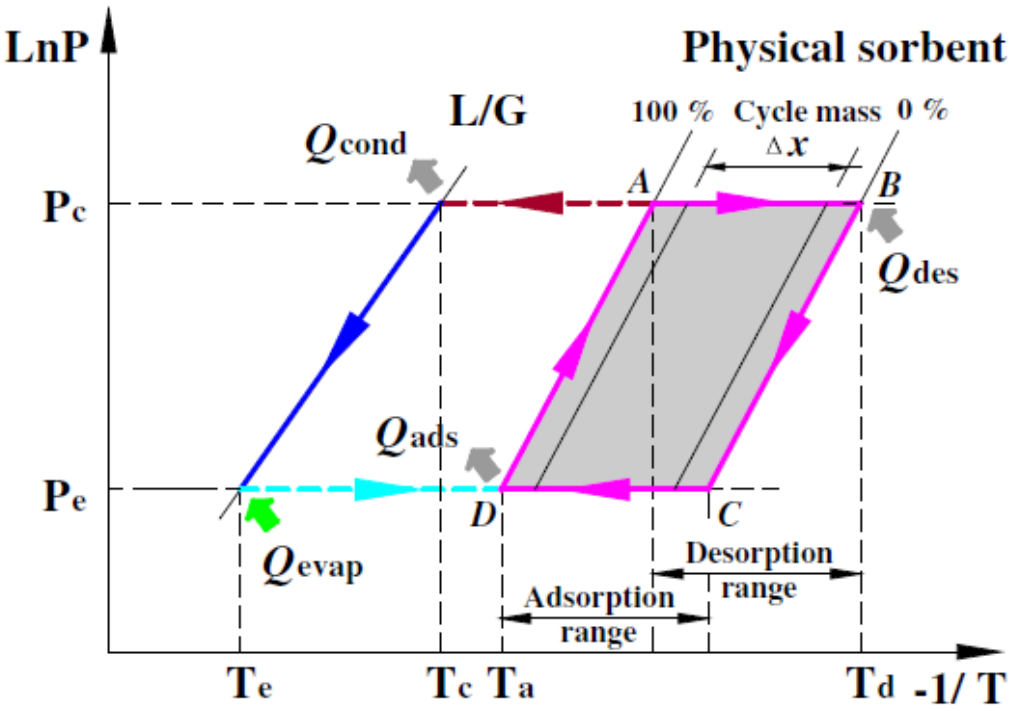

Figure 2.16 Working principle of physical sorption refrigeration cycle [50]

Chemical sorption

Different from physical sorption refrigeration, thermochemical sorption occurs with chemical changes. The working principle of chemical sorption is based on the reversible chemical reaction process as shown in Fig. 2.17 [50].

Chemisorption is a mono-variant process. The working temperature and pressure are of one variable functional equation, and this sorption works right on the solid-gas equilibrium line. Once the working pressure/temperature is not the equilibrium pressure/temperature, there occur chemical changes between the sorbent and the refrigerant. For the chemical reaction, only the equilibrium drop drives the solid-gas thermochemical sorption refrigeration cycle.

Based on the different interaction force of the molecules, for example, complexation, coordination, hydrogenation and oxidisation, chemical adsorption has many working pairs,

including metal chloride-ammonia [91], metal hydride-hydrogen [92], and metal oxide-oxygen.

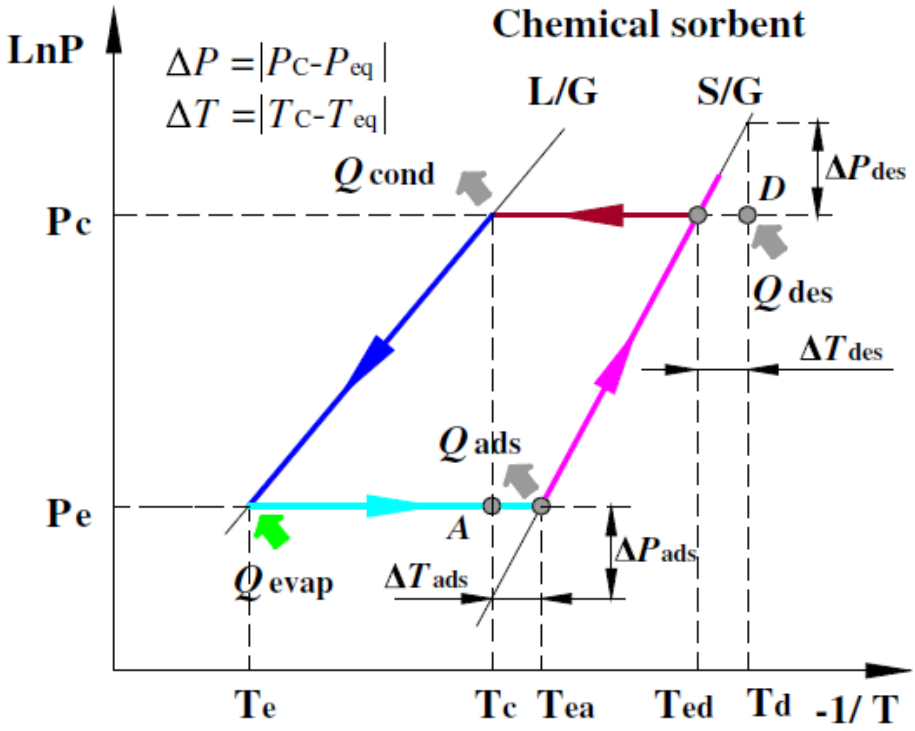

Figure 2.17 Working principle of thermochemical sorption refrigeration cycle [50]

Among them, Metal Chlorides-Ammonia (M_aCl_b-NH_3) and Metal Hydrides-Hydrogen (MH_n-H2) are more commonly used, Equation 2.3 and Equation 2.4 respectively present their reactions. The metal chlorides can form more than one complex with ammonia as the equations indicated. ΔH_r is the molar enthalpy for the chemical reaction, which is also the required heat to desorb the refrigerant of ammonia. At the starts of the reaction, the adsorption and desorption are very quick.

$$M_aCl_b + cNH_3 \leftrightarrow M_aCl_b(NH_3)_c + c\Delta H_r \quad \text{2.3 (a)}$$

$$M_aCl_b(NH_3)_c + (d-c)NH_3 \leftrightarrow M_aCl_b(NH_3)_d + (d-c)\Delta H_r \quad \text{2.3 (b)}$$

$$MH_n + mH_2 \leftrightarrow MH_n \cdot mH_2 + m\Delta H_r \quad \text{2.4}$$

Different from the metal chlorides using the latent heat of the ammonia to produce refrigeration, the metal hydrides use the endothermic reaction heat during the decomposition of the compound $MH_n \cdot mH_2$. Because hydrogen is flammable and combustible, and the

manufacturing cost of the metal hydrides is high, this working pair is mainly applied in cryogenic or high-temperature heat pumps [93].

Salt	$\Delta H\ (J \cdot mol^{-1})$	$\Delta S\ (J \cdot mol^{-1} \cdot K^{-1})$	m	n	Mr $(g \cdot mol^{-1})$
NH_4Cl 3/0	29,433	207.9	3	0	53.4
KI 4/0	32,015	219.8	4	0	166
LiBr 5/4	33,689	225.9	1	4	86.8
$PbCl_2$ 8/3.25	34,317	223.6	4.75	3.25	278
NaBr 5.25/0	35,363	225.2	5.25	0	102.9
CaI_2 8/6	35,991	229.3	2	6	293.8
LiCl 4/3	36,828	224.6	1	3	42.3
$PbBr_2$ 5.5/3	37,665	229.4	1	2	367
$BaCl_2$ 8/2	38,250	232.4	8	0	208.2
$PbCl_2$ 3.25/2	39,339	230.1	1.25	2	278
$PbBr_2$ 3/2	39,758	229.4	1	2	367
PbI_2 5/2	40,595	229.1	3	2	461
$CaCl_2$ 8/4	41,013	230.1	4	4	110.8
NaI 4.5/0	39,339	224.5	4.5	0	149.9
$BaBr_2$ 8/4	41,850	229.8	4	4	297.1
$SrCl_2$ 8/1	41,432	228.6	7	1	158.4
$CaCl_2$ 4/2	42,269	229.7	2	2	110.8
$BaBr_2$ 8/4	42,687	230.7	2	2	297.1
LiCl 3/2	44,780	229.8	1	2	42.3
$SrBr_2$ 8/2	45,617	229.3	6	2	247.4
BaI_2 6/4	46,454	231.6	2	4	391.1
BaI_2 4/2	47,291	230.3	2	2	391.1
$MnCl_2$ 6/2	47,416	227.9	4	2	125.7
LiCl 2/1	48,128	230.6	1	1	42.3
$CaBr_2$ 6/2	48,965	230.4	4	2	199.8
$ZnCl_2$ 4/2	49,467	230.0	2	2	136.2
$FeCl_2$ 6/2	51,266	227.8	4	2	126.6
SrI_2 6/2	52,731	230.5	4	2	341.4
$MnBr_2$ 6/2	53,066	228.3	4	2	214.7
$CoCl_2$ 6/2	53,987	227.9	4	2	94.3
$MgCl_2$ 6/2	55,661	230.4	4	2	95.1
$FeBr_2$ 6/2	55,828	228.1	4	2	215.6
BaI_2 2/0	56,079	235.0	2	0	391.1
CaI_2 6/2	58,590	231.0	4	2	293.8

$CoBr_2$ 6/2	58,590	227.5	4	2	218.7
$NiCl_2$ 6/2	59,218	227.6	4	2	129.5
MnI_2 6/2	59,301	227.4	4	2	308.7
FeI_2 6/2	60,683	227.5	4	2	309.6
$MgBr_2$ 6/2	63,612	230.2	4	2	184.1
$NiBr_2$ 6/2	64,240	227.2	4	2	218.5
NiI_2 6/2	65,453	224.1	4	2	312.5

Reversible: $Solid \cdot (n+m)NH_3 + \Delta H \leftrightarrow Solid \cdot nNH_3 + mNH_3\ (gas)$

Table 2.3 Thermodynamic reaction values of common metal chloride/bromide/iodide-ammonia sorption pairs [94]

The thermodynamic reaction values of common metal chloride/bromide/iodide-ammonia sorption pairs are presented in Table. 2.3 [94]. The chemical adsorbents have large adsorption capacities. Different adsorption working pairs show different performances. For instance, -40 ºC to -10 ºC is the lowest refrigeration temperature for the working pairs of metal chloride-ammonia, whereas the lowest refrigeration temperature for the working pairs of metal oxide-oxygen is -30 ºC to 0 ºC.

The following criteria were proposed by Lebrun et al. [95] for the selection of working pairs: the investment including the price of the adsorbents and the generator and the performances such as the temperature of the refrigeration, the cooling quantity of per kilogram adsorbents, and the total mass of the adsorbent. Also, the comprehensive consideration of both like the refrigeration quantity per unit mass of the total system and per unit heat transfer area or the change of the temperature per unit area of the heat exchangers is of importance. Regarding the criteria as mentioned earlier, the International Institute of Refrigeration has designated the metal chloride-ammonia as the substitution of chlorofluorocarbons (CFCs) and hydrochlorofluorocarbons (HCFCs) among all the working pairs of chemical adsorption refrigeration [96]. The working pair of metal chloride-ammonia has far higher adsorption refrigeration capacity than that of the metal hydride-hydrogen and also a far lower price than that of the metal hydride, proving itself to be the advanced working pair for this technology.

Resorption

Based on the chemical sorption, a special example, resorption refrigeration cycle, evolves [97-102]. It replaces the refrigerant container by a second sorbent reactor, and the latter reactor consumes the decomposition heat at a lower temperature with a different sorbent to produce the useful cold as shown in Fig. 2.18 [50]. At the beginning of the 1990s, the concept of resorption was first used into refrigeration [99]. A thermochemical working pair of $NiCl_2$-

$BaCl_2$ was used, and the influence of external temperature for the resorption speed was simulated in this study.

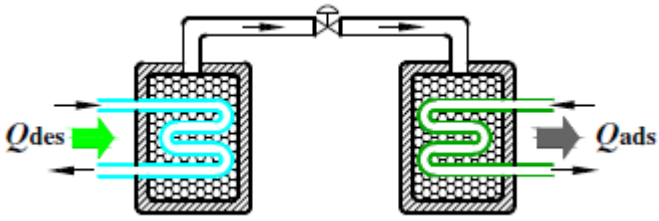

Figure 2.18 Schematic diagram of thermochemical solid-gas resorption cooling [50]

The resorption cycle reaches a higher cooling capacity than the conventional thermochemical sorption refrigeration process, as the reaction heat of the salt is usually higher than the vaporisation heat of the liquid for the same amount of refrigerant consumption. Therefore, the former cycle can theoretically achieve a higher coefficient of performance (COP). Moreover, the resorption system contains no liquid refrigerants in the devices, which enables this technology to be applied in vibration conditions such as on the vehicles.

Despite the advantage aforementioned, the low driving pressure drop constraints the resorption cycle with the low chemical reaction rate and the long cycle time [103]. $MnCl_2$ and $SrCl_2$ are explored in the following chapters as they have been proven to be one of the optimal pairs in the resorption refrigeration, theoretically.

Composite sorption

The disadvantage for the basic solid-gas sorption refrigeration, whether the physical or the chemical sorption cycle, is the low working performance. The coefficient of performance (COP) is usually too low to be commercially competitive, and this challenge pushes the researches to enhance the solid-gas sorption refrigeration technology [104]. This low efficiency is mainly caused by the conglomeration and aggregation phenomenon in the sorbents, during the manufacturing or sorption cycles.

The composite sorbent is constructed of porous matrixes (Some common porous matrices: expanded graphite [48, 105, 106], carbon fibres [107-109], activated carbon [110-112], silica gel [113-115]) and chemical sorbents. It is fabricated to enhance the heat transfer and mass transfer process of the sorption. The high thermal conductivity of some porous materials provides superior heat transfer of sorbent while the porosity ensures enough permeability for the mass transfer in the sorbent. Moreover, due to the component of the chemical salt, the

composite sorbent has the advantage of huge adsorption capacity. Table 2.4 is a summary of the working pairs applied in solid-gas sorption [50].

Solid-gas sorption working pairs		Heat source temperature	Remarks (application, main advantages and disadvantages)
Physical sorption working pairs	Silica gel-water	60-85℃	Application for solid-gas sorption air-conditioning. Advantages: high latent heat of vaporization of water, suitable for solar-powered cooling systems and desiccant cooling systems, the reutilization of low-temperature waste heat. Disadvantages: unsuitable for the refrigeration application below 0 ℃, vacuum system and it is very sensitive to the leakage risk.
	Zeolite-water (The common kinds of zeolite include zeolite 13X and zeolite 4A)	>150-200℃	Application for solid-gas sorption air-conditioning. Advantages: high latent heat of vaporization of water, suitable for the reutilization of high-temperature exhaust gas and desiccant cooling systems. Disadvantages: only used for the refrigeration higher than 0℃, high desorption temperature.
	Activated carbon/activated carbon fiber-methanol	80-110℃	Application for air-conditioning, refrigeration, ice-making. Advantages: large sorption capacity, low adsorption heat, suitable for solar-powered refrigeration systems. Disadvantages: low latent heat of vaporization of methanol, unsuitable for heat source temperatures higher than 120℃.
	Activated carbon/activated carbon fiber-ammonia	>130-150℃	Application for air-conditioning, refrigeration, ice-making. Advantages: good mass transfer, relative high latent heat of vaporization of ammonia, wide range of heat source temperatures. Disadvantages: toxicity, the incompatibility with copper used in heat exchanger.
	Activated carbon/activated carbon fiber-134a	>90-100℃	Application for air-conditioning, refrigeration, ice-making. Advantages: good mass transfer, wide range of heat source temperatures. Disadvantages: low sorption capacity and cooling power per mass unit, low latent heat of vaporization of refrigerant, relative high GWP value.
Chemical sorption working pairs	Metal chloride (calcium, barium, strontium, nickel chloride, etc.) /bromide/iodide-ammonia	>50-350℃	Application for air-conditioning, refrigeration, ice-making, deep-freezing. Advantages: high sorption capacity per mass if sorbent, wider range of heat source temperatures, suitable for refrigeration and heat transformer. Disadvantages: the swelling and agglomeration of salt, poor heat and mass transfer, reduction in the sorption capacity after many cycles.
	Metal oxides (calcium oxide, lead oxide, magnesium oxide, titanium oxide, etc.)-oxygen/water/carbon dioxide	>150-1000℃	Application for refrigeration, cryogenic, high-temperature heat pump. Advantages: high sorption capacity, wider range of heat source temperatures, suitable for cryogenic conditions and high-temperature heat pump. Disadvantages: the swelling and agglomeration of salt, poor heat and mass transfer, reduction in sorption

			capacity after many cycles, unsuitable for low-temperature heat source due to their high desorption temperatures.
	Metal hydrides (advanced porous metal hydrides and the misch metal matrix alloys containing Ni, Fe, La, Al, H, etc.)-hydrogen	>110-400℃	Application for air-conditioning, refrigeration, deep-freezing, heat pump. Advantages: fast sorption kinetics, high reaction heat for heat pump, high packed density, wider range of heat source temperatures. Disadvantages: low specific cooling power per mass of sorbent, the swelling and agglomeration of salt, poor thermal conductivity after many cycles.
Composite sorption working pairs	Silica gel/metal chlorides (lithium chloride and calcium chloride, etc.)-water	60-85℃	Application for solid-gas sorption air-conditioning. Advantages: high sorption capacity per mass if composite sorbent high latent heat of vaporization of water, suitable for solar-powered cooling systems and desiccant cooling systems. Disadvantages: only used for the refrigeration higher than 0℃, poor heat transfer of composite sorbent, and the risk of salt solution leakage from composite sorbent.
	Metal chlorides/porous matrix (activated carbon, expanded graphite, activated carbon fibers, vermiculite, metallic foams, etc.)-ammonia	>50-350℃	Application for air-conditioning, refrigeration, ice-making, deep-freezing, heat pump, heat transformer. Advantages: high sorption capacity per mass if composite sorbent, good heat and mass transfer of composite sorbent, wider range of heat source temperatures. Disadvantages: the complex fabrication of composite sorbent using mixture or impregnation and consolidation, the incompatibility with the conventional material of copper used in heat exchanger.

Table 2.4 A summary of conventional working pairs for solid-gas sorption refrigeration [50]

2.2.3 Studies on the composite materials

The activated carbon, active carbon fibre, silica gel, graphite and the expanded graphite are the main employed porous matrixes in producing composite adsorbents.

Activated Carbon (AC):

The purpose of using the activated carbon as a matrix is to utilise the rich micropore structure of the activated carbon which enhances the mass transfer performance. Wood, peat, coal, fossil oil, charcoal, bone, coconut shell and nut stone are always the resource of the activated carbon.

The modern manufacturing processes of AC include the carbonization and activation to obtain the desired porous structure and mechanical strength [116]. The measured sections of white oak (Quercus alba) are cut from a block to accurately provide a flat area that is perpendicular to the growing direction [116]. For the acid-treated AC, the samples are then treated with the phosphoric acid solution for an hour at the ambient temperature for the penetration of the wood structure. After that, the mixture needs to be heated for over two hours at the temperature of 170 ^{o}C and the pressure of atmospheric level, under the flowing nitrogen. It

will be held for half an hour and retreated at the temperature of 200 ^{o}C to 650 ^{o}C. At the end of the second heating process, the leached and dried AC is prepared. Original AC will be manufactured in the same way without the acid penetration process.

Fig. 2.19 [117] shows the structure of the activated carbon. The microcrystal of the bone-produced activated carbon is a six element carbon atomic ring, and the functional groups connected to the carbon-atomic ring influences the adsorption performance[117]. For instance, the connection of the arene-group to the ring will increase the adsorption performance whereas the sulfonic group will work inversely. Moreover, the different original carbonaceous materials and the activation method lead to different functional groups on the activated carbon surface. Irregular channels, having larger pore area at the surface of the grain and narrow pore area within the grain, compose the net structure of activated carbon [118]. The specific area of activated carbon varies from 500 m^2/g to 1500 m^2/g. And the activated carbon pairs have a lower adsorption heat than that of other categories of physical adsorbent pairs.

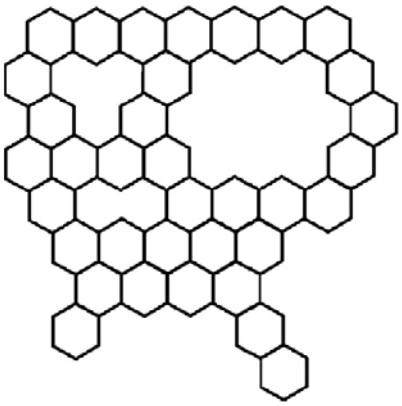

Figure 2.19 Structure of activated carbon [117]

Activated Carbon Fibre (ACF):

Compared with the traditional granular, extruded and powder grades of activated carbon (GAC, EAC and PAC), activated carbon fibres (ACF) possess advantages such as easy separation, high rates of adsorption and uniform tailored porosity [119]. Activated carbon fibre is generally utilised in fabric production such as cloth and tissue. Since the 1960s, the carbon fibre has been rapidly developed and widely applied because of their ability to improving the strength and stiffness of the structural components. Compared with the granular activated carbon material, the carbon fibre has advantages of much larger specific surface area, more uniform pores, better heat transfer performance and better mass transfer performance [120].

It is currently manufactured by some commercial companies, from PAN (polyacrylonitrile), cellulosic, pitch precursor fibres and phenolic. For example, polymer fibres can be manufactured by the fibre company, and they are converted to ACF later by the carbon firm [119]. The manufacturing of ACFs has three main processes: stabilisation/pre-treatment of the precursor fibres (pitch, polyacrylonitrile, cellulosic fibres, and phenolic resin), carbonization of the fibres after the stabilisation and activation of the fibres by physical or chemical means [121]. Moreover, the various processes can result in the specific porosities and functionalities. In principle, acrylic fibres, including pre-oxidized acrylic fibres, can be directly carbonised or activated without the stabilisation, thereby saving the cost on fabrication.

Composing AC fibre with chemical adsorbents has the apparent improvement on the heat transfer performance of the chemical adsorbents by the good thermal conductivity from the AC fibre, and the other advantage is developing the mass transfer performance by remitting the swelling and caking problems of the chemical adsorbents due to its rich microporous structure. Attributed to T. Dellero [107, 122] and L.L. Vasiliev et al. [66, 102], activated carbon fibre is successfully employed to enhance the chemical adsorption performance of metal chloride, but also suppress the expansion and agglomerate phenomenon.

However, activated carbon fibre also has some disadvantages when compared with granular activated carbon, such as its anisotropic thermal conductivity and the higher contact thermal resistance between the fibre and the wall of the adsorbent bed.

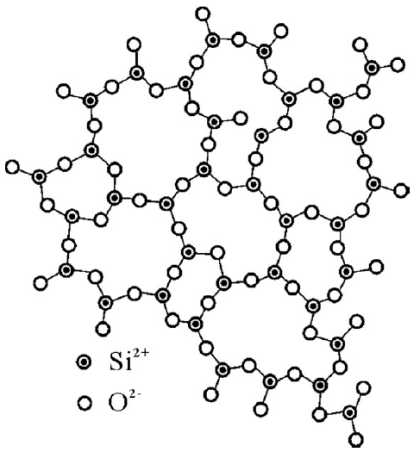

Figure 2.20 Array of SiO4 in silica gel [118]

Silica gel:

The silica gel is the amorphous synthetic silica with a rigid and continuous net of colloidal spherical silicon dioxide particles, as presented in Fig. 2.20 [118]. The pore diameters of one kind of silica gel are only and narrow. Ordinary silica gel has the pore diameters of 2,3nm (A

type) and 0.7nm (B type), and the specific surface area is around 100m^2/g to 1000m^2/g. Due to a considerable adsorption ability, silica gel is widely used in desiccation as A-type silica gel can be applied on all occasions of desiccation whereas B-type silica gel only can be used where the relative humidity is over 50%. However, it also has a defect when silica gel absorbs water and releases huge amount of heat at the same time, which could increase the temperature of the silica gel to 100ºC and then smash the silica gel.

$$Na_2SiO_3 + 2HCl + nH_2O \rightarrow 2NaCl + SiO_2 \cdot nH_2O + H_2O \qquad 2.5$$

The silica gel is always manufactured by mixing sodium silicate and an inorganic acid such as sulfuric acid and hydrochloric acid in the industry as Equation 2.5 indicates. This reaction produces one kind of hydrosol of silica acid, which can generate white settlings like jelly when it has been statically placed for a while. After washing, drying and activating the settlement, silica gel is finally obtained. Besides, changing the concentration, temperature, pH and activation temperature can manufacture many types of silica gel like having huge surface area or large pore volume.

Graphite:

The graphite has similar properties to pure carbon. Under the condition of high temperature and high pressure, the hydrocarbons can turn to the carbon of a graphite structure [150].

The graphite has following characteristics in the application: lubricity, small thermal expansion performance, good thermal and electrical conductivity, applicability in a wide range of temperature, stable chemical performance and non-toxic, plasticity and other properties. In addition, graphite can be easily coated and encapsulated.

Expanded Graphite (EG):

Expanded Graphite (EG) has other merits other than the good heat and mass transfer performance, anisotropic thermal conductivity and permeability inherited from the natural graphite.

It is made of natural graphite through high-temperature expansion progress. S. Mauran proposed one expansion method [123-126]: Dry the graphite in the oven under the temperature of 60 ºC for 10 h, then turn the temperature up to 400 ºC to 700 ºC for 12 min to 15 min expansion. After expansion, the expanded graphite is obtained as shown in Fig. 2.21, and the sheet structure of it get changed to spiral vermiform as presented in Fig. 2.22 [123].

Figure 2.21 Expanded graphite

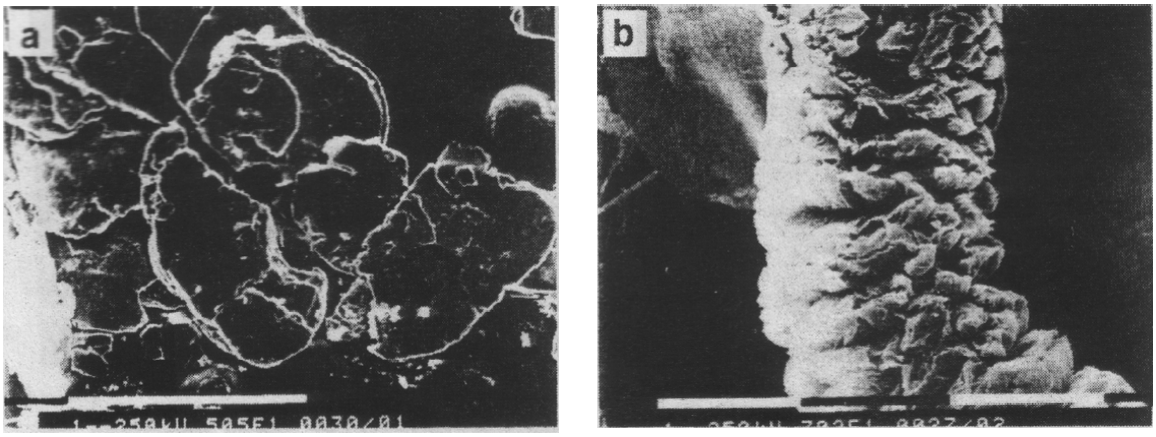

(a) Sheet structure of the graphite (b) Spiral vermiform of EG

Figure 2.22 SEM photos of graphite [123]

Many researchers studied on the thermal properties of EG and proved this material had the potential to improve the sorption behaviours.

T. Eun [127] produced silica-EG composite for adsorption heat pumps and advised the expansion time for EG was 10 min at 600 ^{o}C. In the research, expandable natural graphite was expanded at 400–600°C in ambient atmosphere with the treating time varying. The manufacturing procedures of Eun's composite are presented in Fig. 2.23. Fig. 2.23 (a) is the expandable graphite powder and (b) is the heat treatment for expansion. Fig. 2.23 (c) is the powder of prepared EG. Procedure (d) is the slurry of expanded graphite and water in the ratio of 5.00 ml water per gram graphite, while after that Fig. 2.23 (e) shows the mixture of the slurry and silica gel. The mixture was compressed in process (f) and then vacuum dried at the temperature of 80°C for an hour. Finally, the block of the silica gel-EG was obtained after a further drying in vacuum at the temperature of 145°C for over two hours with the aim of removal of all moisture in procedure (h). The result also found that the thermal conductivity (over 10 W/(m·K))was improved by the implement of EG with an acceptable permeability value (over 10^{-12} m^2), but influence on the favourable properties of heat and mass transfer are

actually contradictory to each other. Therefore, the characteristics of the composite should be optimised for applications.

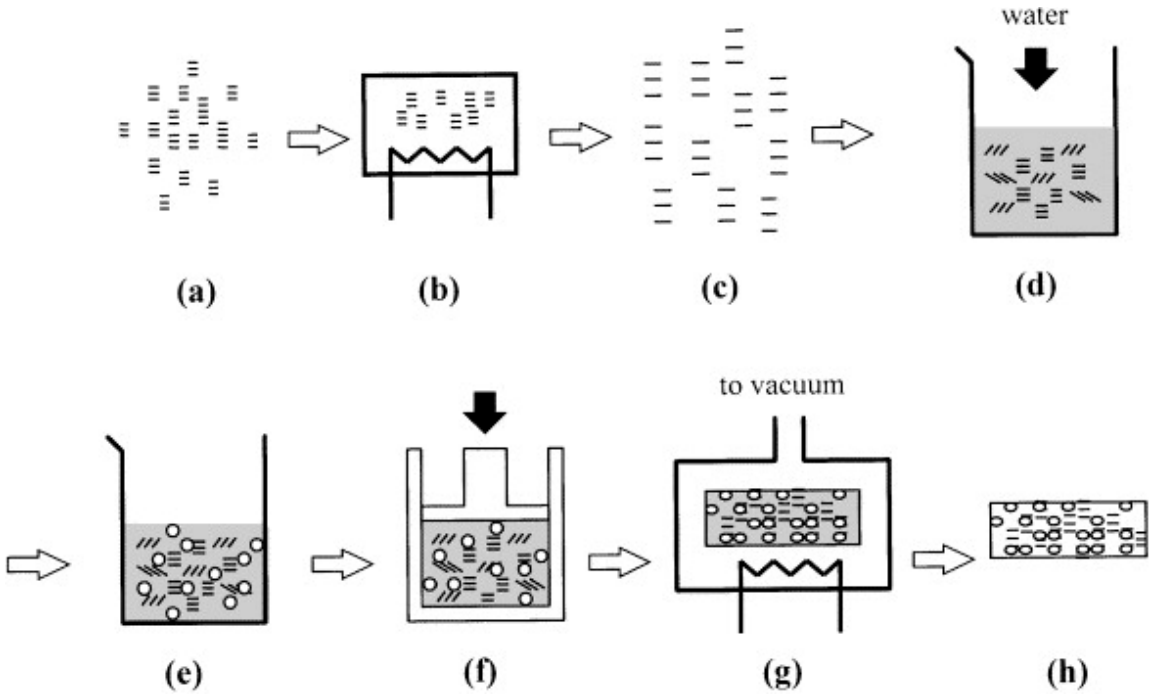

Figure 2.23 Manufacture procedure of composite blocks

Shanghai Jiao Tong University K. Wang [46] and R.G. Oliveira [128] conducted a study on the composite adsorbent of expanded graphite with $CaCl_2$ ($CaCl_2$-EG). The expandable graphite was heated through a thermal treatment at the temperature of 300 °C under the atmospheric pressure for two hours. The procedures of manufacturing the consolidated composite were the same used by T. Eun [129]. The powder of Calcium Chloride was solved in the water and then was added to the slurry of water and EG. Later, the mixture was compressed and dried to the obtain the consolidated sorbents. Under the condition of vaporisation temperature of -10ºC to -20ºC and the cooling temperature of 20ºC to 30ºC, the specific cooling power and volume refrigeration capacity of this kind of composite adsorbent is respectively higher than 1000W/kg $CaCl_2$ and 290kg/m^3 $CaCl_2$, respectively. Testing on the adsorbent, under the condition of forming $CaCl_2 \cdot 2NH_3$, the thermal conductivity reaches to 787W/ (kg·ºC). And the COP is calculated to 0.35.

L.W. Wang et al. have studied the thermal conductivity of compacted expanded natural graphite with different bulk density and expanded graphite after sulfuric acid treatment with the different composite ratio as shown in Fig. 2.24 [130-132]. In her study, EG was made by being heated in the oven at 600 ºC to 700 °C for the processing of 12 min to 15 min, from the graphite manufactured by Shanghai YiFan Graphite Company at 50 mesh to 80 mesh with a higher purity than 99 %. This graphite is also the material used in this PhD projects. For the

production, AC and EG were mechanically mixed, pressed and consolidated. She studied the perpendicular direction to the compression direction as it would provide a better heat and mass transfer performance than the paralleled direction. The thermal conductivity of these different compound adsorbents indicates that the salt ratio of the composite adsorbents affects the thermal conductivity of ammoniated salts strongly, and so does the consolidated density [133].

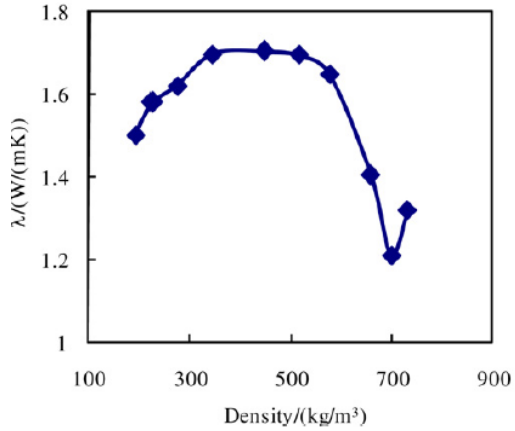

(a) Average thermal conductivity of disc compacted expanded natural graphite blocks (DCENG)

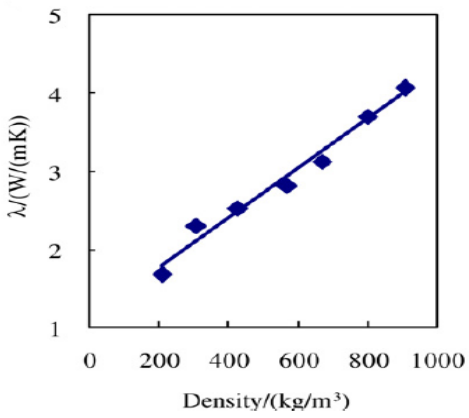

(b) Average thermal conductivity of plate compacted expanded graphite blocks (PCENG)

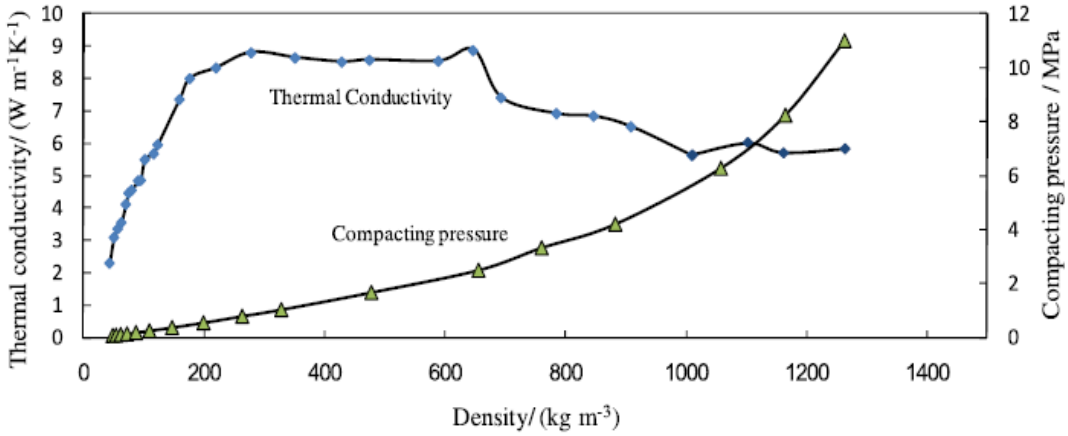

(c) Thermal conductivity and compacting pressure of consolidated disk of expanded graphite treated by the Sulfuric Acid (ENG-TSA)

Figure 2.24 Thermal conductivity tests on different expanded graphite materials [130-132]

Oliveira et al. [134] conducted an experimental investigation on a resorption system, using the $MnCl_2$-EG as the high-temperature salt composite (HTS) and the NaBr-EG as the low-temperature salt composite (LTS). At the temperature of 15℃, the SCP and the COP of this system could be 129 kW/kg and 0.46, respectively.

Some other enhancement of the thermal property or the sorption performance has been reported, such as multi-walled carbon nanotubes/ EPDM rubber, carbon nanotubes/reinforced

syntactic foam, graphite Nano-platelets/silicone resin, reduced graphene oxide/PVDF-HFP polymer, and carbon coated copper nanoparticles/silica gel composites [135-138].

A few researchers studied on the heat transfer properties of the composite sorbents adding carbon nanomaterials. The ammonia adsorption and thermal transfer performance of pure multi-walled carbon nanotubes (MWCNTs)and the composite adsorbent made of $CaCl_2$ and carbon nanotubes have been studied.

The fabrication of the composite $CaCl_2$-MWCNTs can be stated as follows. The MWCNTs was manufactured by a catalytic carbon vapor deposition methodology, declared by the company of Nanjing Jcnano technology Co., LTD (China) [139]. With the residual catalyst, the purity of the nanotubes is still higher than 95 %. The average diameter and length of the MWCNTs is 11 nm and 10 μm, respectively. By impregnating the MWCNTs into the $CaCl_2$ solution, the wet chemisorption composite sorbent of $CaCl_2$ and MWCNTs could be fabricated. To obtain the dry sorbents, the wet mixture needs to be heated in the oven at a temperature of 180 °C. After the water in the sorbents is removed, the salt content should be 80 wt.%.

The pure MWCNTs and $CaCl_2$-MWCNTs are experimentally investigated, and the results show that although the pure multi-walled carbon nanotubes are not appropriate for being adsorbent in solid-gas sorption individually due to its low the refrigeration capacity, they can be applied as the additives to some other chemical adsorbents to enhance their heat transfer performance [140, 141].

As the additives as well as the other composite ingredients are curved, aggregated and entangled together, it cannot easily be dispersed homogeneously, which has a negative influence on the sorption performance. The simple implementation by soaking material into the salt solution or the manual mechanical stirring can only mix the material but not evenly disperse the ingredients. During the drying process, uneven components of the sorbents gather together and produce blocks, and the fine grinding and sieving are required.

It seems to be a solution studying on new fabrication methodologies and exploring other additives. The new manufacturing method should solve the problem of the conglomeration and aggregation. Thus, the uniformity of the sorbents could be improved and so could the thermal properties. With the enhanced thermal property, the comprehensive heat and mass transfer processes can be potentially developed, and the energy performance as well as the energy efficiency of chemisorption could be improved. For the new additives, they should meet the requirement either having an enhancement on the heat transfer or making positives

on the mass transfer. By achieving these requirements, the additives can potentially develop the sorption performance. In addition, they must not react with the sorbent, working fluid, or the reactor.

Carbon coated metal, which is also known as nanoparticles with core-shell structure has several advantages. Carbon coatings can protect the metal core in the ambient environment, maintaining several excellent thermal properties and offering an economically attractive broader use of metal nanoparticles [138, 142-144]. The granule shape in nanometre size can be more easily to spread and occupy a little space in the adsorbent, which could avoid causing great obstruction of mass transfer. Therefore, carbon coated nanoparticles are expected to become a promising effective additive for adsorbents. The copper is one of the best heat conductive metals, but it is not suitable to be used in the adsorbents for the ammonia adsorption and desorption as it reacts with ammonia. Besides, Iron is one natural metal element that could be easy to obtain, and Aluminium takes the advantages of low density and high thermal and electricity conductivity. As a result of this, this project selects typical carbon nanomaterials of nickel, Iron and Aluminium core encapsulated in a carbon shell (Ni@C, Fe@C and Al@C) to be added into the conventional composite adsorbents of $MnCl_2$-EG (high temperature salt composite) and $SrCl_2$-EG (low temperature salt composite) for the experimental sorption performance studying.

2.3 Integrated sorption-Rankine Cycle systems for cooling and power

Apart from the cycles producing a single type of the power output, many combined systems were designed and investigated to convert the heat into the electricity and refrigeration at the same time. Absorption and adsorption cogeneration systems are the two crucial types to be integrated with Rankine Cycle and form the cogeneration systems. Moreover, the combinations of multiple technologies can improve the energy efficiency, as they can either reduce the heat release or yield more productions, given the same heat source.

2.3.1 Integrated absorption-Rankine Cycle

Due to the overlapping of the working fluids, absorption was combined with Rankine Cycle by many researchers to form a cooling and power system.

In fact, Goswami Cycle in Section 2.1.2 is one of the cogeneration systems. It uses the ammonia-water binary mixture as the working fluid [145] and could achieve a maximum second law efficiency of 65.8% at the heat source temperature of 147℃ [28]. Even a sensible heat source such as a solar thermal collector at 77 ºC can dive Goswami Cycle to reach the second law efficiency greater than 60 %. However, the second law efficiency of Goswami

Cycle would not increase when the temperature of the heat source is higher than 147 ^{o}C despite the increase of the first law.

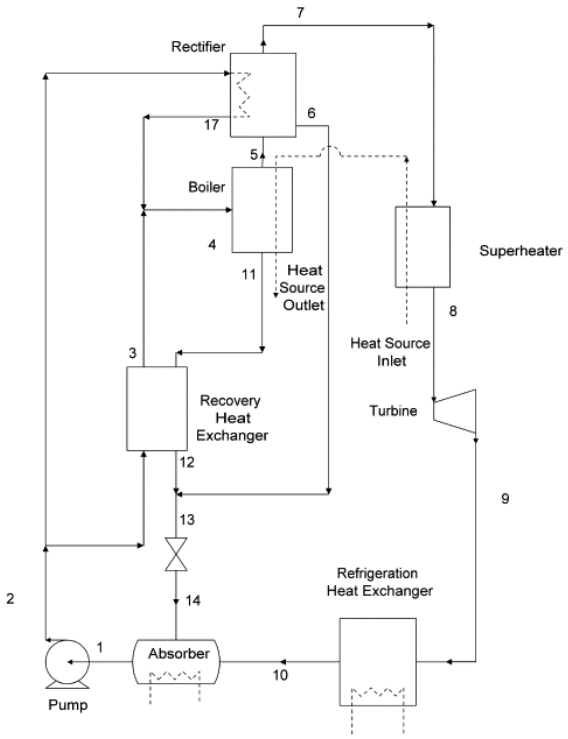

(a) A basic combined power and refrigeration cycle

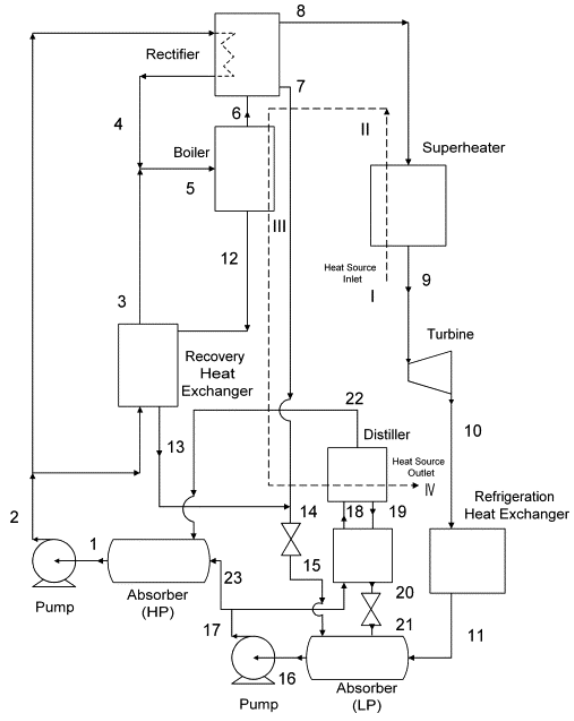

(b) Cogeneration cycle using the heat source for distillation

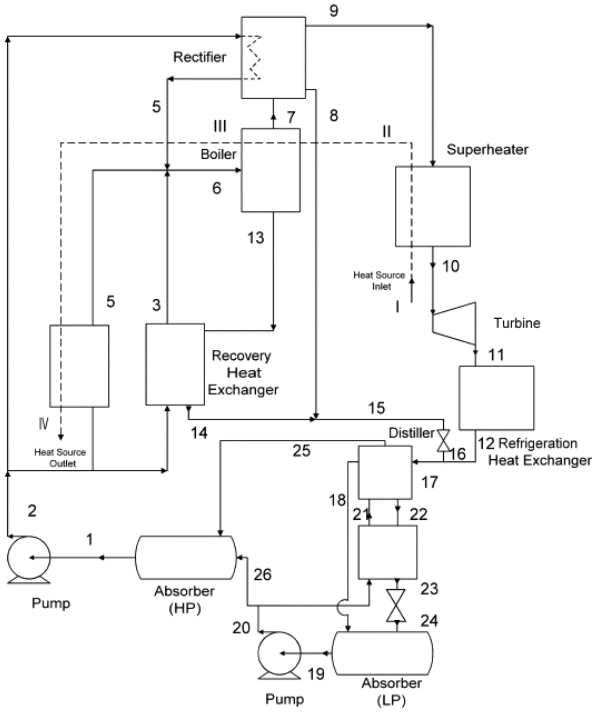

(c) Cogeneration cycle using the condensation heat for distillation

Figure 2.25 Combined power and refrigeration cycles based on Goswami Cycle [146]

Fig 2.25 (a) is a basic cogeneration cycle developed from the original Goswami Cycle, combining the absorber and the turbine [146]. Fig 2.25 (b) and Fig 2.25 (c) draws the

configurations of the cogeneration systems using either the heat source or the condensation heat to produce the vapour for the distiller [146]. The result showed that both modified systems could improve the resource utilisation efficiency over the optimized basic cogeneration cycle in Fig 2.25 (a). The configuration using the heat source for distillation in Fig 2.25 (c) had a slightly higher resource utilisation efficiency when the heat source was at a lower temperature [146]. Besides, when the heat source was at a higher temperature and the output included power only, the discussed cycles roughly equalled to Kalina Cycles.

Based on the absorption and Kalina Cycle, Zheng et al. [147] analysed a cooling and power system employing the absorption technologies as displayed in Fig 2.26. The comparison of the results included the log p-T, log p-h, *T*-*s*, and Gibbs function analysis for the heat pump or the heat engine sub-cycles. The study presented an overall thermal efficiency of 24.2% and an exergy efficiency of 37.3%. It demonstrated the improvement of the Kalina Cycle, due to the capacity of the power and the refrigeration.

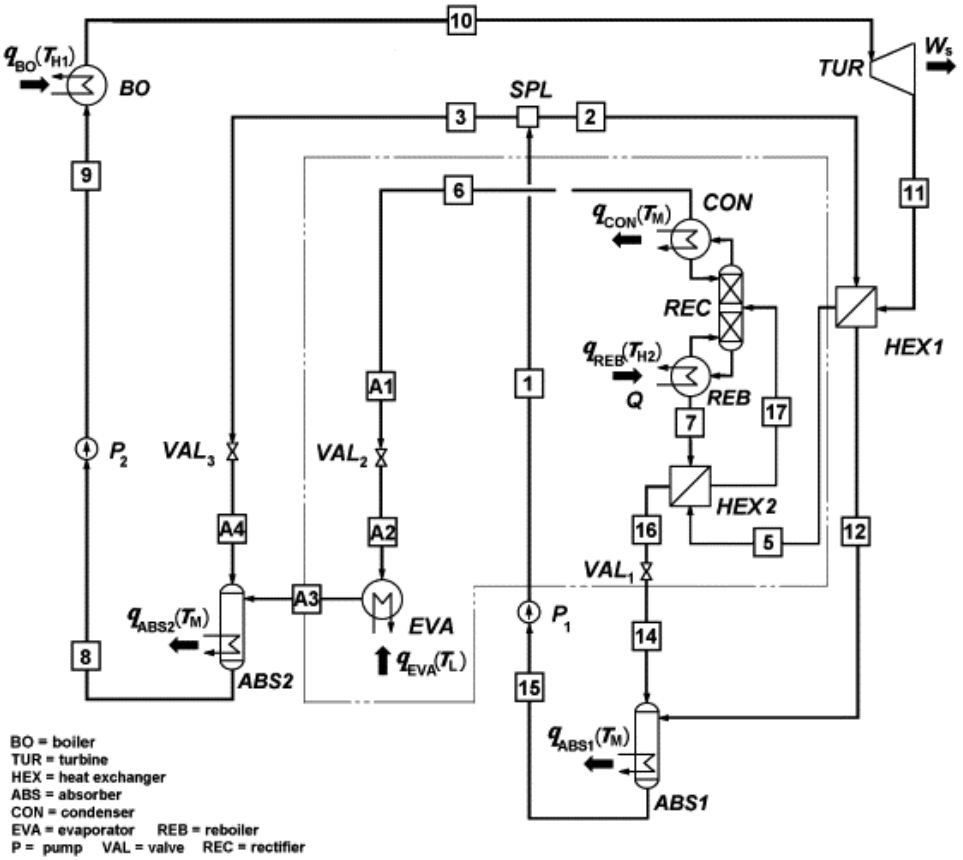

Figure 2.26 Absorption combined cooling and power cycle based on Kalina Cycle [147]

Another cogeneration system was proposed by Liu et al. [148], integrating the ammonia-water Rankine cycle with the ammonia absorption refrigeration cycle. The heat source was around 450℃, and the results achieved a maximum exergy efficiency of 58% and a reduction by 18.2% on the general energy consumption based on separate systems. A parallel mode for a

Rankine Cycle and an absorption refrigeration cycle working together was explore by Zhang et al. [149] with an energy efficiency of 27.7% and an exergy efficiency of 55.7% at the temperature of 450℃. Even the efficiency was improved, the heat source temperature was out of low-grade heat source range.

2.3.2 Integrated adsorption-Rankine Cycle

However, absorption cogeneration systems have drawbacks like a large size. The adsorption technology, who has a robust construction and is easy to be installed, is more advantageous than the absorption in many cases. It has several advantages such as very few moving components, a wide range of working temperatures, high reliability and environmentally friendly refrigerants [150].

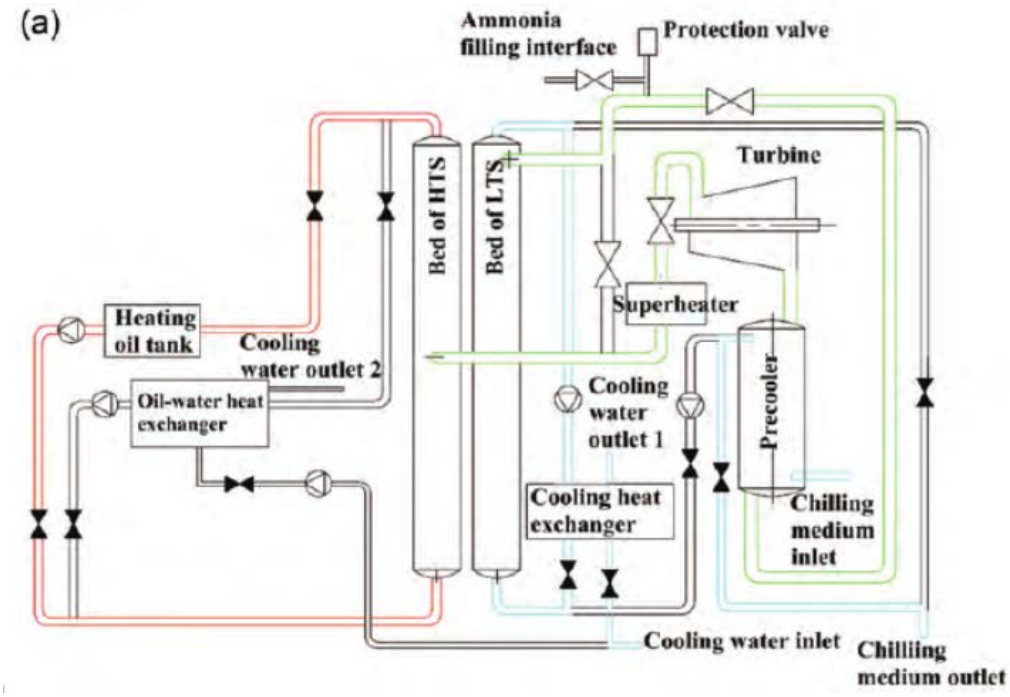

Figure 2.27 A resorption cogeneration cycle proposed by Jiang et al. [151]

Jiang et al. [151] introduced a resorption cogeneration system based on Kalina Cycle as illustrated in Fig 2.27. When the system worked with the heat recovery process, the theoretical energy coefficient of performance (COP) for electrical generation and COP for refrigeration had the improvements up to 0.03 and 0.16, respectively. Moreover, the system features a 50 % higher refrigeration performance than Goswami Cycle.

Wang et al. [152] proposed a resorption cogeneration cycle as drawn in Fig 2.28. The cycle applied the resorption cycle with a turbine to enable the cooling and power functions at the same time. A superheater and a pre-cooler were integrated with the resorption to optimise the performance. The results demonstrate that the cycle could achieve a COP of 0.77 in an

ammonia-based system at a driving temperature higher than 100℃. Compared to Goswami Cycle, this cycle had an over ten times higher COP for refrigeration and an up to 60% higher total exergy efficiency. It was pointed out by the authors that this cycle had a significant market potential as the heat sources of waste heat are dispersed in a relatively small amount. Thus, the systems were required to be simple and have low cost. On the one hand, the superheater could be eliminated due to no liquid fraction after desorption of HTS, which is crucial for the turbine. On the other hand, the pre-cooler could be potentially removed and further simplify the system. In this case, the cycle could use a 10 kW waste heat at 200 ^{o}C to produce approximately 1.42 kW electricity and up to 6 kW refrigeration in an ideal condition.

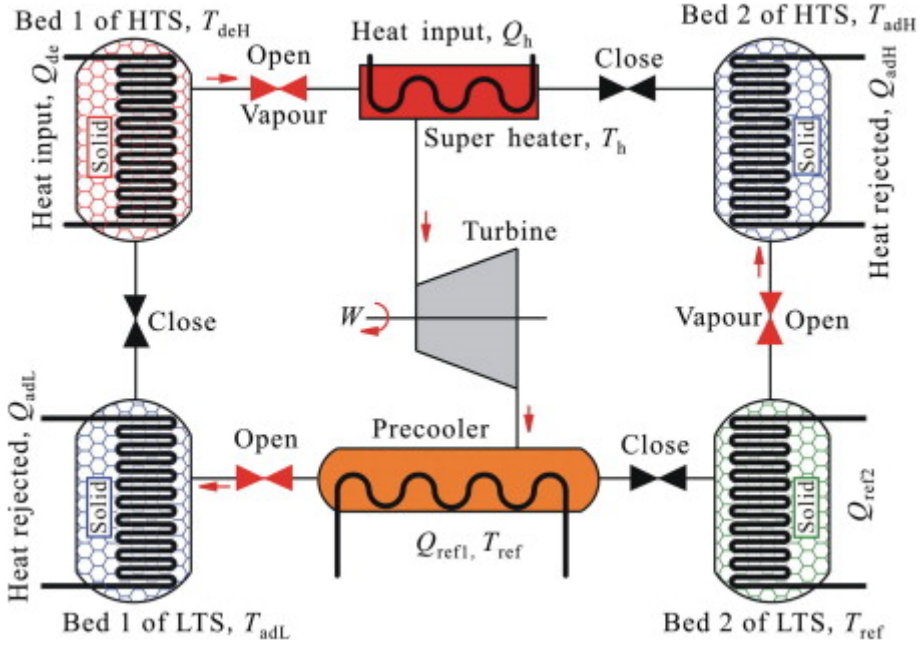

Figure 2.28 A resorption cogeneration cycle proposed by Wang et al. [152]

Bao et al. [49] experimentally integrated the two adsorption units with the scroll expander to simultaneously produce the cold and electricity, as illustrated in Fig 2.29. Different with the configuration shown in Fig 2.28, this system utilised HTS and LTS but still had two condensers and two evaporators. In this aspect, the configuration was more complex. Other major challenges mentioned by the authors included the contradiction between the desorption and the turbine. The rate of the ammonia vapour released from desorption had a peak curve while the turbine required for a stable inlet pressure to produce electricity. This cycle could produce a maximum electricity production of 490 W or a minimum cooling temperature of 5.4 ^{o}C.

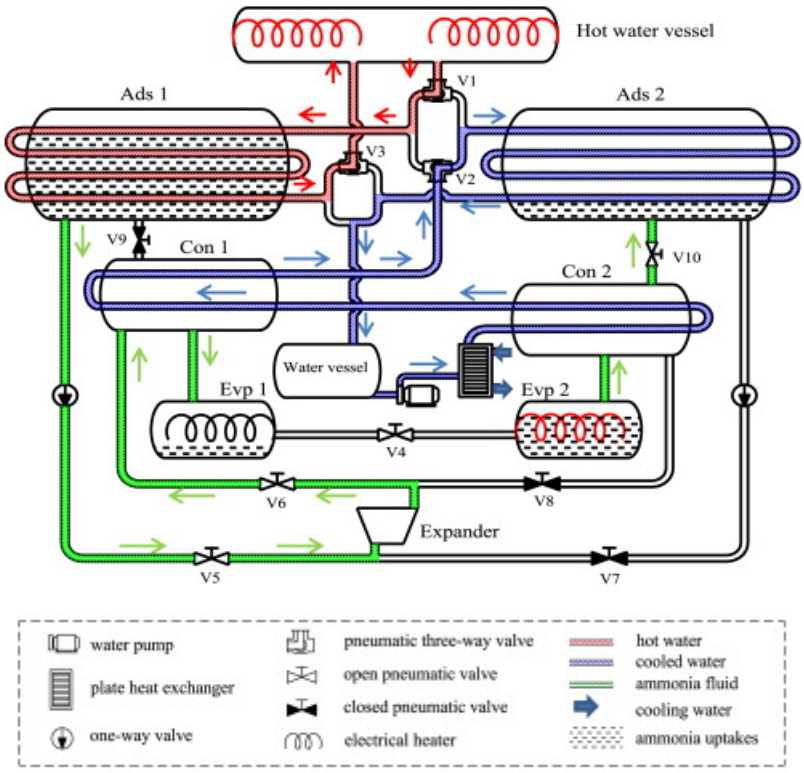

Figure 2.29 A chemisorption cooling and electricity cogeneration system [49]

Later, Bao et al. [153] conducted a modelling investigation to another cogeneration system as shown in Fig 2.30. This configuration simplified one condenser and one evaporator. The highest theoretical COP and exergy efficiency of this cogeneration is 0.57 and 0.62. The results demonstrated that the integrated cogeneration performance was about one third of the expectation of 1 kW power output considering individual components, due to the mismatch between the adsorption part and the expansion part. A compromise of both parts would cause the decrease of the global performance.

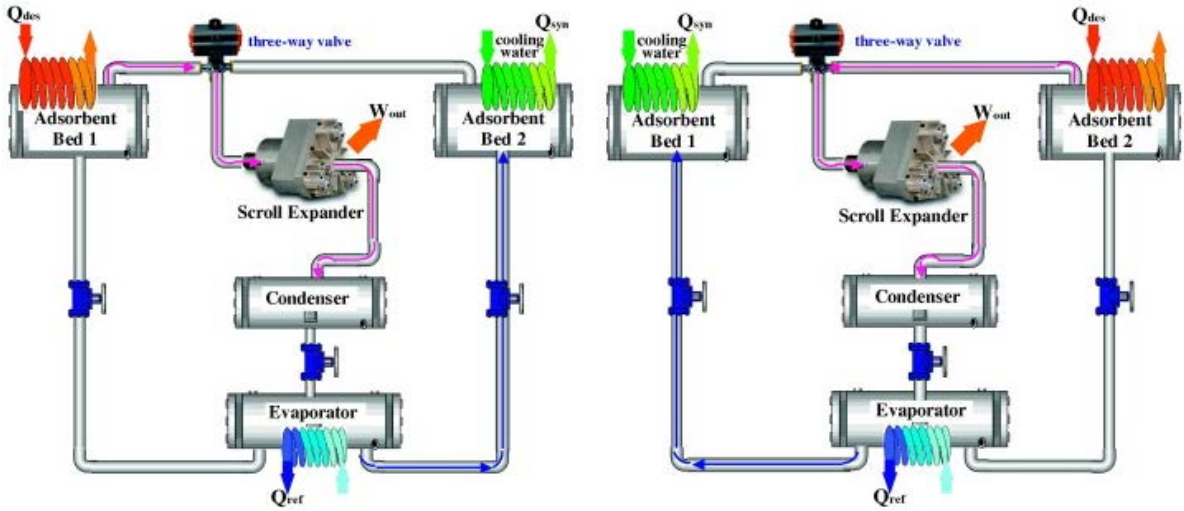

Figure 2.30 A chemisorption refrigeration and power cogeneration system [153]

Jiang et al. [154] combined a scroll expander with the $MnCl_2$-$CaCl_2$-NH_3 resorption cycle as shown in Fig 2.31. Different with the configuration in Fig 2.26, this cogeneration cycle had two additional phase change material (PCM) energy storage tanks. In this cycle, high temperature PCM could store the redundant heat of oil tank 1, and low temperature PCM could maintain the continuous refrigeration production. The maximum total energy efficiency of the cogeneration cycle is 37.6 %.

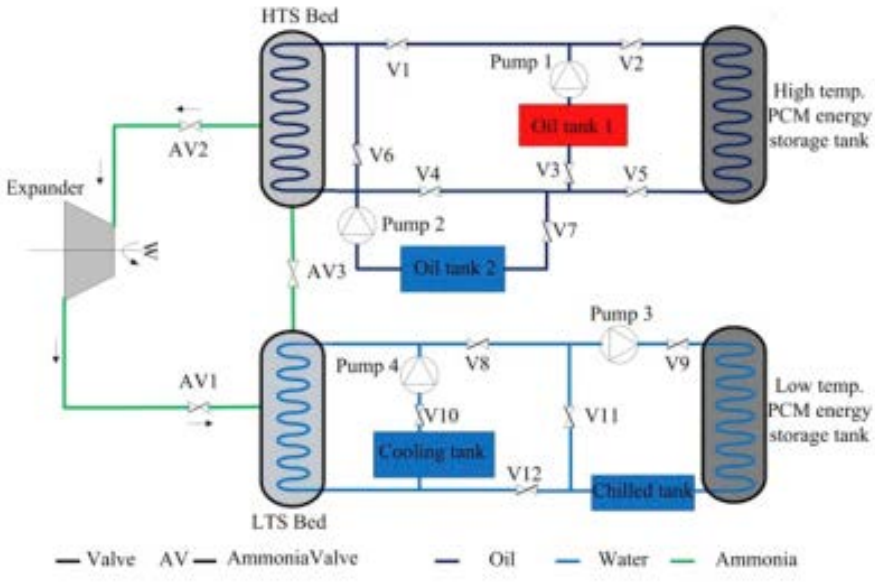

Figure 2.31 A cogeneration cycle proposed by Jiang et al. [154]

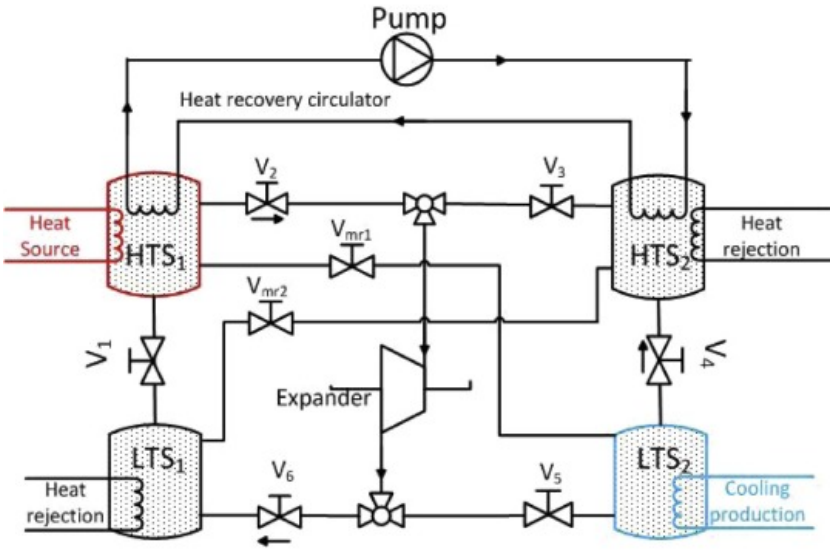

Figure 2.32 A resorption cogeneration cycle with heat and mass recovery processes [155]

Lu et al. [155] improved one resorption cogeneration cycle with the heat and mass recovery process, as shown in Fig 2.32. Two sets of the resorption units were applied to overcome the intermittent chemisorption processes for a continuous cooling and power production. Between

the switch time, the heat of one HTS bed was recovered to pre-heat another HTS bed. During the mass recovery, the HTS bed and LTS bed were connected to balance the excess of the pressure in HTS bed and the lack of the pressure in LTS bed after their desorption. The results showed that the mass recovery played a more crucial role in the refrigeration than the heat recovery. COP of the cogeneration system could be improved by 38% and 35% through the combined heat and mass recovery, respectively using $NiCl_2$ and $MnCl_2$ as HTS.

A two-bed adsorption system was simulated by Al-Mousawi et al. [156], generating cooling and power at the same time. This system had a similar configuration with that in Fig 2.30. However, different working pairs of AQSOA-ZO2/water, MIL101Cr/water and Silica-gel/water were studied in the cogeneration system, achieving a specific power (SP) of 73W/kg and the SCP of 681W/kg. The maximum overall cycle efficiency was 67%, using silica-gel. Al-Mousawi et al. [157] also designed a small scale radial inflow turbine for the cogeneration system. In this case, using silica-gel/water as the working pair could improve the maximum overall cycle efficiency to 69%.

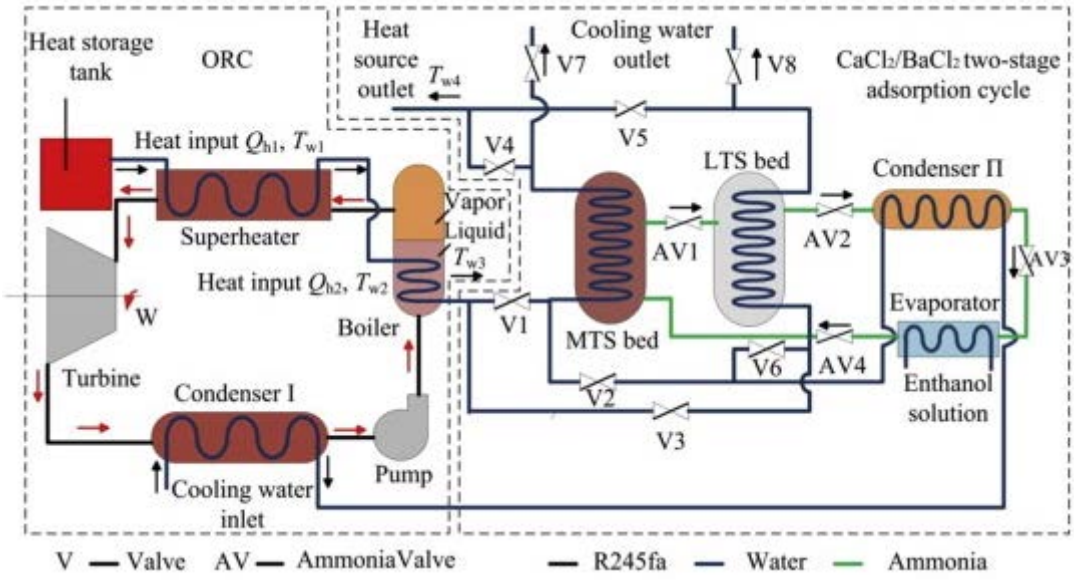

Figure 2.33 A $CaCl_2$-$BaCl_2$ adsorption freezer integrated with the ORC [158]

Jiang et al. [158] proposed a $CaCl_2$-$BaCl_2$ adsorption freezer integrated with the ORC as presented in Fig 2.33. The configuration of the system was quite complex as it combined the dependent adsorption and ORC modules rather than directly converting the pressure difference of the desorbed vapour into power by the turbine. The heat source was first used by ORC then by adsorption units. Moreover, the cooling water out from the condenser in ORC was applied to cool the condenser for a second utilisation. The results demonstrated the total energy efficiency up to 13.1% and the exergy efficiency up to 20.3%.

Al-Mousawi et al. [159] introduced four different configurations of integrated adsorption-ORC systems using two expanders. In the first configuration, ORC used the cold source of the Bed 1 as the heat source to evaporate the working fluid. In the second system, the given heat source first went through Bed 2 and then ORC. In the third cycle, the heat source first entered Bed 2, and then mixed with cold source of Bed 1 to provide the heat source to the evaporator in ORC. In the last configuration as shown in Fig 2.34, the heat source was first used by ORC then by Bed 2. Results showed the maximum SP and SCP achieved were 288W/kg and 552W/kg, respectively, using AQSOA-ZO2 in configuration 4 proposed in the paper.

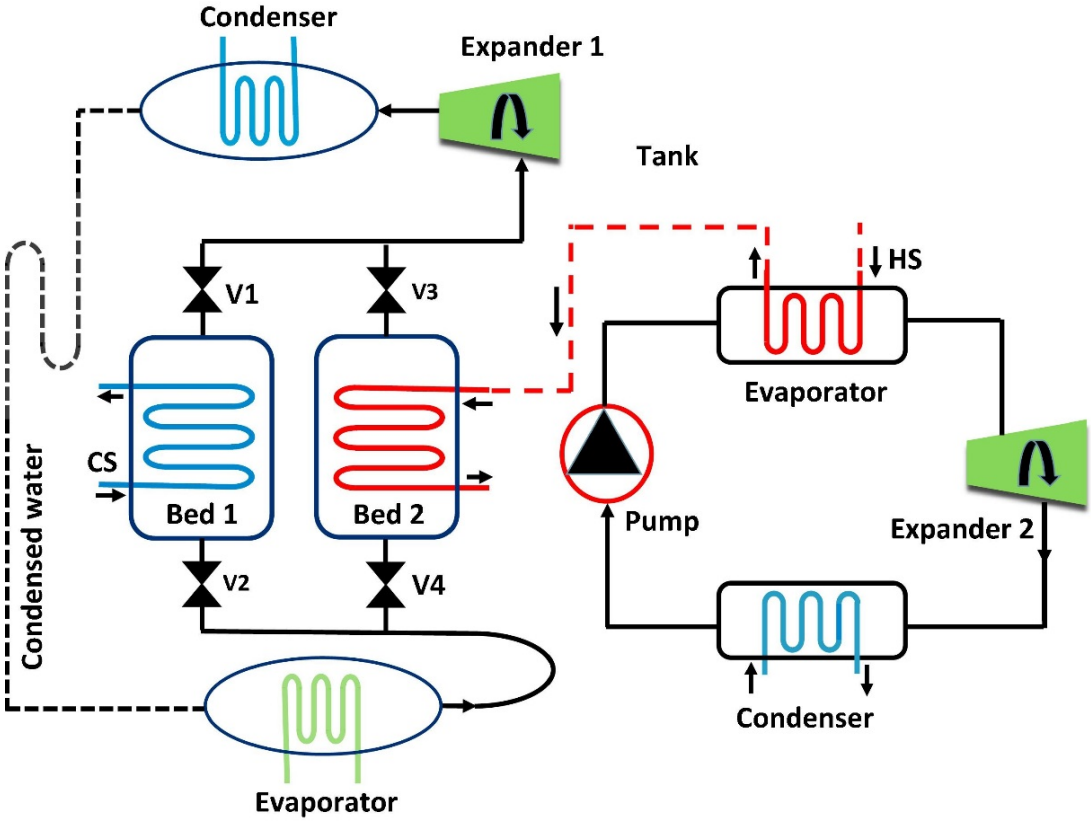

Figure 2.34 Schematic diagram of configuration 4 of the integrated adsorption-ORC system [160]

Many researchers studied the cogeneration cycle by integrating Rankin Cycle with either adsorption or absorption technology as stated in Section 2.3. The integrated cogeneration cycle using absorption suffered from the large size, while the incorporating the adsorption cycle with an expander showed a limited power output [160], due to the low refrigerant rate during desorption. Thus, the configurations combining the adsorption cycle with ORC to form a cascaded energy system would be preferable, rather than directly using the pressure difference of the refrigerant to produce power.

2.4 Summary

To conquer the contradiction between the environment and the rapid increasing energy demand, Chapter 2 displays many heat-driven power generation or refrigeration technologies, highlighting ORC for electricity or solid-gas sorption for cooling. At the end of this chapter, some layouts of the cascaded Rankine Cycle-sorption systems are reviewed for their abilities to realise the simultaneous cogeneration in the low-grade heat applications.

- In Section 2.1, the previous studies of the heat-driven power generation cycles were reviewed from Carnot Cycle to different configurations of ORC. Carnot Cycle is the thermal cycle in theory, and it is not practical to build such a cycle approximately close to it. Following Carnot Cycle, Rankine Cycle is found to have some problems such as the temperature range is not suitable to use water in the low-grade thermal energy field. Due to the mentioned drawbacks, organic fluid is applied in Rankine Cycle to fit the cycle into the low-grade thermal energy conversion field. Later, the review compares ORC, Kalina Cycle and Goswami Cycle, and the result demonstrates that ORC is one of the widely recognised technology in low-grade heat conversion applications. Some other layouts are compared in the review, including SRORC, DRORC, RORC, ORC with a recuperator, DLORC, steam-ORC system, and Transcritical cascade-ORC system. ORC with IHX and DLORC are two superior configurations for their simple but reasonable alterations. The criteria for the selection of the working fluid is essential to the application of ORC, and the dry or isentropic fluid is suggested to be used in this cycle. Moreover, according to the working condition, different criteria should be considered. The review indicates that the potential of ORC to be enhanced is quite limited, as this technology is relatively mature after a long exploration history with several variations. However, ORC is still attractive to be integrated with other cycles and to form a cascaded energy system.
- Apart from ORC, the heat-driven chemisorption refrigeration is a high-efficiency energy-capturer in turning low-grade heat into cooing power. The most significant disadvantage for the physical and thermochemical sorption cycle, is the low working performance. The composite adsorbents can conquer the problem, composed by the porous media (porous structure and high thermal conductivity) and chemical salts (large adsorption and desorption quantities). Many studies have been done to improve the material of the sorbents. However, the composite still suffers from conglomeration and aggregation problems, which has negative influence on the sorption performance. A developed fabrication method is required for the homogeneous quality of the

manufactured composite. Moreover, nano carbon materials are proved to be suitable additives for conventional sorbents. Carbon-encapsulated metals, with a carbon coat preventing the metal core reacting with the ambient, maintains the excellent thermal properties of their metal cores. The granule shape in nanometre size can be more easily to spread and occupy a little space in the adsorbent, which could avoid causing great obstruction of mass transfer. Therefore, the author selects Ni/Al/Fe@C as the additives to prepare and explore the novel adsorbents based on the conventional $SrCl_2/MnCl_2$-EG.

- In the third section of Chapter 2, the cogeneration systems integrating Rankine Cycle with sorption technologies, are investigated for the configuration and the performance. Through the background digesting, due to the low cooling capacity, absorption-ORC system has the drawback of the large size, more costs and less flexibility to produce the same amount of cooling production as adsorption system does. Moreover, integrating an expander with adsorption cooling cycle suffers from the limited power production due to the low refrigerant rate through the turbine.

Therefore, cascaded ORC-adsorption/resorption system will be explored in this PhD project. It is expected to relieve the contradictions between the environmental depletion and the energy demands, as they can improve the overall energy conversion of low-grade heat.

Chapter 3 Methodology

3.1 Introduction

Based on the discovery in literature review, integrating ORC with chemisorption technologies could be a solution to improve the energy conversion of low-grade heat, which has a practical application in the condition requiring for electricity and cooling at the same time. A simulated model of integrated ORC-adsorption (ORC-AD) system is tested to support the idea that the cascaded system can enhance the utilisation of the low-grade heat. The reasons for selecting the simplest ORC and adsorption cycle in the thermodynamic study are:

- The basic ORC has the lowest energy efficiency compared to other ORC configurations, which sets the bottom line of the conversion efficiency of the low-grade heat. In this case, using any other variations of ORC used in the integrated cycle could only have a higher efficiency than the systems based on the simplest ORC. Therefore, if this cogeneration system is proved to have improved the low-grade heat utilisation, it is revealed that all ORC can improve the utilisation of the low-grade heat integrating with chemisorption cycles. Moreover, the basic ORC has the advantages of the simplest layout of the system requiring the least number of the components.
- Compared with absorption, adsorption refrigeration has larger cooling capacity, which means smaller space requirements and more productions. Moreover, conventional chemisorption composite has its limitations of unsuitable manufacturing processes, conglomeration and low thermal conductivity. Potential enhancement can be achieved by exploring the material for chemisorption technology. Thus, adsorption cycles are decided to be integrated with the basic ORC.

However, ORC has a long history of development and it is a relatively mature technology, which means the limitation of the potential improvements.

To further enhance the performance of low-grade thermal energy, chemisorption is focused in the respect of improvement as the main components in the integrated system.

Composite sorbents inherent the advantages from the chemical and physical sorbents, regarded as the superior chemisorption sorbents, but they still suffer from the adsorption performance as the present manufacturing has the limitation to enable the uniformity of the sorbents. A developed methodology for the chemisorption sorbents fabrication is reported, through many times experiments, which is observed to have eliminated the conglomeration and aggregation problems of the sorbents.

Moreover, inspired by the desired property of the metals, carbon coated metals are applied in the manufacturing as the additives into the conventional composite. With the metal core, the thermal characteristics of the carbon nano material are improved, and with the carbon jacket, the metals are prevented to react with the ammonia or the salt. As heat and mass transfer processes are the main influence of the sorption performance, the additives are expected to have positive to the sorption performance as it can potentially enhance the heat transfer process of the sorbents.

After prepared the sorbents, the thermal-physical properties of the sorbents are tested to prove if the additives have the positive impact of the chemisorption composite and thus will potentially enhance the sorption performance. Scanning Electron Microscopy (SEM) and Energy Dispersive X-ray spectroscopy (EDX) are applied to observe the surface morphology and to distinguish if the ingredient of the sorbents are evenly distributed, while SEM Laser Flash Analysis (LFA) is utilised to estimate the thermal property of the composite and thus to assess the possibility of the additives to improve the heat transfer process during sorption tests.

Later, the fabricated chemisorption composites are experimentally explored on the sorption performance to evaluate the influence of the novel sorbents on the comprehensive heat and mass transfer processes.

Apart from the original version of ORC-Adsorption (ORC-AD) system, other combinations of ORC and chemisorption (adsorption and resorption) are written into models and compared according to the various orders of the top cycle, using the advanced physical model from the experimental adsorption units.

Consequently, the optimal candidates of the system use the optimised chemisorption composite from the experimental results to evaluate the most improvement could be made in this PhD project.

Thus, the methodology would be divided into:

- Thermodynamic study of ORC-AD system
- Manufacturing and thermal-physical property tests of the composite
- Experimental tests of the composite sorption performance
- Comparison of ORC-AD/resorption and AD/resorption-ORC
- Fit and use the kinetic model of the optimal novel sorbents into the optimal ORC-chemisorption simulation

3.2 Integrated ORC-adsorption system for cooling and power

3.2.1 Principle of the cogeneration system

Fig. 3.1 presents the basic principle of the coupling ORC-AD system. The red line is the heat source of low-grade heat such as solar energy or industrial waste heat. The module on the left of the figure with four orange components is ORC, and the module on the right with two sets of adsorption units is the chemisorption part.

From point 1 to point 4, the red line represents the heat source:

- During process 1 – 2, ORC is the top cycle using the external thermal source;
- When the heat source flows from point 3 to point 4, the adsorption/desorption system is the bottom system recovering the rest of the heat consumed by ORC.

The processes of ORC can be described as follows:

- During the process 5 – 6, the working fluid of ORC is heated and evaporated by the heat source to the superheated stage at point 6;
- From point 6 to point 7, the working fluid of ORC flows through the expander to produce mechanical power or electricity;
- During process 7 – 8, the working fluid of ORC is condensed in the condenser with heat rejected to the cold source;
- From point 8 to point 5, the working fluid of ORC is pumped to a higher pressure, prepared for the next evaporation process.

The adsorption module can be explained as follows:

- Desorption: When the adsorbent bed is heated by low-grade heat, ammonia is desorbed from the sorbent and it results in the high pressure in the sorbent bed. The pressure difference drives ammonia to flow into the ammonia vessel. In this stage, the ammonia vessel works as a condenser. With the condensation heat rejected to the ambient, the ammonia vapour is then condensed in the condenser.
- Adsorption: When the first set of adsorption unit is in the desorption process, the second set sorption cycle is switched into adsorption mode. In this stage, the sorbent bed is at a low pressure after the desorption of the last stage, which drives the ammonia in the ammonia vessel at a high pressure to evaporate and move into the sorbent bed. Thus, the ammonia vessel in the second set works as the evaporator. During this process, the cooling power is provided in the evaporator, as a result of the heat consumption by the evaporation of ammonia. Besides, when ammonia flows into

the reaction bed, it is adsorbed by the sorbents and the adsorption heat is rejected to the environment.

- Simultaneous refrigeration: Two sets of sorption cycles could be switched into adsorption and desorption modes in turns. Thus, as the sorption module always has one set is in adsorption, the refrigeration is produced during the cycle time. Otherwise, the cogeneration is intermittent with only one set of adsorption apparatus.

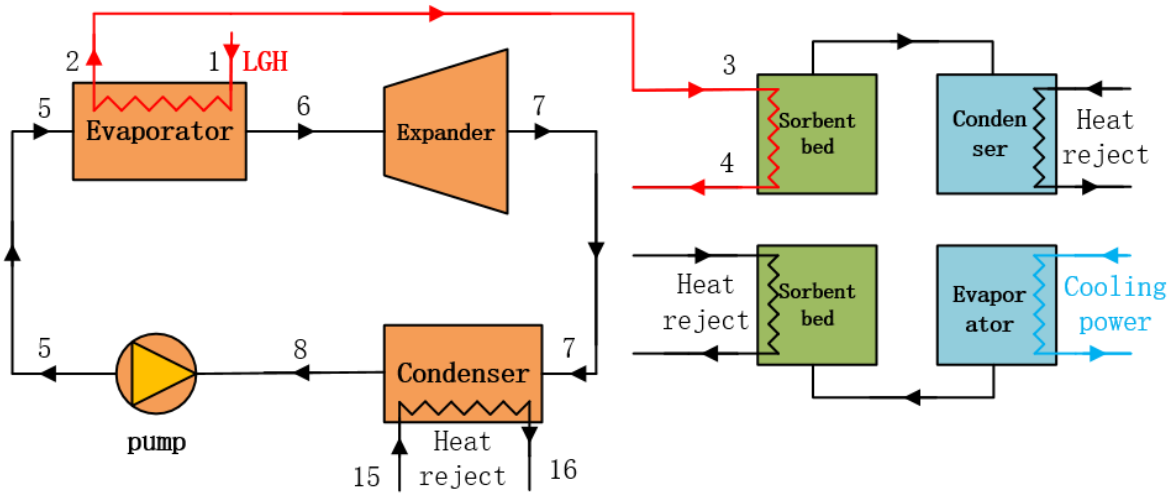

Figure 3.1 Schematic diagram of ORC-AD system

The basic ORC and adsorption models are applied as illustrated in the figure to simplify the simulation. The reason for selecting the simplest mode of ORC has been stated in Section 3.1. The investigation of the cogeneration system focuses on the preliminary thermodynamic analysis corresponding to different working conditions.

The working fluid simulated in ORC is R245fa with the reason stated below. This PhD project mainly focus on the system layouts and the improvement of the chemisorption composites, so the selection is based on the common working fluids. R245fa is a very common working fluid used in ORC, refrigeration or air-conditioning, with advantages such as easy to purchase and low cost. Moreover, it matches the recommendation from the literature review as it is one of the dry working fluids.

3.2.2 Software used in simulation

MATLAB and REFPROP are used to code the models. MATLAB is a numerical computing environment and programming language software developed by MATHWORKS Company. The second tool used in the modelling, REFPROP, could combine a desktop environment with a programming language for iterative analysis and design processes. REFPROP is the acronym for the reference fluid properties, developed by the National Institute of Standards

and Technology (NIST). The database enables the calculation of the thermodynamic and transport characteristics of industrially crucial fluids and their mixtures without the cumbersome work of referring to the literature one by one.

Fig. 3.2 gives an example of using REFPROP in MATLAB codes. The code is written in the Editor window in the centre of the screenshot in either the order of Equation. 3.1 or Equation 3.2. The term prop_req is the wanted property constrained by other two characteristics of spec1 and spec2 with the corresponding values (value1 and value2). Substance1, substance2, ...x are the name of the first, second and other substances in the fluid. The green bar in the Editor window turns into red in the condition that some mistakes are made in the texts. After finishing the writing of the codes, scripts are saved and run. Both buttons for running and saving the document are in the top column. The command window is at the bottom of the screen as shown in Fig 3.2, if the coding is correct. The result referring to the database in REFPROP will be displayed in the right top window of workspace.

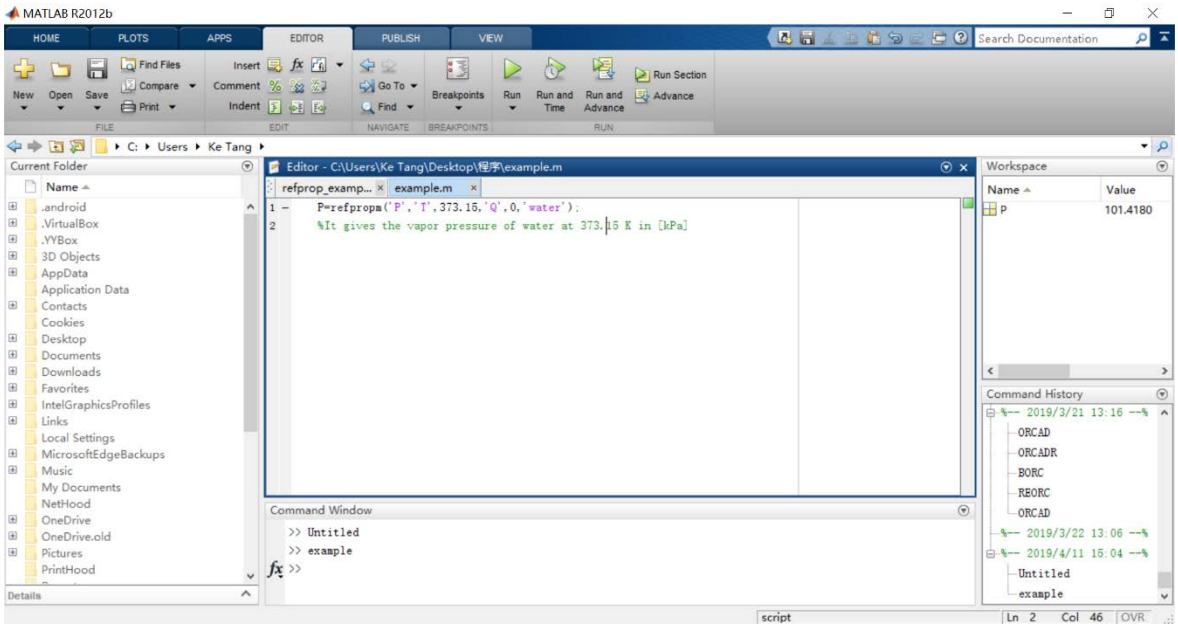

Figure 3.2 An example using REFPROP in MATLAB

Result=refpropm(prop_req, spec1, value1, spec2, value2, substance1) 3.1

Result=refpropm(prop_req, spec1, value1, spec2, value2, substance1, subastance2, ….x) 3.2

The characters representing various properties are listed in Appendix A with their default units required by the REFPROP, which should be treated with extreme carefulness during the coding period. Otherwise, the errors of the units are hard to found and corrected once happen with not enough attentions.

By applying REFPROP, the wanted properties of the fluid can be obtained through any two given properties. Thus, the equations for several characteristics are sometimes ignored in below sections as the values are retrievde by this method.

The simulation of the cooling and power system combines the adsorption cycle with an ORC by the heat source, which means the properties of the heat source entering the adsorption bed are the same with the characteristics quitting the evaporator of ORC. The models of ORC and adsorption modules are built separately in Section 3.2 and Section 3.3.

3.2.3 Mathematical model of the ORC

An ORC is employed in the system as the top cycle. The basic ORC model consists of four main modules: an evaporator, an expander, a condenser and a pump, as illustrated in Fig. 3.3. In this case study, ORC uses R245fa as the working fluid. The heat source for ORC is the engine exhaust, and the cold source for the condenser is the tap water with the given parameters in Table 3.3.

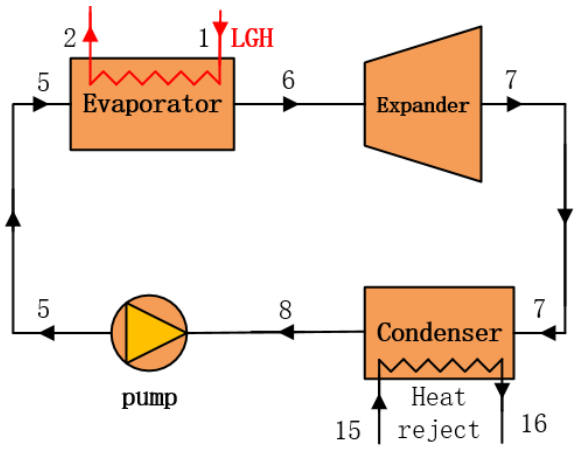

Figure 3.3 Traditional ORC module simulation

Pump (point 8 to point 5):

The working fluid is pumped to a high pressure from p_8 to p_9. Equation 3.3 is the temperature of the fluid, defined by the cold source temperature T_{15} and the condenser properties. $\Delta T_{cond,ORC}$ is the temperature difference between the inlet water and the outlet organic fluid of the condenser. By applying REFPROP, the other properties of the organic fluid such as the entropy or the enthalpy can be determined by the condition of the saturated liquid phase and a given pressure p_8 at point 8. This process is used throughout the simulation work to obtain other characteristics of the fluid, but it is sometimes not directly stated in the calculation.

$$T_8 = T_{15} + \Delta T_{cond,ORC} \tag{3.3}$$

Equation 3.4 indicates the increased pressure of the working fluid, which consumes the extra power W_{pump} exclude the heat source from low-grade thermal energy. Δp_{pump} is the pressure difference caused by the pump.

$$p_5 = p_8 + \Delta p_{pump} \quad 3.4$$

Theoretically, this process is isentropic compression as shown in Equation 3.5. $s_{5\_}$ is the ideal specific entropy of the working fluid at point 5 when exiting from the pump, while s_8 is the actual entropy of the working fluid at point 8 when the liquid starts to enter in the pump.

$$s_{5\_} = s_8 \quad 3.5$$

However, the pump has the practical isentropic efficiency $\eta_{i,pump}$ and mechanical efficiency $\eta_{m,pump}$, as indicated in Equation 3.6 and Equation 3.7. $h_{5\_}$ is the ideal enthalpy of the fluid after isentropic compression at point 5 and h_5 and h_8 are the actual enthalpy of the fluid at point 5 and 8, respectively.

$$(h_5 - h_8) \cdot \eta_{i,pump} = h_{5\_} - h_8 \quad 3.6$$

$$\dot{W}_{pump} \cdot \eta_{m,pump} = \dot{m}_w \cdot (h_5 - h_8) \quad 3.7$$

Evaporator (point 5 to point 6) and heat source (point 1 to point 2):

Compared to the process in the pump, that in the evaporator is more complicated as displayed in Fig. 3.4. In this illustration, the red line represents the heat source of low-grade heat, while the black one is the organic fluid working in ORC.

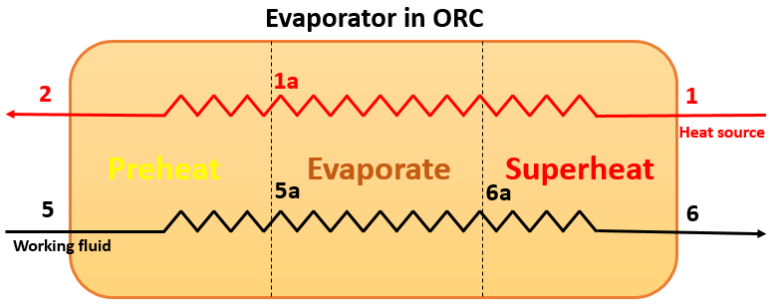

Figure 3.4 Three stages of the processes in the evaporator

The process in the evaporator is divided into three stages when the working fluid is at a constant pressure $p_{5,}$ as expressed in Equation 3.8. The subscripts of 5, 5a, 6a and 6 refer to the points when the working fluid enters the evaporator, starts to evaporate, finishes phase conversion, and exits the evaporator.

$$p_5 = p_{5a} = p_{6a} = p_6 \quad 3.8$$

The working fluid is firstly heated from T_5 to the evaporation temperature T_{5a}. After that, the liquid evaporates at the constant temperature T_{5a} and it consumes the heat from the heat

source until the phase conversion completes. Finally, the vapour increases the temperature to the outlet temperature T_6, which is at the superheated stage. Equation 3.9 and 3.10 show the temperature equations of the working fluid at various points. ΔT_{sup} is the superheated temperature change of the evaporator. The evaporation temperature is determined by the type and the pressure of the working fluid.

$$T_{6a}=T_{5a} \quad 3.9$$

$$T_6=T_{6a}+\Delta T_{sup} \quad 3.10$$

The numbers of 1 and 2 stand for the stages when the heat source enters and quit the boiler. Point 1a is the stage of the heat source corresponding to point 5a of the working fluid. The relationship between the heat source and the working fluid in the evaporator is calculated by Equation 3.11, where the mass flow rate of the heat source is $\dot{m}_h$ and that of the working fluid is $\dot{m}_w$. The effectiveness of the heat exchanger of the evaporator is η_{evap}. h_1 and h_2 are the inlet and outlet specific enthalpy of the heat source. Therefore, the outlet temperature of the heat source can be calculated by REFPROP with h_2 given in Equation 3.11 and p_2 equal to p_1.

$$\dot{m}_w \cdot (h_6 - h_5) = \dot{m}_h \cdot (h_1 - h_2) \cdot \eta_{evap} \quad 3.11$$

Equation 3.12 calculates the overall heat consumption of ORC, $Q_{in,ORC}$. h_5 and h_6 are the inlet and outlet specific enthalpy of the working fluid.

$$\dot{Q}_{in,ORC} = \dot{m}_w \cdot (h_6 - h_5) \quad 3.12$$

Expander (point 6 to point 7):

In the theoretical isentropic expansion process 6 - 7, the ideal specific entropy of point 7, $s_{7\_}$, is calculated by Equation 3.13. It maintains the same with the specific entropy of point 6, s_6.

$$s_{7\_}=s_6 \quad 3.13$$

Thus, the actual specific enthalpy of point 7, h_7, is given by Equation 3.14, where $\eta_{i,exp}$ is the isentropic efficiency of the expander.

$$h_6 - h_7 = (h_6 - h_{7\_}) \cdot \eta_{i,exp} \quad 3.14$$

With the mechanical efficiency $\eta_{m,exp}$ of the expander, Equation 3.15 calculates the power produced by ORC.

$$\dot{W}_e = \dot{m}_w \cdot (h_6 - h_7) \cdot \eta_{m,exp} \quad 3.15$$

Condenser (point 7 to point 8) and cold source (point 15 to point 16):

The organic fluid flows through the condenser and is converted to the liquid phase, as drawn in Fig. 3.5.

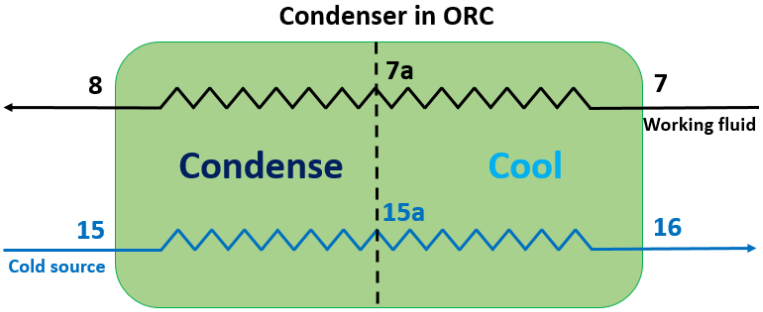

Figure 3.5 Processes in the condenser

During the first stage in the condenser, the mixture of gas and liquid is cooled to saturated gas from point 7 to point 7a as shown in Equation 3.16.

$$T_{7a}=T_8 \tag{3.16}$$

After that, the temperature of the working fluid maintains the same from T_{7a} to T_8 during the condensation. The pressures are the same at point 7 and point 8, as expressed in Equation 3.17.

$$p_7=p_8 \tag{3.17}$$

For the cold source in the condenser, point 15a corresponds to point 7a. Equation 3.18 expresses the relationship between them. ΔT_{cond} is the minimum temperature difference between the working fluid and the cold source in the condenser.

$$T_{15a}=T_{7a}+\Delta T_{cond} \tag{3.18}$$

Equation 3.19 and Equation 3.20 are the heat exchange processes in the condenser for cooling and condensation stages. $\dot{m}_c$ is the mass flow rate of the cold source and T_{16} is the outlet temperature of the cold source. η_{cond} is the effectiveness of the heat exchanger of the condenser, and C_{pc} is the specific heat of the cold source.

$$\dot{m}_c \cdot (h_{15a} - h_{15}) = \dot{m}_w \cdot (h_{7a} - h_8) \cdot \eta_{cond} \tag{3.20}$$

$$\dot{m}_c \cdot (T_{16} - T_{15a}) \cdot C_{pc} = \dot{m}_w \cdot (h_7 - h_{7a}) \cdot \eta_{cond} \tag{3.19}$$

Equation 3.21 calculates the heat consumed by the cold source.

$$\dot{Q}_{out} = \dot{m}_c \cdot (h_{16} - h_{15}) \tag{3.21}$$

Evaluation of ORC

Some of the essential assessments are given in 3.2.1, such as the heat consumed by the pump ($\dot{W}_{pump}$) and by the evaporator ($\dot{Q}_{in,\,ORC}$) and the power produced by the expander ($\dot{W}_e$). The net output of ORC is calculated by Equation 3.24, where $\dot{W}_{ORC}$ is the work loss in the cycle.

$$\dot{W}_{net} = \dot{W}_e - \dot{W}_{pump} - \dot{W}_{ORC} \quad 3.22$$

Equation 3.23 gives the thermal efficiency of a cycle, while Equation 3.24 expresses the calculation of the dump heat.

$$\eta_{th,ORC} = \dot{W}_{net}/\dot{Q}_{in,ORC} \quad 3.23$$

$$\dot{Q}_{dump,ORC} = \dot{m}_h \cdot (h_1 - h_0) - \dot{W}_{net} \quad 3.24$$

In Equation 3.25, the term on the left side is the exergy efficiency of the ORC. h_0 and s_0 are the specific enthalpy and specific entropy of the environment.

$$\eta_{exe,ORC} = \dot{W}_{net}/\{[(h_1 - h_0) - T_0 \cdot (s_1 - s_0)] \cdot \dot{m}_h\} \quad 3.25$$

3.2.4 Simulation of the adsorption unit

Adsorption conversion ratio

The adsorption conversion ratio x determines the heat consumption and heat release in the chemisorption cycles. In the thermodynamic study, the cycle time is given, resulting in a fixed adsorption conversion ratio used in the simulation. However, the adsorption kinetics is still introduced in Section 3.3 for the explanation of the concept and the fluency and coherence of the contents. Moreover, the kinetic model will be used in Chapter 6.

The form of the reaction rate is given, as shown in Equation 3.26, indicating the three primary parameters of the temperature, pressure and the degree of the conversion. In Equation 3.26, x is the global conversion ratio of the refrigerant, whose value equals to the ratio between the masses of the actual and the maximum reacted ammonia. It starts from zero to one in adsorption but reversely changes during desorption with the time t elapsing from zero. The term k(T, p) is the specific rate, representing the influence of the deviation between the operating conditions (T,p) and the equilibrium ones.

$$\frac{dx}{dt} = k(T,p)f(x) \quad 3.26$$

There are three types of chemisorption kinetic models as classified: local, global and analytical models [50]. The first one mainly considers the influence of heat and mass transfer, which uses the partial differential equations to establish the models. The second method requires the parameters such as the permeability, thermal conductivity and specific heat capacity of the adsorbents and the exact dimensions of the adsorption unit. Different from local or global models, the analytical model, using the average values of the parameters, can calculate the dynamic relationships during the sorption process.

Therefore, the desirable model used in this section is one of the analytical models that has been widely recognised as an effective method to mathematically predict the overall sorption performance by previous researchers [105, 153, 161]. The kinetic model of the adsorption progress is written in Equation 3.27, while that of desorption is expressed in Equation 3.28. They reasonably simplify the numerical simulation but still optimally controls the system with sufficient information.

$$\frac{dx}{dt} = Ar_a \cdot (1-x)^{Mr_a} \cdot \frac{P_c - P_{eq}}{P_c} \quad 3.27$$

$$\frac{dx}{dt} = Ar_d \cdot x^{Mr_d} \cdot \frac{P_c - P_{eq}}{P_c} \quad 3.28$$

In Equation 3.27 and Equation 3.28, A_r is the Arrhenius factor, which shows the correlations between the working temperature and the chemical reaction speed. M_r reflects the impact of the vacant sites of the chemical reaction [154, 161]. Both symbols are considered as constant referring to the previous researches. P_c is the constraining pressure versus the temperature of the condenser/evaporator, corresponding with the liquid-vapour equilibrium line of the selected refrigerant. In this PhD project, the refrigerant is ammonia. P_{eq} is the equilibrium pressure according to the average temperature of the sorbent, which can be calculated by the Clausius-Clapeyron equation as written in Equation 3.29. ΔH is the reaction enthalpy between the adsorbent and the refrigerant, while ΔS is the entropy of the chemisorption. Besides, R is the gas constant in nature and T_c is the constraining temperature of the adsorbent.

$$P_{eq} = \exp\left(\frac{-\Delta H_r}{RT_c} + \frac{\Delta S}{R}\right) \quad 3.29$$

For the salts selected in this PhD project, Equation 3.30 to Equation 3.33 show the reaction equations. Low-temperature salt composite (LTS) of $SrCl_2$-EG will be used in the adsorption units to consume low-grade heat and generate cooling power. High-temperature salt composite (HTS) of $MnCl_2$-EG will be applied in the resorption cycles in Chapter 6, cooperating with LTS. As the desorption processes in Equation 3.30 and Equation 3.32 require much heat input than those in Equation 3.31 and Eq. 3.33, the exploration work in this project only considers the second stage of each chemisorption.

$$SrCl_2 + NH_3 \leftrightarrow SrCl_2 \cdot NH_3 + \Delta H_r \quad 3.30$$

$$SrCl_2 \cdot NH_3 + 7NH_3 \leftrightarrow SrCl_2 \cdot 8NH_3 + 7\Delta H_r \quad 3.31$$

$$MnCl_2 + 2NH_3 \leftrightarrow MnCl_2 \cdot 2NH_3 + 2\Delta H_r \quad 3.32$$

$$MnCl_2 \cdot 2NH_3 + 4NH_3 \leftrightarrow MnCl_2 \cdot 6NH_3 + 4\Delta H_r \quad 3.33$$

Huang et al. [162] built the kinetic sorption models for $SrCl_2$-ammonia as written in Equation 3.34 and Equation 3.35, which are slightly different from Equation. 3.27 and Equation 3.28. In his study, x is the ammonia advancement starting with a value of zero in both equations when the time is zero.

$$\frac{dx}{dt} = k_{0a} \cdot exp\left(-\frac{E_a}{RT}\right) \cdot (1-x)^{M_{ra}} \cdot \left(\frac{P_c}{P_{eq}} - 1\right) \quad 3.34$$

$$\frac{dx}{dt} = k_{0d} \cdot exp\left(-\frac{E_d}{RT}\right) \cdot (1-x)^{M_{rd}} \cdot \left(1 - \frac{P_c}{P_{eq}}\right) \quad 3.35$$

The values of k_{0a}, k_{0d}, E_a, E_d, M_{ra} and M_{rd} are given in Table 3.1.

Symbol	Value
k_{0a} (s^{-1})	0.019
k_{0d} (s^{-1})	0.125
E_a ($J \cdot mol^{-1}$)	6921
E_d ($J \cdot mol^{-1}$)	9000
M_{ra} (-)	2.96
M_{rd} (-)	3.02

Table 3.1 Kinetic parameters used in $SrCl_2$-Ammonia

Han et al. [105] recognised the kinetic equations for the working pair of $MnCl_2$-ammonia as reliable. The related parameters determined by the researchers are listed below. However, they were mentioned as retrieved from Choir's dissertation, and the model of desorption was not directly stated in the reference [98, 163]. The text of the dissertation is not obtained through any approaches that the author has tried. Therefore, no direct information of the desorption parameters is provided. It is worth to notice that some scientists regard the desorption process as an ideal reversible process of the adsorption process [153], so the values of the parameters used in the simulation for $MnCl_2$-NH_3 are the same in either adsorption or desorption stage. The other essential parameters are included in Table 3.2.

	$SrCl_2$-1/8NH_3	$MnCl_2$-2/6NH_3	NH_3
A_{ra} (s^{-1})	-	0.001018	-
A_{rd} (s^{-1})	-	-	-
M_{ra} (-)	2.96	1.185	-
M_{rd} (-)	3.02	-	-
ΔH_r ($J \cdot mol^{-1}$)	41431	47416	23366
ΔS ($J \cdot mol^{-1} \cdot K^{-1}$)	228.8	228.07	150.52

C_p ($J \cdot mol^{-1} \cdot K^{-1}$)	75.53	72.86	80.27 (liquid)
R ($J \cdot mol^{-1} \cdot K^{-1}$)		8.314	

Table 3.2 Other essential kinetic parameters

Thermodynamic simulation of desorption:

During the desorption process, the inlet temperature of the heat source is given from the outlet of the evaporator in ORC. Each parameter is the same at point 2 and point 3. The physical shape of the adsorbent bed is not considered in Chapter 3.

In the first stage of desorption, the temperature of the sorbent increases from T_0 to the temperature starting to desorb (T_{sd}). The time consumed in this stage (t_{sd}) can be calculated by Equation 3.36. C_{paam}, m_{aam}, and C_{ph} are respectively the specific heat and the mass of the sorbent with $7NH_3$, and the specific heat of the heat source. $T_{4'}$ is the temperature of the outlet heat source of the sorbent bed.

$$t_{sd} = (T_{sd} - T_0) \cdot C_{paam} \cdot m_{aam} / \left[C_{ph} \cdot \dot{m}_h \cdot (T_3 - T_{4'})\right] \quad 3.36$$

In the second stage, when the temperature of the sorbent is high enough to activate the desorption, ammonia starts to be released from the sorbent. The desorption heat adsorbed by the sorbent is written in Equation 3.37. n_x is the molecular number of the reacted ammonia during this process, which could be retrieved from the adsorption kinetics mentioned in Equation 3.27 and Equation 3.28.

$$Q_{de} = n_x \cdot \Delta H_r \quad 3.37$$

The heat intake of the whole desorption process is calculated is Equation 3.38, as the sorbent temperature still grows with a second consumption of the sensible heat. On the right side of the equation, the second term is the sensible heat caused in the activation stage, while the third term represents the sensible heat in the desorption stage. C_{pa} and m_a are the specific heat capacity and the mass of the sorbent, separately. Equation 3.39 expresses the heat utilized by the adsorption per unit time. t is the cycle time.

$$Q_{in,ad} = Q_{de} + (T_{sd} - T_0) \cdot C_{paam} \cdot m_{aam} + C_{pa} \cdot m_a \cdot (T_a - T_{sd}) \quad 3.38$$

$$\dot{Q}_{in,ad} = Q_{in,ad} / t \quad 3.39$$

Thermodynamic analysis of adsorption (refrigeration):

The refrigeration is yielded during the adsorption stage. Equation 3.40 and Equation 3.41 present the calculations of the cooling production and the cooling production per unit time,

respectively. In these equations, n_x is the molecular number of the adsorbed ammonia and ΔH_r is the evaporation heat of ammonia.

$$Q_{ref} = n_x \cdot \Delta H_r \quad 3.40$$

$$\dot{Q}_{ref} = Q_{ref}/t \quad 3.41$$

Specific cooling power (SCP) is calculated in Equation 3.42. SCP represents the cooling capacity of the sorbents per unit mass.

$$S\dot{C}P = \dot{Q}_{ref}/m_a \quad 3.42$$

Equation 3.43 calculates the coefficient of performance (COP), which evaluates the cooling performance by the relationship between the cooling generation and the heat consumption.

$$COP = \dot{Q}_{ref}/\dot{Q}_{in,ad} \quad 3.43$$

3.2.5 Evaluation of the cogeneration

Other evaluations are given to assess the performance of the whole system. Equation 3.44 is the thermal efficiency of the coupling system. Equation 3.45 calculates the exergy efficiency of the integrated cycle, which represents the performance of the system running in a reversible condition. Moreover, Equation 3.46 expresses the dump heat of the cogeneration system.

$$\eta_{th} = \left(\dot{Q}_{ref} + \dot{W}_{net}\right)/[\dot{m}_h \cdot (h_1 - h_4)] \quad 3.44$$

$$\eta_{exe} = \left(\dot{Q}_{ref} + \dot{W}_{net}\right)/\{[(h_1 - h_0) - T_0 \cdot (s_1 - s_0)] \cdot \dot{m}_h\} \quad 3.45$$

$$\dot{Q}_{dump} = \dot{m}_h \cdot (h_1 - h_0) - \dot{Q}_{ref} - \dot{W}_{net} \quad 3.46$$

3.2.6 Identification of parameters

The parameters used for ORC and the sorption unit are given in Table 3.3. In this case study, the cold source is the tap water, and the heat source is waste heat from an engine. However, the heat source of the system could be any low-grade thermal energy mentioned in the literature review. The pressure difference of the inlet and outlet working fluid of the pump was tested from 100 kPa to 1000 kPa [172]. However, in this study, the difference would be set from 200 k Pa to 3200 kPa, for a further exploration of the informative performance, which may not be practical for the real operations. The overall of the pump and the expander is set to 72%, which is in a reasonable range in the literature reviews [173, 174]. The superheat temperature is set as small as 5 K to because that superheating is not favourable for the dry-type working fluid used in the simulation [175-177]. The minimum temperature setting of each heat exchanger is acceptable according to the literature [178]. The mass flow rate of the working fluid used in the simulation is from 0.2 kg/s and grows per 0.05 kg/s until

the outlet heat source temperature is lower than the temperature required by the sorption units, referring to the available range in the literature [179].

The following assumptions are made to simplify the models.

- The flows of the working fluid and gas waste heat are stable and steady.
- The efficiencies keep the same during whole simulation processes.
- The heat losses of the system are ignored including the pipes and the heat exchangers.

Symbol	Description	Value
	Cold source (tap water)	
T_{15} (K)	Inlet temperature of the cold source at the condenser	298
$C_{p,c}$ ($kJ \cdot kg^{-1} \cdot K^{-1}$)	Specific heat capacity of the cold source	4.2
	Environment	
T_0 (K)	Ambient temperature	298
P_0 (kPa)	Ambient pressure	101
	Heat source (engine exhaust)	
X_{N2} (%)	Mass ratio of nitrogen in the heat source	75
X_{CO2} (%)	Mass ratio of carbon dioxide in the heat source	25
$\dot{m}_h$ (kg/s)	Mass flow rate of the heat source	1.00
p_1 (kPa)	Inlet pressure of the heat source at the evaporator	120
p_2 (kPa)	Outlet pressure of the heat source at the evaporator	120
T_1 (K)	Inlet temperature of the heat source at the evaporator	473
	ORC	
Δp_{pump} (kPa)	Increased pressure of the working fluid by the pump	1000
$\eta_{m,pump}$ (%)	Mechanical efficiency of the pump	90
$\eta_{i,pump}$ (%)	Isentropic efficiency of the pump	80
η_{evap} (%)	Effectiveness of the evaporator	100
η_{cond} (%)	Effectiveness of the condenser	100
$\eta_{m,exp}$ (%)	Mechanical efficiency of the expander	90
$\eta_{i,exp}$ (%)	Isentropic efficiency of the expander	80

ΔT_{sup} (K)	Superheat of the evaporator	5
ΔT_{evap} (K)	Minimum temperature difference for heat transfer in the evaporator	11
ΔT_{cond} (K)	Minimum temperature difference for heat transfer in the condenser	9
$\Delta T_{c,ORC}$ (K)	Temperature difference between the inlet water and the outlet working fluid at the condenser	20
$\dot{m}_h$ (kg/s)	Mass flow rate of the working fluid	0.2
	Adsorption	
$n_s\ (mol)$	Molecular number of the salt	2
$M_{NH_3}(g \cdot mol^{-1})$	Molecular mass of NH_3	17
$M_{SrCl_2}(g \cdot mol^{-1})$	Molecular mass of $SrCl_2$	158.5
$M_{MnCl_2}(g \cdot mol^{-1})$	Molecular mass of $MnCl_2$	125.8
$C_{p\_NH_3}$ (kJ·kg^{-1}·K^{-1})	Specific heat capacity of the ammonia	2.06
C_{p_EG} (kJ·kg^{-1}·K^{-1})	Specific heat capacity of the EG	0.71
$C_{p\_SrCl_2}$(kJ·kg^{-1}·K^{-1})	Specific heat capacity of the $SrCl_2$	0.48
$C_{p\_MnCl_2}$ (kJ·kg^{-1}·K^{-1})	Specific heat capacity of the $MnCl_2$	0.58
$T_{sd,SrCl_2}\ (K)$	Starting temperature for $SrCl_2$ desorption	363
$T_{sd,MnCl_2}\ (K)$	Starting temperature for $MnCl_2$ desorption	423
$t_d\ (s)$	Time of adsorption/desorption between switches	3000

Table 3.3 Parameters used in simulation

3.3 Manufacturing and thermal-physical study of the composite

3.3.1 Manufacturing of the novel-sorbents

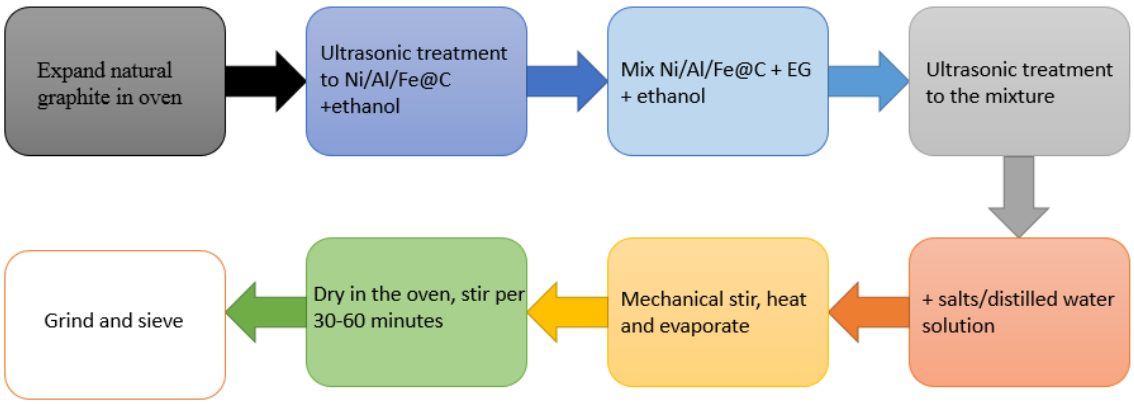

Figure 3.6 Upgraded manufacture method

The conventional manufacture processes of making composite sorbents have been reported by many researchers, along with the method on adding other Nano carbon materials [164] [165]. The most common procedures in their reports to integrate salts with porous matrix include weighing ingredients, dissolving salts in water, mechanically mixing, drying and grinding. It is important to find an improved method of preparing the adsorbents, as the unevenly mixing would cause the heat and mass transfer problems during the sorption process. However, the previous preparation procedures are not good enough that some problems still exist in the sorbents such as agglomeration and congregation.

Through several times exploring and attempting, the author develops an innovative manufacturing methodology of producing chemisorption composite with carbon coated additives, $SrCl_2$-EG-Ni/Al/Fe@C and $MnCl_2$-EG-Ni/Al/Fe@C, as shown in Fig. 3.6. Corresponding to different stages and equipment needed, the sorbents are made in Bio Lab, Mechanical Workshop, and Ammonia Lab, situated in the building for Mechanical Engineering, Newcastle University.

Figure 3.7 Oven used in expanding and drying

The manufacturing includes eight procedures in total:

- The first step is to prepare one of the ingredients, EG. The natural graphite is produced with a mesh size of 50-80, which means the diameters of the graphite is within 0.177-0.297 mm, and the purity of the material is larger than 99%, declared by the provider of Shanghai Yi Fan Graphite Company[166]. To produce the expanded graphite, the raw material is heated in the oven at a constant temperature of 600 ºC for a period of 10 min. Fig. 3.7 is the oven used in this expanding process. Limited by the volume of

the oven and the operation convenience, the metal pot could hold 30 g to 40 g material to the oven at once. Otherwise, a huger metal case in the shape of cuboid at such a high temperature could be extremely hard for the manufacturer to move in and out. The pot requires for a lid, without which EG would explosively fly out of the oven once open it. Between the batches, wait for another 10 min to cool the pot down. In a high temperature day, the waiting time could be longer. Otherwise, the high temperature pot can destroy the EG container. Collect EG in a sealed container in case that the material adsorbs water and affects the precise of weighing.

- The second procedure is the ultrasonic bath treatment to the carbon nanoparticles, as shown in Fig. 3.8. This 30 min process largely vibrates and smash the tiny conglomerate of the nanoparticles into the ethanol, which could potentially improve the uniformity of the mixture. One reason using ethanol as the media is that the density of this organic fluid is smaller than water, enabling a lower resistance of the particle movements. Moreover, ethanol is very easy to volatile without any residue at the room temperature. The additives of Ni/Al/Fe@C should have been scaled in bottles with lids tightened before the treatment, and any operations exposing people to the nano materials should only be undertaken in the fume cupboard, as the nano additives might raise respiratory problems.
- The third process is to mix EG with the nano materials in the bottles. EG is very light and loose material, and even the air flow during moving EG may cause the explosively flying of the powder. Therefore, the bottle used in the figure largely restrict the preparation time as the neck of the bottle is too slim for filling with EG. The only way to weigh EG is spoon by spoon. A limited mass of 0.07 g EG could be obtained by one spoon, and a bottle can hold a maximum of 6 g EG. For one type of the sorbent, 24 bottles need to be prepared, which means over 2000 times repeated work of using spoon to move EG. It is suggested by the author to use wide neck bottles instead of the slim ones for saving time. Moreover, a mask as well as patient and careful actions are advised to avoid inhaling the flying EG during the preparation, as the light and loose material cannot be processed in the fume cupboard.
- The fourth step is to treat the mixture from the third step for another 30 min ultrasonic bath. The ultrasonic bath in Fig 3.8 can only treat two bottles, which also constrains the processing time. In the experiments later, the ultrasonic bath is substituted with a bigger machine which could contain six bottles, but the bottles retain the same until the end of the project.

Figure 3.8 Ultrasonic treatment

- In the fifth stage, prepare a beaker with distilled water, and put in the salt of $SrCl_2$/$MnCl_2$. Water is still needed as the chemical salt cannot be dissolved in ethanol. Place the beaker on a magnetic hotplate in the fume cupboard and set the temperature to 150 ºC and the stirring speed to 3. This process is advised to be done during the fourth ultrasonic. The mass ratio among $SrCl_2$/$MnCl_2$, EG and Ni/Al/Fe@C is 40:20:1 referring to the study conducted by Wu et al. [167]. The masses of EG and Nano-additives are 6 g and 0.3 g in one bottle, respectively. For one kind of the sorbents, it requires 24 bottles or 12 beakers to be prepared, which means at least 192 bottles mixture are made for $SrCl_2$-EG-0/Ni/Al/Fe@C and $MnCl_2$-EG-O/Ni/Al/Fe@C. The accuracy of the analytical balance, product code Sartorius AZ612, is ±0.02 g. Extra bottles of different salt mass ratios are manufactured for the tests of thermal diffusivity and conductivity later.

(a) beaker on the hotplate

(b) Mechanical mixing in a fume cupboard

Figure 3.9 Mechanical mixing and evaporation process

- The sixth step is to move the mixture of ethanol, nanoparticles and EG into the beaker to be stirred with the solution made in the last procedure. The mixing and evaporating process by the magnetic hotplate could last for three to four hours, alleviating the deposition problems the mechanical mixing stage. Fig. 3.9 displays the hotplate and

the mixing step in fume cupboard. The fume cupboard could hold three hotplates for once.

(a) Before drying

(b) Crystallisation in drying

(c) Detail in crystallisation

Figure 3.10 Crystallisation problem with rapid temperature rise

- The seventh procedure of the manufacturing is to dry the sorbent after evaporation. When all the procedures above are done, move the black mixture into a ceramic tray and starts the drying process in the oven. Due to the large specific surface area of the carbon coated metals, the nanoparticles at this stage firmly adheres on the skeleton of the porous matrix, EG. Therefore, the open container is suitable to be used here. The temperature of the oven is 80 ℃ at beginning, and it requires to be stirred once an hour during the first eight hours drying process. After that, the temperature is increased by 10 ℃ per hour, until the temperature is 120 ℃. The frequency of stirring is once per half hour at the second stage. The aim for two-stage drying process is to prevent the severe crystallisation problem during the rapid temperature increasing if the oven is

set to 120 ℃ at the start. Fig. 3.10 reflects the crystallisation problem in a failed drying process, which would result in the uneven-distributed sorbents and negatively influence the sorption performance. The dried product looks the same with the final composite as shown in Fig. 3.11.

- Finally, sift the dried sorbents through a 2 mm sieve and grind the oversized residue to be sifted again. By this process, the agglomeration during the drying stage is reduced, resulting in the uniformity of the sorbents. Fig. 3.11 is the produced sorbent, which is mainly in black and some parts reflect a silver light. The loose sorbent needs more treatment like compression to fill various adsorption bed before being used in various applications.

Figure 3.11 Dried sorbent

3.3.2 Surface morphology of the prepared sorbents

The prepared composites are made into samples and sent to Scanning Electron Microscopy (SEM) and Energy Dispersive X-ray spectroscopy (EDX) to observe the surface morphology. This technology is expected to prove the developed manufacturing procedure to be superior for the evenly mixing of various ingredients, by presenting the microscopic surface and the elements mappings of the sorbents.

Principles of SEM and EDX

Fig. 3.12 illustrates the principle of SEM, by which the images of the sample surface could be produced using a focused beam of electrons to scan the sample surface.

The procedures in SEM tests are listed below:

- An electron gun thermally ejects a beam in the electron column. Tungsten benefits from its highest melting point and lowest vapor pressure among all metal materials, thereby allowing it to be electrically heated for electron emission. Therefore, the tungsten filament cathode is normally used in the thermionic electron gun. It also has the advantage of a low cost. Other types of electron emitters include lanthanum hexaboride cathodes or field emission guns (FEG).
- The beam is focused by the condenser lenses (one or two) to a spot around 0.4 nm to 5 nm in diameter.
- The beam passes through pairs of the scanning coils and deflector plates and then interacts with the sample, generating signals that contain the information about the topography and composition of the sample surface. The electrons lose typical energies by repeated random scattering within the interaction volume when the electron beam meets the atoms on the surface of the sample. The size of the interaction volume is determined by the landing energy of the electrons and the density and the atomic number of the sample.
- The specialized detectors detect the energy exchange between the beam and the specimen. Thus, they can create the images of the distribution map reflecting the signal intensity emitted from the scanned area of the sample.

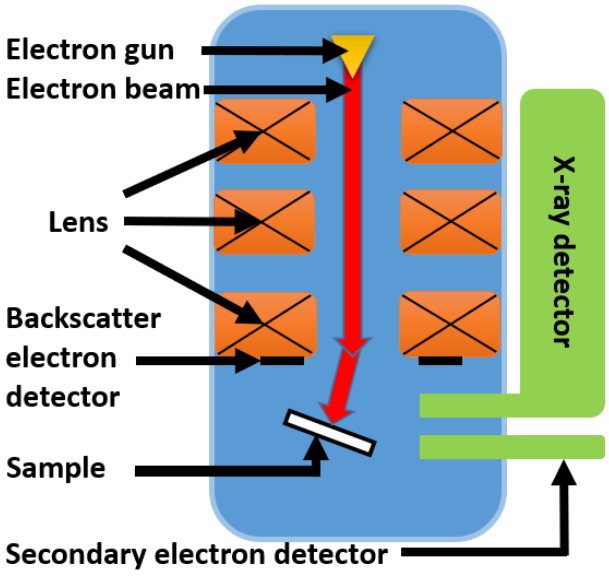

Figure 3.12 Schematic diagram of SEM

Various signals could be produced by the electron gun, such as reflected or back-scattered electrons (BSE) and secondary electrons (SE). Very few single machines have detectors for all possible signals. BSE are beam electrons reflected from the specimen by elastic scattering,

which emerge from a deeper location compared with the beams of SE emitted from very close to the sample surface. Consequently, the resolution of BSE images is less than that of SE images. However, in analytical SEM, BSE is more often used, along with the characteristic X-rays spectra, because the intensity of BSE is strongly related with the atomic number of the sample. BSE images can provide information about the distribution, but not the identity of different elements in the sample. Although in biological samples, BSE imaging can image colloidal gold immuno-labels of the diameter from 5 to 10 nm diameter, which is otherwise impossible for SE, SE detectors are still one of the most popular equipment in all SEMs [168].

SEM has some advantages in the scientific research field. Because the electron beam is very narrow, the micrographs of SEM have a large depth of field producing a characteristic appearance for understanding and analyzing the surface structure of the tested sample[169]. Also, SEM has a wide range of magnifications, from about 10 times to over 500000 times of the original. It even reaches about 250 times the maximum magnification of the light microscopes. Besides, SEM can achieve a resolution finer than 1 nm.

The testing condition of SEM could vary according to the request. Specimens can be tested in either high vacuum by conventional SEM, in low vacuum or wet conditions by variable pressure or environmental SEM, or at a cryogenic temperature with a specialized equipment [170].

Figure 3.13 SEM machine of Hitachi TM3030

The used machine in this PhD study is Hitachi TM3030, as shown in Fig. 3.13. Applying a detection system of a high semiconductor and a 4-segment BSE detector, Hitachi TM3030

can achieve the magnification from 15 times to 60000 times. The limits for the sample size are no higher than 50 mm and no larger diameter than 70 mm, according to the specification from the supplier.

Energy-dispersive X-ray spectroscopy (EDX) is an analytical technique professional for the chemical characterization or the elemental analysis. Similarly, it relies on the interaction of the sample and some X-ray excitation. The fundamental principle of EDX is the unique atomic structure of each element, which allows the typical set of peaks on the electromagnetic emission spectrum [169]. In this study, EDX is cooperated with SEM to observe the surface morphology of the manufactured sorbents.

Sample preparation

The samples are made to meet the requirement of SEM tests. First, they should be small to fit the sample stage in the instrument. Moreover, some special preparations are required to increase the electrical conductivity of the sample or to stabilize the sample on the sample plate. Otherwise, the samples are unable to withstand the high energy beam of electrons or the high vacuum condition during the tests. For example, the samples those can be peeled by the high vacuum will potentially destroy the very expensive equipment. Besides, for conventional SEM, specimens must be at least electrically conductive at the surface. The metal object only needs little preparations such as conductively mounting to a specimen stub while non-conducting materials requires additional ultrathin coating of electrically conducting substance. Currently, conductive materials for specimen coating include gold, platinum, iridium, gold/palladium alloy, tungsten, chromium, and graphite.

(a) Polished side of the silicon plate (b) Unpolished side of the silicon plate

Figure 3.14 Polished and unpolished sides of the silicon plate

A silicon plate is used as the sample plate for its electrical conductivity. It is polished on a single side as shown in Fig 3.14. The plate has a thickness of 400±10 um, a diameter of 50.8±0.3 mm, and an electrical resistivity less than 0.001 Ω·cm, provided by the Company of Zhejiang Li Jing Light and Electricity.

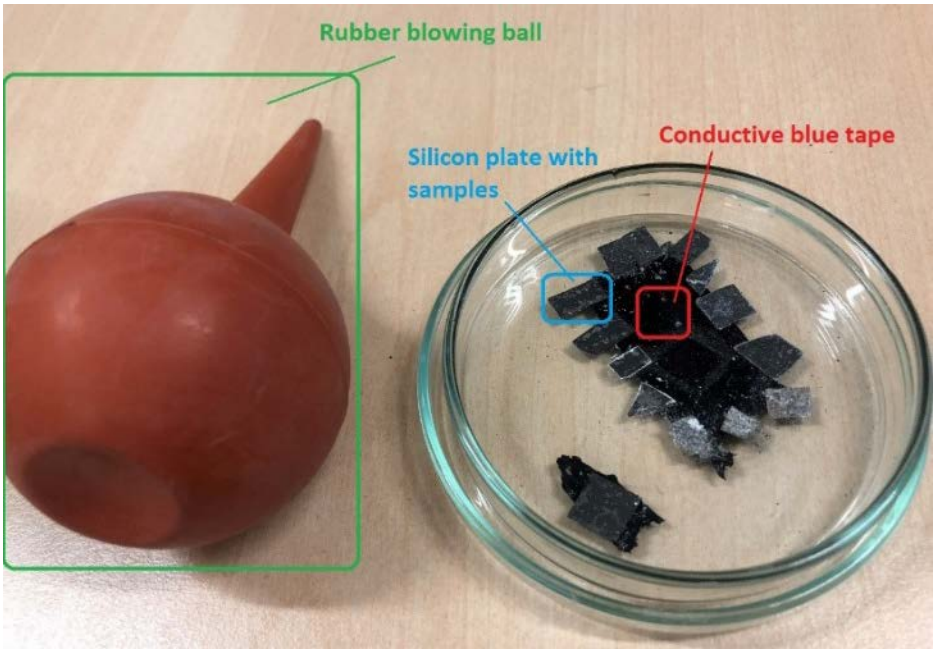

Figure 3.15 A rubber blowing ball and SEM samples on the conductive blue tape

In this project, the samples are prepared by the following steps. Cut a silicon plate to a suitable size. Drip a droplet of the mixture from the nearly evaporated stage to form a homogeneous liquid membrane on the polished side of the silicon plate. Blow the loose parts away by a rubber blowing ball after its naturally drying. Stick the silicon plate with samples to the testing stage by the conductive blue tape when doing SEM tests. Fig 3.15 displays the rubber ball and the samples made on a plate.

3.3.3 Thermal diffusivity and thermal conductivity of the adsorbents

Heat transfer is one of the most essential aspects that affect the sorption performance. The best method of thermally characterizing various materials attracts researchers and engineers. Many challenges in this field can only be met with precise exploration on two fundamental properties: thermal diffusivity and thermal conductivity.

The samples of the sorbents with or without carbon coated metals are sent for Laser Flash Analysis (LFA) to test their thermal properties. By this accurate, reliable and elegant solution, the thermal diffusivity and thermal conductivity are tested to investigate the influence of the Nano-additives.

Principle of LFA

Fig 3.16 is the LFA apparatus used in this project. The mode is LFA 467 Hyper Flash® produced by NETZSCH Company. It can measure the thermal diffusivity from 0.01 mm^2/s to 2000 mm^2/s and the thermal conductivity from 0.1 W/(m·K) to a maximum of 4000 W/(m·K).

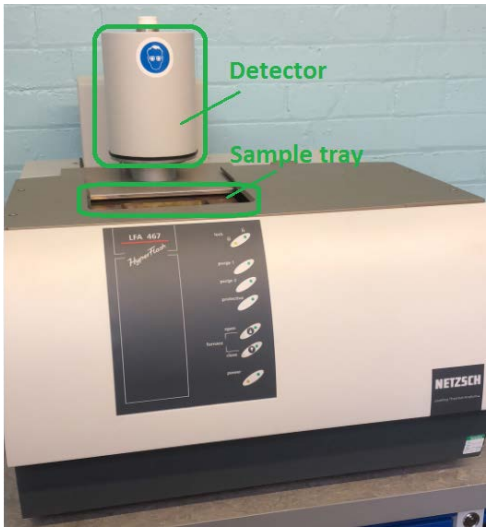

Figure 3.16 Photo of LFA 467 Hyper Flash®

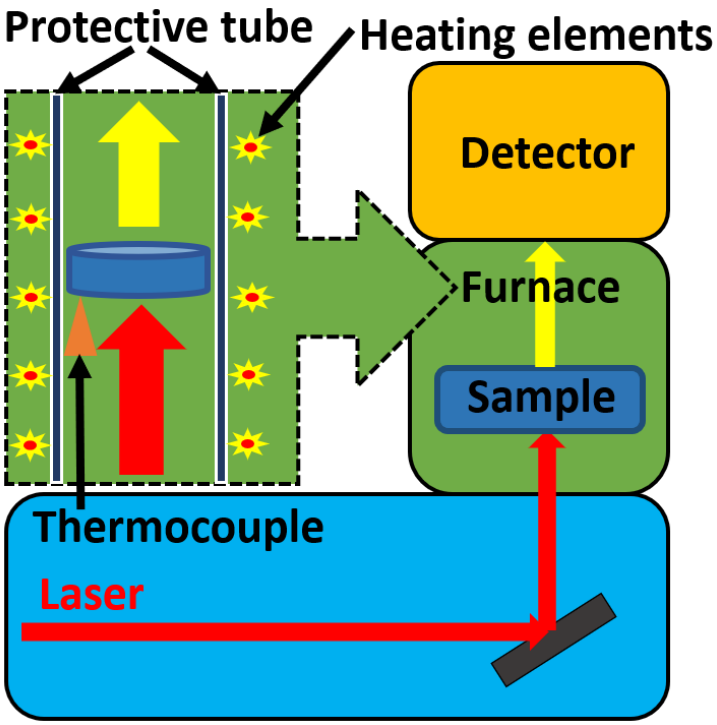

Figure 3.17 Structure of the LFA machine

Fig 3.17 presents the internal structure of the LFA equipment. The vertical system is designed with a source of laser at the bottom, a sample carrier inside the furnace in the centre and a detector on the top. A xenon lamp is the source of the flash, whose variable energy pulses are controlled by the integrated software. The width of the pulse ranges from 20 μs to 1200 μs in

LFA 467. During LFA tests, a laser sends the energy pulse to heat one side of a plane-parallel sample, resulting in a time-dependant temperature rise on the other side of the specimen. The temperature rise is then measured by an infrared (IR) detector. Figure in the dash box displays this process in detail.

The thermal diffusivity is therefore obtained by the machine as expressed in Equation 3.47, where α is the thermal diffusivity, d_{sam} is the thickness and $t_{1/2}$ is the time to the half maximum.

$$\alpha=0.1388 \cdot \frac{{d_{sam}}^2}{t_{1/2}} \tag{3.47}$$

Besides, given a reference specimen, the specific heat capacity C_p of the sample is detected as well. Equation 3.48 calculates the thermal conductivity k combining the bulk density ρ with these properties.

$$\mathrm{k} = \alpha \rho \mathrm{c_p} \tag{3.48}$$

Normally, C_p of the sorbent is determined by the components as Equation 3.49 shows.

$$C_{\mathrm{p}} = X_{salt} \cdot C_{\mathrm{p,salt}} + X_{EG} \cdot C_{\mathrm{p,EG}} + X_{add} \cdot C_{\mathrm{p,add}} \tag{3.49}$$

X_{salt}, X_{EG} and X_{add} is the mass ratio of the salt, EG and Nano-additives, while $C_{\mathrm{p,salt}}$, $C_{\mathrm{p,EG}}$ and $C_{\mathrm{p,add}}$ are the specific heat capacity of those mentioned above, respectively. The sum of X is 100 %.

According to Error Propagation Formula, the error analysis of the thermal conductivity obtained by LFA could be calculated as follows.

Calculate the natural logarithm of each side for Equation 3.50.

$$lnk = \ln\left(\alpha \rho \mathrm{c_p}\right) = \ln \alpha + \ln \rho + \ln \mathrm{c_p} \tag{3.50}$$

Calculate the first partial derivative of the thermal conductivity and two variables (thermal diffusivity and the specific heat), based on Equation 3.51.

$$\frac{\partial lnk}{\partial k} = \frac{1}{k}, \frac{\partial \ln \alpha}{\partial \alpha} = \frac{1}{\alpha}, \frac{\partial \ln \mathrm{c_p}}{\partial \mathrm{c_p}} = \frac{1}{\mathrm{c_p}} \tag{3.51}$$

The relative accuracy of the thermal conductivity for this LFA machine is calculated in Equation 3.52, Δk, Δα, and ΔCp is the uncertainty of the thermal conductivity, diffusivity, and specific heat, respectively. The accuracy of the thermal diffusivity and specific heat is ±3% and ±5%, respectively, while the repeatability of them is ±2% and ±3%, claimed by the supplier.

$$\frac{\Delta k}{k} = \left|\frac{\partial \ln \alpha}{\partial \alpha}\right| \cdot \Delta\alpha + \left|\frac{\partial \ln C_p}{\partial C_p}\right| \cdot \Delta C_p = \frac{\Delta\alpha}{\alpha} + \frac{\Delta C_p}{C_p} = 8\% \quad 3.52$$

The testing atmosphere of LFA can vary to fit different needs. itis controlled by either three integrated frits or the mass flow rate of two purge and one protective gases. With a single instrument setup, LFA 467 can carry out a measurement from -100 °C to 500 °C, which considerably reduces measurement times. It also allows for heating rates with a maximum limit of 50 K/min, while maintaining the excellent thermal stability at the meantime. Liquid nitrogen is used in the cooling devices, which can even be operated in conjunction with an evacuation system. As well as the temperature, the pressure for the measurement can be altered by pumping. A pressurized air device is available for a measuring temperature between 0 °C and 500 °C. It especially benefits the testing of oxygen-sensitive samples. In this project, only the condition of temperature is altered to test the samples.

Sample preparations

LFA 467 Hyper Flash has an integrated automatic sample changer which could hold up to 16 specimens. In the sample carrier, there is a tray for four holders. Holders vary for the round or square samples made of liquids, powder, pastes, resins, fibres, laminates or anisotropic materials. Each inset could contain one sample with a maximum diameter of 25.4 mm or four samples with a highest diameter and thickness of 12.7 mm and 10.0 mm, respectively. The sample holder applied in Chapter 4 is the latter one, which enables four specimens to be inserted.

A typical sample maker was designed in the laboratory, belong to Sir Joseph Swan Centre for Energy Research, as shown in Fig 3.18. The inner diameter of the compression cylinder is 12.70 mm, and the metal gasket to control the thickness parameter is 3.00 mm.

The preparation of the LFA samples can be described as following. Fill the tube with an exactly measured amount of the sorbents, and then tighten the lid and the nut to compress the powder into the desired dimension. Eventually, remove the lid and gasket, and further screw the nut to push the compressed sorbent out, so the specimens are obtained. The random error of the volume is less than ± 1%, by this method.

Fig 3.19 presents the prepared samples. Fig 3.19 (a) is the photo taken from a sample holder with four compressed sorbent specimens. In Fig 3.19 (b), B1 is the prepared sample, and B2 is the reference of graphite provided by NETZSCH, and the rest of the insects are filled with metal plates. Fig 3.19 shows the sample tray with four holes, filling with two sample holders and two large metal panels. The metal plates along with the panels aim to block the empty

positions, otherwise, the leakage of the light may cause errors in detection or even destroy the LFA machine.

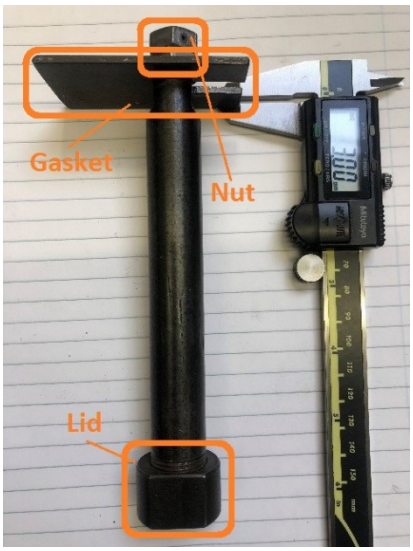

(a) Measure the gasket

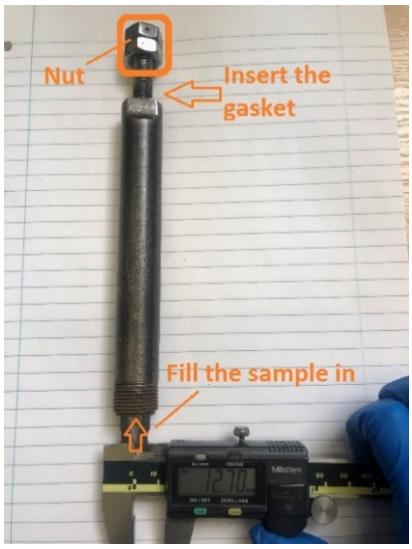

(b) Measure the inner diameter

Figure 3.18 A simple specimen compressor made in lab

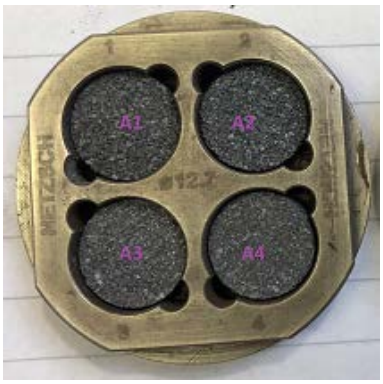

(a) Four in a holder

(b) One in a holder

(c) Samples in the tray

Figure 3.19 Prepared samples in the holder and the tray

3.4 Experimental investigation of the sorption performance

3.4.1 Experimental apparatus and principle

The sorption performance test system mainly consists of an adsorbent bed and an ammonia container with other accessorised equipment, as shown in Fig 3.20. The adsorbent bed on the left of the figure and the condenser/evaporator on the right are circled in the red dash lines. The tubes are set between the thermal fluid (orange) and the adsorbent (green) /ammonia (indigo) /adiabatic material (dark grey) to separates the substances. It is established in Ammonia Lab, School of Mechanical Engineering, Newcastle University.

The principle of the adsorption and desorption could be explained as follows:

- During adsorption, the ammonia evaporates from the ammonia vessel to be adsorbed by the sorbent in the sorption reactor. The oil bath exchanges heat with tap water to cool the thermal fluid running through the sorbent bed. Thus, the heat generated from adsorption is rejected. The cryostat is set to simulate the environmental temperature, and the ammonia vessel works as an evaporator. In adsorption process, the evaporator produces the cooling effect, due to the heat consumption by ammonia evaporation.
- Switched to the desorption mode, ammonia is desorbed from the sorbent and condensed in the ammonia vessel, when the sorbent bed is heated. The cylinder storing the ammonia works as a condenser in desorption. The oil bath is controlled at a high temperature to supply the heat source to the sorption bed. The adsorbent absorbs the heat and releases refrigerant gas.

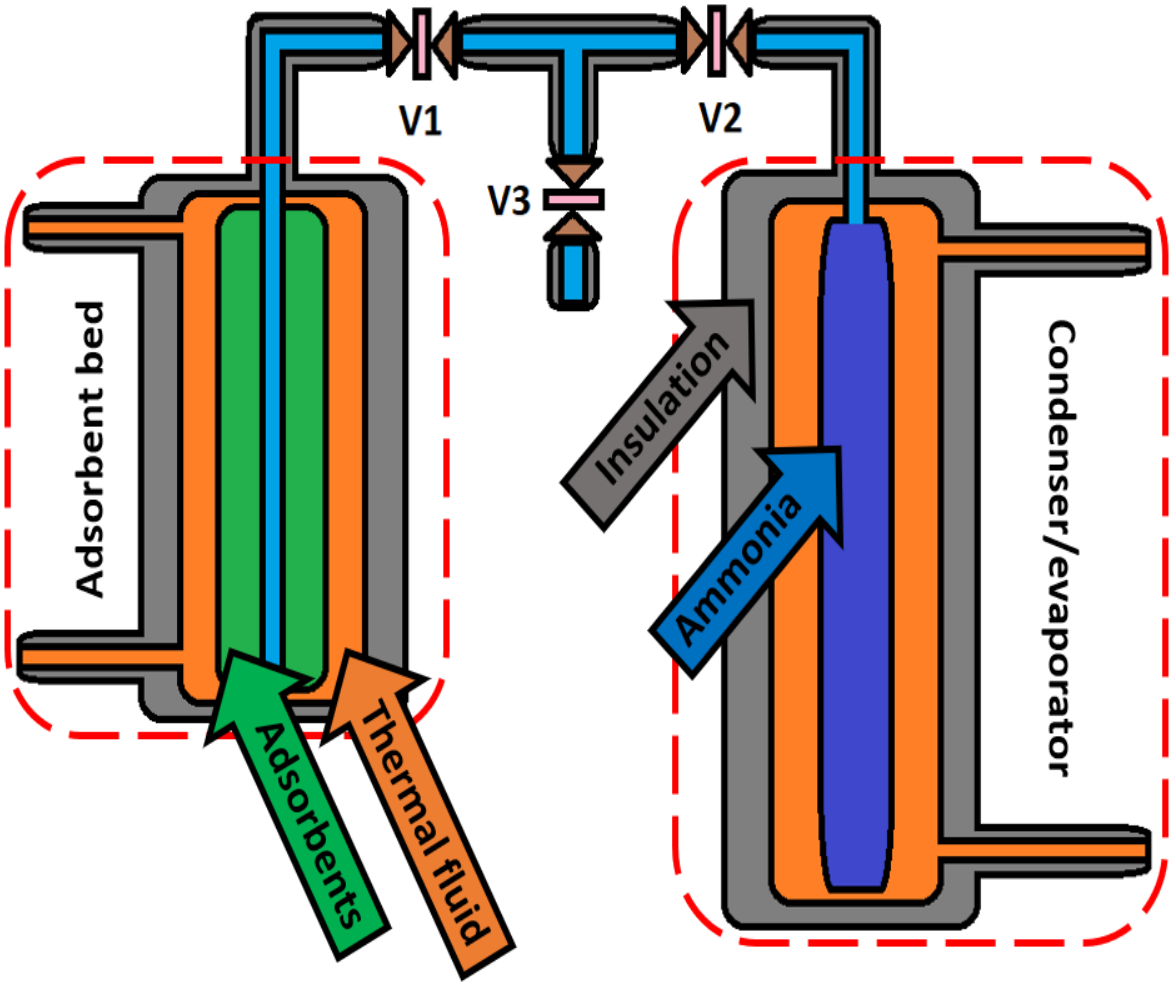

(a) Diagram of the sorption test rig

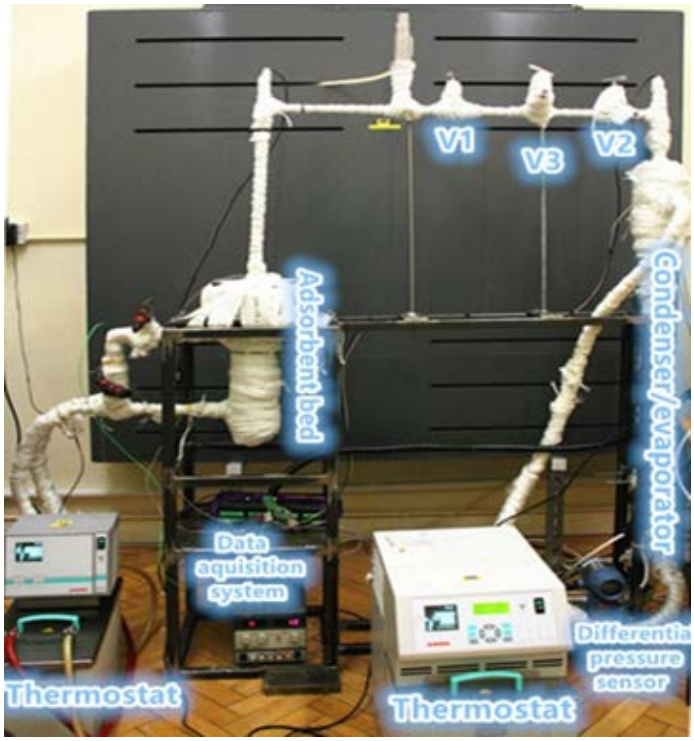

(b) Photo of the rig

Figure 3.20 Test rig of the adsorption and desorption performance

The data acquisition system of the test rig includes the power supply, the pressure sensors and the temperature sensors. A power supply maintains a stable working voltage for the pressure sensors (error within 0.25% of full scale) and the differential pressure sensor. The readings from the sensors are converted into 4-20 mA signals, recorded via the data taker of DT85. In the adsorbent bed, the temperature sensor is Pt 100, while other sensors for temperature detecting are all K-type thermocouples with a measuring error of 0.4%.

Fig 3.21 (a) is the designing illustration of the adsorbent bed. The sorption reactor could bear a working temperature to 300 ℃ with a pressure limit of 30 bar, which enables the tube to be used for all metal chlorides. The height of the sorbent chamber is 300 mm, and the diameter is 52.48 mm. A four-wire RTD temperature sensor with the accuracy of ± 0.01℃ is inserted in the centre of the tube for the accurate measurement of the sorbent temperature. The designed volume for the sorbent is 612.88 cm^3. The manufactured sorbent are compressed to 450 kg/m^3 to be filled in the sorption reactor. An oil bath is connected to the sorbent bed to control the sorption or desorption temperature. A 120 stainless mesh forms a gas channel in the centre of the adsorbent for the ammonia flow, and it could prevent the solid sorbent from collapsing away.

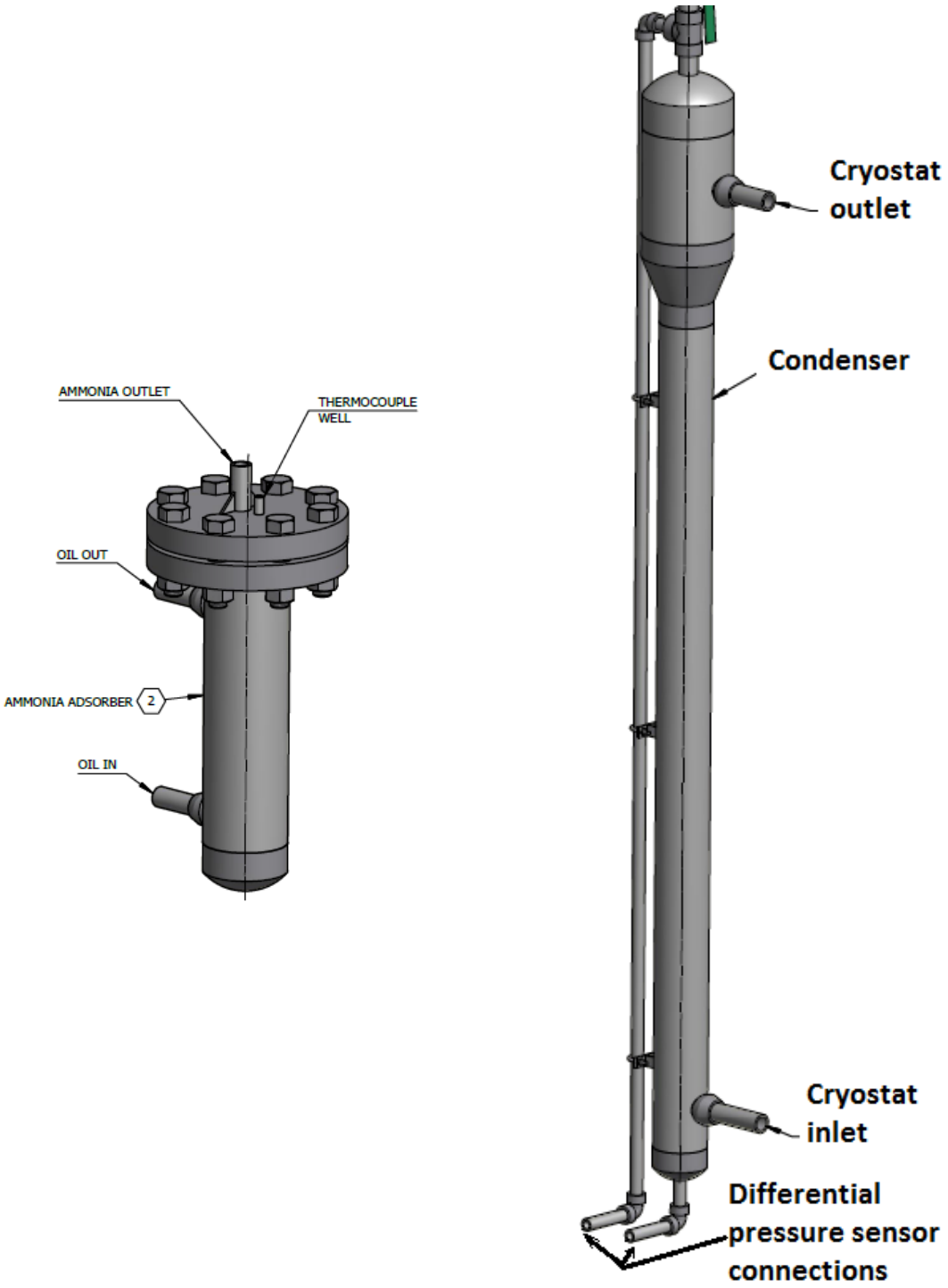

(a) Adsorbent bed (b) Condenser/Evaporator

Figure 3.21 Diagram of two tubes

Fig 3.21 (b) is the design of the ammonia vessel. In desorption, it works as the condenser, while in adsorption, the tube serves as the evaporator. The inner diameter of the ammonia vessel is 24 mm, and the designed volume for liquid ammonia is 45.24 cm^3, at the environmental temperature. At the beginning of the experiments, the cylinder allows a maximum amount of 17.86 mol or 303.62 g liquid ammonia inside, at the controlled temperature of -25 ℃. A spiral-shaped pipe is specially established in the upper body of the

condenser, reducing the possibility for the condensed ammonia to flow out of the condenser. The pressure sensor for the measurement of the pressure difference between the top and the bottom of the tube is supplied from Rosemount with a range from -623 bar to 623 bar and the uncertainty of 0.1%. With this application, the readings from the differential pressure sensor would be more reliable.

The thermostat connected with the adsorbent bed is JULABO SE-6 Heating Circulator, as displayed in Fig 3.22 (a). It can provide a maximum working temperature of 300 ℃ with the appropriate thermal fluid. The actual working temperature of the oil bath ranges from 20 ℃ to 220 ℃ with ±0.01 ℃ stability, corresponding to the characteristic of used oil, JULABO Thermal H20S.

(a) JULABO SE-6 (b) JULABO CF41

Figure 3.22 Photos of both thermostats

The cryostat connected to the evaporator is JULABO CF41, as presented in Fig 3.22 (b). It can control the temperature from -20 ℃ to 170 ℃, maintaining the stability of ±0.02 ℃. The working fluid in the cryostat is Kryo 70.

3.4.2 Test procedures

The test procedures of the sorption performance are described as follows:

- **Adsorbent compression**: Compress the manufactured sorbent into the reactor at a density of 450 kg/m^3. Install the insulation materials of the adsorbents bed.

- **Leakage check:** Switch on Valve 1 and Valve 3, vacuum the system through Valve 3. Charge the system with nitrogen to 20 bar through Valve 3. Switch Valve 3. Record the pressure in the adsorbent. When the pressure drop over 24 hours is lower than 0.1 bar, vacuum the system through Valve 3. Switch Valve 3 off. Switch Valve 2 on to let the ammonia go through. Start the tests.
- **Adsorption:** Alter the temperature of the oil bath connected with adsorbent bed to 20 ℃. Switch on the water valve. Set the cryostat to the testing temperature. Wait until the temperatures achieve the wanted temperatures and they are constant for at least 5 min. Switch on Valve 1 to start the adsorption. Retrieve the data from the data taker after completing the adsorption test. Shut down Valve 1. For each adsorption test, a complete desorption must be finished in advance. It requires to heat the sorbent bed at a temperature of 180 ℃ for two hours, and then cool the adsorbent bed until it reaches the environmental temperature.
- **Desorption:** Set the temperature of the thermostat connected with the sorbent bed to the experimental temperatures such as 180 ℃. Wait until the reading of the oil is 180 ℃ for at least 5 min during the internal heat circulation. Control the condenser temperature to -20 ℃. Wait until the temperature is stable. Start the external heating of the oil bath. Switch on Valve 1 to start the desorption test. Obtain the data after finishing the desorption test. Switch off Valve 1. The reason for setting such a low temperature at the condenser is to condense ammonia as quick as possible and accelerate the reaction in the rig with a long pipe. For every desorption experiment, full adsorption must be completed in advance. It requires to cool the adsorbent bed with tap water and control the evaporator to the ambient temperature of 20 ℃ for at least two hours.
- **Adsorbent removes:** When all tests are finished, switch Valve 1 and Valve 2 on. Heat the sorption bed at 200 ℃ for at least 8 hours. Wait until the temperature of the bed is safe for manual operations. Switch Valve 2 off. Switch Valve 3 on. Vacuum the adsorbent bed through Valve 3. Remove the insulation. Open the sorbent bed. Remove the adsorbent.

3.4.3 Evaluation of the sorption performance

Mass of ammonia

The gross mass of the ammonia in the container is calculated in Equation 3.53. It consists of both liquid and gas phases. The derivation processes are stated below.

$$m_{am} = m_{am,g} + m_{am,l} = \rho_{am,g} \times A_c \times h_{am,g} + \rho_{am,l} \times A_{cond} \times h_{am,l}$$
$$= (\rho_{am,g} \times g \times h_{am,g} + \rho_{am,l} \times g \times h_{am,l}) \times A_c \div g$$
$$\rho_{am,l} \times g \times h_{am,l} = \Delta p$$
$$\rho_{am,g} \times g \times h_{am,g} = \rho_{am,g} \times g \times \left(V \div A_c - h_{am,l}\right)$$
$$= \rho_{am,g} \times g \times \frac{V}{A_c} - \rho_{am,g} \times g \times \frac{\Delta p}{\rho_{am,l} \times g}$$
$$m_{am} = \left(\rho_{am,g} \times g \times \frac{V}{A_c} - \rho_{am,g} \times g \times \frac{\Delta p}{\rho_{am,l} \times g} + \Delta p\right) \times A_c \div g$$
$$= \rho_{am,g} \cdot V - (1 - \frac{\rho_{am,g}}{\rho_{am,l}}) \cdot \frac{A_c}{g} \cdot \Delta p \qquad 3.53$$

According to the error propagation, Equation 3.54 is the accuracy of m_{am}, based on the accuracy of the pressure difference $\Delta(\Delta p)$.

$$\Delta m_{am} = \left|(1 - \frac{\rho_{am,g}}{\rho_{am,l}}) \cdot \frac{A_c}{g}\right| \cdot \Delta(\Delta p) \qquad 3.54$$

m_{am}, m_g and m_l - Mass of overall, gas phase and liquid phase ammonia in the condenser.

h_g and h_l - Height of the gas phase and liquid phase ammonia.

ρ_g and ρ_l - Density of the gas and liquid ammonia.

v_g and v_l - Specific volume of the gas and liquid ammonia.

V (4.524×10^{-4} m^3) and A_c (4.524×10^{-4} m^2) – Volume and cross-sectional area of the condenser.

Δp - Differential pressure tested between the top (gas phase pressure) and the bottom (liquid phase pressure adds gas phase pressure) of the condenser.

g (9.80 m/s^2) - Gravitational acceleration.

Ammonia conversion ratio

For the convenience of the comparison, the global conversion ratio of ammonia is calculated to assess the sorption performance as shown in Equation 3.55 and Equation 3.56. For the first term of the numerator on the right side, m_{7NH_3} or m_{4NH_3}, it is the mass of the seven portions reacted ammonia for the $SrCl_2$ or four portions reacted ammonia for $MnCl_2$ added with the reaction-free ammonia. M_{7NH_3} and M_{4NH_3} is the mass of maximum reacted ammonia for $SrCl_2$ and $MnCl_2$, respectively. Thus, the numerator represents the mass of the actual reacted ammonia.

$$x_{SrCl_2} = \frac{m_{7NH_3} - m_{am}}{M_{7NH_3}} \quad 3.55$$

$$x_{MnCl_2} = \frac{m_{4NH_3} - m_{am}}{M_{4NH_3}} \quad 3.56$$

Equation 3.57 and Equation 3.58 are the calculations of the errors.

$$\Delta x_{SrCl_2} = \frac{1}{M_{7NH_3}} \cdot \Delta m_{am} \quad 3.57$$

$$\Delta x_{MnCl_2} = \frac{1}{M_{4NH_3}} \cdot \Delta m_{am} \quad 3.58$$

SCP and COP

Specific cooling power (SCP) and coefficient of performance (COP) are calculated to evaluate the refrigeration performance. SCP represents the cooling capacity of the unit mass of the sorbent during the unit time. Equation 3.59 is the cooling power yielded in adsorption process. Equation 3.60 is the calculation of the sorbent SCP. Q_{ref} is the refrigeration produced by the adsorption process in the reaction time t_{ad}. $n_{r,am}$ is the reacted molar number of the ammonia. ΔH_{evap} is the evaporation heat of the ammonia. m_{ad} is the mass of the adsorbent. COP is calculated by Equation 3.61. It reflects the relationship between the cooling production and the heat consumption. Q_{in} includes the sensible heat of the sorbent and sorbent bed and the desorption heat consumed by the sorbents.

$$Q_{ref} = x \cdot n_{r,am} \cdot \Delta H_{evap} \quad 3.59$$

$$SCP = Q_{ref}/(m_a \cdot t_{ad}) \quad 3.60$$

$$COP = Q_{ref}/Q_{in} \quad 3.61$$

3.5 Simulation study of integrated ORC-chemisorption systems using novel sorbents

3.5.1 Physical model of the sorption reactor

The physical model of the adsorption bed is built with the required parameters to use the analytical equations exploring the aspect of heat transfer.

A tube-type reactor designed and set in the lab provides the physical dimensions. Fig. 3.23 illustrates the simplified schematic diagram of the adsorption unit. Outside of the tube is the adiabatic materials to reduce the heat loss of the unit, and the tube is constructed of 304 stainless steel (304 SS) to isolate the adsorbents with the thermal fluid. The fluid runs inside the steel case to exchange the heat with the adsorbents as yellow colour shown in the figure. In the centre of the adsorbents is the gas channel made by a stainless-steel mesh to let the ammonia flow through, which is drawn in green. The steel wall separating the sorbents and

the thermal fluid is coloured in purple. Moreover, the orange part represents the compressed adsorbents. Several essential parameters are defined in the illustration such as the length of the tube (L) and the diameter of the gas channel (d_{gc}).

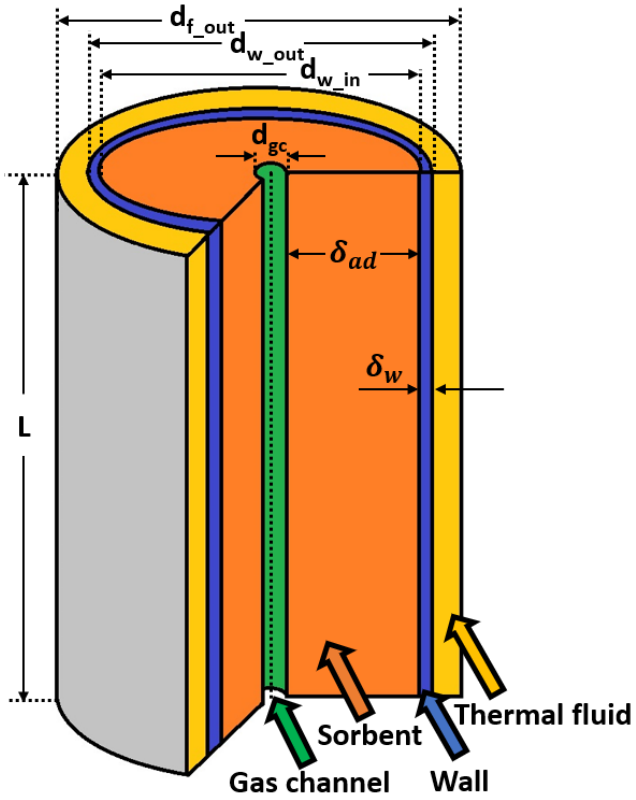

Figure 3.23 Simplified illustration of the adsorption unit

Table 3.4 lists the physical dimensions of the adsorption unit, including the thicknesses of the sorbent and wall, the diameter of the gas channel, the inner and outer diameter of the wall and so on.

Symbol	Description	Value
δ_{ad} (mm)	Thickness of the adsorbent	18.74
δ_w (mm)	Thickness of the wall	3.91
d_{gc} (mm)	Diameter of the gas channel	15.00
d_{w_in} (mm)	Inner diameter of the wall	52.48
d_{w_out} (mm)	Outer diameter of the wall	60.30
d_{f_out} (mm)	Outer diameter of the thermal fluid	77.92
h_{fw} ($W \cdot m^{-1} \cdot K^{-1}$)	Convective heat transfer coefficient of the fluid to wall	3.60
λ_w ($W \cdot m^{-1} \cdot K^{-1}$)	Thermal conductivity of the wall	16.20
λ_{SrCl_2-EG} ($W \cdot m^{-1} \cdot K^{-1}$)	Thermal conductivity of the $SrCl_2$-EG	1.40
λ_{MnCl_2-EG} ($W \cdot m^{-1} \cdot K^{-1}$)	Thermal Conductivity of the $MnCl_2$-EG	1.50

L (mm)	Length of the tube unit	300

Table 3.4 Physical dimensions of the sorption unit

Thermal resistance in the sorption bed

The thermal resistance from the fluid to the sorbent is illustrated with the describing equations in Fig. 3.24. For this cylindrical tube, the heat transfers first through the thermal fluid to the wall and then from the wall to the adsorbent. In this circumstance, the one-dimensional analysis is reliable to be used for simplifying the calculation of the heat transfer process. Therefore, the heat flow includes convection between the thermal fluid and the outer side of the wall, the conduction between the outer side and the central of the wall, the conduction between the central and the inner side of the wall, and convection between the inner side of the wall and the central of the adsorbent.

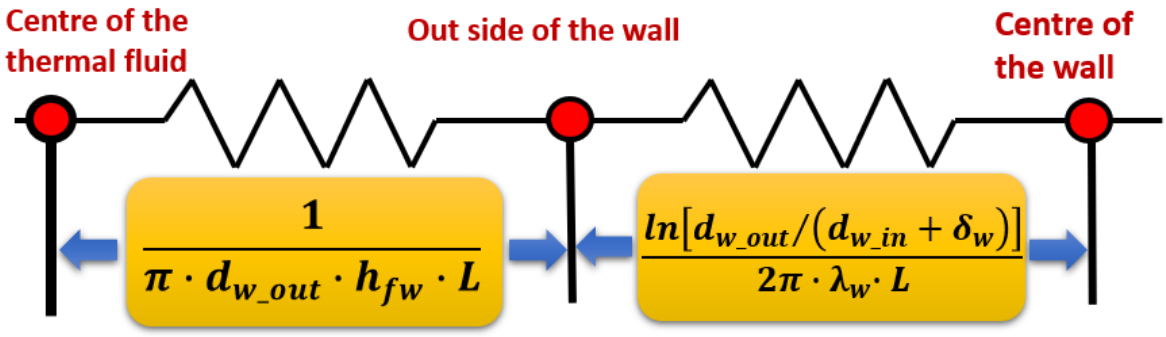

(a) Thermal resistance between the thermal fluid and the wall

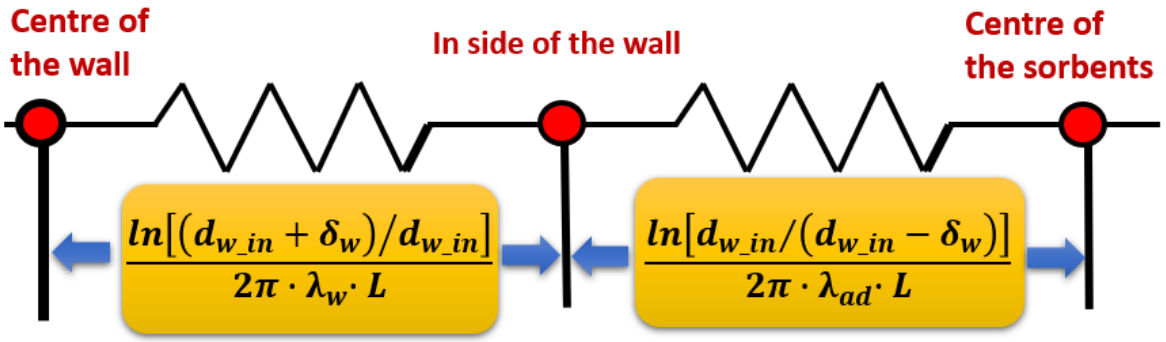

(b) Thermal resistance between the wall and the adsorbents

Figure 3.24 One-dimensional thermal resistance

Equation 3.62 calculates the heat resistance between the thermal fluid and the wall, R_{f_w}. The value of R_{f_w} is 7.086 x 10^{-6} $m^2/(K \cdot W)$.

$$R_{f\_w} = \frac{1}{\pi \cdot d_{w\_out} \cdot h_{fw} \cdot L} + \frac{ln[d_{w\_out}/(d_{w\_in}+\delta_w)]}{2\pi \cdot \lambda_w \cdot L} \quad 3.62$$

Equation 3.63 expresses the heat resistance between the wall and the sorbent, R_{w_ad}. The value of R_{w_ad} is 1.741 x 10^{-4} $m^2/(K \cdot W)$.

$$R_{w\_ad} = \frac{ln\left[\left(d_{w\_in} + \delta_w\right)/d_{w\_in}\right]}{2\pi \cdot \lambda_w \cdot L} + \frac{ln\left[d_{w\_in}/\left(d_{w\_in} - \delta_w\right)\right]}{2\pi \cdot \lambda_{ad} \cdot L} \quad 3.63$$

Heat transfer in the sorbent bed

The heat transfer analysis uses the lumped parameter model to simulate the unsteady-state heat process of the adsorption bed. This method assumes that the temperatures of the materials are always uniform.

Equation 3.64 is the expression of the log mean temperature difference between the thermal fluid and the wall.

$$\mathrm{LMTD}_{f\_w} = \left(T_{f\_in} - T_{f\_out}\right)/ln\frac{T_{f\_in} - T_w}{T_{f\_out} - T_w} \quad 3.64$$

Equation 3.65 describes the heat exchange between the thermal fluid and the wall, of which the terms on the right include the total energy processed by the fluid during convection and the energy changes in conduction between the wall and the fluid. C_{p_f}, V_f, ρ_f, and $\dot{m}_f$ are the specific heat capacity, volume, density, and the mass flow rate of the fluid, respectively.

$$\rho_f C_{p\_f} V_f \frac{\partial T_f}{\partial t} = \dot{m}_f C_{p\_f}\left(T_{f_{in},j} - T_{f_{out},j}\right) - \frac{LMTD_{f\_w,j}}{R_{f\_w}} \quad 3.65$$

Equation 3.66 stands for the internal energy change of the wall. The terms on the right side of the equation displays the heat transfer processes between the fluid-wall and the wall-adsorbent.

$$\rho_w C_{p\_w} V_w \frac{\partial T_w}{\partial t} = \frac{LMTD_{f\_w,j}}{R_{f\_w}} - \frac{T_{w,j} - T_{ad,j}}{R_{w\_ad}} \quad 3.66$$

Equation 3.67 calculates energy balance. The first term on the left is the internal energy change of the adsorbent, and the second term represents the energy of the reacted ammonia. The molar number of the chemical sorbent is n_{ad} and (d-c) is stated in chapter 2 when describing the equation of metal chlorides-ammonia. In this equation, $\sum_{i=1}^{N} \rho_i C_{p\_i}$ is the total specific volumetric heat capacity of the used composite sorbent, which is calculated by Equation 3.68.

$$\left(\sum_{i=1}^{N} \rho_i C_{p\_i}\right) V_{ad} \frac{\partial T_{ad}}{\partial t} - (d-c) n_{ad} M_{rNH_3} \Delta H_{ad} \frac{dx}{dt} = \frac{T_{w,j} - T_{ad,j}}{R_{w\_ad}} \quad 3.67$$

$$\sum_{i=1}^{N} \rho_i C_{p\_i} = \underbrace{\rho_{EG} C_{p\_EG}}_{expanded\ graphite} + \underbrace{\rho_{salt} C_{p\_salt}}_{salt} + \underbrace{x(d-c) n_{ad} M_{rNH_3} C_{p\_NH_3}/V_{ad}}_{ammonia} \quad 3.68$$

Lumping the thermal mass of the wall and the fluid together simplifies the calculation and improves the applicability of the model [171]. It means the same slope of the changes in T_f and T_w. Therefore, Equation 3.65 and Equation 3.66 can be written in Equation 3.69.

$$(\rho_f C_{p\_f} V_f + \rho_w C_{p\_w} V_w) \frac{\partial T_w}{\partial t} = \dot{m}_f C_{p\_f} \left(T_{f\_in,j} - T_{f\_out,j}\right) - \frac{T_{w,j} - T_{ad,j}}{R_{w\_ad}} \qquad 3.69$$

There are several assumptions applied in the model as described below.

- Both the temperature and the pressure of the adsorbent are homogeneous.
- During the chemical reaction, the ammonia is evenly desorbed or adsorbed by the sorbent.
- The ammonia is treated as an ideal gas in the calculations.
- The heat loss of the thermal fluid is ignored, either to the adsorbent or to the ambient.
- The pressure loss of the system is also neglected.

Table 3.5 supplies other necessary parameters used in the physical model built of the adsorption reactor.

Symbol	Description	Value
m_a (g)	Mass of the adsorbent	210
m_{EG} (g)	Mass of the EG	105
C_{p_f} (kJ·kg^{-1}·K^{-1})	Specific heat capacity of heat transfer fluid	1.02
C_{p_w} (kJ·kg^{-1}·K^{-1})	Specific heat capacity of the 304 SS wall	0.50
$C_{p\_NH_3}$ (kJ·kg^{-1}·K^{-1})	Specific heat capacity of the ammonia	2.06
C_{p_EG} (kJ·kg^{-1}·K^{-1})	Specific heat capacity of the EG	0.71
ρ_f (kg/m^3)	Average density of the thermal fluid	0.81
ρ_w (g/cm^3)	Density of the 304 SS wall	7.99
V_{ad} (cm^3)	Volume of the adsorbent	595.9
V_f (cm^3)	Volume of the thermal fluid	573.8
V_w (cm3)	Volume of the wall	207.8

Table 3.5 Other parameters used in the physical model

3.5.2 ORC-AD and AD-ORC

Apart from ORC-AD, AD-ORC system is investigated to assess the influence by using the adsorption module as the top cycle to use the heat source. Fig 3.25 draws the structure of AD-

ORC system. In this configuration, low-grade heat firstly enters into the sorbent bed in the adsorption cycle instead of firstly being used by ORC, compared with ORC-AD system.

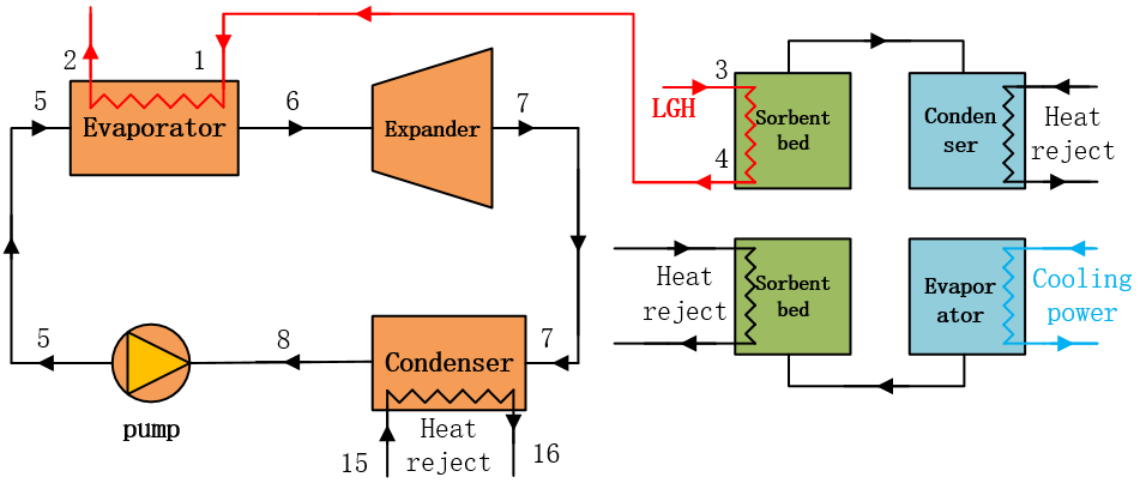

Figure 3.25 Schematic diagram of AD-ORC system

Different with ORC-AD, low-grade heat outlet temperature of the adsorption bed equals to the low-grade heat inlet temperature of ORC, as shown in Equation 3.70.

$$T_1=T_4 \tag{3.70}$$

Other calculations are not changed, except that T_3 is 200 ^oC. The mass flow rate of working fluid is controlled to 0.20 kg/s, while the pressure increase by the pump is 1000 kPa. Under this condition, the outlet temperature of the heat source is 157.38 ^oC.

3.5.3 Resorption-ORC and ORC-resorption

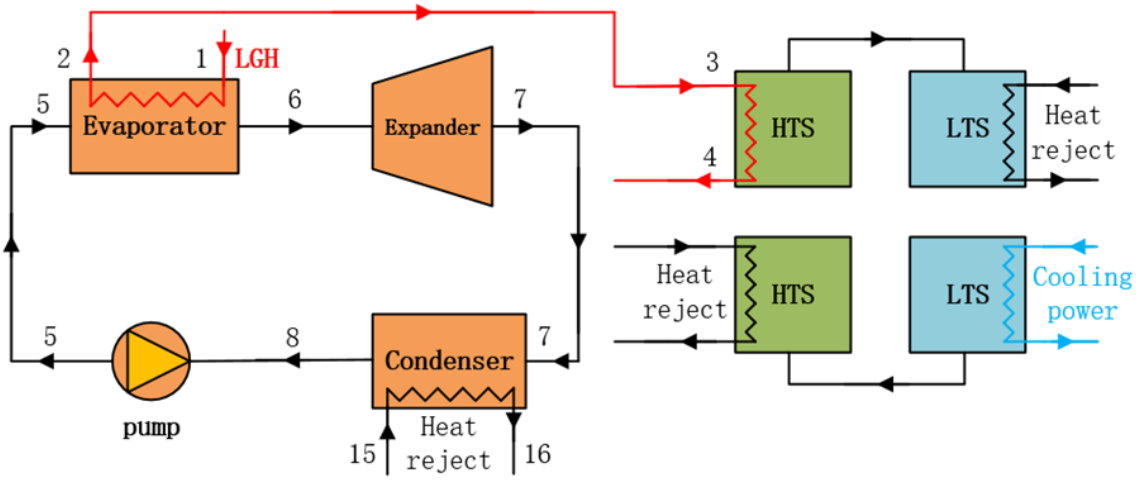

Figure 3.26 Schematic diagram of ORC-resorption system

Fig. 3.26 and Fig. 3.27 are two configurations of ORC-resorption and resorption-ORC systems. Resorption substitutes the adsorption cycle in the cogeneration systems. As stated in previous chapters, $SrCl_2$-$MnCl_2$ is the working pair used in LTS-HTS resorption module. The

essential parameters of both two salts have been recorded in Section 3.2. Unlike the single salt adsorption, Pc is the equilibrium pressure of LTS at its testing temperature (environmental temperature 25 ^{o}C in this study) in the kinetic equations.

The difference between ORC-resorption and resorption-ORC system is the utilisation order of the heat source. In Fig 6.9, low-grade heat goes through the sorbent bed later than being used by ORC while the condition is adverse in Fig 6.10. The cooling power produced is calculated by the amount of reacted ammonia and desorption heat of LTS rather than the evaporation heat of ammonia.

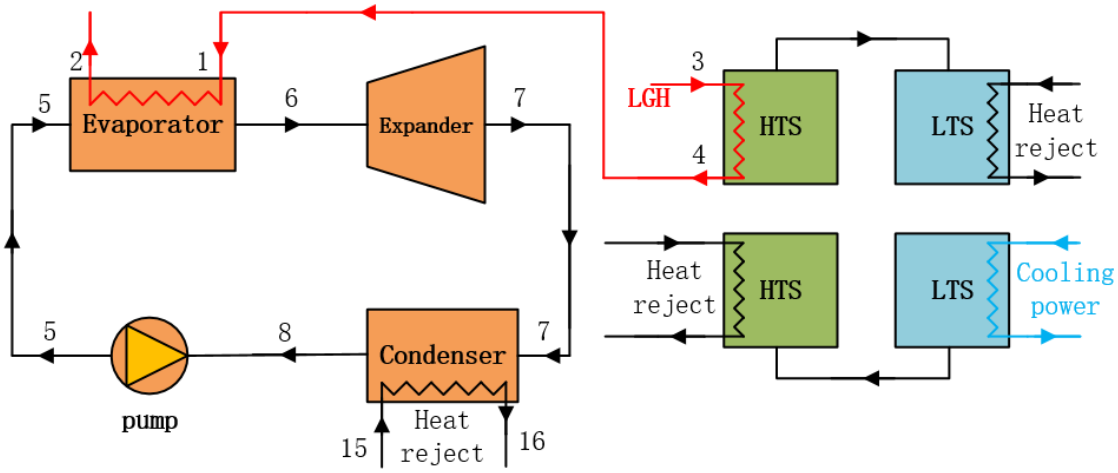

Figure 3.27 Schematic diagram of resorption-ORC system

3.6 Kinetic model of the optimal sorbents

The kinetic model for calculation of the global ammonia conversion ratio has been clearly introduced in Section 3.2.4.

The experimental data from Section 3.4 will be used to fit the kinetic model of the optimal chemisorption composite found in the study, and the kinetic model will be employed in the better integration system resulted from the comparisons above to evaluate the improvements of the low-grade heat conversion by these methods.

3.7 Summary

This PhD project aims to enhance the utilisation of the low-grade heat by integrating ORC with chemisorption cycles. The methodologies used in the thesis could be concluded as:

- Establish a model of ORC-AD system to evaluate the feasibility of integrating ORC with chemisorption to improve the conversion of the low-grade heat. MATLAB, the professional simulation software, is introduced as the modelling tool, as well as

REFPROP. The computational calculations are individually written for ORC and adsorption units. The evaluation of each component and the overall cogeneration performance is also stated in Section 3.2.

- For a further improvement of the cogeneration system driven by low-grade thermal energy, the chemisorption technology is explored in the respect of the development of the material, as ORC has a limited enhancing potential. An innovative methodology is developed for eliminating the conglomeration and aggregation of the chemisorption composite and improving the uniformity of the material ingredients. Carbon coated Ni, Al and Fe are selected as the additives to the conventional chemisorption composite with the expectation to potentially enhance the sorption performance with its good thermal properties. SEM and EDX are utilised for the surface morphology observation of the composite sample to prove that the methodology could evenly mix the sorbents materials. LFA tests are applied to assess the thermal characteristics of the chemisorption composite.
- After the manufacturing and the thermal-physical tests of the sorbents, the experimental investigation will be done for the sorption performance tests of the composites. The experimental apparatus and principle are introduced in Section 3.4, as well as the test procedures. Several critical indicators are also stated for the assessment of the sorption performance of the manufactured chemisorption composites.
- Using the data from the experimental adsorption units, the simulation model of the ORC-AD is advanced to fit more reality, and another three combinations of ORC with chemisorption are induced to compare the influence of the chemisorption to be the first user or not.
- The optimal sorbents obtained from the results of the sorption performance is fitted into the kinetic models and applied in the optimised integration system to evaluate the most improvement by the methods explored in this PhD project.

Chapter 4 Integrated ORC-adsorption system for power and cooling

During the exploration of various thermal cycles recovering low-grade heat, the idea of integrating ORC with adsorption technologies inspired many researchers to enhance the overall energy efficiency and comfort the condition simultaneously requiring cooling and power. Computational modelling offers the flexibility on altering the simulating conditions and enables the repeatability of the predictions. Thus, it can save money and time on forecasting and optimising system behaviour, designing control systems and characterising system response.

Chapter 3 describes the simulation of a cogeneration system, integrating the adsorption units and a traditional ORC to evaluate the feasibility of achieving the goals mentioned above. The software used in this project is MATLAB. REFPROP is another vital part of the simulation, providing the properties of reference fluid. The assessment of this system versus various working conditions has been reported such as net power, cooling generation and thermal efficiency.

4.1 Identification of T_2

It is critical to identify the suitable situations of T_2, as the outlet temperature of the heat source T_2 from the evaporator is the only connection for ORC and adsorption modules. Otherwise, the temperature of the heat source to be used in adsorption may be out of range.

Fig. 4.1 shows the temperature T_2 of the heat source when it goes out of ORC. Δp_{pump} is altered from 200 kPa to 3200 kPa to figure out the influence from the pump, with a gradient of 200 kPa. Δp_{pump} higher than 3200 kPa would cause errors as the value is the invalid supercritical pressure. The mass flow rate of the working fluid varies from 0.20 kg/s to 0.50 kg/s. The results show that T_2 increases with Δp_{pump} negatively developing, while T_2 decreases with $\dot{m}_w$ growing larger. The first result is due to the enlarged pressure of the working fluid, which leads to a higher evaporation temperature T_{6a} in the evaporator. With a fixed value of ΔT_{sup}, the outlet temperature of the working fluid T_6 becomes higher as well. However, T_5 almost keeps the same when Δp_{pump} is altered. Thus, the increased temperature difference between the inlet and outlet working fluid of the evaporator caused more heat consumption with a constant mass flow rate of R245fa. The latter result is because the increased mass flow rate requires the working fluid to consume more heat from the heat source, which would lead to the decrease of the heat source temperature. The maximum temperature reached among these testing conditions is 162.31 ^{o}C with the mass flow rate of

0.20 kg/s at Δp_{pump} of 200 kPa, while the minimum T_2 is 85.24 ^{o}C retrieving from the mass flow rate of 0.50 kg/s at Δp_{pump} of 3200 kPa.

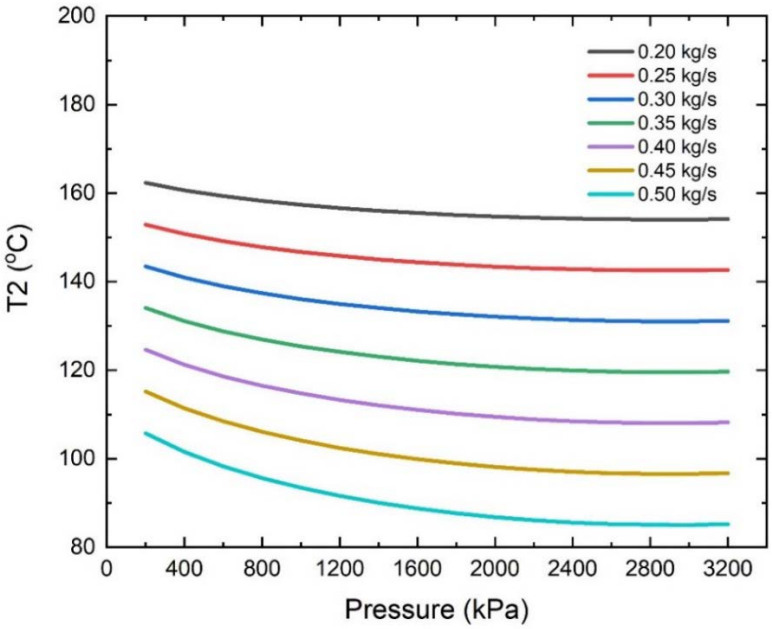

Figure 4.1 T_2 versus Δp_{pump}

Only the temperature points of the outlet heat source from ORC that are higher than 90 ^{o}C could meet the temperature requirement for $SrCl_2$-EG to desorb the ammonia.

Thus, the simulation of Chapter 3 would only test the performance in the suitable conditions ($\dot{m}_w$: 0.20 kg/s to 0.45 kg/s; Δp_{pump}: 200 kPa to 3200 kPa).

4.2 Performance anaylsis

Fig 3.7 illustrates the net power produced by ORC altering Δp_{pump} from 200 kPa to 3200 kPa. The black, red, blue, green, purple, brown and light blue curves represent the results from the working fluid with the mass flow rate of 0.20 kg/s to 0.45 kg/s. The results show that the output increases with the mass flow rate positively developing or with Δp_{pump} growing. Corresponding to the results found in Fig 4.2, the reason is that the increased Δp_{pump} or $\dot{m}_w$ lead to more energy consumed by the working fluid. Thus, the amount of the energy production increases after expansion with fixed expander efficiencies. The maximum power yielded by ORC is 13.21 kW, obtained when $\dot{m}_w$ is 0.45 kg/s and Δp_{pump} is 3200 kPa, while the minimum value for that is 1.35 kW, observed at the lowest $\dot{m}_w$ and Δp_{pump}. It is suggested to use the maximum Δp_{pump} and mass flow rate of the working fluid in the suitable working range for an optimal result of the power production.

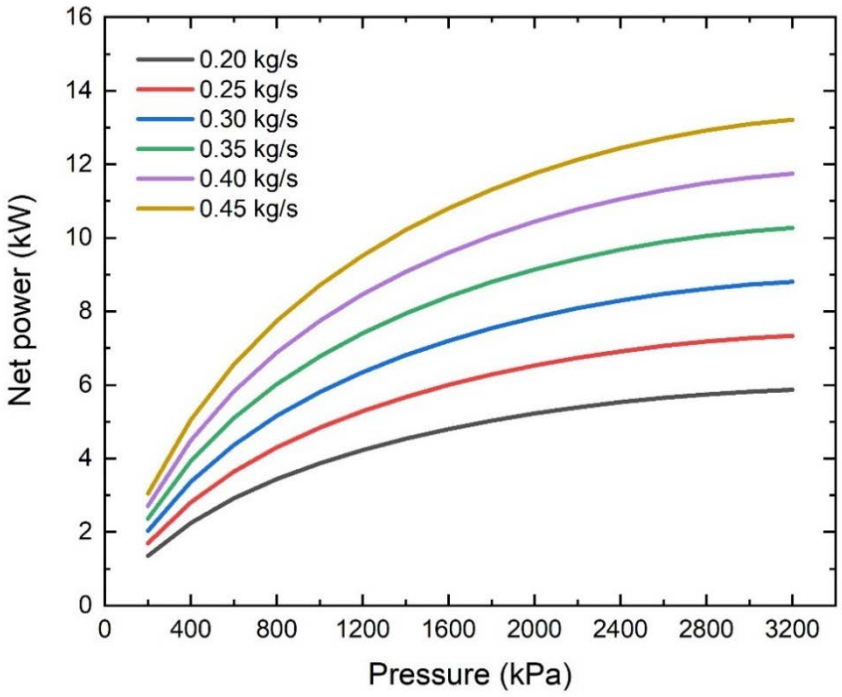

Figure 4.2 Net outputs of ORC versus Δp_{pump}

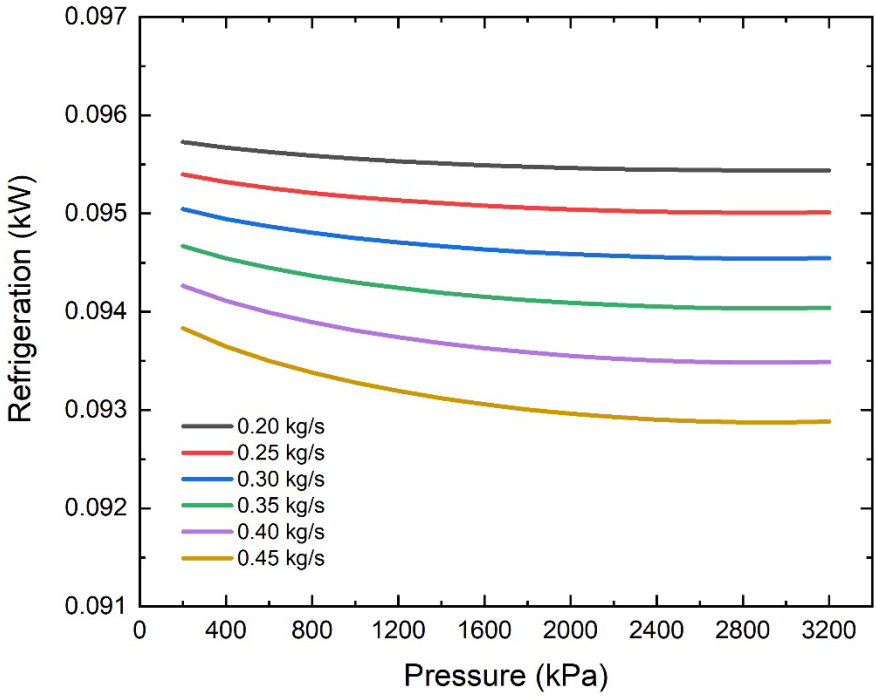

Figure 4.3 Refrigeration from adsorption cycle versus Δp_{pump}

Fig 4.3 presents the refrigeration produced by the adsorption module in the integrated system. The testing conditions are the same as those in Fig 4.2. The curves develop following a similar trend with the outlet temperature of the heat source at the evaporator. It is easy to understand as a higher desorption temperature causes more void space for ammonia to be adsorbed in the evaporation process when the cycle time is the same. The enlarged amount of evaporated ammonia then results in increased cooling production. The highest value for

refrigeration output is 0.0957 kW at the smallest of $\dot{m}_w$ and Δp_{pump} while the minimum cold is 0.0929 kW with the hugest testing of $\dot{m}_w$ and Δp_{pump}. The difference of the refrigeration is tiny due to the long cycle time. From the result of the refrigeration, it is advised to set Δp_{pump} to the minimum value and $\dot{m}_w$ to the maximum value for a most production of cooling power. Moreover, the shortening of the cycle time setting has the potential to improve the generation of the refrigeration.

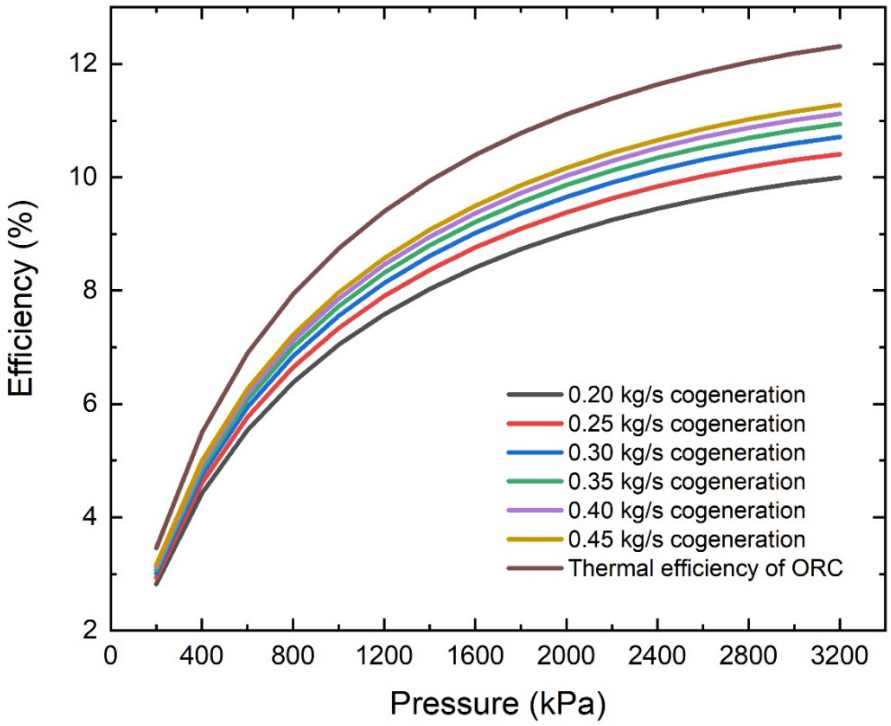

Figure 4.4 Thermal efficiency of ORC or the cogeneration system versus Δp_{pump}

Fig 4.4 displays the thermal efficiency of ORC and the cogeneration system, changing the testing $\dot{m}_w$ and Δp_{pump}. The trends of the curves are similar with those observed in Fig 3.6, as all of them climbs from the left bottom to the right top with a reducing speed of growth. The result shows that the thermal efficiency of ORC is constant regardless of $\dot{m}_w$ alterations, mainly determined by the pumped pressure, the type of working fluid, the superheated temperature and the mechanical or isentropic efficiency of the equipment. However, the evolutions of other curves show that the thermal efficiency of the cogeneration system is lower than the thermal efficiency of the single ORC. The reason is that for the same heat source, the integrated system could adsorb more energy, which means a larger denominator in the calculation equation of the thermal efficiency. For the cycle time set in this study, the growth of the refrigeration cannot match the growth of the heat intake. Thus, the larger increase of the numerator would result in a reduced value of the thermal efficiency. The result also presents that a larger mass flow rate of the working fluid could have a higher gross

thermal efficiency of the system. It is because that the numerator, refrigeration, increases when the mass flow rate of the working fluid grows. It is found to reduce the cycle time for the optimisation of the thermal efficiency. Moreover, a larger mass flow rate of the working fluid would also make improvement of the thermal efficiency.

The dump heat of ORC is illustrated in Fig 4.5. It decreases with the enlarged $\dot{m}_w$ or Δp_{pump}. The explanation is that the larger $\dot{m}_w$ and Δp_{pump} cause more heat consumed by ORC. Thus, the heat released to the ambient is reduced. The least dump heat of ORC is 164.58 kW when $\dot{m}_w$ and Δp_{pump} are 0.45 kg/s and 3200 kPa, respectively. For ORC, increasing both $\dot{m}_w$ and Δp_{pump} could convert more low-grade heat into useful productions.

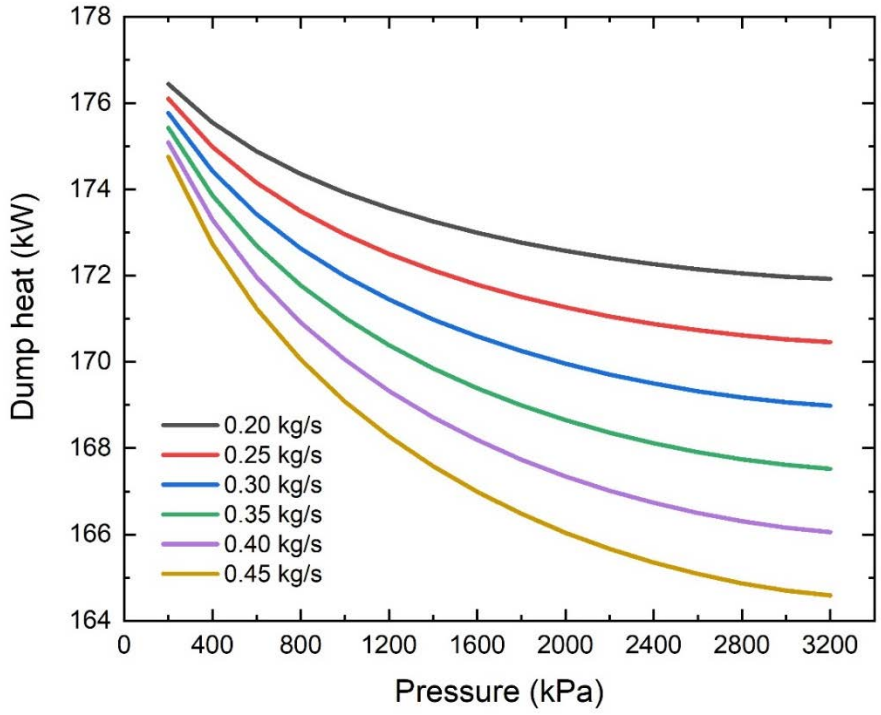

Figure 4.5 Dump heat of ORC versus Δp_{pump}

Fig 4.6 is the reduced percentage of the dump heat, integrating ORC with the adsorption units. The result shows that whatever the condition is in, the cogeneration could reduce the heat released to the ambient. With $\dot{m}_w$ and Δp_{pump} increasing, the reduction grows, while from Δp_{pump} of 600 kPa to 1200 kPa, the reduction values have some overlapping parts among different $\dot{m}_w$ settings. The reason is that the adsorption module could consume the rest heat of the heat source after the consumption of ORC. Besides, increase of $\dot{m}_w$ and Δp_{pump} causes the growth of the heat adsorbed by sorption units. Therefore, the dump heat of the cogeneration is reduced. In the lower Δp_{pump} range, a smaller $\dot{m}_w$ is desirable. However, in a higher Δp_{pump} range, a larger $\dot{m}_w$ results in more waste reduction. The maximum reduction is obtained at 3200 kPa using 0.45 kg/s flow rate with the value of 0.0564 %. This phenomenon is due to

the development of T_2 under these testing conditions. The smaller mass flow rate of the working fluid enables a more stable T_2 as shown in Fig 4.1, which also reflects on the smoother curve of heat utilization. Thus, the larger mass flow rate has a sharper growth in the illustration. For more reduction of dump heat, $\dot{m}_w$ and Δp_{pump} are suggested to be larger. It is also revealed that the alteration of $\dot{m}_w$ has more impact on the dump heat reduction than the change made on Δp_{pump}.

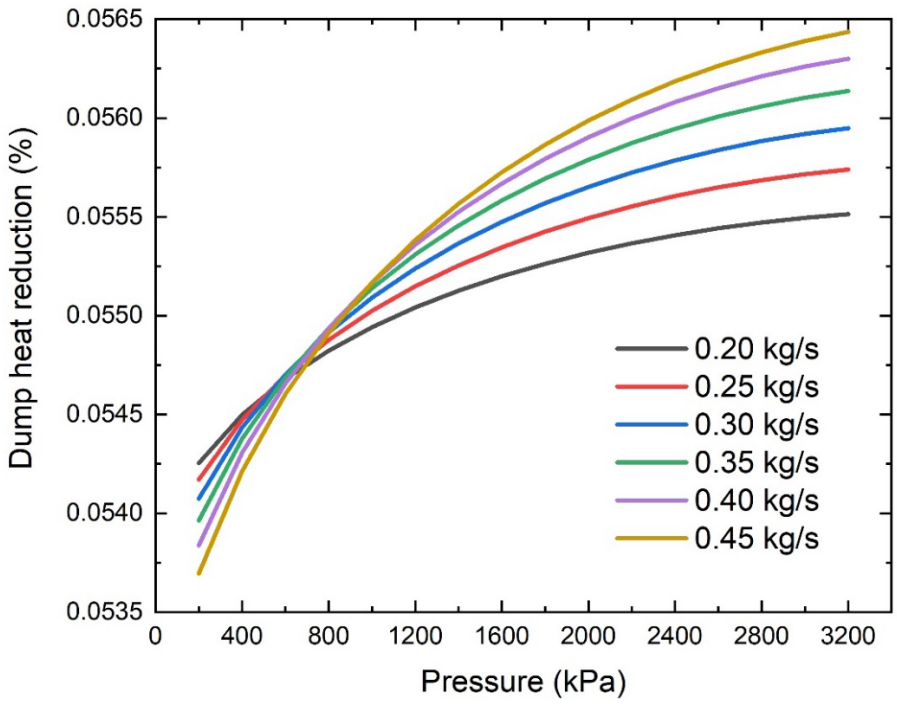

Figure 4.6 Dump heat reduction versus Δp_{pump}

Fig 4.7 is the calculated exergy efficiency of ORC and the cogeneration system, which presents the effectiveness of them in the aspect of reversible performances. The testing conditions are the same as the statement in other figures above. The value of exergy efficiency grows with $\dot{m}_w$ increasing from 0.20 kg/s to 0.45 kg/s. It also decreases with Δp_{pump} shrinks from 3200 kPa to 200 kPa.

The highest exergy efficiency of ORC and the cogeneration is 34.62 % and 34.87 % with the mass flow rate of the heat source of 0.45 kg/s at the increased pressure of 3200 kPa, respectively. On the adverse direction, the lowest exergy efficiency of basic ORC and the cogeneration system is 3.55 % and 3.80 %, separately, with the mass flow rate of the heat source of 0.20 kg/s at the increased pressure of 200 kPa. The discovery matches the findings in the results of net power produced by ORC as the denominator is a constant and the W_{net} increases. From the results, it is suggested to set both $\dot{m}_w$ and Δp_{pump} to their maximum value to obtain the most exergy efficiency of ORC or the integrated cooling and power system.

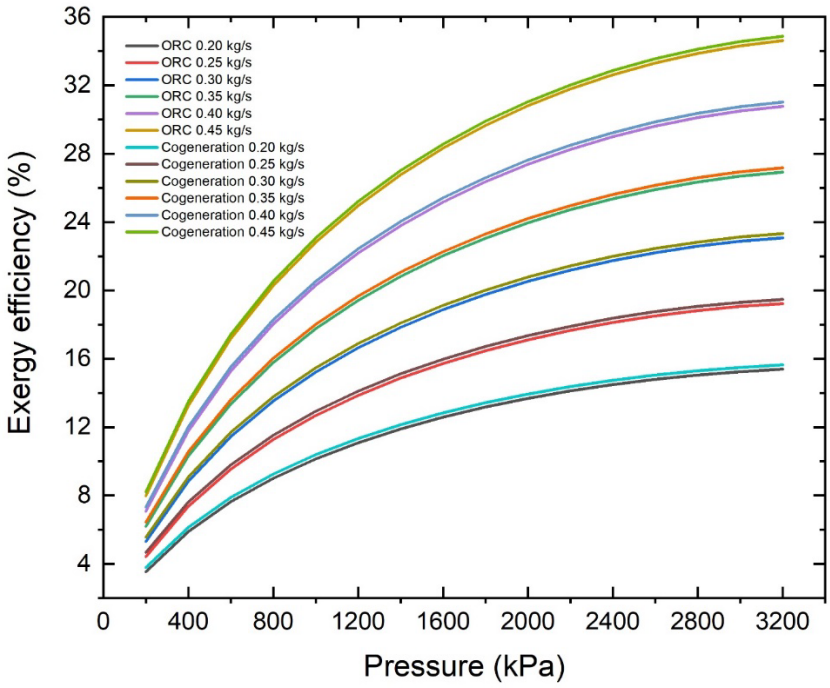

Figure 4.7 Exergy efficiency of ORC and the cogeneration system versus Δp_{pump}

For a clearer observation of the improvement made by the integration of adsorption units and ORC, Fig 4.8 presents the improved percentage of the exergy efficiency. The adsorption cycle provides a positive development on the exergy efficiency evolution in all testing conditions. However, the growth is reduced from low Δp_{pump} to high Δp_{pump}. As indicated in the definition equation of the exergy efficiency, the denominator is the same, while the numerator increases with the additional cold produced by adsorption. Due to the more increase of the net output of ORC compared to refrigeration work in value, the increase ratio made by the refrigeration shrinks with the same growth of $\dot{m}_w$ and Δp_{pump}. The improvement of exergy is up to 7.07 %. From the result, it is revealed that integrated ORC-adsorption system improves the exergy efficiency of the system. However, smaller $\dot{m}_w$ and Δp_{pump} are desired in the system for more improvement of the exergy efficiency under the testing conditions.

Fig 4.9 is the SCP obtained from the sorption part in the integrated system. The development of the values matches with the results from Fig 3.8, as SCP is the refrigeration divided by the sorbent mass. The maximum SCP is 0.2013 kW/kg while the minimum SCP is 0.1953 kW/kg. The difference between various conditions is small, which is quite similar with the refrigeration result. The result reveals that the decrease of Δp_{pump} and $\dot{m}_w$ can improve SCP of the sorbent. However, the improvement is tiny when the refrigeration is low due to the long cycle time.

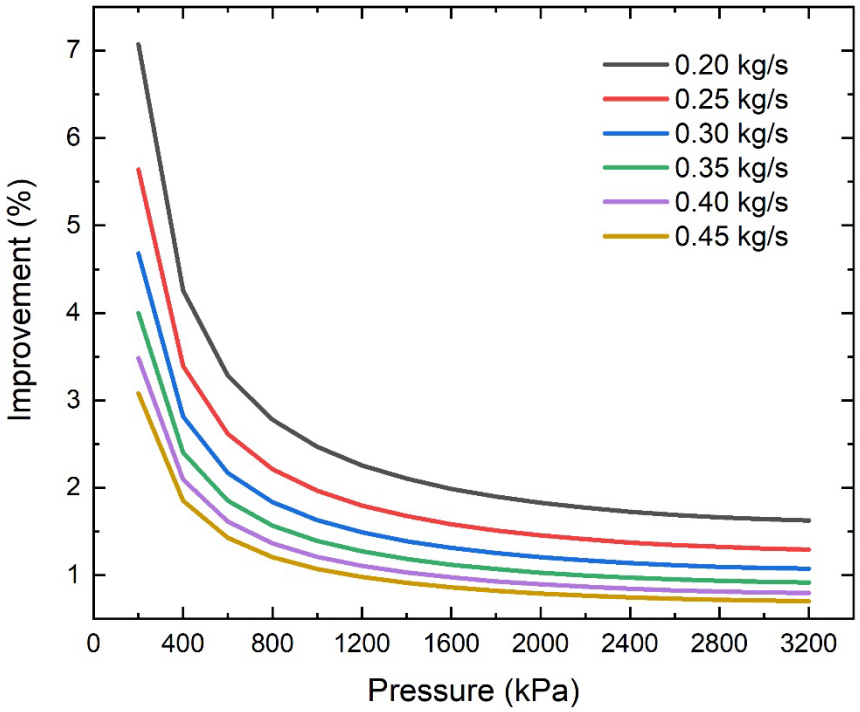

Figure 4.8 Improvement of exergy efficiency versus Δp_{pump}

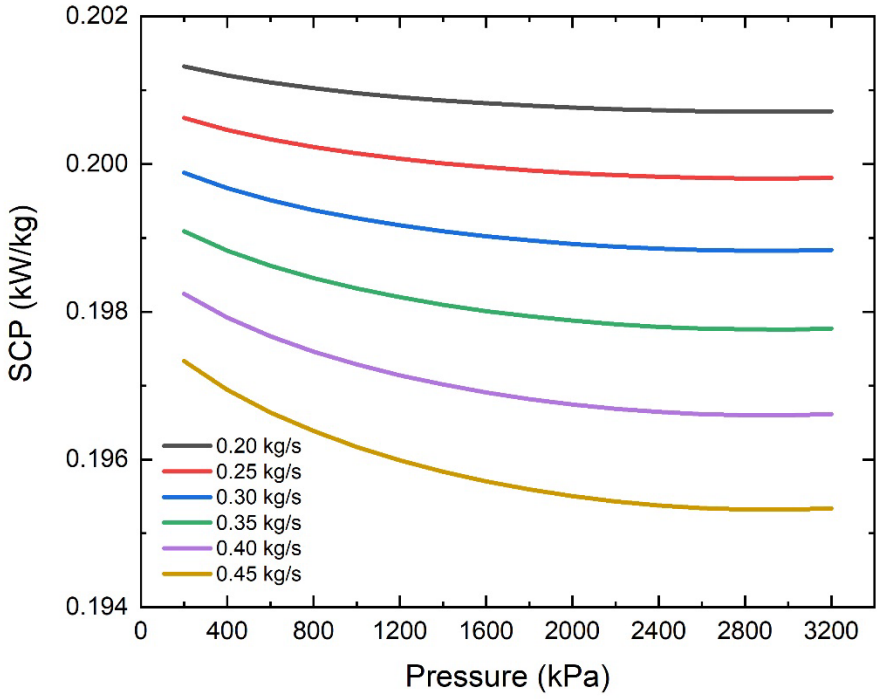

Figure 4.9 Specific cooling power of the system versus Δp_{pump}

Fig 4.10 is the COP of the cogeneration system using $SrCl_2$-EG. The result presents that COP increases with the enlarged $\dot{m}_w$ and Δp_{pump}. The reason could be following. The increase of $\dot{m}_w$ and Δp_{pump} decreases the heat source temperature of desorption. However, the cycle time is long enough for the sorbent to desorb the similar amount of ammonia, which means the refrigeration per unit time is the same. Moreover, the desorption heat is the same, and the

sensible heat is reduced because of the temperature decrease of the heat source. Thus, COP increase with $\dot{m}_w$ and Δppump growing. The highest COP retrieved from the included conditions is 0.5190, with the maximum $\dot{m}_w$ and Δp_{pump}. Contrarily, the lowest COP is 0.5012, obtained from the minimum testing $\dot{m}_w$ and Δp_{pump}. To improve COP of the system, it is suggested that $\dot{m}_w$ and Δp_{pump} should be increased.

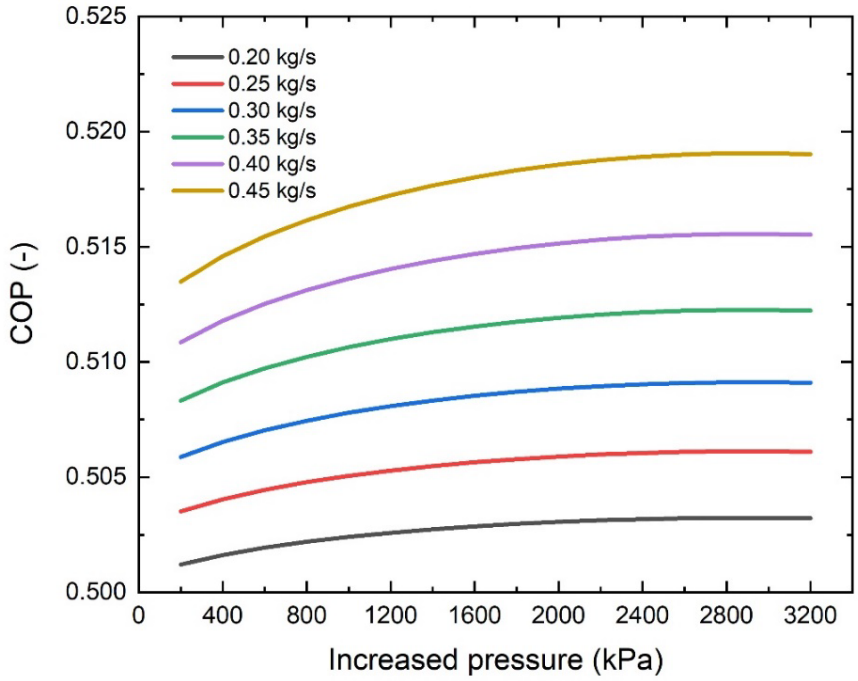

Figure 4.10 COP of the system versus Δp_{pump}

4.3 Summary

A coupling system of ORC and adsorption cycles is built. ORC first utilises the heat source of low-grade thermal energy and the bottom cycle of ORC applies the rest of the low-grade heat after the consumption of ORC. In this way, the cascaded utilisation of the energy could be realised. The modules of ORC and adsorption are introduced in detail to clarify the principle and the processes of the cogeneration. Various performance indicators are calculated and analysed in the result section. The model is coded in MATLAB with the supplementary tool of REFPROP.

- The result of T_2 points out that the suitable range for the mass flow rate of the working fluid r245fa is 0.20 kg/s to 0.45 kg/s and for Δp_{pump} is 200 kPa to 3200 kPa. Besides, it is indicated that the heat source temperature of the sorption modules decreases with either $\dot{m}_w$ and Δp_{pump} increasing.
- The evolution of the results influenced by various working conditions are summarised in Table 4.1. Given the parameters in Chapter 3, $\dot{m}_w$ and Δp_{pump} are suggested to be

increased to improve the net power, the thermal efficiency, the reduction of the dump heat, the exergy efficiency, and COP of the cogeneration. However, to make the enhancement of the refrigeration and SCP, $\dot{m}_w$ and Δp_{pump} are advised to be reduced. The reason causes the phenomenon found in the results are discussed in the contents, which could always be that the changes of the heat consumption of ORC influence the heat source temperature of adsorption units.

- The shortening of the cycle time could make a compromise of all performance indicators, as the low production of refrigeration is due to the long cycle time set in the simulation. The reaction rate of the chemisorption is very fast at first, but the adsorption conversion ratio could still occupy a large proportion of the maximum. It would be reasonable to reduce the cycle time and optimise the cogeneration performance. Moreover, if the cycle time is decreased, the negative influence of the increased $\dot{m}_w$ and Δp_{pump} has the potential to be reduced or eliminated. Thus, an optimal condition of the integrated cycle could be obtained by balancing all indexes into the optimised state.
- The optimal mass flow rate of working fluid is 0.45 kg/s, while the pressure difference of the pump is 3200 kPa. In this case, the system reaches the maximum net power, refrigeration, thermal efficiency, and exergy efficiency of 13.21 kW, 0.0957 kW, 0.1127, and 34.87 %, respectively. Besides, this condition enables the minimum waste heat after the utilization of the engine emission, 164.49 kW. COP of adsorption also achieves the highest value of 0.5190.

Chapter 4 demonstrates the improvement of the production and the heat conversion of a given low-grade heat, by integrating ORC with adsorption technologies. The results show that $\dot{m}_w$ and Δp_{pump} need to be increased to optimise the system efficiency.

Result	$\dot{m}_w$ increases	Δp_{pump} grows
T_2	decreases	decreases
Net power	increases	increases
Refrigeration	decreases	decreases
Thermal efficiency of ORC	keeps same	increases
Thermal efficiency of cogeneration	increases	increases
Dump heat of ORC	decreases	decreases
Reduction of dump heat	increases	increases
Exergy efficiency of ORC	increases	increases

Improvement of exergy efficiency	decreases	decreases
SCP	decreases	decreases
COP	increases	increases

Table 4.1 Summary of the results in Chapter 4

Chapter 5 Thermal-physical study of the adsorbents

Chapter 5 reports the experimental study of the thermal-physical properties of the newly developed composite sorbents for the sorption system.

The type of the sorbents is composite, and the salts in the composites are $SrCl_2$ for low temperature desorption (above 90 ℃) and $MnCl_2$ for high temperature desorption (above 150 ℃). The matrix of the adsorbents is expanded graphite (EG). Besides, the additives are Carbon Coated Ni, Al and Fe (Ni@C, Al@C and Fe@C).

Innovative methodology of the manufacturing developed by the author is reported. The observation on the sorbents surface are tested to prove the methodology to be superior for a uniform distribution of various ingredients. Other properties like the thermal diffusivity and conductivity are analysed and included.

5.1 SEM and EDX results

The conventional composite adsorbents of $SrCl_2$-EG and the novel composite $SrCl_2$-EG-Ni/Al/Fe@C are analysed by SEM and EDX in NEXUS Lab, Mechanical Engineering School, Newcastle University.

$SrCl_2$-EG:

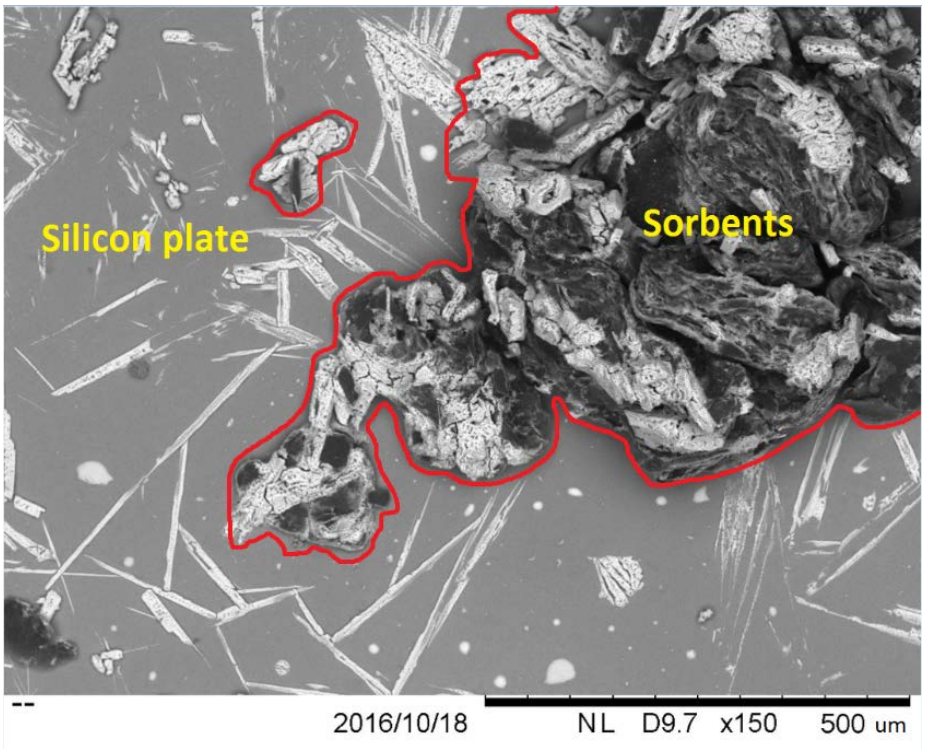

(a) SEM image of 150 times magnification

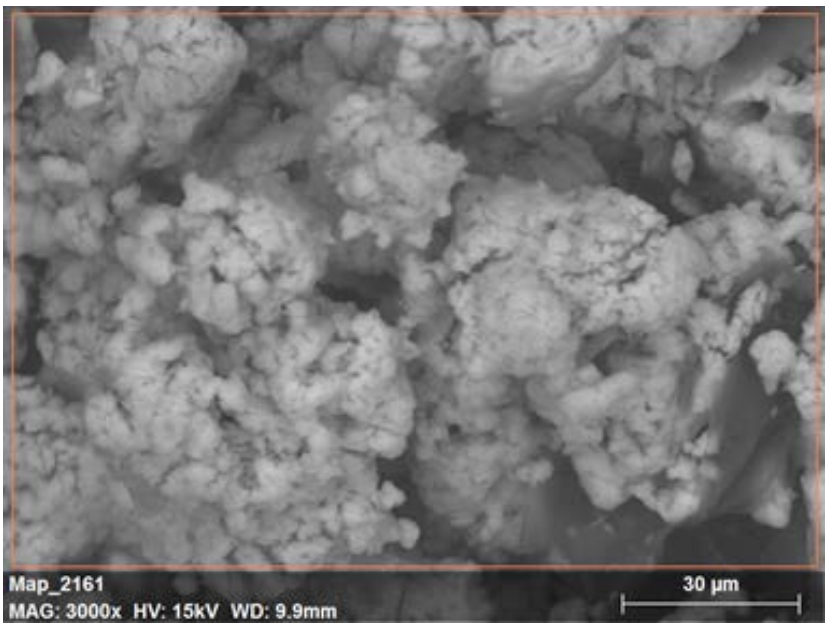

(b) SEM image of 3000 times magnification

Figure 5.1 SEM image of $SrCl_2$-EG

Fig. 5.1 displays the SEM images of the conventional $SrCl_2$-EG at different magnifications. In Fig 5.1 (a), the sorbents on the top of the right side are circulated by the red curve, which is taken at the magnification of 150 times. They are the main objects in the tests, while a small accumulating of sorbents like an island at their left is normally ignored. The rest of the figure is the background of the silicon plate. After having the researching object in sight at the lower magnification, the next step is to enlarge the photo at a certain point and re-scanning to form a new picture as shown in Fig 5.1 (b), which is at the magnification of 3000 times, under the voltage of 15 kV.

Fig 5.2 presents the SEM images corresponding to Fig 5.1 (b). Fig 5.2 (a) displays a complex elements mapping, including carbon (C) and chloride (Cl). In next two figures, separate mappings of C and Cl elements indicate that the lighter colour in Fig 5.1 (b) refers to the salt components of the composite, as the shape of substance in light grey colour is the same with the profile of the green spots in Fig 5.2 (c), which stands for the element of Cl. Besides, the darker part at the top of the left side and the bottom of the right side in Fig 5.1 (b) matches the shape of the blue spots in the same positions in Fig 5.2 (b). The fact reveals the darker background is the carbon matrix of EG, as the blue spots represents C element. On the other hand, it reflects the well-adhered/wrapped salt-EG structure of the sorbents, as the darker area is small. Fig 5.2 (d) is the energy dispersion retrieved from the X-ray spectroscopy. The peaks of C and Cl elements explain the principle of EDX, which analyses the energy intensity to detect the category of various elements. Moreover, the results from EDX also indicate the correct ingredients of the tested adsorbent $SrCl_2$-EG.

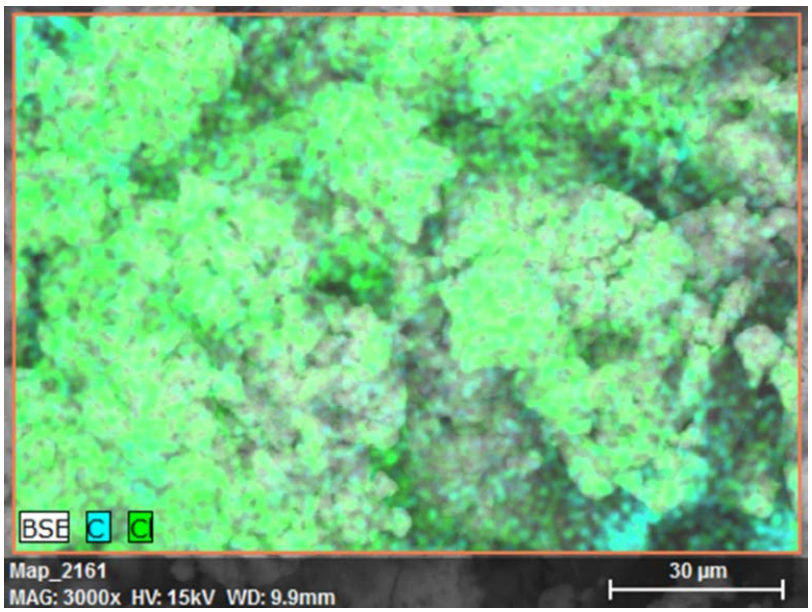

(a) EDX image of various elements in 3000 times magnification

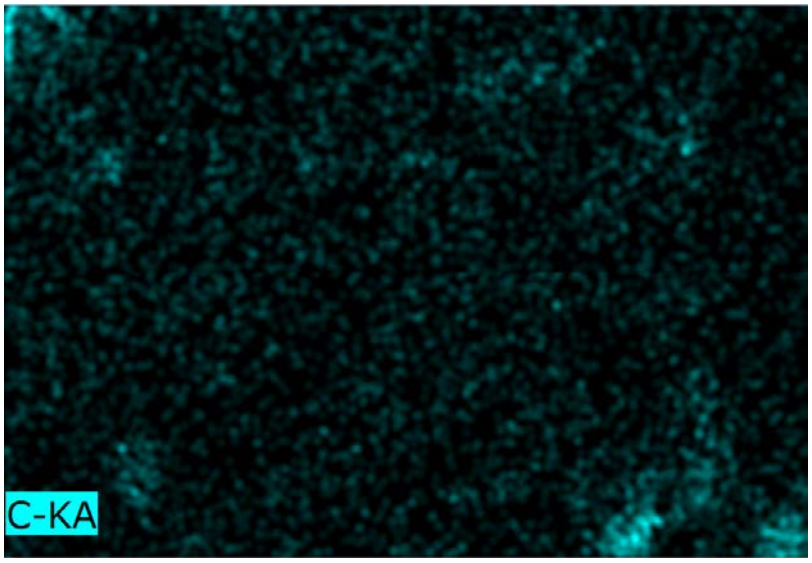

(b) EDX image of C-element

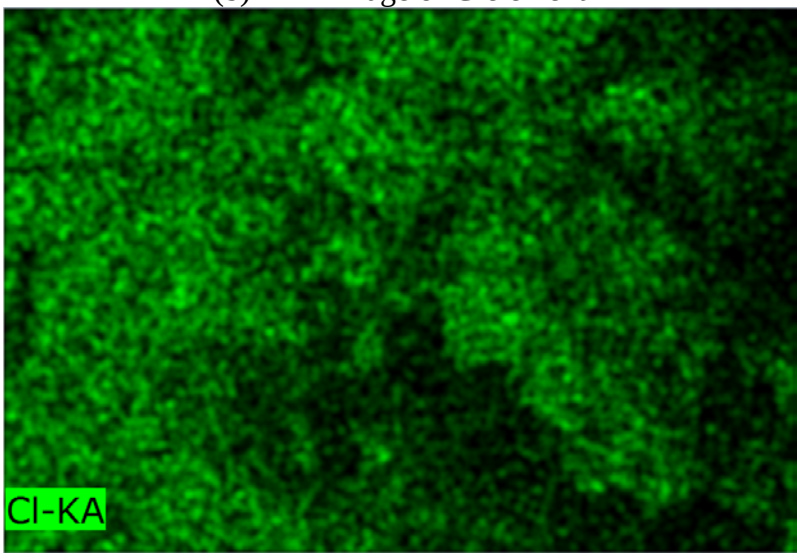

(c) EDX image of Cl-element

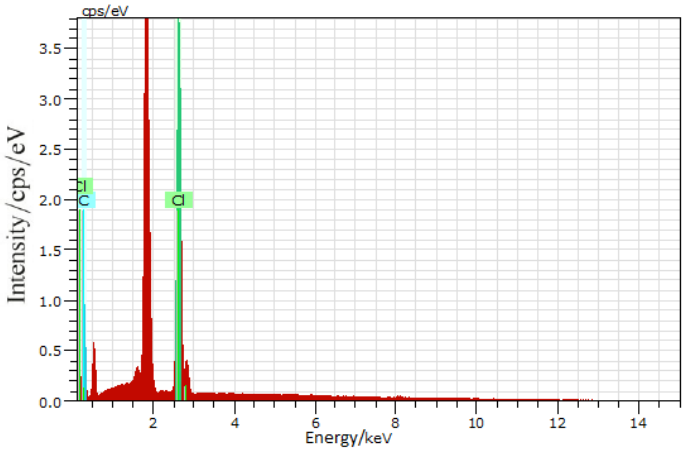

(d) EDX illustration of the energy-intensity

Figure 5.2 EDX images of conventional $SrCl_2$-EG

$SrCl_2$-EG-Ni@C:

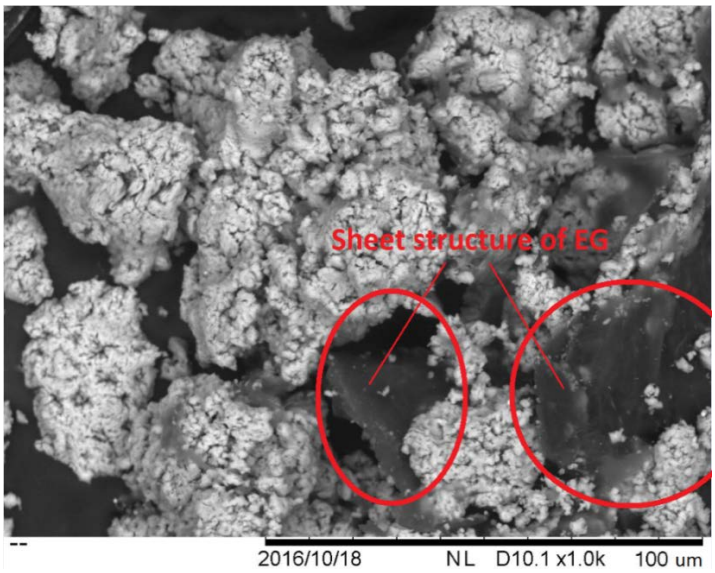

(a) SEM image of 1000 times magnification

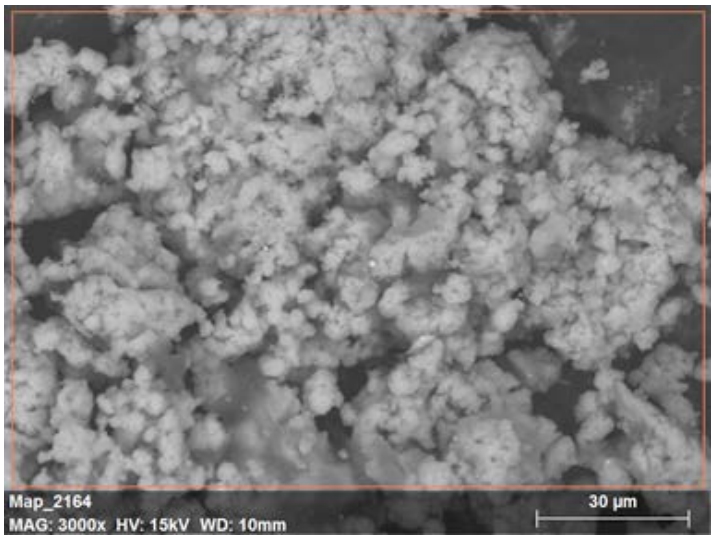

(b) SEM image of 3000 times magnification

Figure 5.3 SEM images of $SrCl_2$-EG-Ni@C

Fig. 5.3 presents the results of SEM from $SrCl_2$-EG-Ni@C samples. Fig 5.3 (a) is the photo obtained from the scanning with an amplification of 1000 times, while Fig 5.3 (b) is that enlarged by 3000 times. Two red circles circulate the observed sheet structure of EG in Fig 5.3 (a), which is exposed to the ambient condition rather than fully coated by the chlorides. This reveals the nature of not fully filled gaps and surfaces at the salt/EG mass ratio of 2:1. Moreover, it observes one of the superior properties of EG, the large specific surface area due to the sheet structure, which could be charged with desirable materials for widely scientific study and applications. Fig 5.3 (b) provides a more detailed perspective of $SrCl_2$-EG-Ni@C surface, compared with the former picture. Different with the relatively smoothing look of the salts in Fig 5.1 (b), on the top of the chlorides, there are much little black dots witnessed in Fig 5.3 (b). However, it is hard to directly distinguish either the category or the distribution condition of the substance by this image.

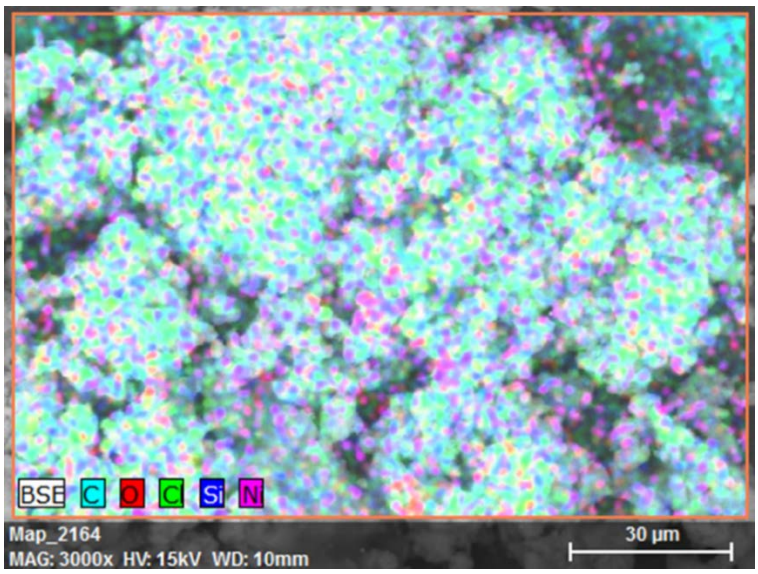

(a) EDX image of various elements

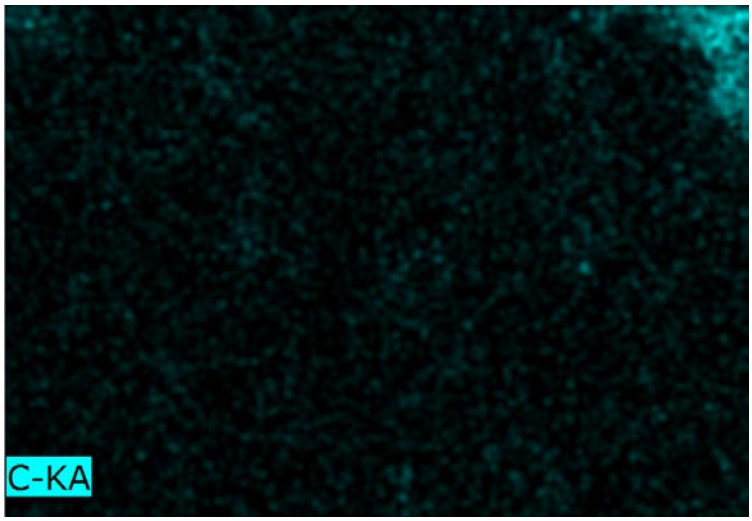

(b) EDX image of C-element

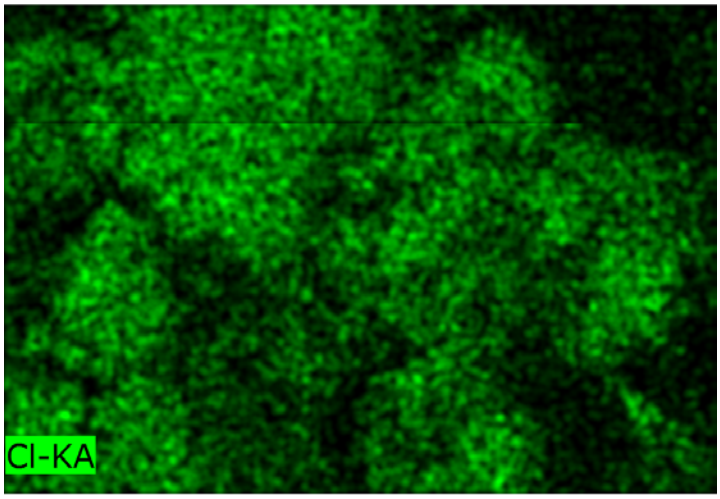

(c) EDX image of Cl-element

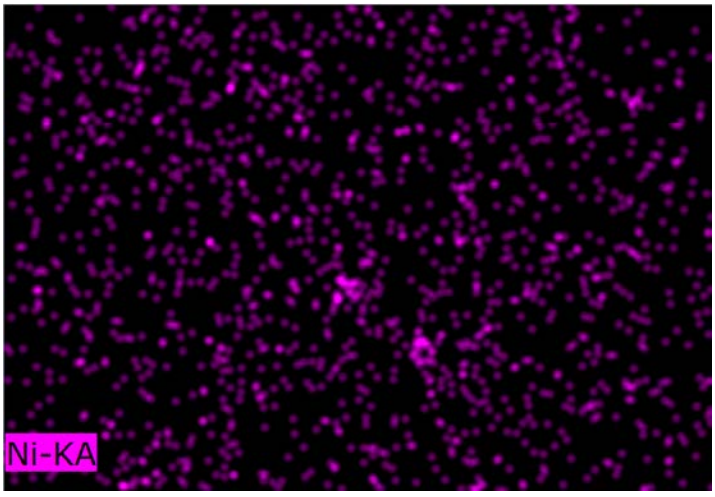

(d) EDX image of Ni-element

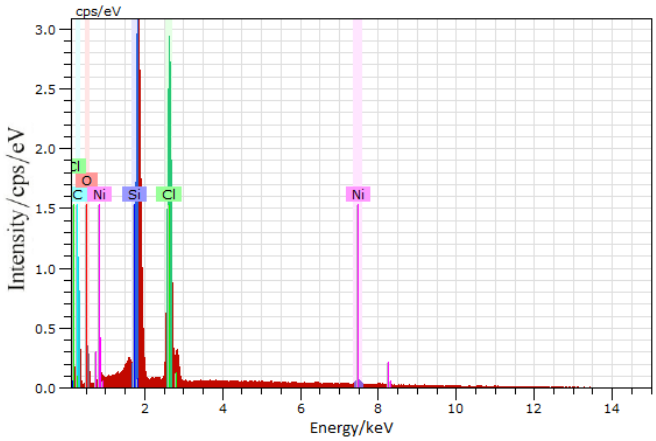

(e) EDX illustration of energy-intensity

Figure 5.4 EDX images of $SrCl_2$-EG-Ni@C

Fig 5.4 presents the result of EDX test corresponding to the SEM photos. The black dots observed in figure above are proved to be the nanoparticles by the further analysis and comparison of EDX images. Fig 5.4 (a) presents the overview of the mixed elements mapping of C in blue, O (Oxygen) in red, Cl in green, Si in indigo, and Ni in purple. Fig 5.4

(b) has only one obvious area of blue assembly, showing a good covering condition of $SrCl_2$ over EG. In Fig 5.4 (c), green colour is the dispersion of $SrCl_2$, which has the same shape with the light grey districts in Fig 5.3 (b), proving correctness of the discussion in non-additive adsorbents, again. The spots in purple colour are compared with the dark dots in Fig 5.3 (b). They scatter in a same trend all over the mapping, ensuring that the substance of the dots is Ni@C. Despite two very small area, the nanoparticles are dispersed homogeneously as the random purple dots indicate. Fig 5.4 (e) explains the foundation of the elements mapping is the detection of the energy spectrum. The peaks of Ni, Si, O, Cl and C are drawn in the illustration.

The result proves the developed methodology a superior way to mix the sorbent ingredients, as the salt well wraps EG and the nano additives are evenly distributed in the sorbent. By this method, the negative influence caused by the sorbent agglomeration and congregation could be alleviated. Thus, the sorption performance is expected to be improved.

$SrCl_2$-EG-Al@C:

Fig 5.5 shows the SEM images retrieved from $SrCl_2$-EG-Al@C samples. Similar with the analysis of $SrCl_2$-EG and $SrCl_2$-EG-Ni@C, Fig 5.5 (a) is the 1000 times amplified illustration of the sample surface, showing the covering of the salts on the surface or between the gaps of the graphitic sheet layers. Gaining experience from above SEM and EDX tests, the author retrieved SEM image of 3000 times magnification based on the red box area in the former image. By this method, it could be more convenient for the audience to understand and track the observed area. In Fig 5.5 (a), the red rectangle marks the further amplified field. The corner pointed by red curve is the silicon plate.

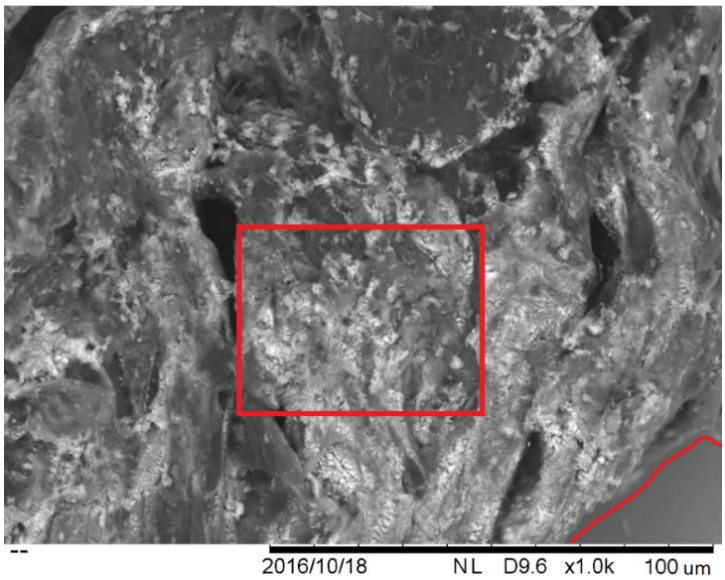

(a) SEM image of 1000 times magnification

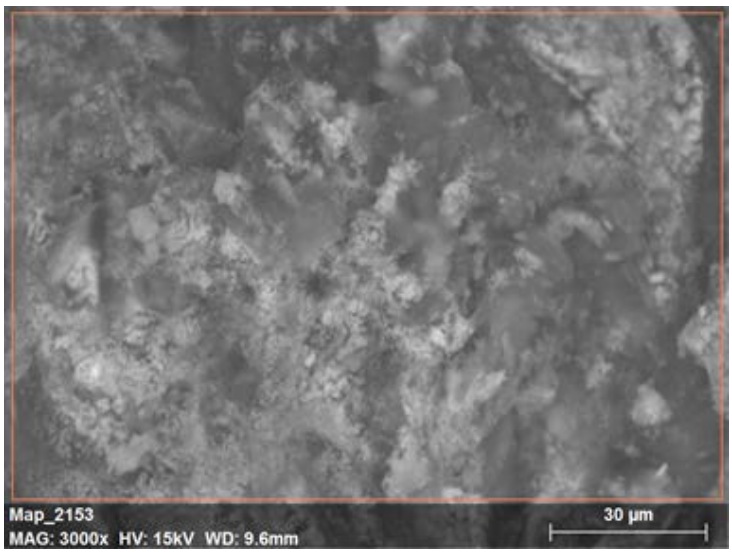

(b) SEM image of 3000 times magnification

Figure 5.5 SEM images of $SrCl_2$-EG-Al@C

Fig 5.6 is the EDX images corresponding to Fig 5.5 (b). Fig 5.6 (a) presents the mapping of the mixed elements. The respective elements mappings of C, Cl and Al are included below, indicating the distributions of the EG, salt and the nano particles. Fig 5.6 (b) and Fig 5.6 (c) show that EG is well covered by strontium chloride. In Fig 5.6 (d), the element of the metal core is coloured in green, indicating a relatively satisfactory in the aspect of scattering. The innovative manufacturing procedures are proved to be feasible for mixing Al@C with the conventional composite of $SrCl_2$-EG, again, on the purpose of uniformly dispersing. Fig 5.6 (e) reports the spectrum of the sample in the terms of energy with intensity. Peaks of C, Cl, Si and Al are there indicating the right components of the sorbent sample.

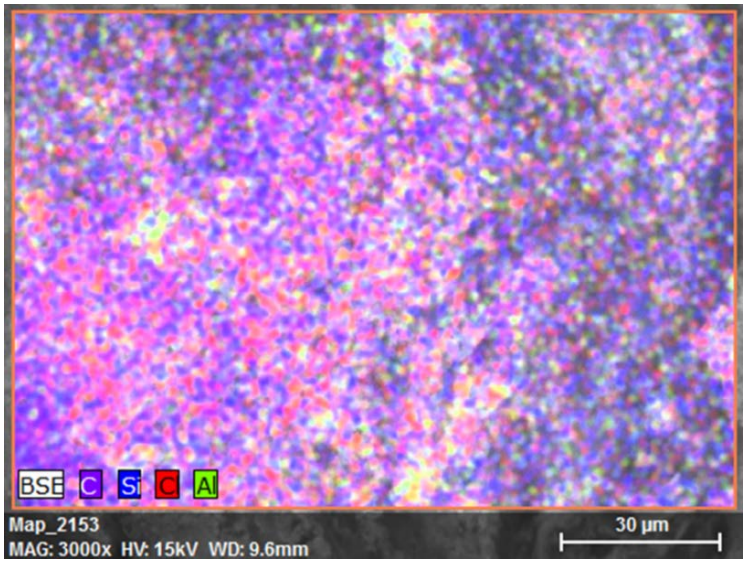

(a) EDX image of various elements

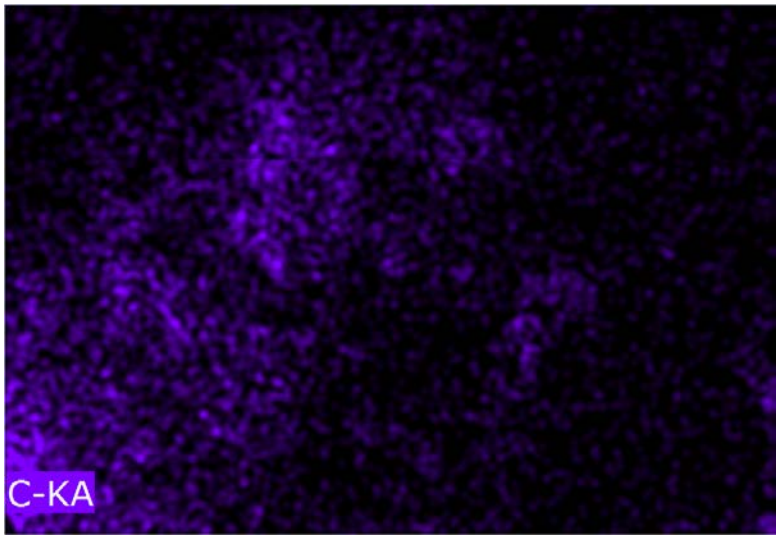

(b) EDX image of C-element

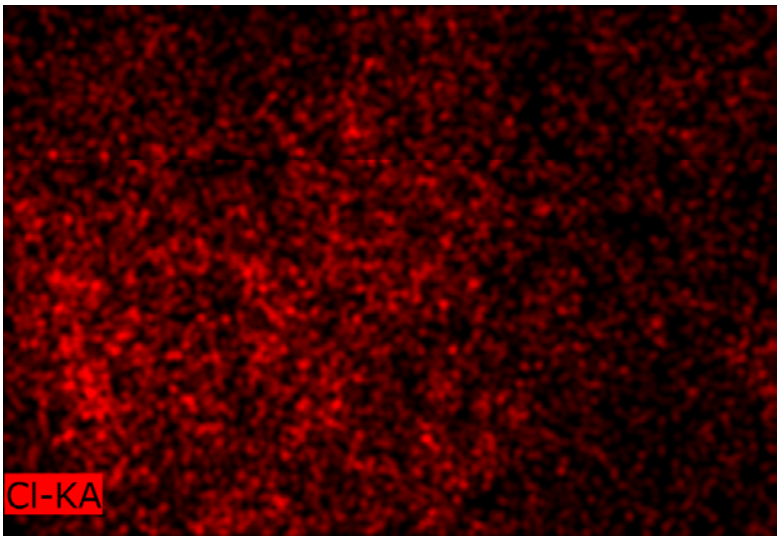

(c) EDX image of Cl-element

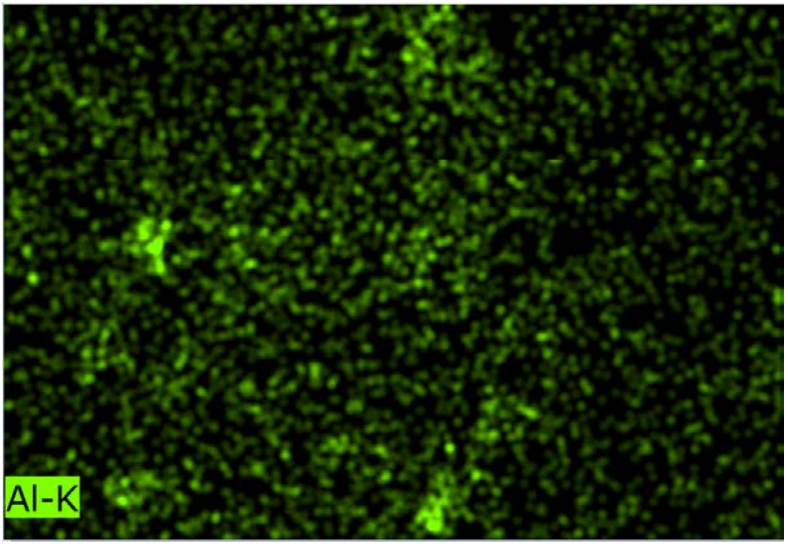

(d) EDX image of Al-element

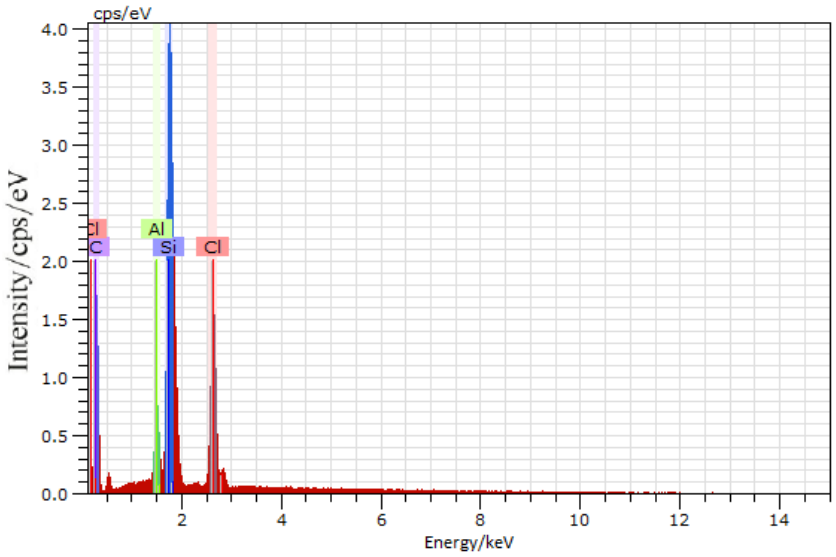

(e) EDX image of energy-intensity

Figure 5.6 SEM and EDX images of $SrCl_2$-EG-Al@C

$SrCl_2$-EG-Fe@C:

Fig 5.7 displays images from the SEM tests of $SrCl_2$-EG-Fe@C. Fig 5.7 (a) is in a lower amplification while Fig 5.7 (b) enlarges the red box area to 2000 more times than the former illustration. The graphitic layer is clearly defined in the observation. In Fig 5.7 (b), the light grey district is in a small area. However, the distributions of the salts and nanoparticles are hard to distinguish in these SEM results. They will be checked by the EDX tests.

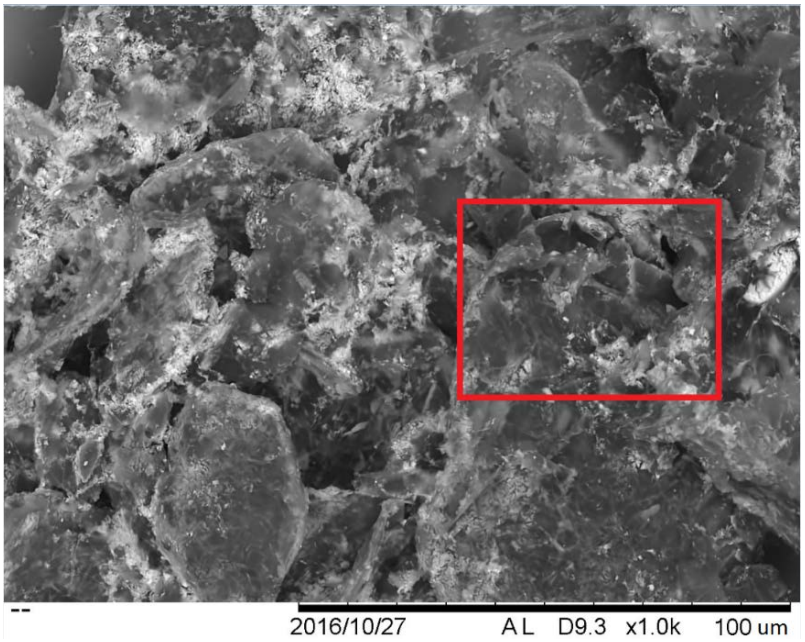

(a) SEM image of 1000 times magnification

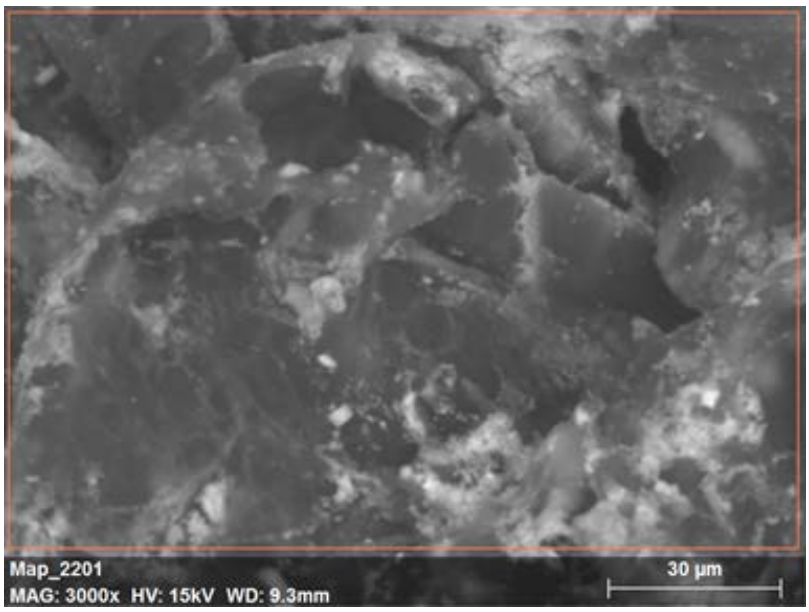

(b) SEM image of 3000 times magnification

Figure 5.7 SEM images of $SrCl_2$-EG-Fe@C

Fig 5.8 shows the images of EDX results corresponding to the SEM tests. The information in the EDX results reflects the similarity on the shape of different coloured districts between the SEM and EDX images. Fig 5.8 (b) demonstrates that only a small proportion of EG is exposed to the air rather than covered by the salts or nano particles. Fig 5.8 (c) reveals that strontium chloride is dispersed evenly in the sorbents, even the light grey part in Fig 5.7 is small in area. In Fig 5.8 (d), the element Fe is discovered to be randomly dispersed in the tested sample. Thus, the treatment to nanoparticles works on Fe@C powders as well. Fig 5.8 (e) shows the peaks of Fe, Cl, Si and C, referring to the detection of the Nano-additives, the chlorides, the silicon plates and the carbon matrix of EG or the carbon coating on the nanoparticles.

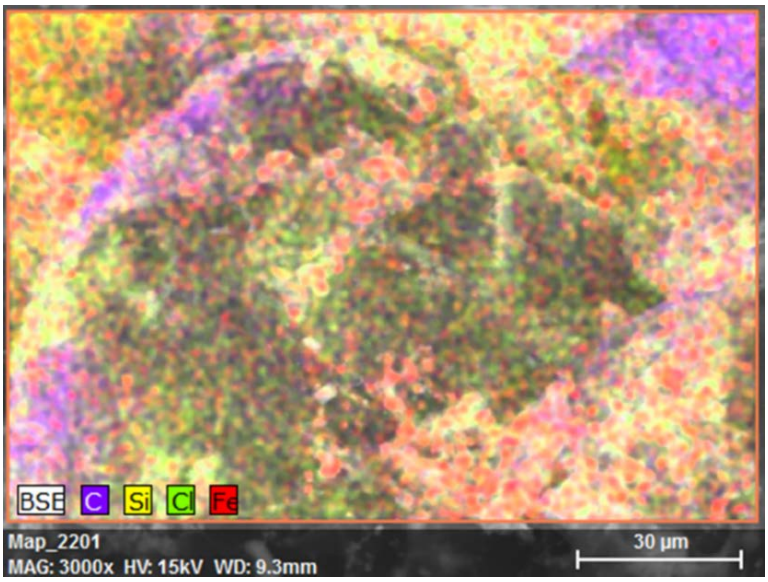

(a) EDX image of various elements

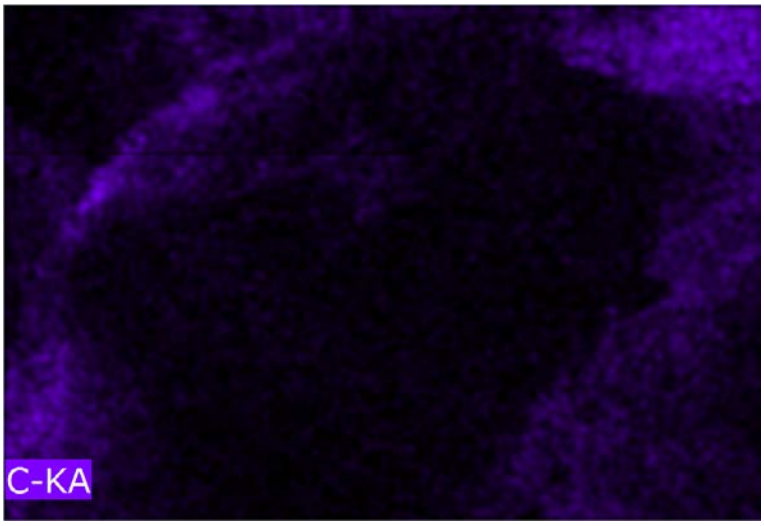

(b) EDX image of C-element

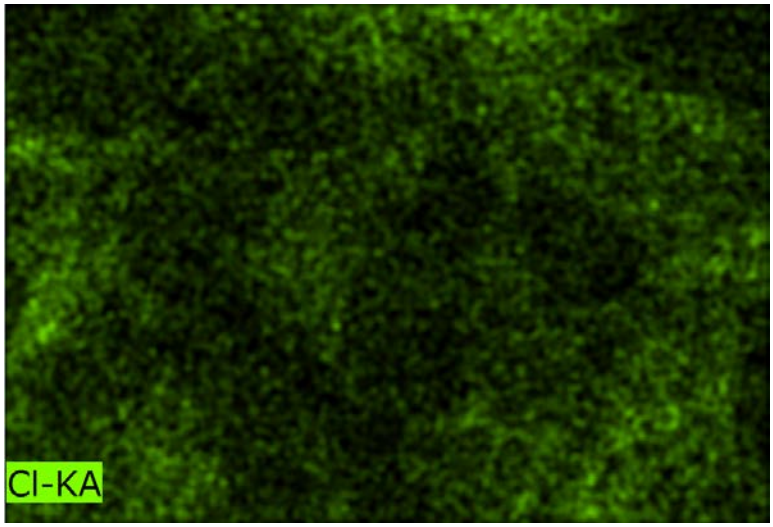

(c) EDX image of Cl-element

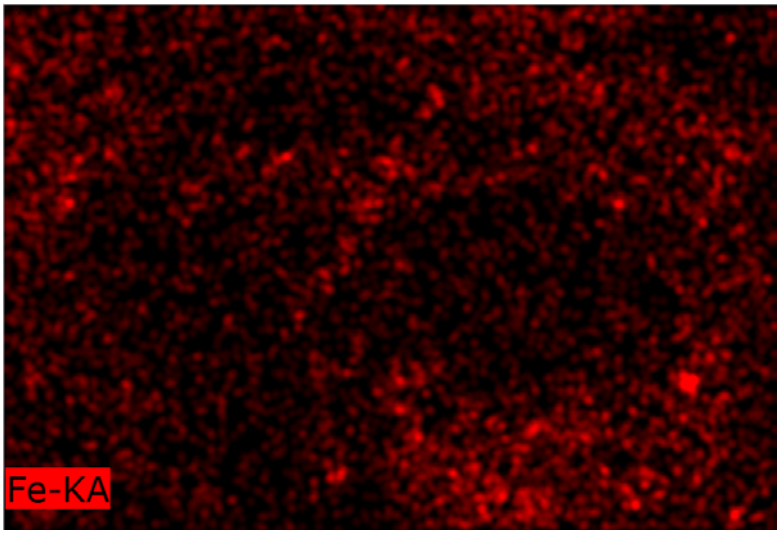

(d) EDX image of Fe-element

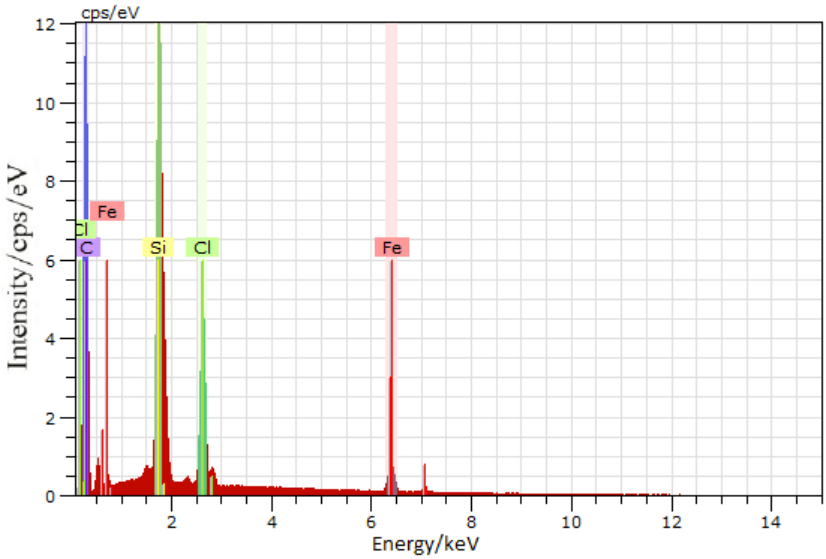

(e) EDX illustration of energy-intensity

Figure 5.8 SEM and EDX images of $SrCl_2$-EG-Fe@C

In a summary, the result of the SEM and EDX tests prove the developed methodology a superior way to mix the sorbent ingredients. The salt well-adheres on the sheet surface of EG or filled in the gaps between the graphic layers. Moreover, the nano additives are evenly distributed in the sorbent. The result indicates that the negative impact caused by the heterogeneous mixing could be alleviated. Therefore, the developed preparation methodology is feasible to improve the sorption performance.

5.2 Thermal diffusivity and conductivity

$MnCl_2$-EG along with its derivative sorbents are analysed by LFA as well. The density of the sample ranges from 600 kg/m^3 to 1000 kg/m^3. And the testing temperatures are 10 ℃, 20 ℃ and 30 ℃ for the environmental temperature range. For desorption temperatures, the alteration is 150 ℃, 160 ℃, 170 ℃ and 180 ℃. An extra temperature of 200 ℃ is set to dry the sorbent in LFA machine before the tests of other temperatures.

Thermal diffusivity:

Fig. 5.9 presents the thermal diffusivity of the sorbents at the high testing temperatures of 150 ^{o}C, 160 ^{o}C, 170 ^{o}C, 180 ^{o}C and 200 ^{o}C, while Fig. 5.10 displays that of the manufactured samples at the low testing temperatures of 10 ^{o}C, 20 ^{o}C and 30 ^{o}C. The colours of the lines are black, red, green, blue and orange, respectively representing the sample density from low to high (600 kg/m^3, 700 kg/m^3, 800 kg/m^3, 900 kg/m^3 and 1000 kg/m^3). The symbols of square, circle, up triangle and down triangle stand for the sorbents of $MnCl_2$-EG, $MnCl_2$-EG-Ni@C, $MnCl_2$-EG-Al@C and $MnCl_2$-EG-Fe@C, separately.

For the thermal diffusivity of the normal $MnCl_2$-EG versus various temperatures, it is obvious that all lines decline with the temperature increasing. From the bottom to the top of the figure, the order of the lines is black, red, green, blue and orange, which represents the increment order of the thermal diffusivity from the minimum density of 600 kg/m^3 to the highest one of 1000 kg/m^3. The maximum thermal diffusivity during the tests is 2.12 mm^2/s, found at the upper left point on purple line standing for a sample density of 1000 kg/m^3 and a testing temperature of 10 ℃. At the right corner at the bottom, the black point presents a lowest thermal diffusivity of $MnCl_2$-EG of 1.69 mm^2/s, at a temperature of 200 ℃, when the specimen is compressed to the density of 600 kg/m^3.

For the results of $MnCl_2$-EG-Ni@C samples, the plot figure displays a decreasing development of the sorbent thermal diffusivity along with the detecting temperature ranging from 10 ℃ to 200 ℃, or with the density dropping from 1000 kg/m^3 to 600 kg/m^3. The highest point among all is the purple point located at the top while the lowest point is the black point situated at the bottom right corner, reflecting the maximum thermal diffusivity of $MnCl_2$-EG-Ni@C is 2.27 mm^2/s and the minimum of that is 1.72 mm^2/s with corresponding testing conditions.

The thermal diffusivity of Al@C-added $MnCl_2$-EG is also tested in LFA, and the result reveals that the positive development of thermal diffusivity along with the reduction of testing temperatures. Besides, the value of the thermal diffusivity becomes larger when the sample density increases from 600 kg/m^3 to 1000 kg/m^3. The highest point among all is the purple one at the top left corner of the illustration with a value of 3.64 mm^2/s, retrieved from the sample compressed to 1000 kg/m^3 and tested under the temperature of 10 ℃. The bottom point of black at the right of the figure shows the smallest thermal diffusivity of 2.12 mm^2/s, obtained by the specimen of 600 kg/m^3 at 200 ℃.

For the chemisorption composite with Fe@C, again, the result of its thermal diffusivity reveals the growth of the material thermal diffusivity when the temperature drops or when the compression becomes stronger.

As a conclusion, for different additives, the thermal diffusivity of the samples is in the increment order as Al@C, Fe@C, Ni@C and non-additive. For the same kind of the composite, the thermal diffusivity of the samples increases with the density growing or the temperature decreasing.

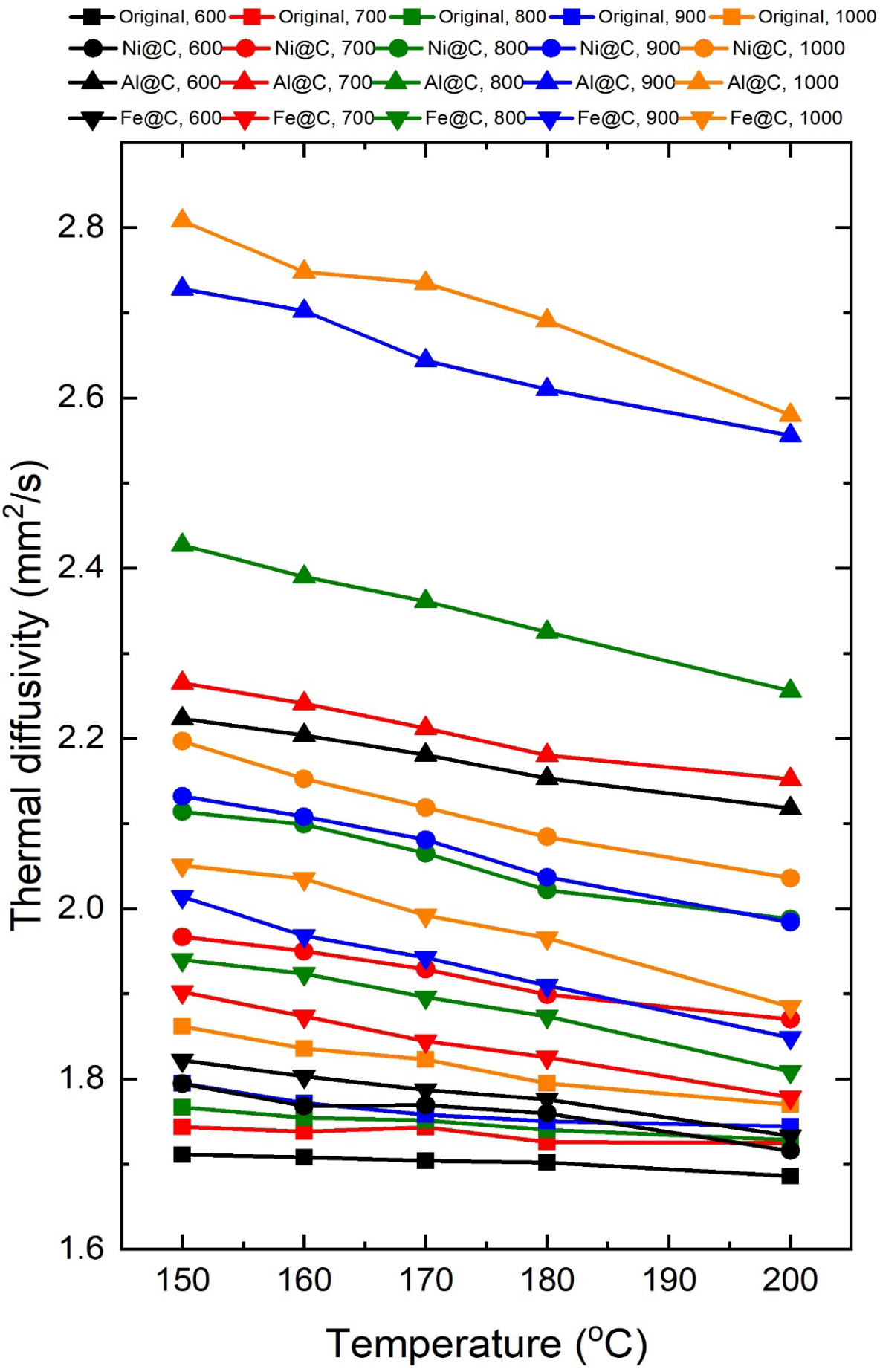

Figure 5.9 Thermal diffusivity of the sorbents at high temperatures

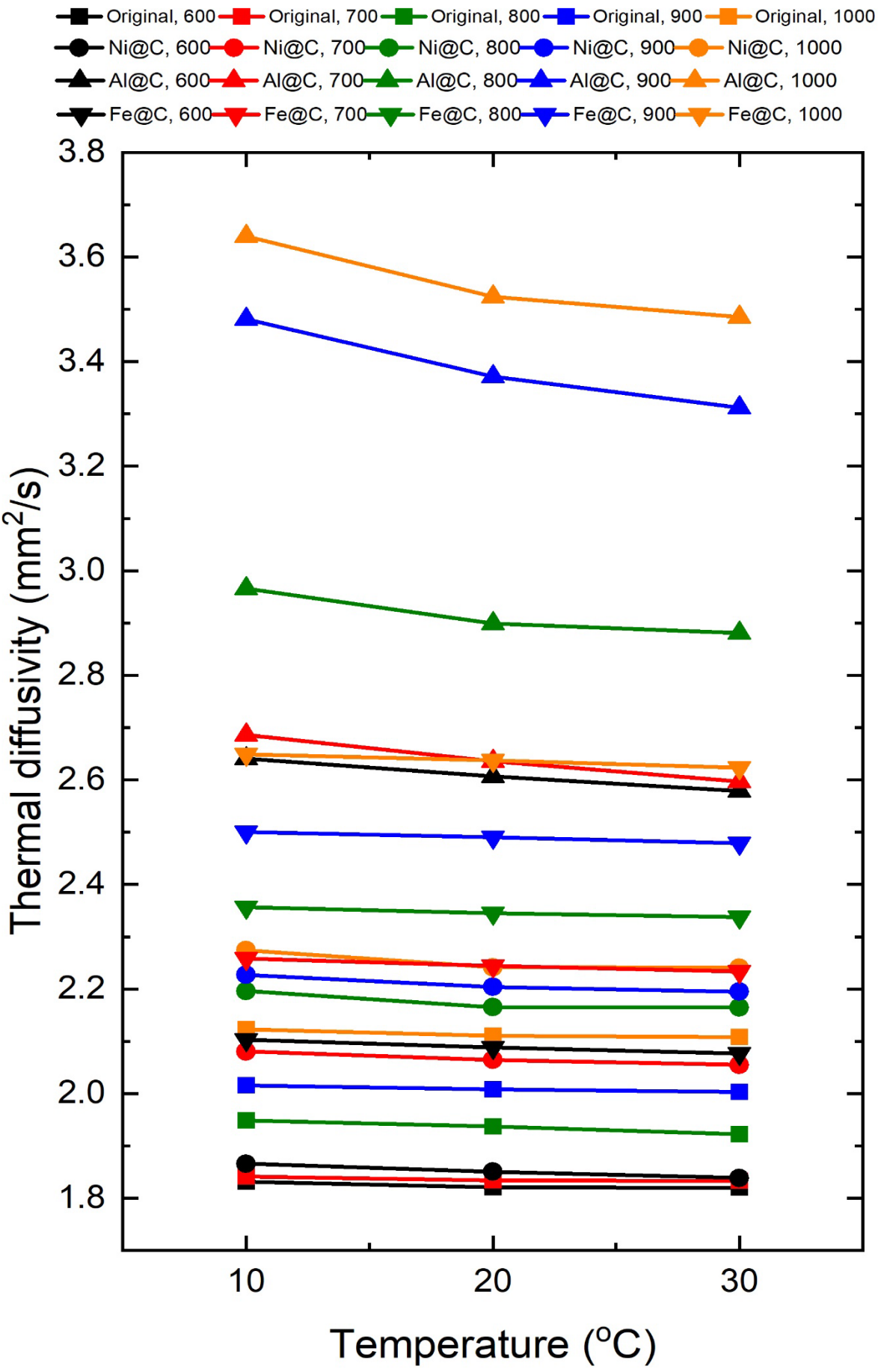

Figure 5.10 Thermal diffusivity of the sorbents at low temperatures

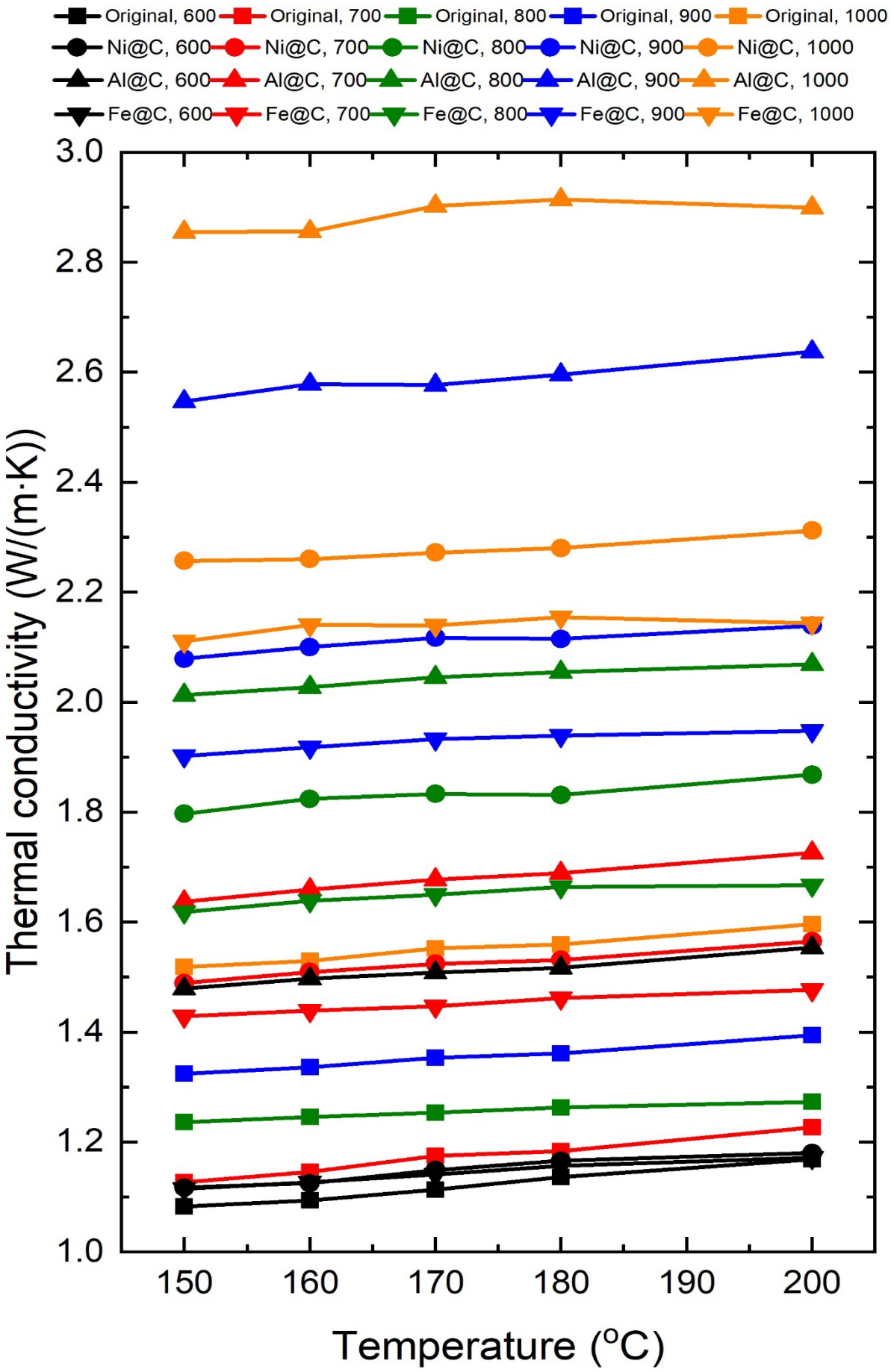

Figure 5.11 Thermal conductivity of the sorbents at high temperatures

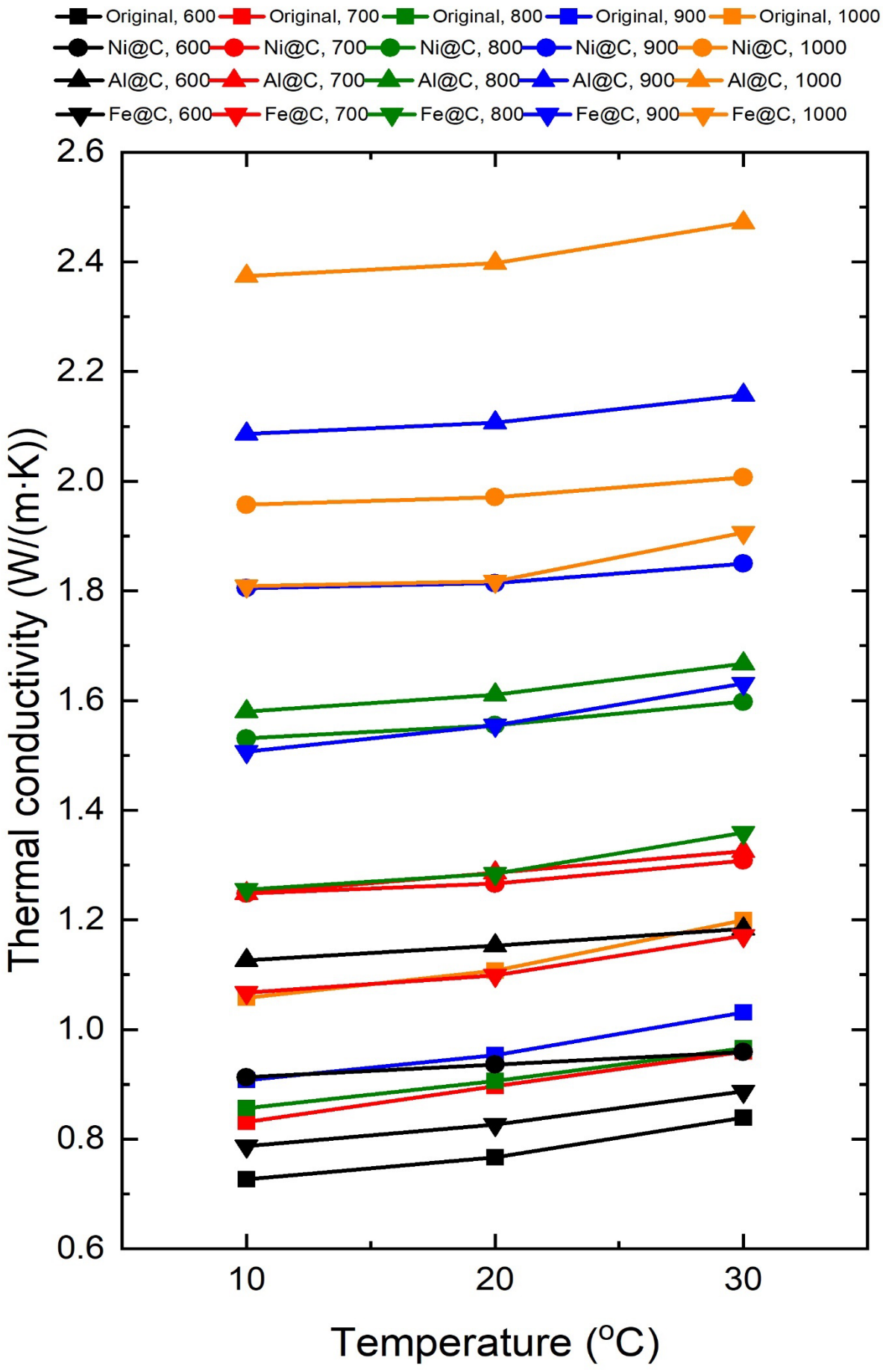

Figure 5.12 Thermal conductivity of the sorbents at low temperatures

Thermal conductivity:

Fig. 5.11 demonstrates the thermal conductivity of the prepared sorbents at the high testing temperatures from 150 ºC to 200 ºC, while Fig. 5.12 shows the thermal conductivity of the samples at the low experimental temperatures from 10 ºC to 30 ºC. The thermal conductivity is calculated through the thermal diffusivity detected by the machine.

For the conventional chemisorption composite of $MnCl_2$-EG, the coloured lines have a same growing trend along with the temperature inclining, indicating the thermal conductivity positively develops with the temperature increasing. Besides, when the density of the specimen drops, the thermal conductivity decreases. The largest value of the thermal conductivity among all points is 1.60 W/(m·K), obtained with a sample density of 1000 kg/m3 and at the detecting temperature of 200 ℃. Moreover, the smallest thermal conductivity of conventional composite sorbent $MnCl_2$-EG is 0.73 W/(m·K), found at 10 ℃ test, with the specimen density of 600 kg/m3.

The thermal conductivity of $MnCl_2$-EG-Ni@C shows an inclining trend of the thermal conductivity tested under a temperature range from 10 ℃ to 200 ℃, when the density grows from 600 kg/m^3 to 1000 kg/m^3. The maximum of the thermal conductivity observed in Fig 4.35 is 2.31 W/(m·K), under a condition when the sorbent is made to 1000 kg/m^3 and the working temperature is set to 200 ℃. The minimum value of $MnCl_2$-EG-Ni@C is 0.91 W/(m·K), found in the 600 kg/m^3 sample tested at 10 ℃.

Compared to the original composite, the novel sorbents with Ni@C has a higher thermal conductivity under all testing conditions. The result demonstrates that the maximum thermal conductivity of the sorbents can be improved by 44.4 %, and the minimum thermal conductivity can be enhanced by 24.7 %. Moreover, the improvement made by the additives of Ni@C proves the manufacturing methodology to be a superior method for the evenly mixing. Besides, it also indicates that the novel sorbent is potential to improve the sorption performance by enhancing the heat and mass transfer of the sorbent.

The result of $MnCl_2$-EG-Al@C samples with the temperature ranging from 10 ℃ to 200 ℃ and the density altered from 600 kg/m^3 to 1000 kg/m^3 demonstrates the increase of the thermal conductivity when the temperature grows higher or the sample density increases. The highest thermal conductivity of $MnCl_2$-EG-Al@C is 2.90 W/(m·K), presented at a testing temperature of 200 ℃ with a specimen density of 1000 kg/m^3. Moreover, the minimum

thermal conductivity in the detected range is 1.13 W/(m·K), retrieved from the sorbent of 600 kg/m^3 at 10 ℃.

The results demonstrate that the thermal conductivity of the composite sorbent is improved by the additives of Al@C. The maximum thermal conductivity of the sorbent is enhanced by 81.3 %, and the minimum thermal conductivity is increased by 54.8 %. The result also reveals that the additives of Al@C can potentially improve the heat and mass transfer of the sorbent. Thus, the novel sorbent is feasible to enhance the sorption performance.

The material thermal conductivity of $MnCl_2$-EG-Fe@C increases with the temperature positively developing from 10 ℃ to 100 ℃ or with the sample density added from 600 kg/m^3 to 1000 kg/m^3. The results display a thermal diffusivity ranging from 1.733 mm^2/s to 2.649 mm^2/s and a thermal conductivity within 0.79 W/(m·K) to 2.14 W/(m·K).

It is found in the results that the thermal conductivity of conventional $MnCl_2$-EG is enhanced by the added Fe@C. For the maximum thermal conductivity, the value is increased by 33.8 %. For the minimum thermal conductivity, the value is increased by 8.2 %. The result indicates that by adding Fe@C into the conventional composite sorbents, it is potential to improve the heat and mass transfer process thus enhance the sorption performance.

5.3 Summary

In Chapter 5, the author finds that the conventional manufacturing procedures cannot prepare the sorbents to a satisfying quality. Thus, an innovative methodology of preparing the novel composite sorbents is developed and reported. The manufactured adsorbents are tested by SEM, EDX and LFA to study their thermal-physical characteristics.

- Some processes are added based on the original methods for the evenly distribution of the sorbent materials. The extra ultrasonic bath treatment is applied to vibrate and smash the tiny conglomerate of the nanoparticles. Moreover, this mixing method is more superior than mixing by hand. Ethanol is used as the mixing media, as it has a lower density than water and thus reduces the resistance of the particle movement in the fluid. In the period of evaporating, the magnetic hotplate is used to reduce the deposition, as the magnetic stirrer keeps spinning to mix the ingredients. During the drying, a two-stage temperature rising and regularly mixing method are applied to alleviate the problem of sorbent crystallisation. Moreover, the bottles used in the manufacturing is suggested to have wide necks.
- The observation of the sample surface morphology by SEM and EDX proved the manufacturing methodology to be useful for the uniformity of the sorbents, which is

potential to improve the mass transfer of the sorbents. In the black and white SEM photo, expanded graphite shows a sheet structure in dark. The chemical salt in light grey adheres the dark sheet structure of EG or fills in the gaps between the graphic layers. The scanning of EDX displays a colourful elements mapping, which presents the distribution of the nanoparticles by the corresponding colours. The results show that Ni/Al/Fe@C is dispersed evenly on the surface of $SrCl_2$-EG, as the Ni/Al/Fe elements rarely gathering together but randomly scatters. The results indicate the feasibility of the innovative manufacturing methodology could potentially improve the sorption performance as it could alleviate the problems of sorbent agglomeration or congregation.

- The LFA tests demonstrate the improvement of the sorbent thermal conductivity made by the additives of Ni/Al/Fe@C. The results show that the thermal conductivity increases with the temperature or the sample density growing. The maximum thermal conductivity obtained in the test is 2.90 W/(m·K), retrieved from the 1000 kg/m^3 $MnCl_2$-EG-Al@C at 200 ^{o}C. The minimum thermal conductivity is 0.73 W/(m·K), obtained from the 600 kg/m^3 $MnCl_2$-EG at 10 ^{o}C. The maximum improvement of the thermal conductivity is 81.3 %, by adding Al@C into the conventional $MnCl_2$-EG. The result presents the potential of enhancing the comprehensive heat and mass transfer performance by using the novel sorbents as they have the improved thermal property.

Therefore, Chapter 4 indicates that it is possible to enhance the sorption performance by applying chemisorption composite with Ni/Al/Fe@C made by the innovative method.

Chapter 6 Experimental investigation of the sorption performance

After demonstrating the improvement of the thermal conductivity of the novel composites made by a developed methodology, Chapter 6 investigates the experimental adsorption and desorption performance of the novel sorbents to analyse the comprehensive heat and mass transfer processes influenced by the additives. The assessment includes the ammonia conversion ratio versus the time, SCP and COP, corresponding to various testing conditions.

6.1 Results from $SrCl_2$ composite

6.1.1 Inlet/outlet oil and adsorbent temperatures of the desorption process

The temperatures of the thermal oil exchanging heat with the sorbent bed are recorded along with the monitoring of the sorbent temperatures, as displayed in Fig 6.1 to Fig 6.4.

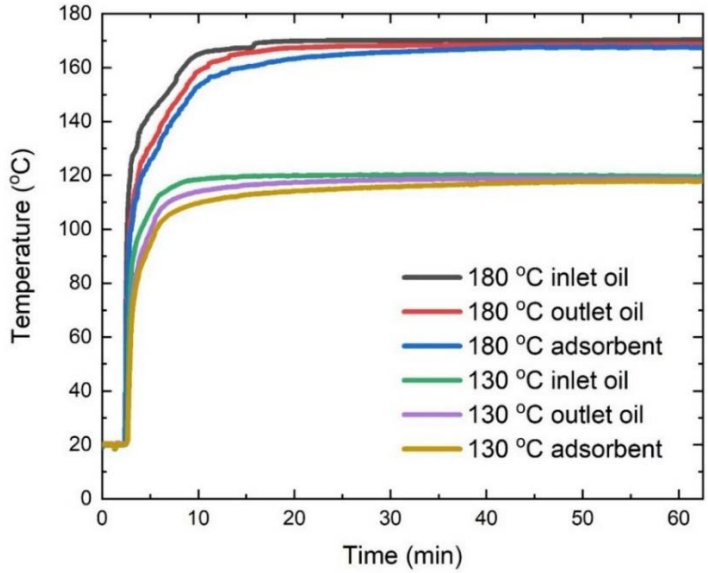

Figure 6.1 Temperature evolution of $SrCl_2$-EG in the desorption process versus time

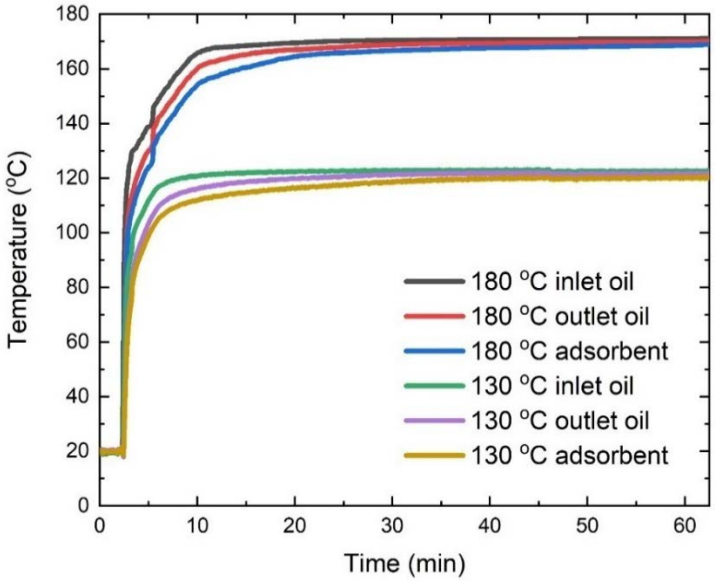

Figure 6.2 Temperature evolution of $SrCl_2$-EG-Ni@C in the desorption process versus time

The composite sorbent based on $SrCl_2$ are tested in the desorption conditions at the heat source temperatures of 180 ℃ and 130 ℃ while the condenser is set to -20 ℃. The monitoring of the inlet and outlet oil temperatures shows a rapid growth when opening the controlling valve to start the external circuit of the oil bath. For a more evident observation of this phenomenon, the time axis in the illustration starts 2.5 min earlier than the fluid begins to flow through the adsorption bed. The whole time for the figure is 62.5 min.

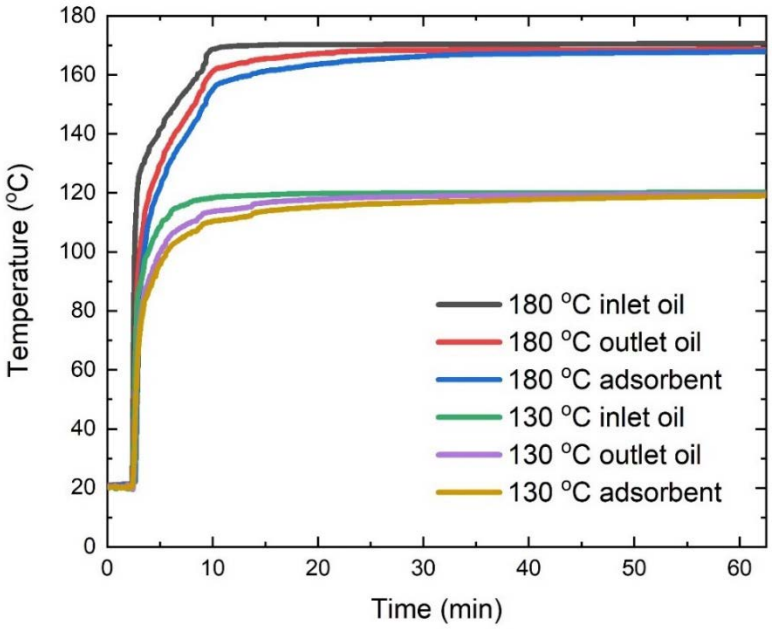

Figure 6.3 Temperature evolution of $SrCl_2$-EG-Al@C in the desorption process versus time

The evolutions of the inlet oil temperature, outlet oil temperature and the sorbent temperature are similar in the trend, during all tests.

A sharp increase is observed after starting the external heat circuits of the oil bath, as each line is almost parallel to the temperature axis. It is because that the heated thermal fluid starts to enter the sorbent bed and increase the temperature of the reactor. At the start, the temperature difference between the internal and external oil or the sorbent is big, which drives the temperature of inlet oil, outlet oil and the sorbent to increase very fast.

Following the very fast rising, the curves still positively develop but with a reduced accelerate until around 7.5 min at the time axis for the 130 ℃ desorption or 10 min for the 180 ℃ desorption. It is because the temperature difference between the internal and external oil is larger in 180 °C desorption test. With the oil and sorbent temperatures increasing, the temperature difference decreases, which reduces the increasing rate of the temperatures. Besides, the composite starts to desorb the ammonia at around 90 ℃. The consumption of the desorption heat also causes the reduced increasing rate of the temperatures. The consumption

rate of the desorption heat is slower than the sorbent temperature increasing speed. The higher inlet oil temperature leads to the faster growth of the adsorbent temperature. Thus, the temperatures recorded in 130 ^{o}C desorption is observed to reduce its rate at an earlier time.

After the gradually growing, the curves tend to be stable but still increase very slowly with some fluctuations caused by the sensor errors or the data taker errors. In this period, the desorption process continues with a meagre reaction rate, which matches the discovery in the later experiments of the sorption performance.

At the end, the difference between the temperatures of the inlet and outlet oil is caused by the heat loss, although the rig installs complete insulations.

The result of the temperature evolution indicates that desorption starts at a very fast rate and gradually reduces the reaction speed, tending to meet the desorption equilibrium. It is reflected by the temperature growth in Fig 6.1 to 6.4. Moreover, it is observed that desorption begins at round the sorbent temperature of 90 ^{o}C. The testing temperature can influence the observation of the temperature for the sorbent to start desorption, as the consumption rate of the desorption heat is slower than the increasing rate of the sorbent temperature and the increasing rate of the sorbent temperature is higher in a high temperature desorption test.

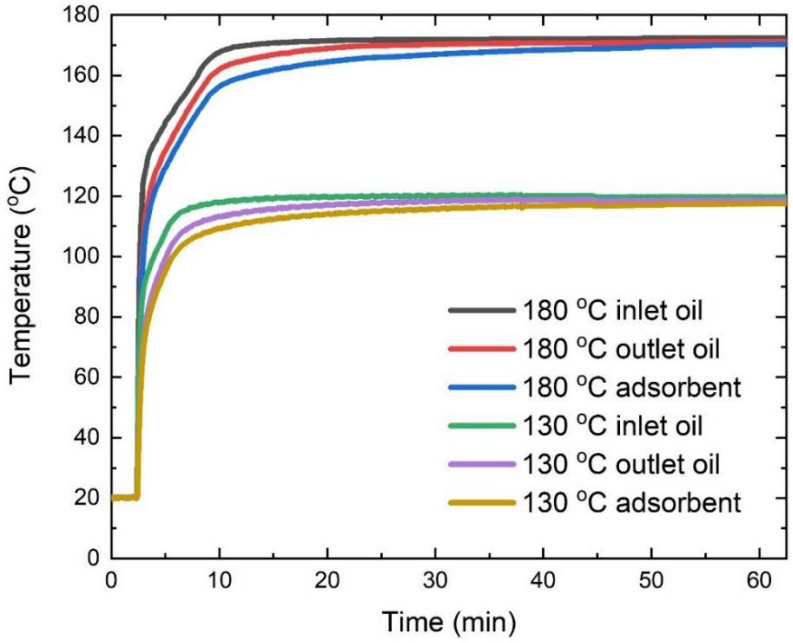

Figure 6.4 Temperature evolution of $SrCl_2$-EG-Fe@C in the desorption process versus time

6.1.2 Ammonia conversion ratio of the desorption process

180 ^{o}C desorption:

Fig 6.5 illustrates the ammonia conversion ratio of $SrCl_2$-EG-0/Ni/Al/Fe@C at a desorption temperature of 180 ℃, when the temperature of the condenser is -20 ℃. It uses the same time scale for the convenience of comparing with the temperature figures.

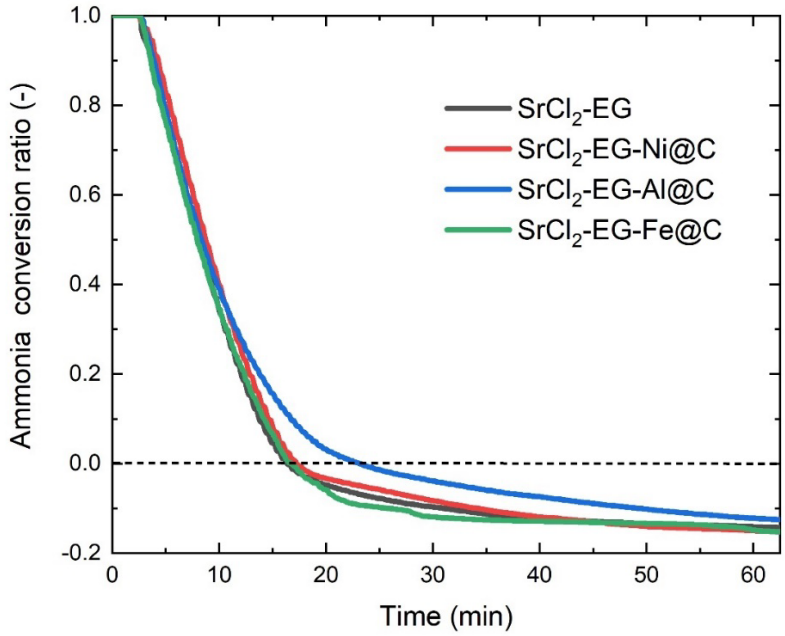

Figure 6.5 Ammonia conversion ratio of $SrCl_2$ composite during 180 ℃ desorption versus time

In the first 20 min, the lines are almost straight, showing a rapid desorption rate compare with that of the next 40 min. The reason is that, at first, the adsorbent fully combines with the ammonia molecules, which is easy to be desorb at a maximum speed given that huge heat source. Controlled by the mass transfer limits, the ammonia conversion ratio lines are almost the same in the first 20 min for sorbents except for $SrCl_2$-EG-Al@C.

After that, the ammonia conversion ratio tends to be stable, symbolising the approaching to the reaction equilibrium. It is because after a time of reaction, the combined ammonia is less. Thus, even the heat source keeps the same, the mass transfer tunnels are not fully used by the adsorbed ammonia, displaying a reduced rate of the desorption process. As $SrCl_2$ is a kind of low-temperature salts, 180 ℃ is high enough for the desorption to process at a maximum rate until the eight portions of ammonia to be fully released. The black dash line demonstrates the ammonia conversion ratio of 0, under which symbolises the further desorption of the last portion of ammonia. Above the black line, the $SrCl_2$ composite desorbs the first seven portions of ammonia.

It is observed that after 10 min the sorbents with Al@C reacts at a slowest rate among all candidates. As the adding amount of each nanoparticle is the same, Al@C possesses a large volume with a smaller value of density. It results in a larger mass transfer resistance from the

increased volume of non-reacted additives within the high enough heating temperature. Thus, Al@C slows the desorption, when the temperature of the heat source is very high.

Other sorbents have a similar ammonia conversion ratio in 180 °C desorption test. The reaction time for the global conversion ratio of the $SrCl_2$-EG, $SrCl_2$-EG-Ni@C, $SrCl_2$-EG-Al@C and $SrCl_2$-EG-Fe@C to reach zero is 13.92 min, 14.75 min, 20.58 min and 14.25 min, if removing the extra 2.5 min at the beginning for the comparison with temperature evolutions. In the 180 ℃ desorption, the fastest desorption rate is obtained from the original $SrCl_2$-EG composite with slight advance. The explanation is similar with the reason why $SrCl_2$-EG-Al@C is slower. It is caused by the mass transfer resistance from the volume of non-reacted additives, when the heat source could activate the heat transfer process to the optimisation.

Error analysis is not necessary for proving the data reliability of this desorption results, as no sorbent with any additives is observed to be superior than other candidates in this condition. The three candidates have overlaps and the blue line is far away from the other three coloured curves.

130 °C desorption:

Fig. 6.6 presents the global ammonia conversion ratio during the desorption at the heat source temperature of 130 ℃. The condensation temperature is set to -20 °C.

The result shows a similar development of the trend in Fig 5.8, as the ammonia conversion ratio changes quickly and then tends to be stable. It is the nature of the chemical reaction to start at a high rate and then develops to the equilibrium at a reduced rate. It shows the heat source of 130 ℃ can push the reaction slightly further than just desorbing seven portions ammonia. The illustration also induces a black dash line to distinguish the release of the seven portions ammonia and the one more portion ammonia. The value of the equilibrium ammonia conversion ratio is larger than the final x obtained from 180 ℃ desorption, for each candidate. It is because that a higher desorption temperature has a higher equilibrium pressure of ammonia, driving the sorbent to desorb more during same time.

In Fig. 6.6, $SrCl_2$-EG has the slowest reaction rate, while $SrCl_2$-EG-Ni@C has the fastest reaction rate. The red line is at the bottom, revealing the fastest reaction obtained from Ni-additive composite among four tested sorbents. The black one is at the top, demonstrating the slowest desorption process retrieved from the conventional sorbent. In this circumstance, the input energy is not high enough to optimise the desorption rate influenced by heat transfer. As

the thermal conductivity is tested to have improvement with the additional carbon coated materials, the divergence of the performance could be caused by the improvement of the heat transfer. The ammonia conversion ratio of the desorption costs 37.92 min for $SrCl_2$-EG from one to zero without calculation of the additional 2.5 min adjustment, while that for Ni, Al and Fe-additive sorbents is 29.42 min, 38.08 min and 34.17min.

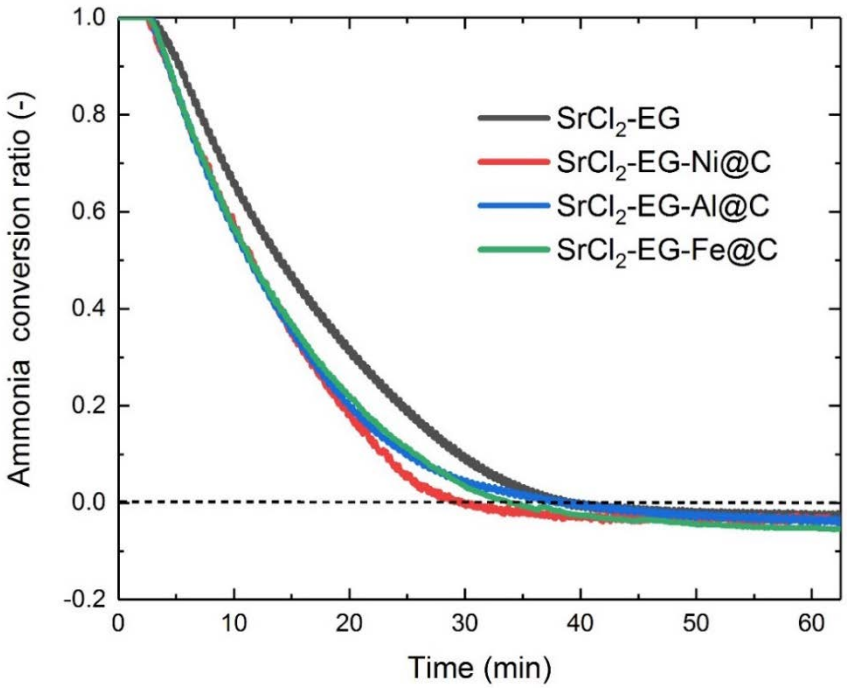

Figure 6.6 Ammonia conversion ratio of $SrCl_2$ composite during 130 ℃ desorption versus time

The result demonstrates the improvement of the desorption rate made by various additives, and Ni@C is the optimal additive among the carbon coated metals. It is because of the enhanced thermal conductivity. However, Al@C is proved to have most improvements of the thermal property when added into the sorbents. Therefore, the fastest reaction is caused by the improvement of the comprehensive heat and mass transfer. It also matches that Al@C is found to have resisted the mass transfer process in 180 ^{o}C desorption test.

Fig. 6.7 is the error analysis of the conventional LTS composite performance at 130 ^{o}C desorption, from which the good repeatability of the data is approved. The darker coloured lines are the ammonia conversion ratio, while the lighter coloured areas are the errors. The result indicate that even small parts of the light green, light blue and light red areas are overlapped before around the first 22.5 min, the red line along with the light red area are obviously at a lower part of the figure than the light green or the light blue area from approximately 22.5 min to 32.5 min. Moreover, the black or the light black components locate at a higher position in the illustration than the red or the light red parts do.

These phenomena observed in the error analysis is the essential evidence to support the results that sorbents with Ni@C in 130 ºC desorption are superior than the other candidates as reliable.

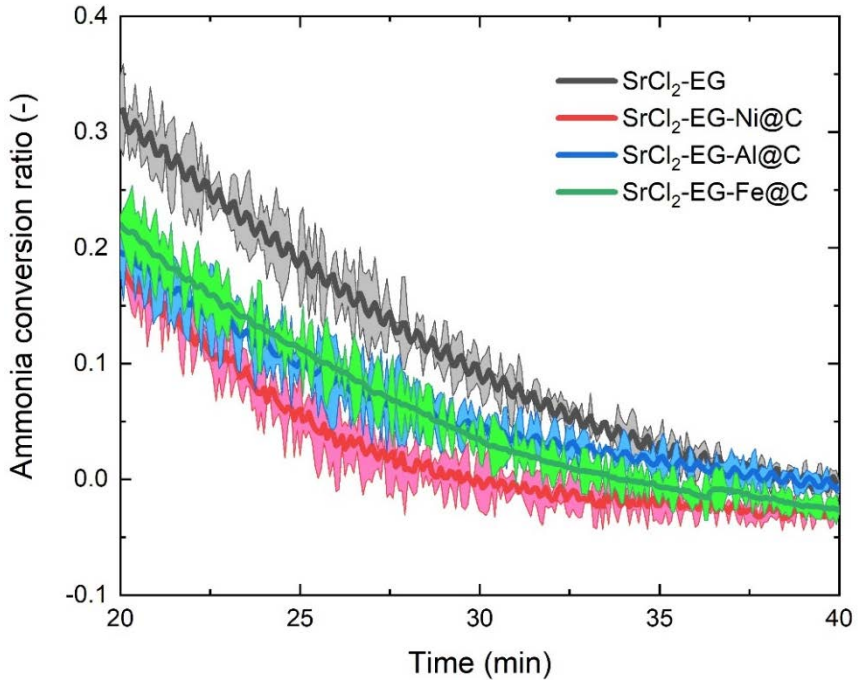

Figure 6.7 Error analysis of the $SrCl_2$ composite performance at 130 ºC desorption

6.1.3 Ammonia conversion ratio of the adsorption process

The reported adsorption performance of $SrCl_2$-EG-0/Ni/Al/Fe@C includes three different evaporator temperatures from 0 ℃ to 20 ℃, while the adsorbent bed rejects the heat to the oil bath exchanging heat with tap water.

20 ºC adsorption:

Fig 6.8 shows that the ammonia conversion ratio changes with the time elapsing, when the evaporator temperature is set to 20 ºC. The time scale is added with another 2.5 min for a better observation of the sharply growing x in the first minute.

Among four sorbents, $SrCl_2$-EG-Ni@C has the fastest reaction speed. In the figure, the red curve is at the left top, showing the maximum reaction rate obtained from $SrCl_2$-EG-Ni@C among all sorbents. Following the $SrCl_2$-EG-Ni@C, the reaction speed in a decrement order is $SrCl_2$-EG, $SrCl_2$-Fe@C and $SrCl_2$-EG-Al@C in the first 15 min. After 15 min, Fe-additive sorbent shows a slower reaction speed than sorbent with Al@C. The intersection is also found in 130 ℃ desorption results, but with a smaller difference between the two lines. After 20 min at the time axis, the evolution of the line is being smooth. The adsorption time for the sorbent

to reach 0.9 conversion ratio in an increment order is 19.92 min for $SrCl_2$-EG-Ni@C, 23.67 min for $SrCl_2$-EG, 26.5 min for $SrCl_2$-EG-Al@C and 34.00 min for $SrCl_2$-EG-Fe@C.

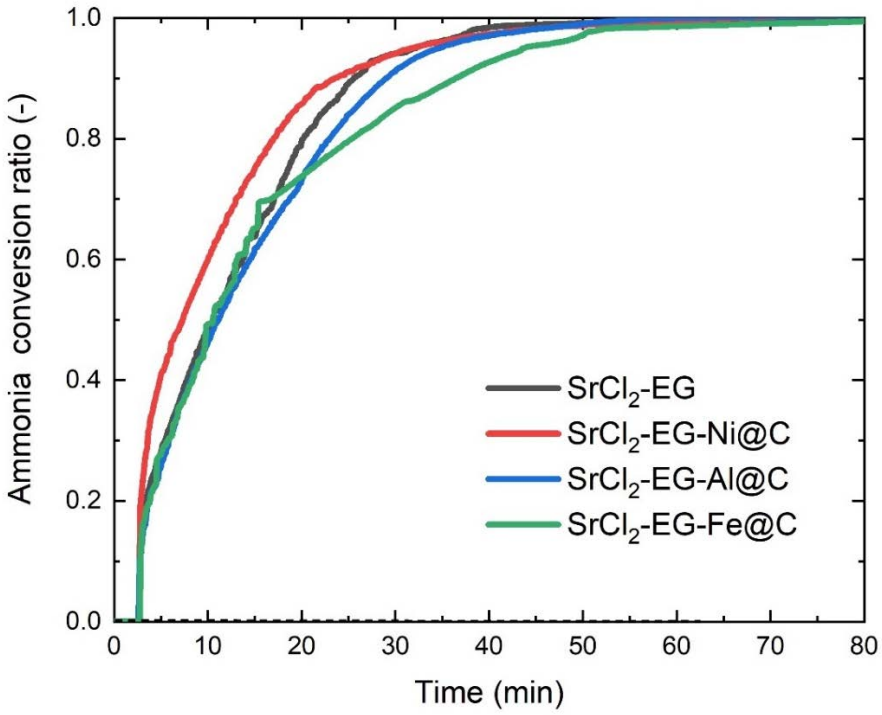

Figure 6.8 Ammonia conversion ratio of $SrCl_2$ composite during 20 ℃ adsorption versus time

The result demonstrates the improvement of adsorption performance made by adding Ni@C into the conventional composite sorbent. However, other novel sorbents have an even slower reaction. It is because that in 20 ^oC adsorption, the sorption performance is dominated by the mass transfer process. Similar with Al@C, Fe@C also has relatively large mass transfer resistance. Ni@C is proved to have comprehensively improved the heat and mass transfer processes. Therefore, the application of $SrCl_2$-EG-Ni@C can improve 20 ^oC adsorption performance, while the other two novel sorbents cannot.

As the space between the red curve and the other three curves is quite big and obvious during the time from around 5 min to 20 min, the error analysis in not required here for the reliability investigation of the results.

10 ^oC adsorption:

Fig. 6.9 is the adsorption performance result of $SrCl_2$-EG-0/Ni/Al/Fe@C at the evaporator temperature of 10 ℃. At the start, the reaction goes at a relatively high speed, while the rate of the reaction is reduced and tend to become stable at the end. It is the same discovery found in each chemical reaction.

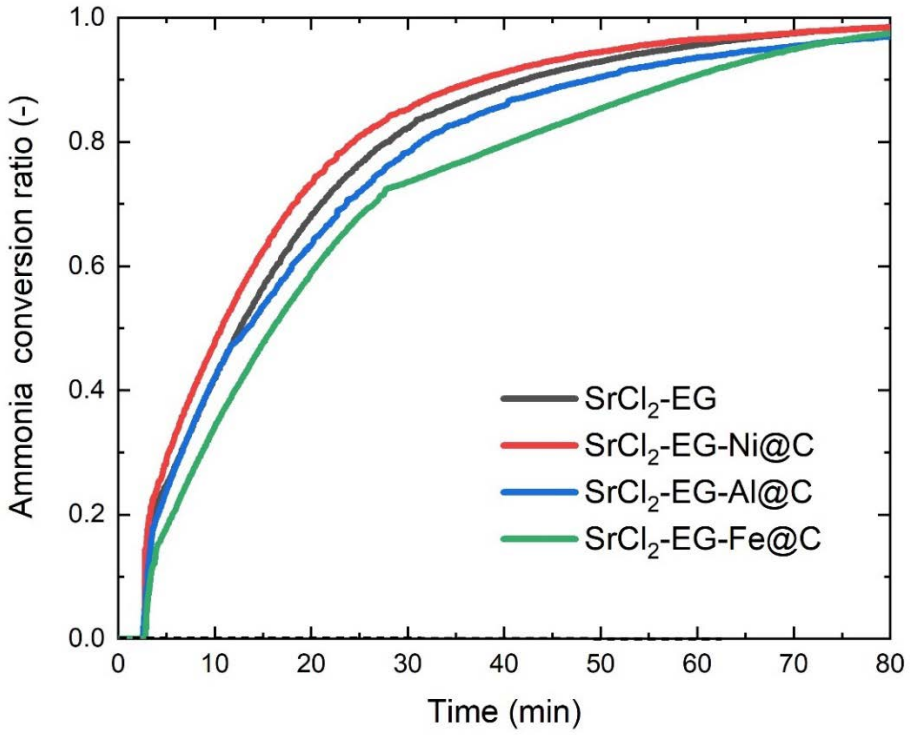

Figure 6.9 Ammonia conversion ratio of $SrCl_2$ composite during 10 ℃ adsorption versus time

The increment order of the reaction speed among the four candidates is $SrCl_2$-EG-Ni@C, $SrCl_2$-EG, $SrCl_2$-EG-Al@C, $SrCl_2$-EG-Fe@C. The red line is at the top of the illustration, demonstrating the fastest adsorption process. All equilibrium ammonia conversion ratios are lower than those of 20 ℃ desorption, as the higher temperature provides a higher pressure in the evaporator and thus improves the adsorption peed and the adsorption. It costs 39.75 min reaction time for $SrCl_2$-EG to adsorb 90% of the seven portions ammonia, and that is 34.92 min for $SrCl_2$-EG-Ni@C, 45.75 min for $SrCl_2$-EG-Al@C, and 54.42 min for $SrCl_2$-EG-Fe@C.

The result demonstrates the improvement of 10 oC adsorption performance made by using the novel sorbent $SrCl_2$-EG-Ni@C, as it could enhance the comprehensive heat and mass transfer processes. The slow reaction rate of $SrCl_2$-EG-Al@C and $SrCl_2$-EG-Fe@C is caused by the mass transfer resistance. It reveals that adsorption is dominated by mass transfer process, again.

Fig. 6.10 shows the error analysis of the 10 ^oC adsorption performance using $SrCl_2$-EG, which demonstrates the result of the improved adsorption performance at 10 ^oC by employing Ni@C as the additive to be valid. Different with Fig. 6.7, Fig 6.10 uses single error bar instead of the error area to show the uncertainty of the data. The time scale is from 5 min to 45 min to enlarge the illustration and make the result clearer for analysing. The result shows that even

the error for black, blue and green curves intertwines together, the gap between the light red bars and the light green bars are obvious. Moreover, the errors of the conventional sorbents and the sorbents with Ni@C have clear gaps from around 15 min to 25 min. The gaps found in the error analysis could prove the reliability of the sorption performance results in the corresponding condition.

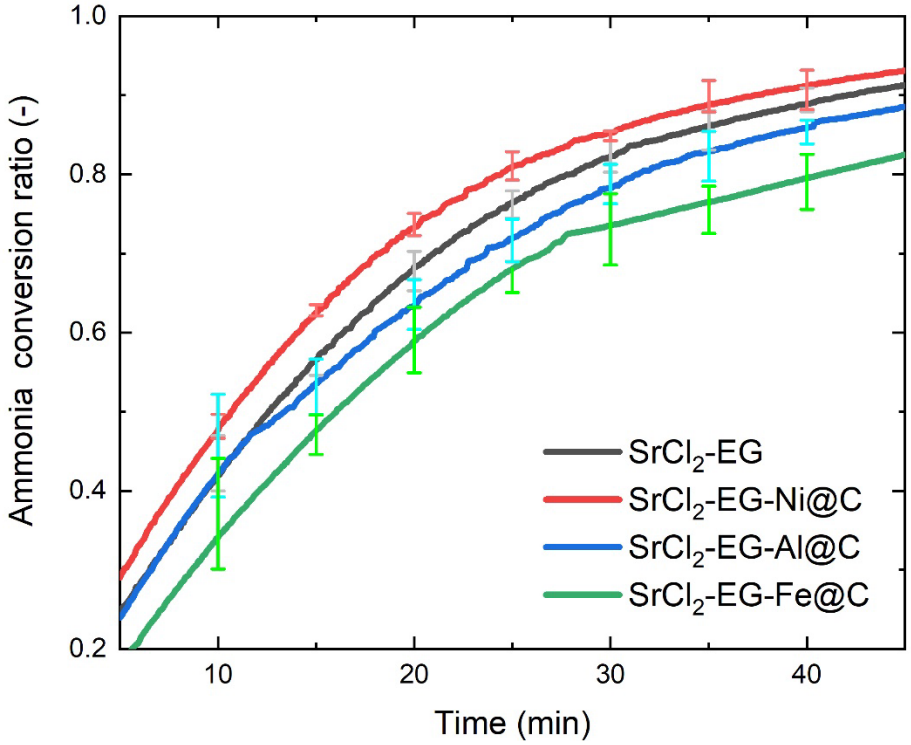

Figure 6.10 Error analysis of $SrCl_2$-EG adsorption performance at 10 ^oC

0 ^oC adsorption:

Fig 6.11 presents the 0 ℃ adsorption performance of the conventional sorbents and the novel composite. This test is extremely important for the ice making application.

The result shows the fastest reaction between the salt and the ammonia is found at the test of $SrCl_2$-EG-Ni@C, and the slowest is obtained from the test of $SrCl_2$-EG-Al@C. At the end of the time axis, the equilibrium global conversion ratio from high to low is 0.949 for $SrCl_2$-EG-Ni@C, 0.864 for $SrCl_2$-EG, 0.739 for $SrCl_2$-EG-Fe@C and 0.708 for $SrCl_2$-EG-Al@C.

The green curve has an advanced adsorption rate from about 5 min to 10 min, which is treated as abnormal data retrieved by the sensors or the data taker. During this time, it is obvious to find the huge fluctuation on the green line, and the reasonable conversion ratio of $SrCl_2$-EG-Fe@C should be similar with the black curve or lower than that. This inference could also be proved by the results in Fig. 6.14, as the green line representing the SCP of $SrCl_2$-EG-Fe@C has two peaks rather than the one regular peak found in other SCP figures.

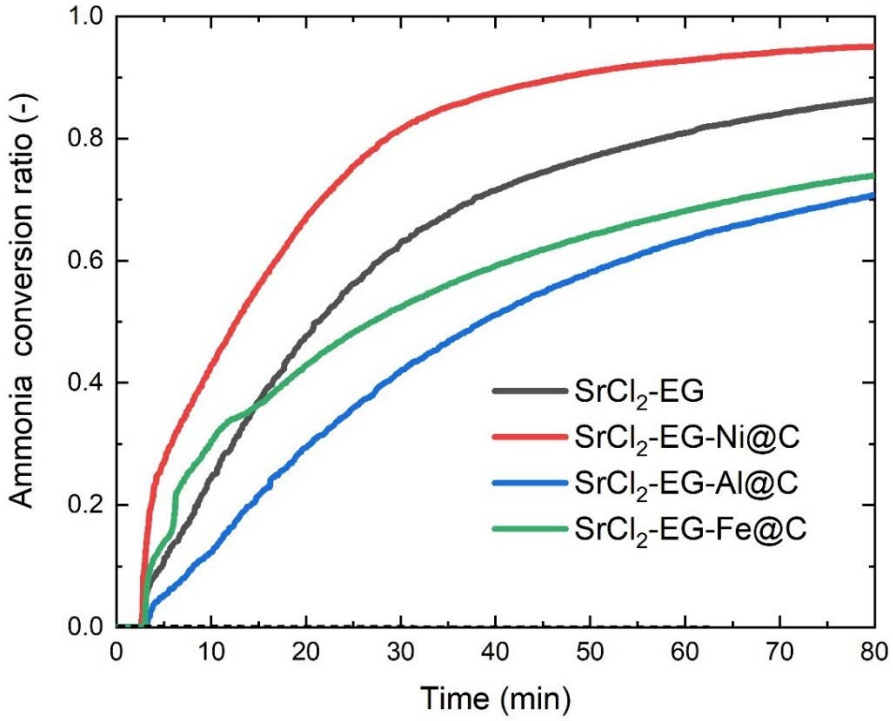

Figure 6.11 Ammonia conversion ratio of $SrCl_2$ composite during 0 ℃ adsorption versus time

The result demonstrates that adding Ni@C into conventional LTS of $SrCl_2$-EG could improve the performance of 0 ºC adsorption, as it could improve the comprehensive heat and mass transfer. The adsorption performance of $SrCl_2$-EG-Al@C and $SrCl_2$-EG-Fe@C is limited by the mass transfer process.

In a summary, for LTS, Ni@C is advised to be the additive for the improvement of the sorption performance. By adding Ni@C into the conventional $SrCl_2$-EG, the sorption rate is accelerated, and the reaction time is shortened. It is potential to use the novel sorbents of $SrCl_2$-EG-Ni@C to improve efficiency of the sorption refrigeration for more production with less heat consumption.

6.1.4 Assessment of SCP and COP

SCP is calculated to evaluate the refrigeration capacity of the unit mass sorbent. Besides, COP of $SrCl_2$-EG-0/Ni/Al/Fe@C is assessed to demonstrate the relationship between the heat consumption and the cooling production of the sorbent.

SCP at 20 ºC:

Fig 6.12 shows the relationship between the adsorption time and the corresponding SCP when the evaporator is 20 ℃.

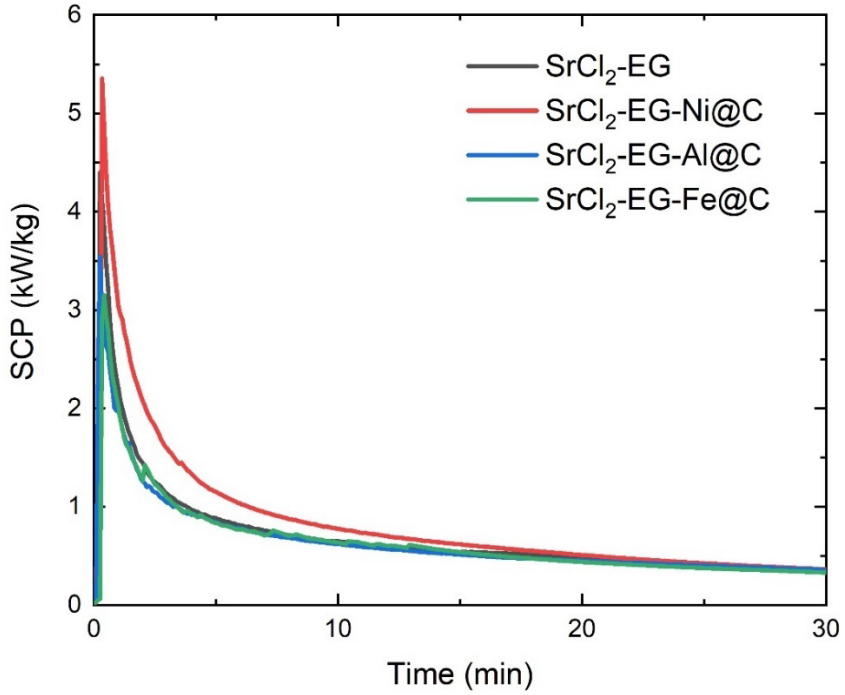

Figure 6.12 SCP of $SrCl_2$ composite at an evaporator temperature of 20℃ versus time

The results show that the SCP sharply increases to a peak and then slowly reduces until stable. The relatively large value of the reaction speed when the chemical reaction starts explains the sharp increase phenomenon in the figure of SCP.

The novel sorbents of $SrCl_2$-EG-Ni@C improves the refrigeration production generated by the unit mass of the sorbent, as it can enhance the adsorption performance. The maximum SCP achieved is 5.35 kW/kg at 0.42 min in the test of $SrCl_2$-EG-Ni@C under this condition. Other peaks include 4.40 kW/kg at 0.33 min for $SrCl_2$-EG, 3.69 kW/kg at 0.42 min for $SrCl_2$-EG-Al@C, and 3.15 kW/kg at 0.50 min for $SrCl_2$-EG-Fe@C.

SCP at 10 ºC:

Fig 6.13 plots the evolution of SCP during the $SrCl_2$-EG-0/Ni/Al/Fe@C adsorption process with the time collapsing, when the temperature of the evaporator is 10 ℃.

Sorbents with Ni@C, again, enhances the refrigeration produced by per unit mass of the sorbent. The increment order for the maximum SCP obtained from each sorbent is 1.24 kW/kg for $SrCl_2$-EG-Fe@C at 1.00 min, 1.91 kW/kg for $SrCl_2$-EG-Al@C at 0.50 min, 2.46 kW/kg for conventional $SrCl_2$-EG at 0.58 min, and 3.98 kW/kg for $SrCl_2$-EG-Ni@C at 0.42 min.

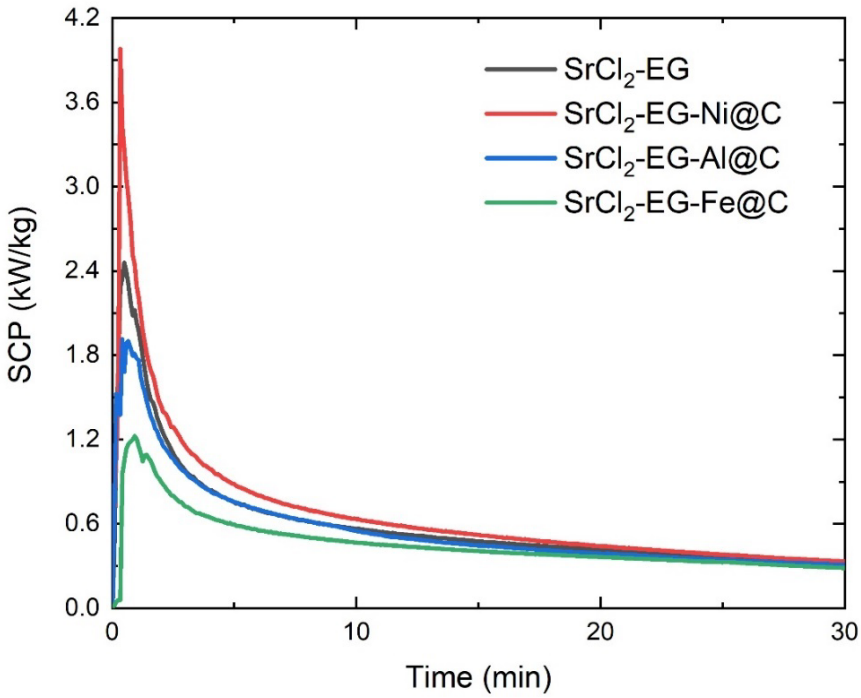

Figure 6.13 SCP of $SrCl_2$ composite at an evaporator temperature of 10℃ versus time

SCP at 0 ºC:

Fig 6.14 presents the SCP evolution under the controlled evaporator temperature of 0 ℃, which has a significant meaning for the ice making field.

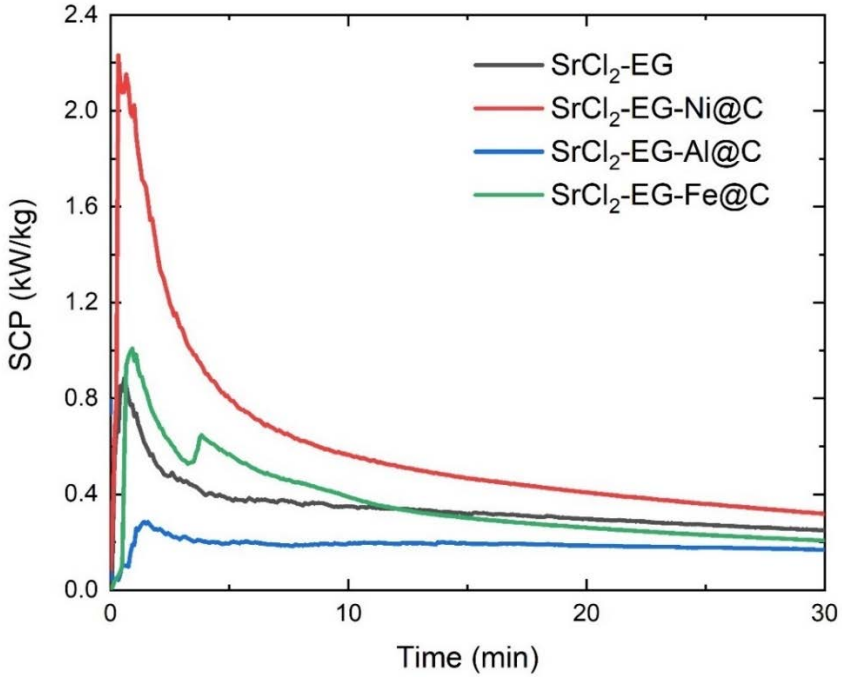

Figure 6.14 SCP of $SrCl_2$ composite at an evaporator temperature of 0℃ versus time

The application of SrCl2-EG-Ni@C improves SCP of the sorption. The yielded SCP among the four types of sorbents follow the same developing trend with the two figures above. The highest SCP retrieved from different sorbents is 2.15 kW/kg at 0.75 min for $SrCl_2$-EG-Ni@C,

1.01 kW/kg at 1.00 min for $SrCl_2$-EG-Fe@C, 0.90 kW/kg at 0.75 min for $SrCl_2$-EG and 0.30 kW/kg at 0.67 min for $SrCl_2$-EG-Al@C in a decrement order.

COP at 20 °C:

Fig 6.15 is COP of $SrCl_2$-EG, at an evaporator temperature of 20 °C. For a clearer observation, the time scale is altered to 5 min, as COP curves after that time is quite close and stable. All curves increase rapidly in the first minute and then tend to be stable.

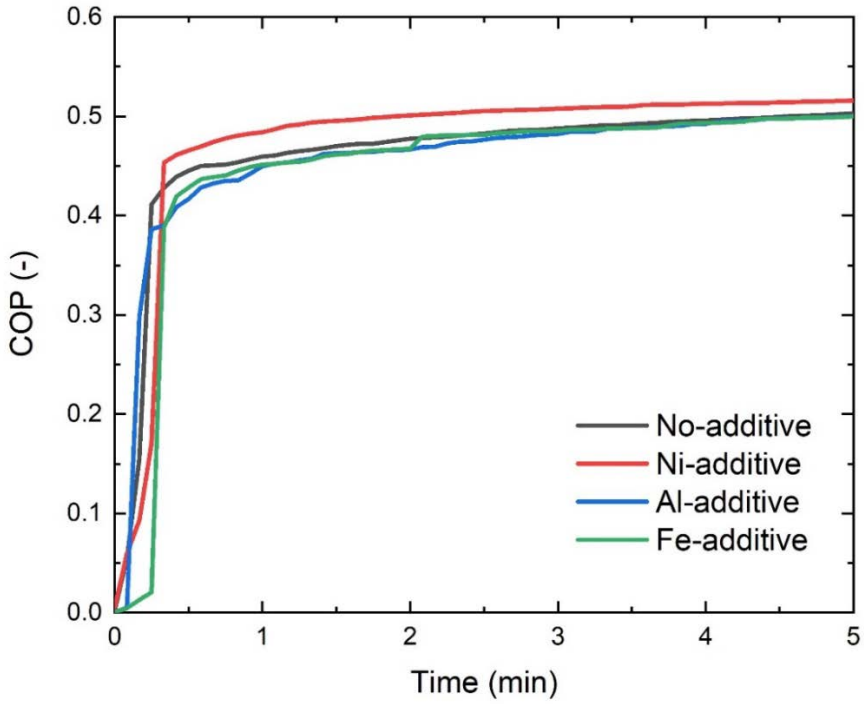

Figure 6.15 COP of $SrCl_2$ composite at an evaporator temperature of 20℃ versus time

Regardless of the rapid increase at the start, the additive of Ni@C improves COP of the original sorbent, which means the more refrigeration produced by the same heat consumption. The red line is at the top of the figure, demonstrating the highest COP among other candidates during the time from about 0.5 min. At the end, due to the limited refrigeration production and the same Q_{in}, COPs of various sorbents tend to be the same with time elapsing.

COP at 10 °C:

Fig 6.16 presents COP of $SrCl_2$-EG-0/Ni/Al/Fe@C, when altering the evaporator temperature at 10 °C, in the reaction time of 10 min.

The result presents that $SrCl_2$-EG-Ni@C improves COP of the sorption, because it enhances the adsorption performance. In this circumstance, the red curve still lies at the top among all other curves, revealing that $SrCl_2$-EG-Ni@C has the maximum COP almost all candidates.

However, adding Al@C and Fe@C into the conventional composite of $SrCl_2$-EG reduces COP of the sorbent.

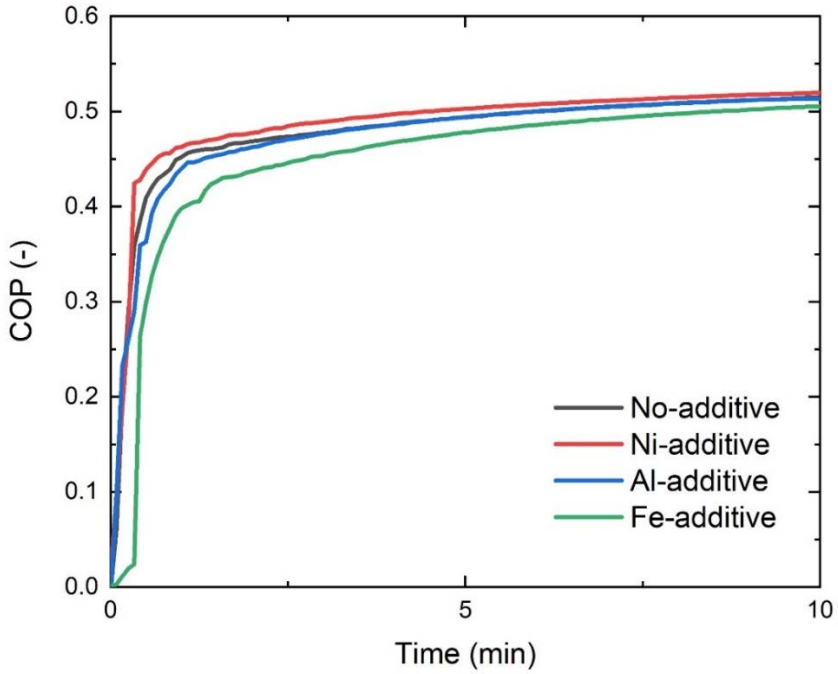

Figure 6.16 COP of $SrCl_2$ composite at an evaporator temperature of 10℃ versus time

COP at 0 ºC:

Fig 6.17 is COP of $SrCl_2$-EG variations in 0 ºC refrigeration.

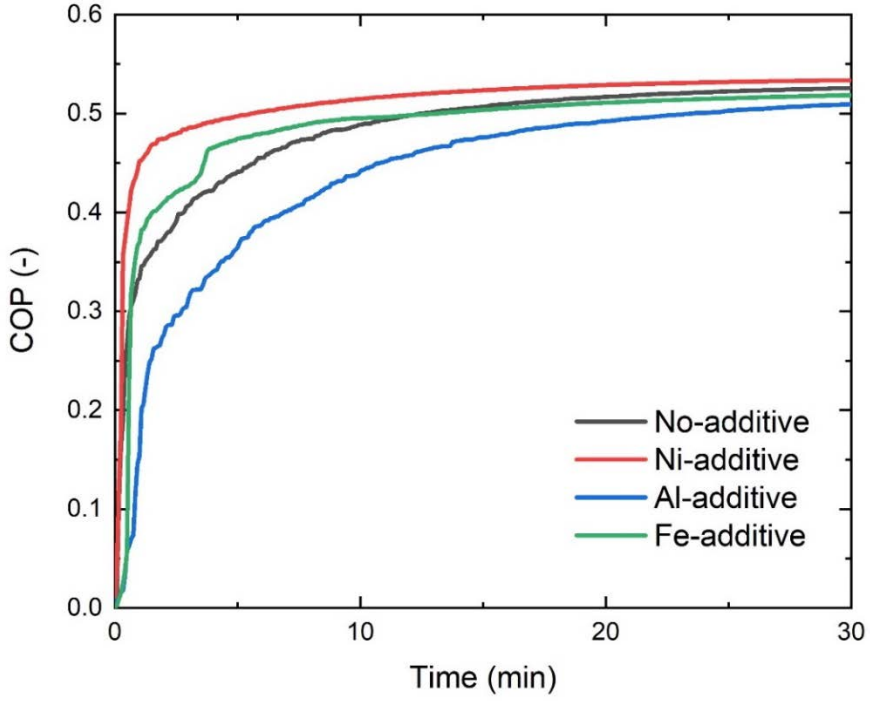

Figure 6.17 COP of $SrCl_2$ composite at an evaporator temperature of 0℃ versus time

Again, COP is improved by applying the novel sorbent, $SrCl_2$-EG-Ni@C. In this condition, as the controlling temperature of the evaporator is low, the equilibrium pressure of ammonia in the vessel is low as well. Therefore, this figure possesses the longest time axis of 30 min. The difference between each curve is larger in the figure, compared to other two COP illustrations. It is because of the divergence in sorbent reaction speed.

In a conclusion, the most superior adsorbent is $SrCl_2$-EG-Ni@C. It improves the desorption and adsorption performance by an increased reaction speed. The reason is that the additive of Ni@C can comprehensively enhance the mass and heat transfer processes. Moreover, it could produce more refrigeration by per unit mass sorbent or by the same heat consumption. Besides, it is suggested to shorten the adsorption time to optimise SCP. The result indicates that it is feasible to use the novel sorbent $SrCl_2$-EG-Ni@C in the sorption field for the improvement of the low-grade heat utilisation.

6.2 Results from $MnCl_2$ composite

The composite sorbent with the chemical salt of $MnCl_2$ is researched as well to assess the impact of the Nano-additives on the high-temperature salt composite sorption performance.

6.2.1 Adsorbent temperature evolution during the desorption process

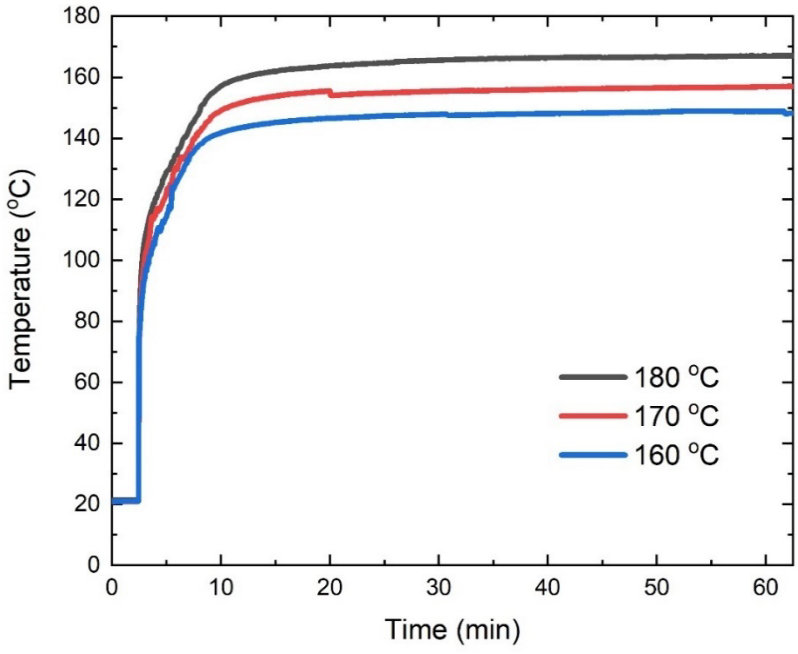

Figure 6.18 Temperature evolution of $MnCl_2$-EG in desorption process versus time

Fig 6.18 is the evolution of the $SrCl_2$-EG temperature. The desorption temperatures range from 160 ℃ to 180 ℃ as the used thermal fluid limits, while the condenser temperature is -20 ℃. The time axis is the same with that in Section 6.1. The development of the oil temperature shows a similar trend with the sorbent temperature but different with values like demonstrated

in the result section for $SrCl_2$. As it would be too messy to include all the inlet and outlet oil temperatures in the illustration, the figures below for the temperature evolution records only display the temperature of the sorbent.

The curves present the likewise development with temperature evolution figures of $SrCl_2$-EG variations. A rapid increase is found at the start around one min and a reduced rate is observed afterwards. At the final stage, the temperature of the sorbent tends to be stable. Moreover, there is always about 10 ℃ temperature drop between the desorption temperature set on the oil bath and the actual temperature of the sorbent.

HTS desorption starts from the sorbent temperature around 110 ℃, as the increasing rate of the temperature is obviously reduced due to the heat consumed by ammonia desorption. In this stage, $MnCl_2 \cdot 6NH_3$ desorbs four portions of ammonia to be converted into the version of $MnCl_2 \cdot 2NH_3$. The second stage for the sorbent temperature evolution lasts for about 10 min for 180 ℃, 170 ℃ and 160 ℃ desorption of different sorbents.

Other temperature evolutions of $MnCl_2$-EG-Ni/Al/Fe@C are similar with Fig 6.18. They are included in Appendix B.

6.2.2 Ammonia conversion ratio of the desorption performance

The global conversion ratio of the $MnCl_2$-EG-0/Ni/Al/Fe@C is calculated through the stated equations based on the readings from the differential pressure sensor. The results are plotted below to analyse the performance of the various sorbents.

180 ^{o}C desorption:

Fig 6.19 is the ammonia conversion ratio of $MnCl_2$ composite tested with a heat source at 180 ℃. All ratios sharply drop during the first 30 min, indicating a high reaction speed at the start of the chemical reaction. Later, the curve tends to be stable.

The additives of Ni@C, Al@C and Ni@C accelerate 180 ^{o}C desorption and improve the performance, as the other curves are under the black curve. The reason could be explained as following. $MnCl_2$-EG is HTS and 180 ^{o}C cannot activate the maximum heat transfer. Even the mass transfer resistance is increased by the carbon coated metals, the improvement of the thermal conductivity can dominate the comprehensive heat and mass transfer processes. Thus, desorption performance is enhanced.

Among all four candidates, the sorbent with Ni@C has the optimal performance. The red curve is observed to be at the bottom in this figure, showing the fastest reaction speed in the period of 180 ℃ desorption when the condenser is restricted to -20 ℃. The sorbent with

Ni@C desorbs all four portions of ammonia within a desorption time of 26.17 min. For other sorbents, the decrement order of the reaction speed is $MnCl_2$-EG-Fe@C, $MnCl_2$-EG-Al@C and $MnCl_2$-EG. The reaction time for them to reach the ammonia conversion ratio of 0.1 is 19.92 min, 22.50 min, 22.92 min and 33.92 min, respectively.

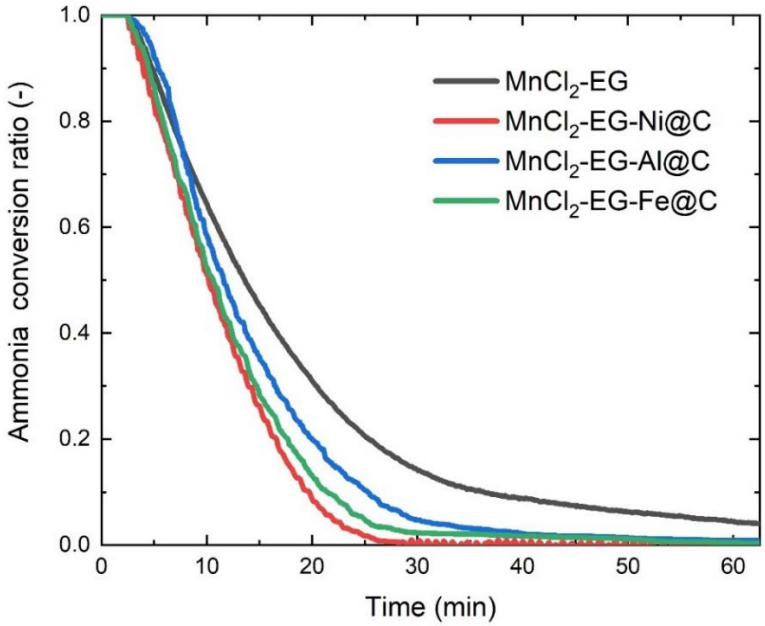

Figure 6.19 Ammonia conversion ratio of $MnCl_2$ composite during 180 ℃ desorption versus time

Fig. 6.20 is the error analysis corresponding to the results from 12 min to 28 min in Fig. 6.19, proving the results to be reliable. The black line is far away from other three lines, while the red line is near to the green curve. However, the reliability is still acceptable from 17.5 min to 22.5 min to identity the MnCl2-EG-Ni@C reacts with ammonia at the fastest rate.

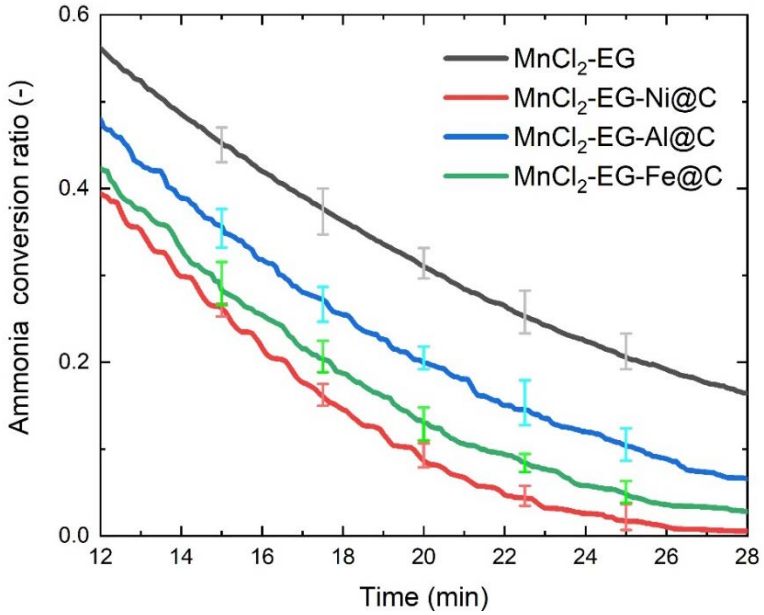

Figure 6.20 Error analysis of $MnCl_2$ composite performance during 180 ℃ desorption

170 ºC desorption:

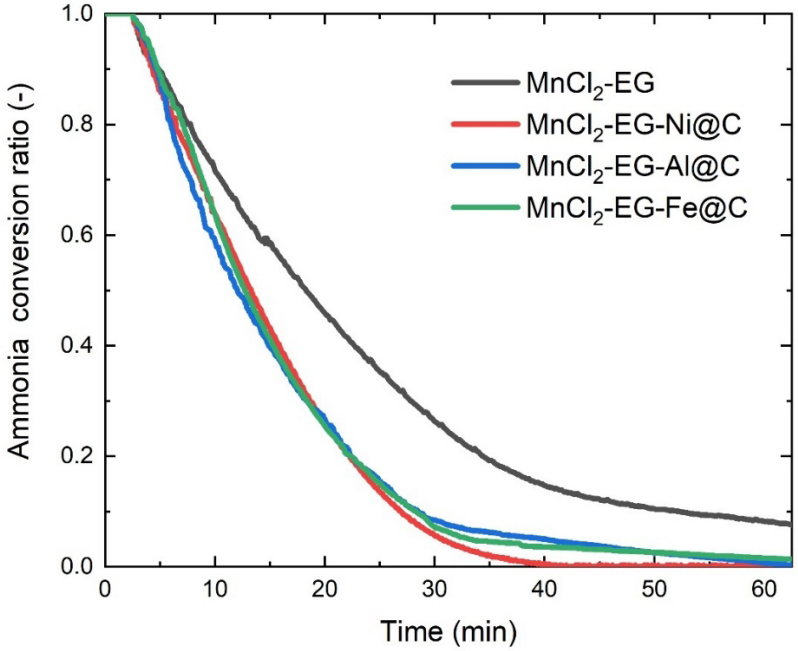

Figure 6.21 Ammonia conversion ratio of $MnCl_2$ composite during 170℃ desorption versus time

Fig. 6.21 presents the relationship of the ammonia conversion ratio and time in different sorbent tests when the heat source temperature is 170 ℃. Before the 35 min point on the time axis, the desorption is at a faster speed, while after the point, the reaction reduces its rate.

In 170 ºC desorption, all additives accelerate and enhance the desorption performance, and the most improvement is made by Ni@C. The phenomenon could be explained by the improvement of the comprehensive heat and mass transfer made by the additives. The reaction time for $MnCl_2$-EG-Ni@C to achieve the ammonia conversion ratio of zero is 40.17 min, declaring for the most rapid reaction again. The increment order of the reaction speed should be Ni, Al, Fe and non-additive sorbents, although the blue curve is at the bottom during the first 20 min. It may be caused by the inaccurate starts point for the desorption process, though the author believes it is the reliable one with a considerable fluctuation in the original data, which symbolises for the reaction start. The reaction time for $MnCl_2$-EG-0/Ni/Al/Fe@C to reach the conversion ratio of 10% is 50 min, 24.5 min, 25.17 min and 25.92 min, respectively.

Fig. 6.22 shows the error analysis that the 170 ºC desorption performance of $MnCl_2$ composite is proved to be repeatable. The black line is far separated with other three candidates, while the red line has intertwined error bars with the green line. However, at 40 min, the error bars of the green and blue curved present a gap with the red line. Although at

35 min or 45 min the error bars of the red, blue and green curves overlap, the data at 2 min or 3 min later and earlier than 40 min that the $MnCl_2$-EG-Ni@C is superior than other three can be treated as almost reliable.

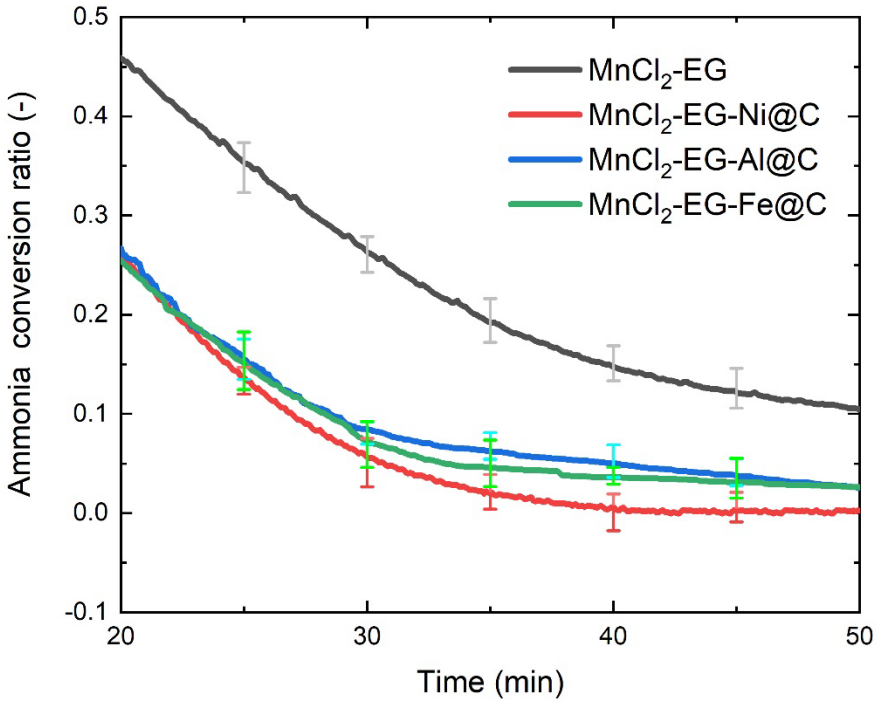

Figure 6.22 Error analysis of $MnCl_2$ composite performance during 170℃ desorption

160 ºC desorption:

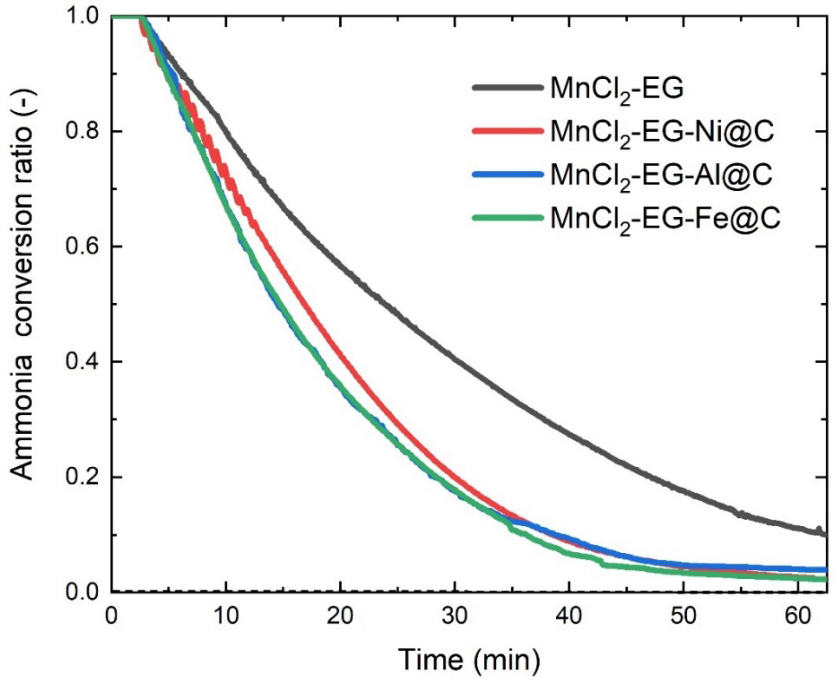

Figure 6.23 Ammonia conversion ratio of $MnCl_2$ composite during 160 ℃ desorption versus time

Fig 6.23 shows the desorption test of the $MnCl_2$ composite, when controlling the oil bath to the temperature of 160 ℃. A heat source at a temperature lower than 160 ºC cannot start desorption of $MnCl_2$-EG/ammonia. The evolution of the ammonia conversion ratio is faster in the first 50 min and becomes smooth after that time point.

The results present that the desorption is improved by the novel sorbents added with Ni/Al/Fe@C. The reason is that the additives enhance the comprehensive heat and mass transfer processes under the given heat source. The conventional $MnCl_2$-EG is always at the top, demonstrating all the carbon coated metals enhances the HTS desorption performance. In this desorption test, the four portions ammonia cannot be fully desorbed by any sorbent. The desorption time cost by the sorbent is 60 min for $MnCl_2$-EG, 37.25 min for $MnCl_2$-EG-Ni@C, 35.75 min for $MnCl_2$-EG-Al@C, and 33.92 min for $MnCl_2$-EG-Fe@C to achieve the ammonia conversion ratio of 0.1.

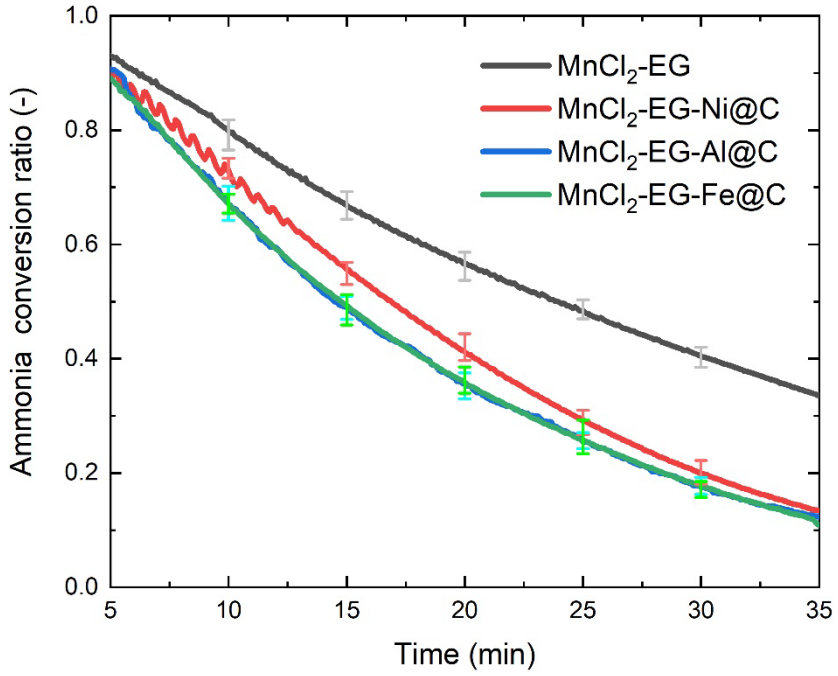

Figure 6.24 Error analysis of $MnCl_2$ composite performance during 160 ℃ desorption

Fig. 6.24 presents the error analysis of the 160 ºC desorption performance using the $MnCl_2$ composite, which proves the result in Fig 6.23 to be reliable. The error bars of the black line are far away from any other error bars, and the error bars for the Ni@C-additive sorbents are separated from the light green or light blue error bars from 10 min to 20 min.

The desorption result demonstrates that the desorption performance is improved by adding Ni@C, Al@C and Fe@C into the conventional $MnCl_2$-EG. Even the mass transfer resistance is proved to be increased in the desorption test of LTS, the improvement of the heat transfer

dominates in the comprehensive heat and mass transfer processes and thus enhances the desorption performance. Among all candidates, Ni@C can make the most improvement.

6.2.3 Ammonia conversion ratio of the adsorption process

The ammonia conversion ratio is also calculated and plotted for analysing the adsorption process of $MnCl_2$ composite. The conditions of the adsorption temperature are 20 ℃, 10 ℃, and 0 ℃.

20 ºC adsorption:

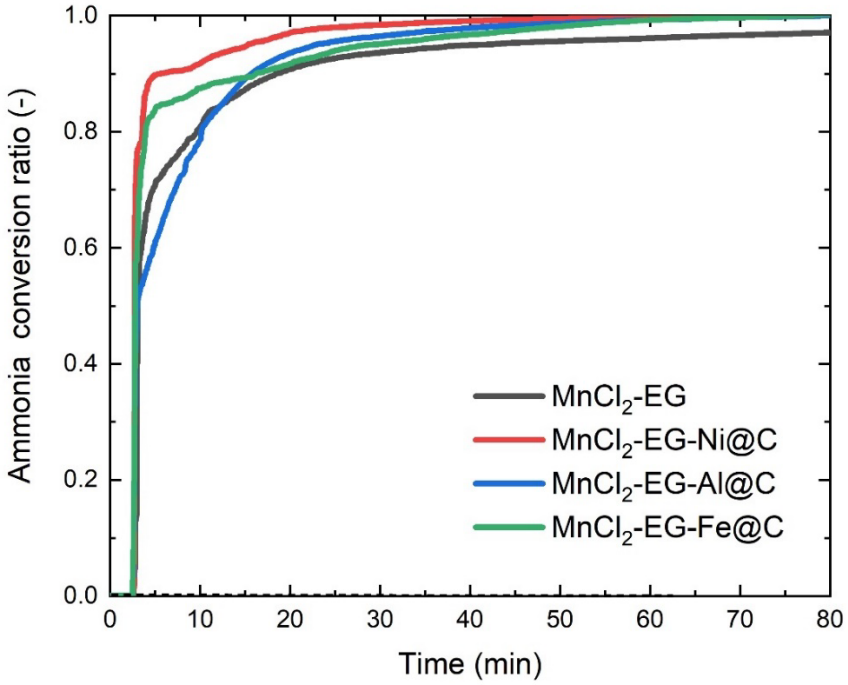

Figure 6.25 Ammonia conversion ratio of $MnCl_2$ composite during 20 ℃ adsorption versus time

Fig 6.25 is the result retrieved at an evaporator temperature set to 20 ℃. In the first minute of reaction, the ammonia conversion ratio sharply rises, and then the speed is slower and slower until the curve is smooth. It is due to the nature of the chemical reaction.

The adsorption performance of the sorbent is improved by the adding of carbon coated metals, as the reaction rate is accelerated. The reason is the same with the explanation given in desorption results. $MnCl_2$-EG-Ni@C obtains the fastest reaction speed among all four candidates, and it completes the adsorption of all four portions of ammonia at 34.08 min after the adsorption starts. For all sorbents, the adsorption time for them to adsorb 90% of the four portions ammonia is 2.33 min for $MnCl_2$-EG-Ni@C, 13.33 min for $MnCl_2$-EG-Al@C, 13.42 min for $MnCl_2$-EG-Fe@C, and 13.67 min for $MnCl_2$-EG, in time increasing order.

Fig. 6.26 is the error analysis of the results in Fig. 6.25, which proves the results to be reliable. From around 5 min to 20 min, the gaps between the error bars of the red and the green curves are obvious, which demonstrates the good reliability of the data.

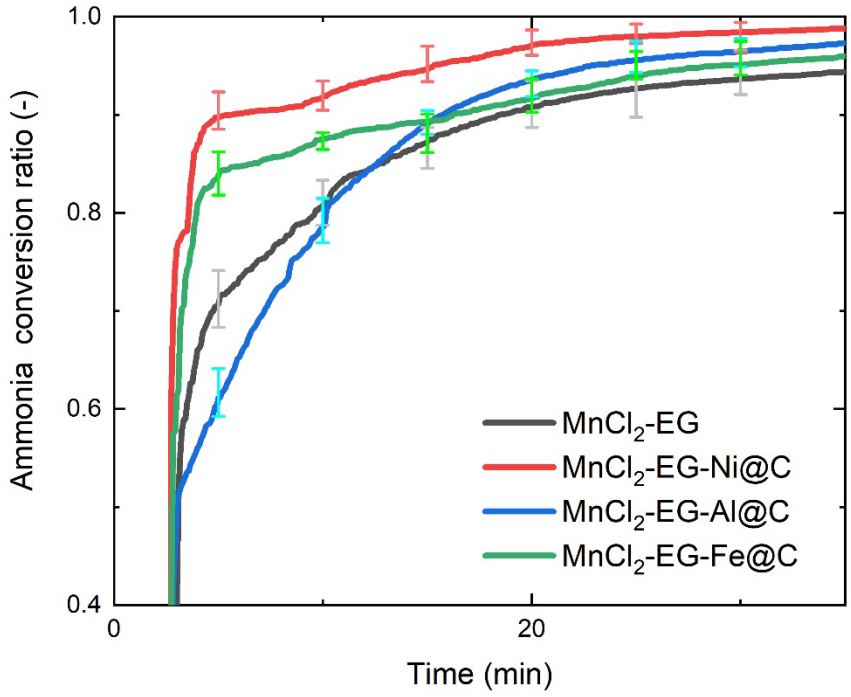

Figure 6.26 Error analysis of $MnCl_2$ composite sorption during 20 ℃ adsorption

10 ºC adsorption:

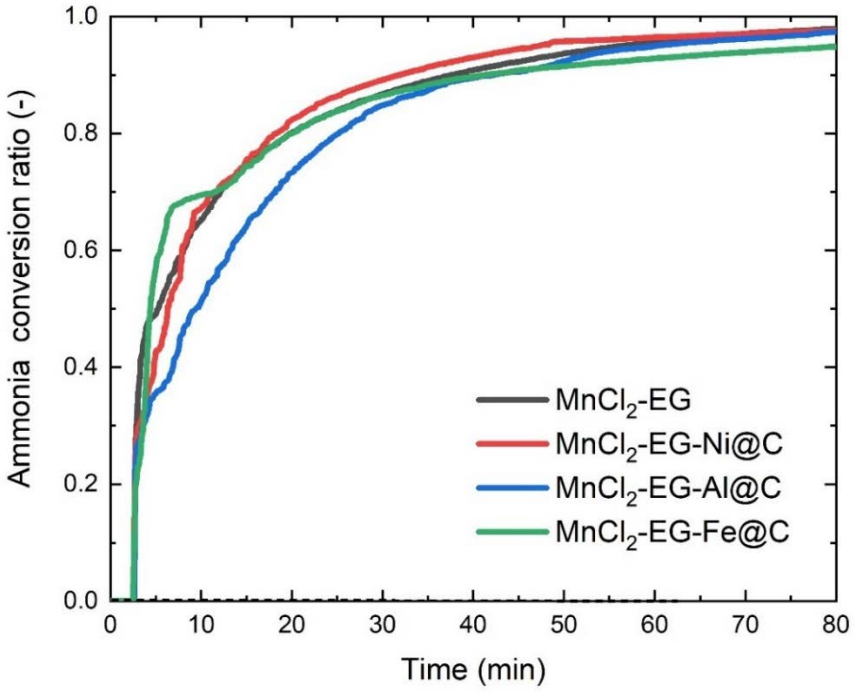

Figure 6.27 Ammonia conversion ratio of $MnCl_2$ composite during 10 ℃ adsorption versus time

Fig 6.27 presents the ammonia conversion ratio of $MnCl_2$-EG-0/Ni/Al/Fe@C adsorbing the ammonia when the evaporator is set to 10 ℃. It also shows a rapid increase at first, but it reduces the reaction speed in an earlier stage compared to the results from Fig 5.23. The reason is that the higher temperature of the evaporator provides a higher pressure of the ammonia, which supplies more ammonia in the unit contact area to react with the chemical salt of $MnCl_2$. Thus, the adsorption at a higher evaporation temperature have a faster reaction than the lower temperature adsorption.

The result of 10 ^oC adsorption shows that Ni@C accelerate the adsorption performance. Other additives have similar performance with the conventional sorbent. However, at the beginning of the curves in green and blue, the big fluctuation is discovered. The similar performance could be caused by the errors of the sensors or the data-taker. In fact, the three carbon coated metals are all expected to improve the adsorption performance. No sorbent could 100% convert the free ammonia to adsorbed ammonia in 10 ^oC adsorption test. The reaction time required to combine 90% of the four portions ammonia with the sorbent is 35.33 min for $MnCl_2$-EG, 29.58 min for $MnCl_2$-EG-Ni@C, 37.25 min for $MnCl_2$-EG-Al@C, 38.67 min for $MnCl_2$-EG-Fe@C.

As the results clarify the overlap of the different conversion ration curves, the error analysis to prove the curve difference is not necessary.

0 ^oC adsorption:

Fig 5.25 displays the illustration using the ammonia conversion ratio to reflect the adsorption performance, when the temperature of the cryostat connected to the evaporator is controlled to 0 ℃. 0 ^oC adsorption performance is crucial for the application of ice-making.

The result shows all additives have positive effect on the sorption performance, as the sorbents react faster than the conventional one. The reason is that the carbon coated metal can comprehensively improve the heat and mass transfer processes during 0 ^oC adsorption. The red curve representing the reaction of the MnCl2-EG-Ni@C is at the top of the figure, indicating the fastest adsorption rate among all candidates. In this circumstance, the equilibrium global conversion ratio is no more than 0.9. The reaction time for the sorbent to reach 0.8 is 48.08 min obtained in the test of conventional $MnCl_2$-EG, 32.25 min in the test conducted on sorbent with Ni@C, 42.83 min in the experiment of $MnCl_2$-EG-Al@C adsorption, and 39.5 min in the exploration on the sorbent with Fe@C.

As the red curve is far away from the other three curves, the superiority of the Ni@C-additive sorbents is obvious, and the error analysis is not required in this condition.

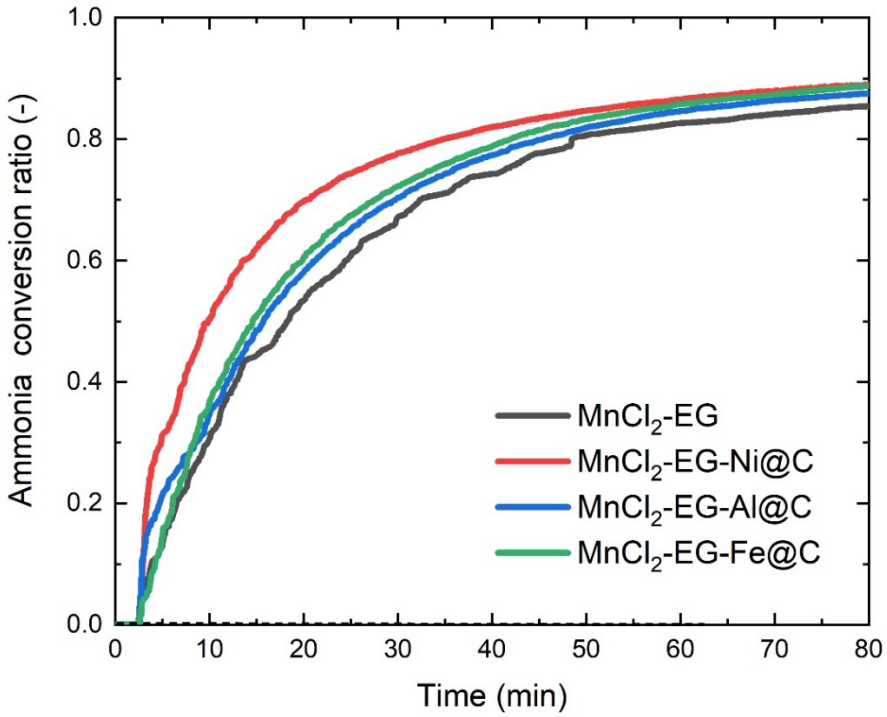

Figure 6.28 Ammonia conversion ratio of $MnCl_2$ composite during 0 ℃ adsorption versus time

The adsorption results at various temperature demonstrate that the additives of Ni@C, Al@C and Fe@C can improve the sorbent adsorption performance by accelerating the adsorption rate. The reason could be the improvement of the comprehensive heat and mass transfer made by the carbon coated metals, even the mass transfer resistance is increased. Moreover, Ni@C is proved to be the optimal additive for $MnCl_2$-EG. By using the novel sorbents, it is potential to increase the refrigeration production of the sorption system and save the energy consumption. Moreover, the result indicates the feasibility of applying the novel sorbent to enhance the utilisation of low-grade heat by sorption cycles.

6.2.4 SCP and COP of $MnCl_2$ composite

The specific cooling power (SCP) of the HTS is calculated and illustrated in the following picture, referring to the adsorption performance retrieved from 20 ℃, 10 ℃ and 0 ℃ adsorptions of MnCl2-EG-0/Ni/Al/Fe@C, when the cooling source for the adsorbent bed is tap water.

SCP at 20 ºC:

Fig 6.29 is SCP obtained from 20 ºC adsorption of $MnCl_2$-EG variations.

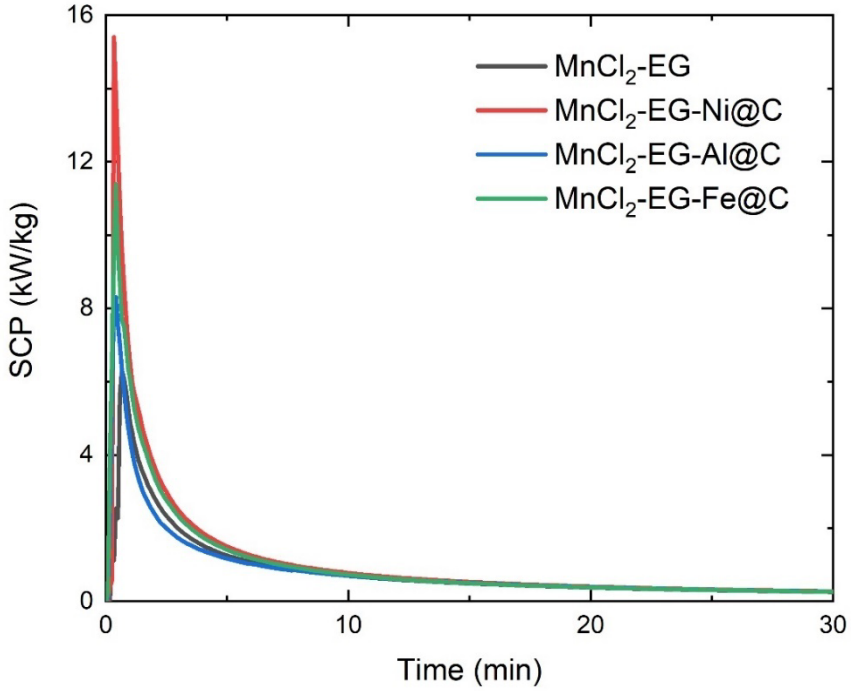

Figure 6.29 SCP of $MnCl_2$ composite at an evaporator temperature of 20 ℃ versus time

A rapid increase is observed at the start of the reaction. The trend of each curve is similar with the regulation found in SCP of $SrCl_2$ composite.

The sorbents with Ni@C, Al@C and Fe@C have the improved SCP, which means more refrigeration capacity of unit mass sorbent. It is because of the enhanced adsorption performance. The peaks of the sorbents are 15.41 kW/kg for $MnCl_2$-EG-Ni@C at 0.33 min, 11.43 kW/kg for $MnCl_2$-EG-Fe@C at 0.42 min, 8.302 kW/kg for $MnCl_2$-EG-Al@C at 0.42 min and 6.42 kW/kg for conventional $MnCl_2$ composite at 0.67 min, in a decrement order. Besides, the SCPs of various sorbents are in the same order at each time point.

SCP at 10 ºC:

Fig 6.30 is SCP retrieved from the 10 ºC adsorption test of HTS with or without additives. A rapid growth is found as well in this figure, during the first minute of the adsorption reaction process. Later, the peaks are eliminated by the long reaction time.

Adding Ni@C into the conventional HTS is found to have improved SCP of the sorbent. The reason is that Ni@C improved the 10 oC adsorption performance of $MnCl_2$-EG. However, it is expected to make improvements of SCP by other two novel sorbents. The reason is given in the discussion of 10 ºC adsorption result. Four peaks of SCP are 6.51 kW/kg for the sorbent with Ni@C at 0.25 min, 6.13 kW/kg for the conventional HTS at 0.33 min, 5.26 kW/kg for the novel $MnCl_2$ composite with Al@C at 0.42 min, and 4.91 kW/kg for $MnCl_2$-EG-Fe@C at 0.25 min in a increment order of the SCP values. There is a noticeable fluctuation in the green

line, but through the comparison with the peak values, it can be concluded that the increasing SCP order at any time point should be the same with the discovery in the order of the peaks.

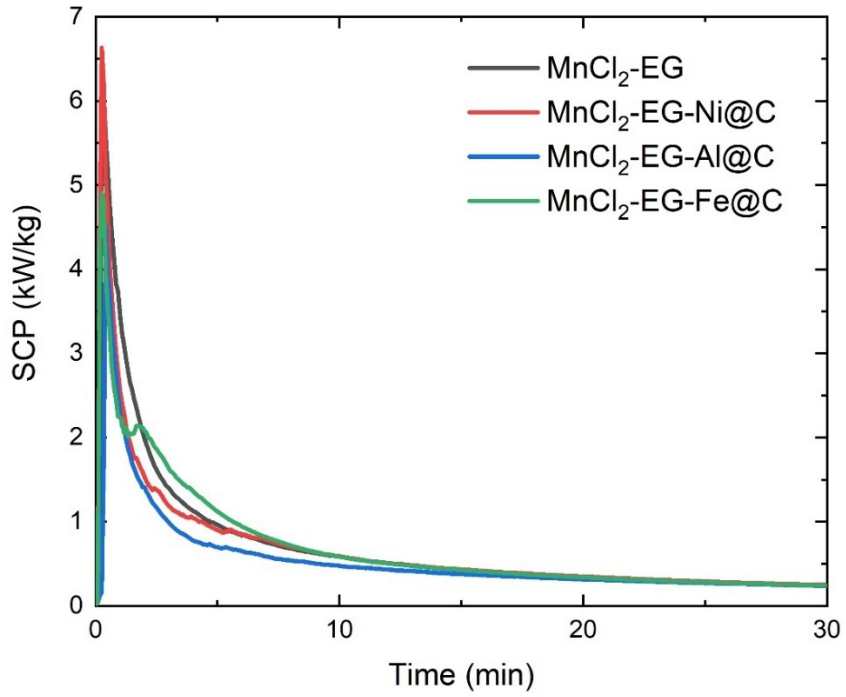

Figure 6.30 SCP of $MnCl_2$ composite at an evaporator temperature of 10 ℃ versus time

SCP at 0 ºC adsorption:

Fig 6.31 presents SCP of 0 ºC adsorption performance test. In the figure, a rapid growth is apparent in the first few minutes.

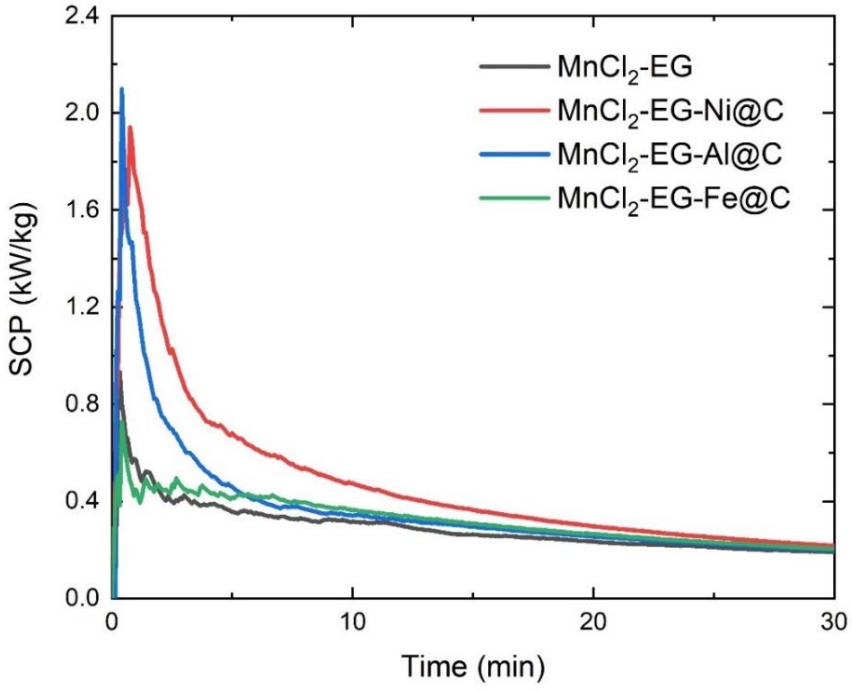

Figure 6.31 SCP of $MnCl_2$ composite at an evaporator temperature of 0 ℃ versus time

The result shows that Ni@C, Al@C and Fe@C improves SCP of the original HTS, even in first 2.5 min, SCP of the sorbent with Fe@C is lower than $MnCl_2$-EG. It can be explained by the results found in 0 ^oC adsorption. The performance of the sorbent is improved by the additives. Thus, the refrigeration is produced with an increased amount by per unit mass sorbent. Although the highest peak among all the sorbent candidates is at the blue line, the corresponding evidence in Fig 6.28 shows the maximum SCP in this condition is expected to be found in the test on $MnCl_2$-EG-Ni@C. The optimum SCP should be 1.94 kW/kg at 0.75 min. Other peaks are included as 1.64 kW/kg for $MnCl_2$-EG-Al@C at 0.75 min, 1.63 kW/kg for $MnCl_2$-EG at 0.42 min and 0.92 kW/kg for $MnCl_2$-EG-Fe@C at 0.5 min, removing the invalid points.

COP at 20 ^oC adsorption:

Fig 6.32 displays COP of $MnCl_2$-EG-0/Ni/Al/Fe@C during adsorption at evaporation temperature of 20 ^oC. After 5 min, the difference between each curve is tiny.

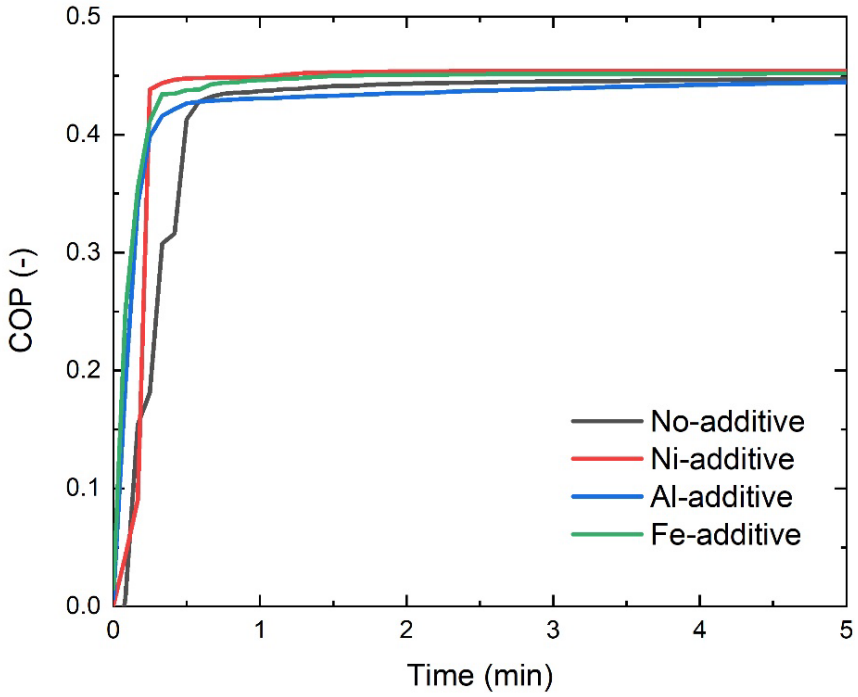

Figure 6.32 COP of $MnCl_2$ composite at an evaporator temperature of 20 ℃ versus time

Regardless of the rapid increasing process, Ni@C and Fe@C improves COP of the sorbent. It is the reflection of 20 ^oC adsorption performance results. The red curve, representing the Ni-additive sorbent, stays at the top of the figure. From the corner of the curves, it is observed to be red, green, black, blue in decrescent order of COP values.

COP at 10 ^oC adsorption:

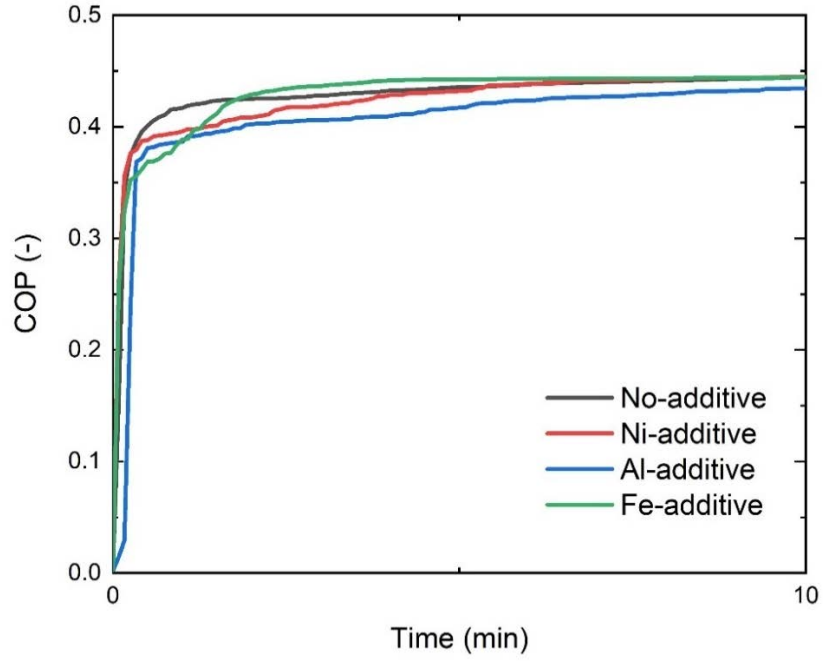

Figure 6.33 COP of $MnCl_2$ composite at an evaporator temperature of 10 ℃ versus time

Fig 6.33 shows COP of conventional and novel HTS, when adsorption temperature at 10 ºC. In this circumstance, the gaps between each curve is tiny.

In 10 min, Ni@C and Fe@C improve COP of the sorbent, as the green and red curves are at the higher positions in the figure. Longer than that, Ni@C makes the most improvement of COP, according to 10 ºC adsorption test results.

COP at 0 ºC adsorption:

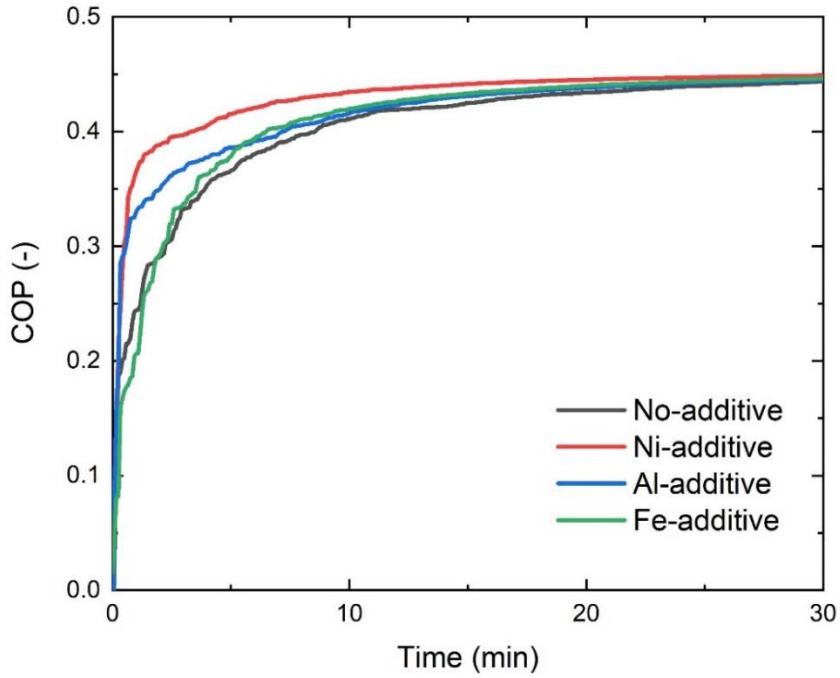

Figure 6.34 COP of $MnCl_2$ composite at an evaporator temperature of 0 ℃ versus time

Fig 6.34 presents COP of $MnCl_2$ composite with or without nanoparticles, during adsorption test at 0 ^oC. COP at 0 ^oC adsorption has a significant meaning of ice-making.

The result demonstrates that COP is improved by these three additives, as the black curve representing the conventional sorbent is at the bottom among all. Ni@C makes the most improvement of COP. The reason can be obtained in the result discussion of 0 ^oC adsorption.

Regardless of the rapid start, the additives improve SCP and COP of the sorbent, which means more refrigeration produced by the unit mass of sorbent or the same heat consumption. It indicates that the Ni@C, Al@C and Fe@C can improve the refrigeration performance of the sorption cycle. They are potential to enhance the low-grade heat conversion technology. Moreover, Ni@C is superior over other candidates, as it has the most improvement of SCP and COP.

6.3 Summary

An experimental system is used to test the sorption performance of the manufactured sorbents with or without the carbon coated metals. Results include the following information:

- All the adsorption and desorption performance display a rapid change during the first few minutes and then the reaction rate is reduced until reaching the equilibrium. It is the nature of chemical reaction.
- $SrCl_2$-EG-0/Ni/Al/Fe@C start to desorb at around 90 ^oC, while $MnCl_2$-EG-0/Ni/Al/Fe@C begin desorption at around 110 ^oC, when the condensation temperature is at -20 ^oC. The low condensation temperature refers to a low equilibrium pressure of ammonia, which drives the HTS desorption to start at a lower desorption temperature.
- The heat loss is not practical to be eliminated. The inlet oil temperature is higher than the outlet oil temperature. The adsorbent temperature is 10 ℃ lower than the temperature set at the oil bath.
- Table 6.1 summarises the improvements of various assessments. LTS desorption performance is improved by adding Ni@C, Al@C and Fe@C into the conventional LTS and Ni@C improves the LTS adsorption performance as the additive. HTS desorption performance is improved by all carbon coated metals, and All additives can improve HTS adsorption performance.
- Ni@C is the optimal additive for LTS. It can reduce the reaction time of 130 ^oC desorption by 22.42 %, 20 ^oC adsorption by 15.84 %, and 10 ^oC adsorption by 12.15

%, to reach ammonia conversion ratio of zero, 0.9, and 0.9, respectively. In 0 ^{o}C adsorption, Ni@C increases the conversion ratio by 9.84 % for 60 min reaction time.

- Ni@C can make the maximum improvement of HTS sorption performance. The desorption time is reduced by 41.27 %, 51.0 % and 37.91 % to reach 0.1 conversion ratio in 180 ^{o}C, 170 ^{o}C and 160 ^{o}C desorption, separately. The adsorption time is decreased by 82.96 %, 16.17 % and 32.92 % to achieve the conversion ratio of 0.9, 0.9 and 0.8 in 20 ^{o}C, 10 ^{o}C and 0 ^{o}C adsorption, respectively.
- SCP of LTS is improved by Ni@C, while SCP of HTS is improved by all additives. The highest value of SCP is 15.41 kW/kg found in $MnCl_2$-EG-Ni@C adsorption test. The maximum SCP value is always observed belong to the sorbent with Ni@C in every testing condition. Ni@C is the optimum additive for HTS and LTS. Besides, it is suggested to shorten the adsorption time to optimise SCP.
- COP of LTS is improved by Ni@C, while that of HTS is improved by Ni@C and Fe@C. Al@C can only improve COP at 0 ^{o}C adsorption. The reason is explained in the discussion of ammonia conversion ratio. At evaporator temperature of 20 ^{o}C, COP of $MnCl_2$-EG-Ni@C is the highest, 0.45, when the reaction time is 5 min.
- The improvement is due to the enhancement of thermal conductivity. Even the mass transfer resistance is increased, the improvement of the heat transfer sometimes dominates in the comprehensive heat and mass transfer processes, according to the salt types and the sorption conditions.

In a conclusion, the most superior adsorbent is $SrCl_2$-EG-Ni@C. It improves the desorption and adsorption performance by an increased reaction rate. Moreover, it could produce more refrigeration by per unit mass sorbent or by the same heat consumption. The improvement indicates the feasibility to use the novel sorbent $SrCl_2$-EG-Ni@C for enhancing the low-grade heat utilisation by sorption cycles.

Improvement	Ni@C	Al@C	Fe@C
		LTS	
180 ^{o}C desorption	No	No	No
130 ^{o}C desorption	Yes	Yes	Yes
Adsorption	Yes	No	No
SCP	Yes	No	No
COP	Yes	No	No
		HTS	

Desorption	Yes	Yes	Yes
Adsorption	Yes	Yes	Yes
SCP	Yes	Yes	Yes
COP	Yes	Positive (0 ^{o}C)	Yes

Table 6.1 Summary of the improved results

Chapter 7 Simulation study of sorption and ORC coupling systems

Chapter 7 proposes and studies four integrated ORC-sorption cooling and power systems, including the one introduced as a case study. Different with the preliminary simulation without considering the physical volume or shape of the adsorption reactor, Chapter 7 builds the models utilising the dimensional data of the investigated experimental sorption reactor. With the physical model of the sorbent bed, the simulation can fit better with the actual conditions. Various combinations of ORC and chemisorption cycles are explored to justify the optimum mode for cascaded utilisation of low-grade thermal energy. Adsorption cycle is the top user of low-grade heat in AD-ORC system, while resorption-ORC and ORC-resorption systems apply resorption cycle to substitute the adsorption modules. An optimal combination will be obtained through the simulation results. Besides, the new kinetic models of the manufactured novel sorbents are found by the author, based on the experiments earlier. They are used in the superior coupling system to evaluate the influence of the novel sorbent.

7.1.1 Comparisons of ORC-AD and AD-ORC

ORC performance:

Table 7.1 presents the ORC performance of net power output, thermal efficiency, waste heat emission and exergy efficiency. ORC-AD has a stable, while AD-ORC has minor changes before the outlet low-grade heat becomes stable. In both systems, the inlet and outlet enthalpies of the evaporator are not affected by the change of heat source temperature, as they are determined by the superheat temperature. The heat source enables the working fluid to reach the superheat temperature. Thus, the net power is the same in ORC-AD and AD-ORC. Besides, the heat consumed by ORC is equal in the two systems. Therefore, the thermal efficiency of ORC is not changed. As the heat source has been partly used in adsorption cycle, the available thermal energy for ORC is reduced in AD-ORC, which results in the 7.39 % reduction of the dump heat or the 13.89 % growth of ORC exergy efficiency.

Mode	$\dot{W}_{net}\ (kW)$	$\eta_{th,ORC}\ (\%)$	$\dot{Q}_{dump,ORC}\ (kW)$	$\eta_{exe,ORC}\ (\%)$
ORC-AD	3.87	8.74	173.92	10.15
AD-ORC (stable)	3.87	8.74	161.06	11.56

Table 7.1 Assessment of ORC performance

Refrigeration:

Fig 7.1 draws the diagram for comparing the refrigeration produced by ORC-AD and AD-ORC system, only considering from the time starting reaction. The calculation of the refrigeration generated per unit time follows the equations stated in Chapter 3.

The results demonstrate that using adsorption units as the top cycle of the cogeneration system could improve the refrigeration. There are two peaks found in Fig 7.1. One is 157.31 W of ORC-AD at 4.25 min and the other is 167.94 W of AD-ORC at the time of 3.83 min. These two curves in the illustration demonstrate the relationship between the cooling power and the cycle time. When the time increases, the gross production becomes larger. However, calculated into the production divided by the cycle time, the refrigeration grows rapidly at first and then drops after the value reaches its peak. The higher refrigeration power also has a shorter reaction time, which could be explained by the top cycle position of adsorption units. It causes the increase of heating temperature, pushing desorption to release more ammonia for the next adsorption progress. In this case, regarding the sorbent has desorbed ammonia as the available sorbent to adsorb ammonia in next stage, more refrigeration is generated with a faster rate in a condition that possesses more active sorbents at the start. At the end of 60 min, the difference between ORC-AD and AD-ORC is only 0.80 W, indicating the refrigeration advance of the AD-ORC will be almost eliminated in a cycle time longer than that. Before the reaction time of 25 min, the gap between the two curves is relatively apparent, which reveals the preferred operational time to take the benefit from AD-ORC.

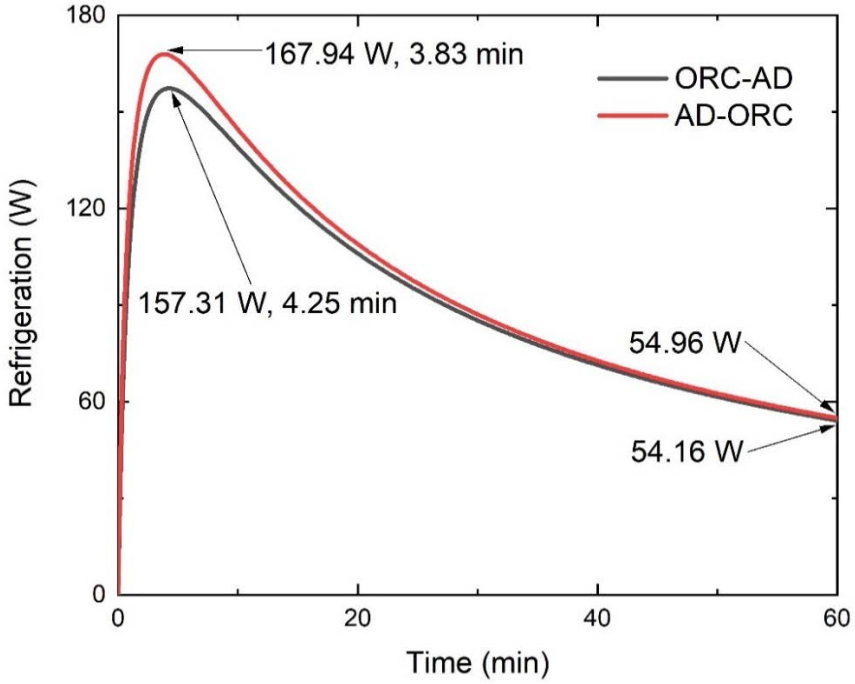

Figure 7.1 Refrigeration produced by ORC-AD and AD-ORC versus time

COP:

Fig 7.2 shows the COP retrieved from the simulated cooling and power systems of ORC-AD and AD-ORC.

The result reveals that ORC-AD has a higher COP than AD-ORC in the testing condition. Even though the higher desorption temperature enables more production of cooling effect, COP of the AD-ORC system is reduced as the increase of the output fails to catch the growth pace of the heat cost, which mainly consists of both the sensible heat and the desorption heat. When desorption time is 60 min, the value of COP is 0.2860 and 0.2689, for ORC-AD and AD-ORC system, separately.

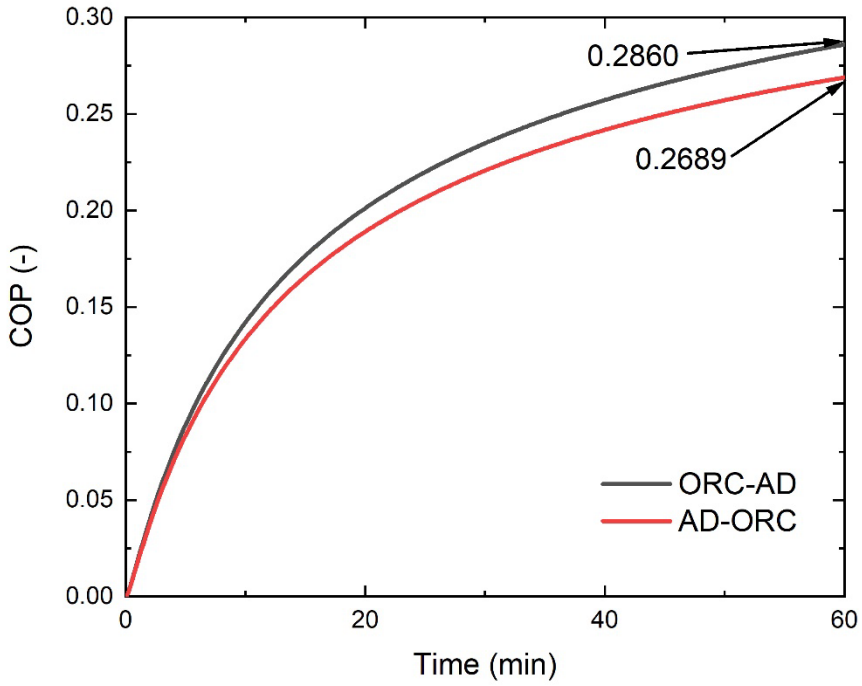

Figure 7.2 COP in ORC-AD and AD-ORC versus time

Thermal efficiency:

The evolutions of the thermal efficiency in both systems are similar with the shape in Fig 6.4, as shown in Fig. 7.4. A rapid increase is found at the start with a reduced rising speed, and the curves drop until the end after meeting a peak in the diagram.

The result presents that before 4.25 min, AD-ORC has a higher thermal efficiency, while after that, ORC-AD has a higher thermal efficiency. The value is the same of the two peaks, 7.10 %, while the time for ORC-AD to reach the peak is 1.08 min later. The phenomenon could be explained by the active sorbent number mentioned in the discussion of refrigeration results. The thermal efficiency of AD-ORC is higher than that of ORC-AD in the first few minutes. However, with the reaction time increasing, the difference between them is reduced, and later the thermal efficiency of ORC-AD is even higher than that of AD-ORC. Corresponding with

COP results in Fig 7.2, the difference between the COPs matches the gap between the refrigeration when the thermal efficiency is the same. After that, due to the low cost from the sensible heat and the desorption heat, ORC-AD shows a higher thermal efficiency than AD-ORC system.

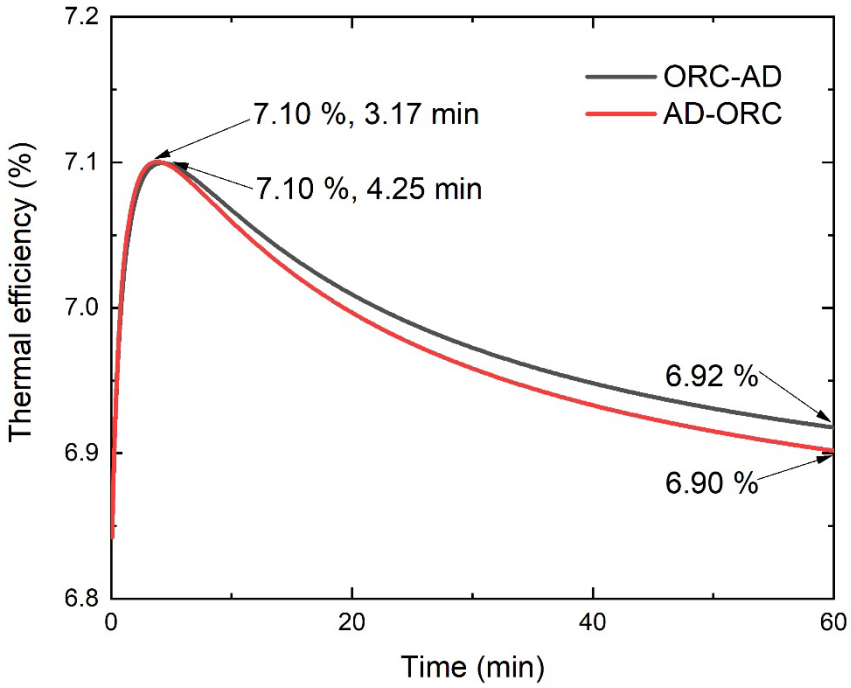

Figure 7.3 Thermal efficiency of cogeneration in ORC-AD and AD-ORC versus time

Exergy efficiency:

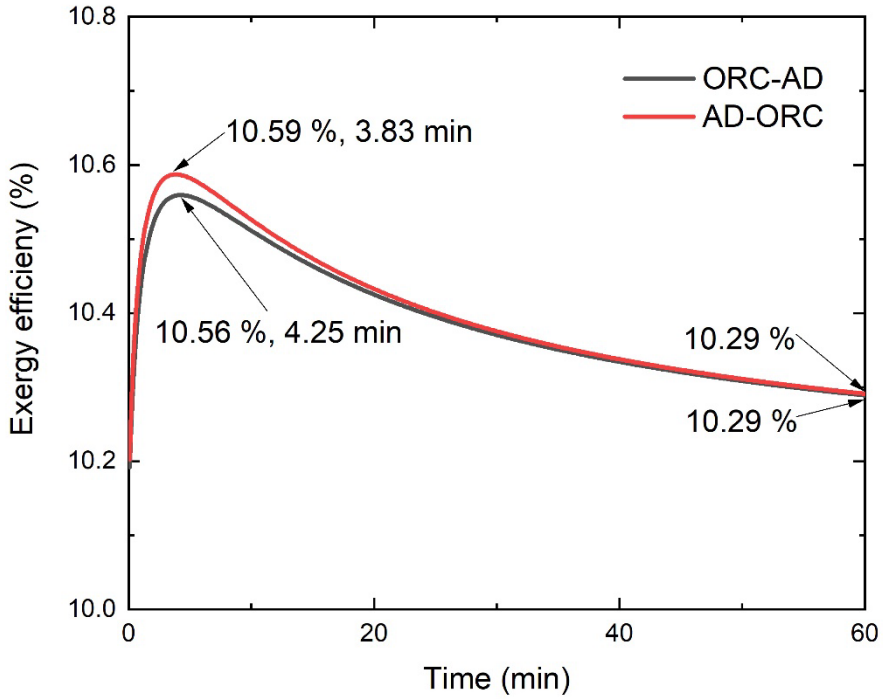

Figure 7.4 Exergy efficiency of cogeneration in ORC-AD and AD-ORC versus time

The exergy efficiency of ORC-AD and AD-ORC is illustrated in Fig 7.4. The exergy efficiency, again, has a very similar shape with that in Fig 7.1.

The results show that AD-ORC has a higher exergy efficiency than ORC-AD system. There are two peaks found in the diagram, one is 10.59 % of AD-ORC at the reaction time 3.83 min, while the other peak is 10.56 % of ORC-AD at 4.25 min. At the reaction time of 60 min, the exergy efficiency is 10.29 % of both systems, ignoring the third number after the decimal point. The result reveals a higher exergy efficiency could be achieved by applying adsorption cycles as the first user for such a hot gas. The reason is that AD-ORC yields more production composed by cooling and power than ORC-AD, using the same heat source. Like the refrigeration results, this minor advantage could be eliminated by the long cycle time. Matching the cooling capacity with the electricity capacity may be a solution to alleviate this problem.

Dump heat:

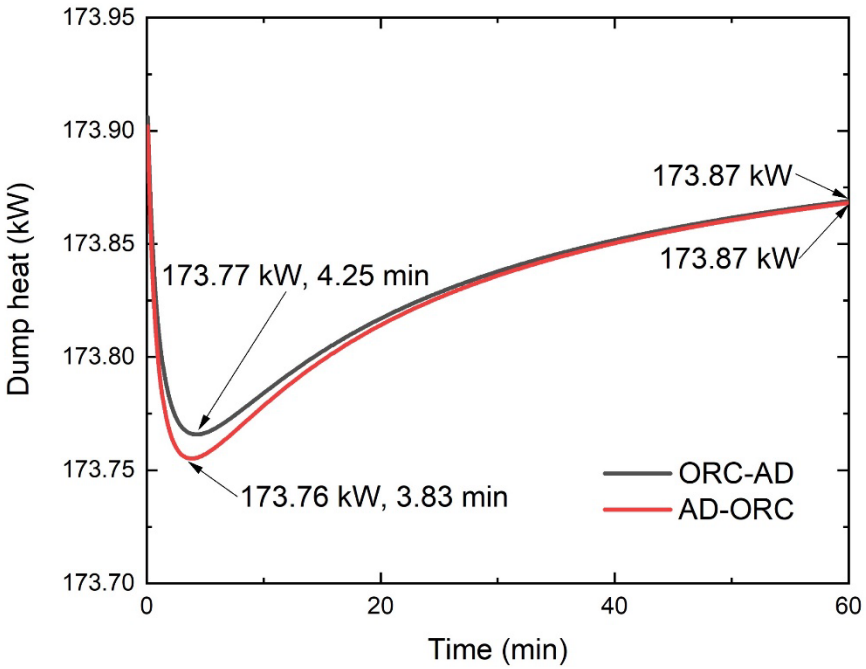

Figure 7.5 Dump heat of cogeneration in ORC-AD and AD-ORC versus time

Fig 7.5 is the results of the dump heat released from ORC-AD or AD-ORC systems, after the utilisation of the heat source.

The result displays that using adsorption units as the top cycle could reduce the dump heat of the system. At the reaction time of 0 min, the dump heat of the cogeneration system is equal to the dump heat of a single ORC system, while after that, it drops rapidly to 173.77 kW in ORC-AD system at 4.25 min, and 170.81 kW in AD-ORC system at the reaction time of 3.83 min. The reductions are caused by the heat consumption of desorption process in sorption

units. Later, the dump heat grows with a reduced increasing speed as the heat cost by the adsorption cycles reduces. Again, using more sorbent in adsorption cycles could be the solution to reduce the waste of the thermal energy.

7.1.2 Comparisons of resorption-ORC and ORC-resorption

ORC performance:

The net power, thermal efficiency, exhaust heat and exergy efficiency of ORC in ORC-resorption and resorption-ORC are the same with those in ORC-AD and AD-ORC systems, when their values are stable. When ORC is the first user of the heat source, the working conditions of ORC are the same for ORC-AD and ORC-resorption system. When ORC is the second user, the working conditions keeps the same for AD-ORC and resorption-ORC, as the heat consumption of the sorption units stay the same.

Refrigeration:

Fig 7.6 presents the refrigeration produced by ORC-resorption and resorption-ORC systems. The red curve represents the latter system, while the black one stands for the former cogeneration system.

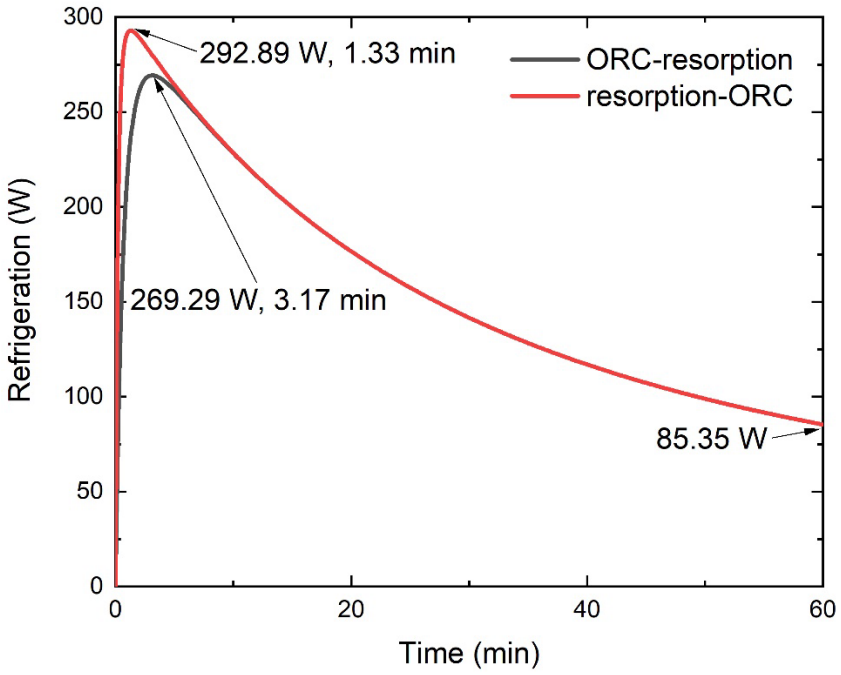

Figure 7.6 Refrigeration in ORC-resorption and resorption-ORC systems versus time

The result shows that resorption-ORC system is superior over ORC-resorption in the aspect of cooling generation. A peak exists in each line with the value of 292.89 W for resorption-ORC at 1.33 min or 269.29 W for ORC-resorption system at the cycle time of 3.17 min. At the end of 60 min, the refrigeration is 85.35 W for both systems. All values mentioned in Fig 7.6 are

higher than that in Fig 7.1, which is caused by larger cooling capacity substituting ammonia container with $SrCl_2$-EG adsorption unit. The difference between peaks is relatively more significant than that found in ORC-AD and AD-ORC comparison, demonstrates the increased temperature of the heat source has more influences on cogeneration systems integrating resorption cycles with ORC. It is worth noting that the curves representing refrigeration of different systems meet quicker than those in Fig 7.1. Thus, the operational time should be shorter to obtain the optimum cogeneration performance.

COP:

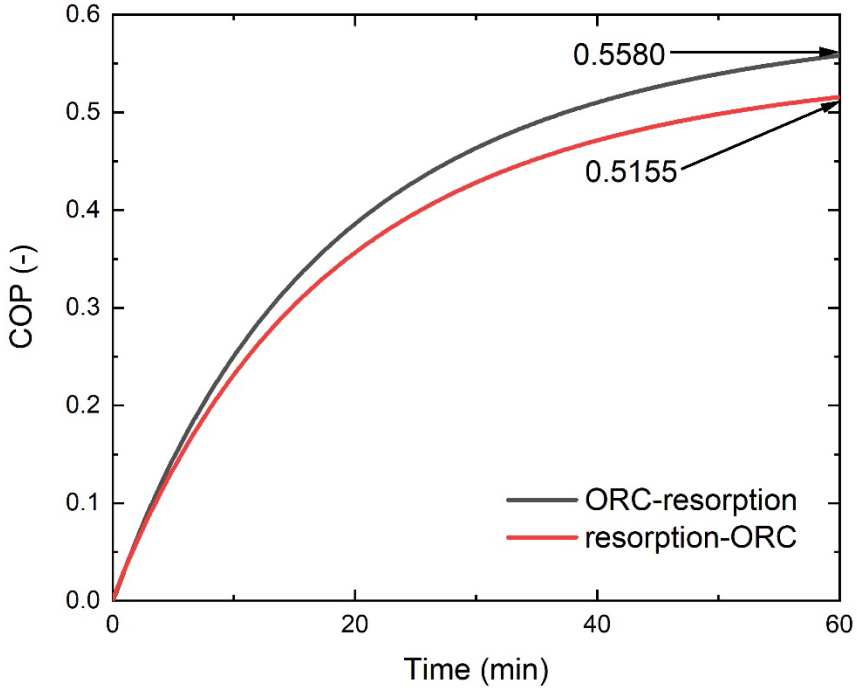

Figure 7.7 COP in ORC-resorption and resorption-ORC systems versus time

Fig 7.7 illustrates COP calculated from the integration system composed by ORC and resorption cycles. It grows with a decreased increasing speed during the reaction time.

The results reveal that ORC-resorption system has a larger COP than resorption-ORC. At the end of 60 min, COP of ORC-resorption is 0.5580 and COP of resorption-ORC is 0.5155. The reason why COP obtained from ORC-resorption is larger is the same with the explanation in Fig 7.2. Moreover, the quicker reaction rate in the first stage is caused by the higher desorption temperature, which enables more active sorbents within the same time scale.

Thermal efficiency:

Fig 7.8 presents the thermal efficiency of the cogeneration systems ORC-resorption and resorption-ORC, which has a similar development with results shown in Fig 7.6.

The results present that resorption-ORC system has a higher thermal efficiency before 3.17 min, while after that ORC-resorption has the higher thermal efficiency. It is reasonable as the thermal efficiency of ORC is stable after minor changes before the entering temperature of the heat source is stable. Thus, the main component dominating the value of the thermal efficiency is the adsorption unit. The thermal efficiency is larger in resorption-ORC than that in ORC-resorption as the more refrigeration produced in resorption-ORC at first few minutes. After that, the thermal efficiency of ORC-resorption becomes larger as the amount of the sensible heat and the desorption heat cost by the adsorption units is smaller. The peaks are 7.32 % at 1.33 min of resorption-ORC and 7.30 % at 3.17 min of ORC-resorption, respectively. At the end of 60 min, the thermal efficiency is 6.97 % of ORC-resorption and 6.96 %of resorption-ORC, separately. All thermal efficiencies are higher than that of ORC-AD and AD-ORC systems, demonstrating the more beneficial systems of replacing the adsorption cycles by resorption cycles.

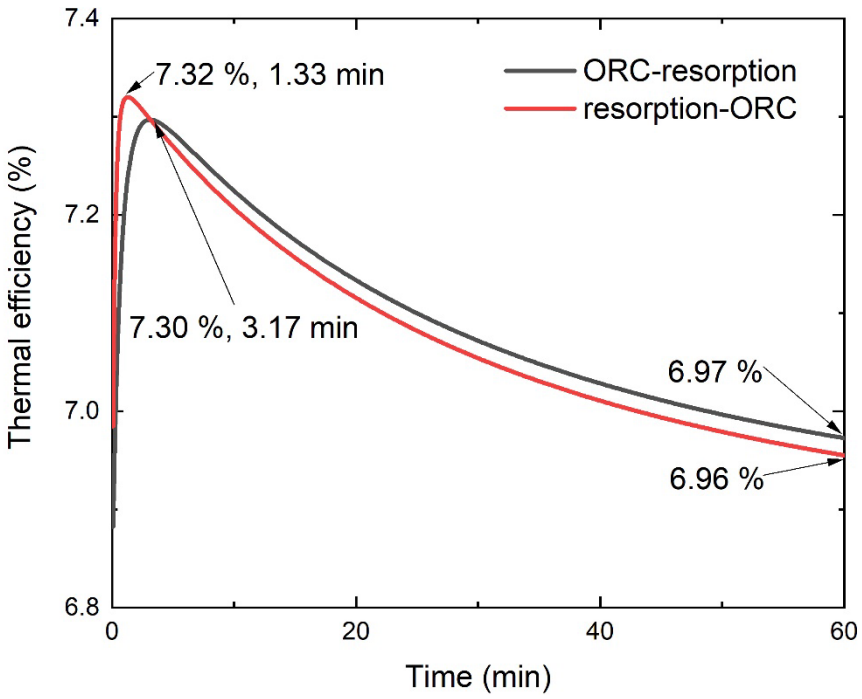

Figure 7.8 Thermal efficiency of ORC-resorption and resorption-ORC systems versus time

Exergy efficiency:

Fig 7.9 presents the exergy efficiency of these two cooling and power systems. The exergy efficiencies of ORC-resorption and resorption-ORC systems also have the similarity with the development in Fig 7.6.

The results demonstrate that resorption-ORC has a higher exergy efficiency, compared with the cogeneration system of ORC-resorption. One of the two peaks of the red and black curves is 10.91 % at 1.3 min of resorption-ORC system, while the other is 10.85 % at the reaction

time of 3.17 min. When the time reaches 60 min, the exergy efficiency is 10.37 %, omitting the third number after the decimal point. With the development of reaction time, the efficiency tends to decrease until stable. Again, the values get higher than that using adsorption cycles.

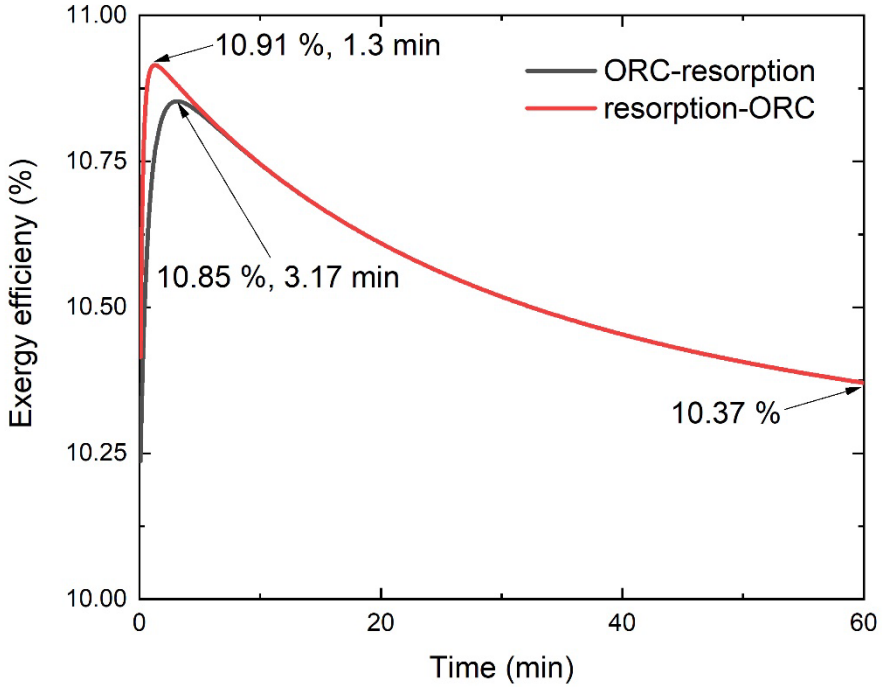

Figure 7.9 Exergy efficiency of ORC-resorption and resorption-ORC systems versus time

Dump heat:

Fig 7.10 shows the dump heat released from the integrated ORC-resorption and resorption-ORC systems.

The result indicates that resorption cycles as the top cycle to be integrated with ORC can reduce the dump heat of a low-grade heat source. The dump heat equals to the value when there is only ORC to use the heat source at 0 min. Once starting the reaction, the value of the dump heat drops sharply. The peak for ORC-resorption is 173.63 kW at 1.33 min while that for resorption-ORC is 173.65 kW at 3.17 min. This phenomenon is caused by the rapid increase of the reacted ammonia during the first stage. After the peak, the dump heat tends to reduce from fast to slow and then be stable, which is caused by the limited heat consumption of resorption cycles and the increased reaction time. At the end of 60 min, the waste heat of the systems is 173.84 kW for both resorption-ORC and ORC-resorption.

In summary, for a comprehensive consideration of the simulation results, AD-ORC or resorption-ORC systems are proved to be superior over ORC-AD or ORC-resorption systems. Even COPs of them are lower, AD-ORC and resorption-ORC systems have higher

refrigeration productions, higher thermal and exergy efficiencies, and more reduction of the dump heat.

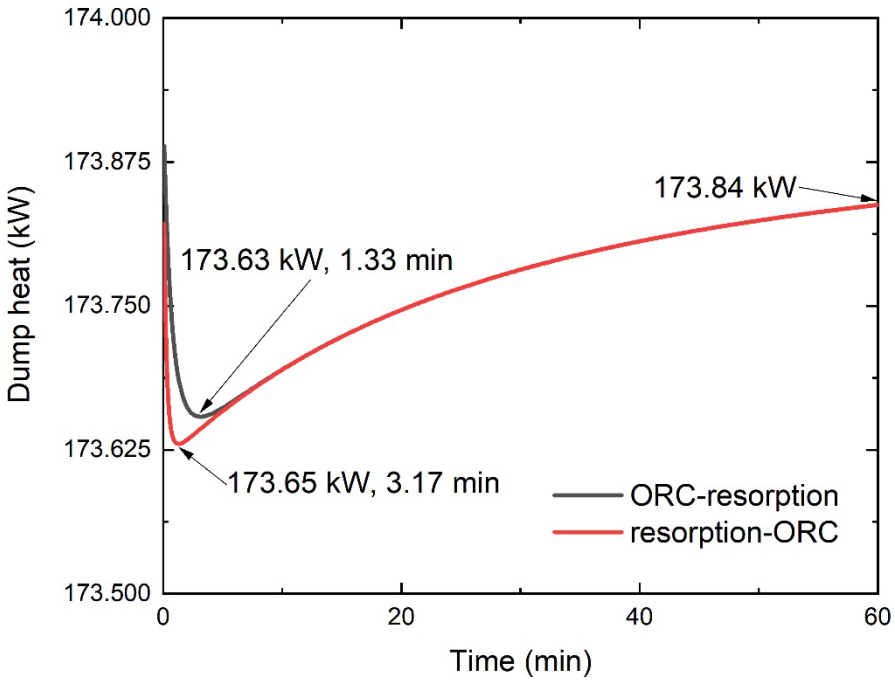

Figure 7.10 Waste heat of cogeneration in ORC-resorption and resorption-ORC systems versus time

7.2 Kinetic models of $MnCl_2$-EG and $MnCl_2$-EG-Ni@C

7.2.1 Kinetic parameters

Table 7.2 describes the kinetic parameters of adsorption and desorption modelling, based on the data retrieved from the sorption performance experiments of $MnCl_2$-EG and $MnCl_2$-EG-Ni@C. The kinetic models are applied into AD-ORC and resorption-ORC to evaluate the improvement of the cogeneration systems by adding Ni@C, as these two systems are proved to be more superior than other two candidates of ORC-AD and ORC-resorption.

	Adsorbent	Ar	Mr
Adsorption	$MnCl_2$-EG	0.009268	1.9
	$MnCl_2$-EG-Ni@C	0.013939	2.0
Desorption	$MnCl_2$-EG	5.9689×10^{-7}	1.115
	$MnCl_2$-EG-Ni@C	1.0319×10^{-6}	1.139

Table 7.2 Kinetic parameters in $SrCl_2$/$MnCl_2$-EG-Ni@C sorption

7.2.2 Validation of the kinetic models

The desorption computational results conform well to the experiments. The validation of desorption includes the 160 °C, 170 °C and 180 °C desorption, controlling the condenser at -20 °C, as shown in Fig 7.11 to Fig 7.13, separately.

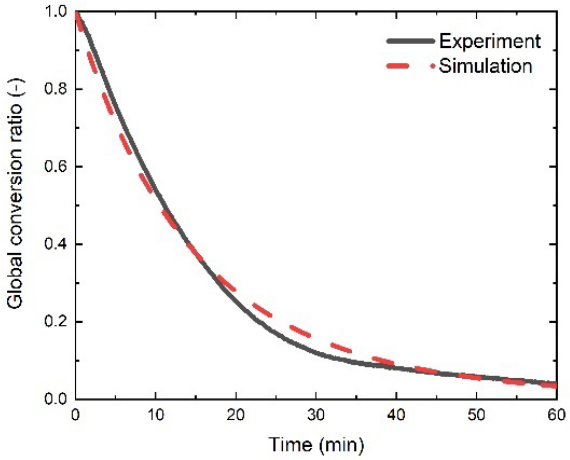

(a) $MnCl_2$-EG

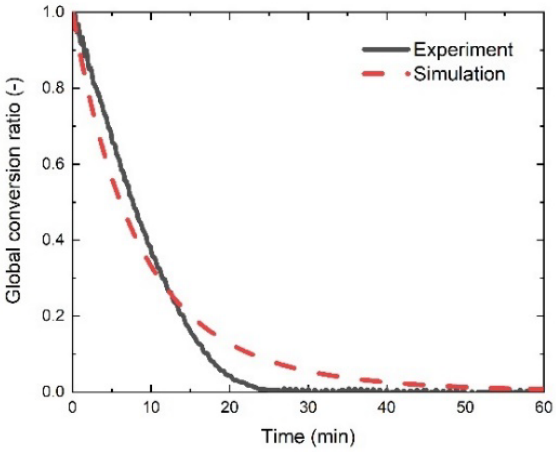

(b) $MnCl_2$-EG-Ni@C

Figure 7.11 Simulated and experimental ammonia conversion ratios (180, -20) versus time

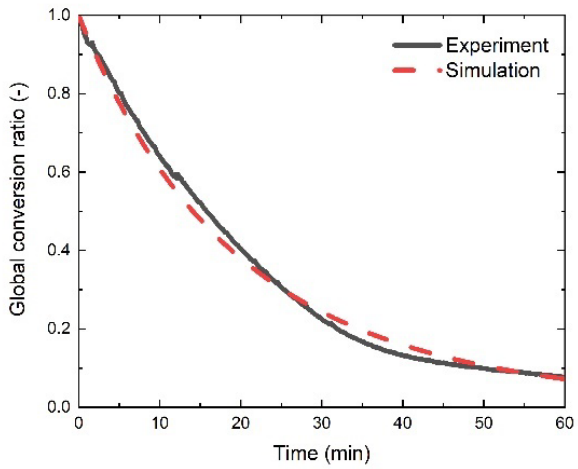

(a) $MnCl_2$-EG

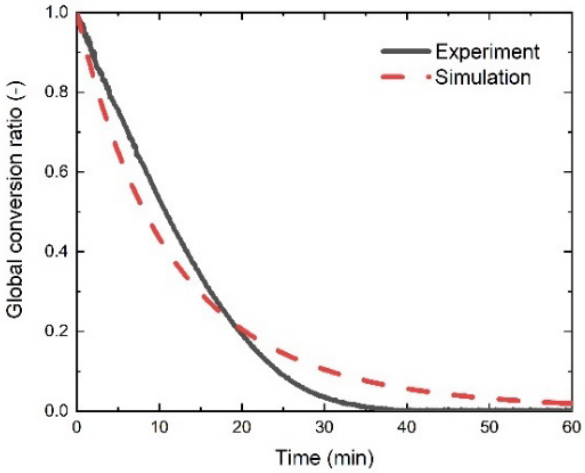

(b) $MnCl_2$-EG-Ni@C

Figure 7.12 Simulated and experimental ammonia conversion ratios (170, -20) versus time

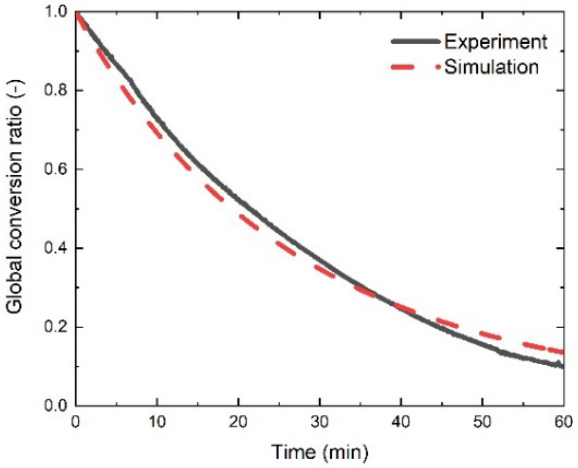

(a) $MnCl_2$-EG

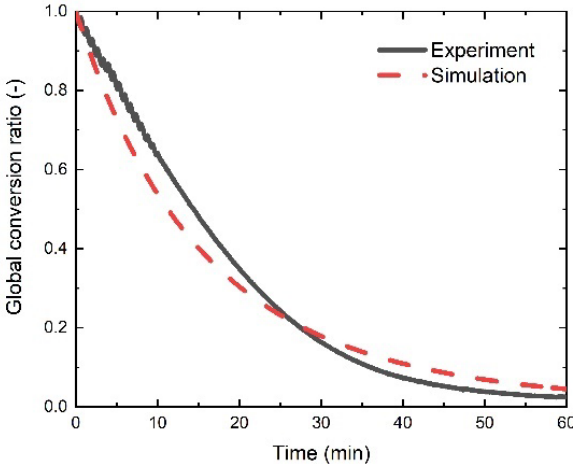

(b) $MnCl_2$-EG-Ni@C

Figure 7.13 Simulated and experimental ammonia conversion ratios (160, -20) versus time

The difference between the simulated and experimental ammonia conversion ratios is up to 0.049 in $MnCl_2$-EG. However, the gap between the modelled and real data is relatively big with the value up to 0.107 in $MnCl_2$-EG-Ni@C. It is due to the reactive sorbents' appreciable

contraction during desorption. The model is still good to be used into the cogeneration systems.

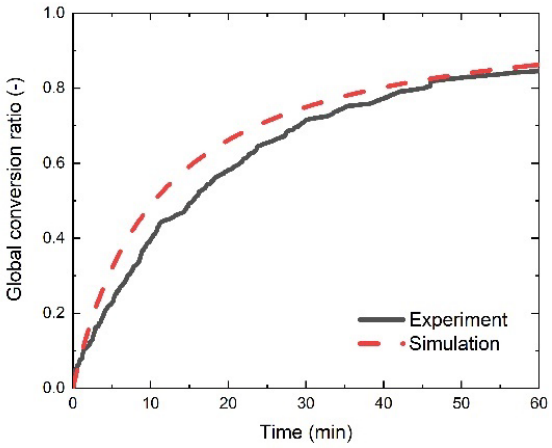

(a) $MnCl_2$-EG

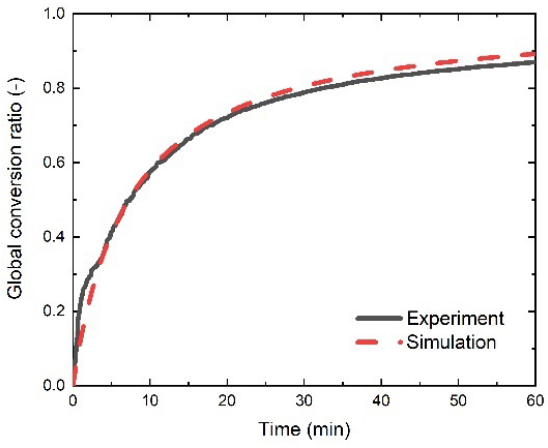

(b) $MnCl_2$-EG-Ni@C

Figure 7.14 Simulated and experimental ammonia conversion ratios (Water T, 0) versus time

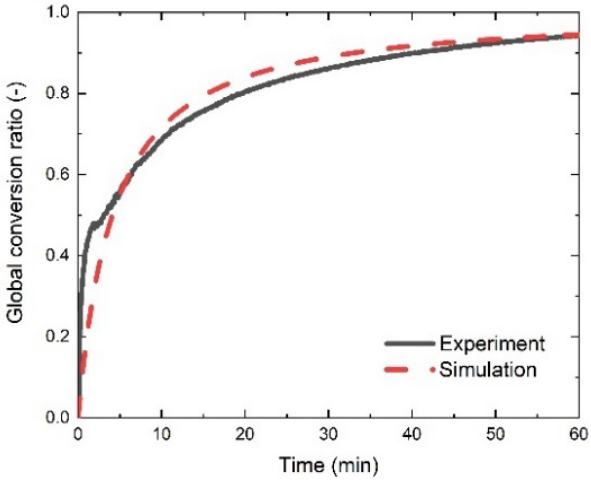

(a) $MnCl_2$-EG

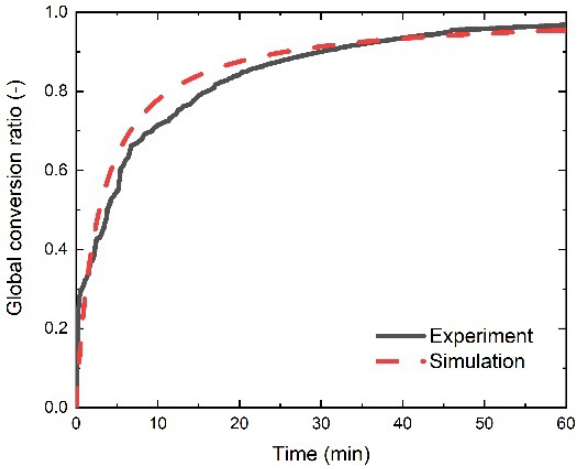

(b) $MnCl_2$-EG-Ni@C

Figure 7.15 Simulated and experimental ammonia conversion ratios (Water T, 10) versus time

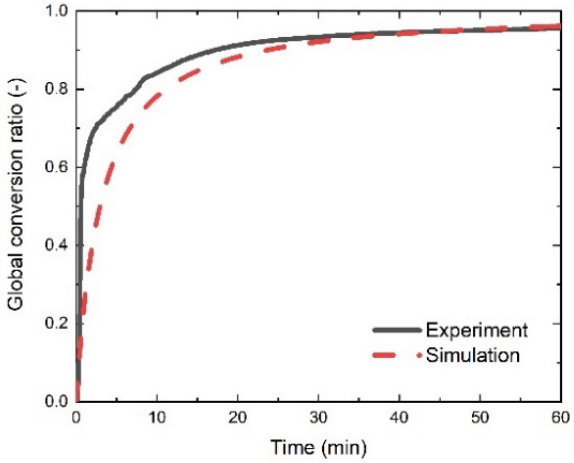

(a) $MnCl_2$-EG

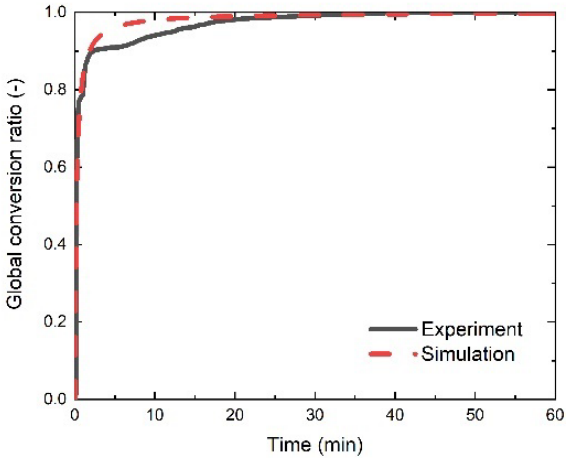

(b) $MnCl_2$-EG-Ni@C

Figure 7.16 Simulated and experimental ammonia conversion ratios (Water T, 20) versus time

The validation of adsorption models includes the 0 °C, 10 °C and 20 °C adsorption. The simulated and experimental data of ammonia conversion ratios are illustrated in Fig 6.19, Fig 7.14 and Fig 7.16, respectively.

Even there are some relatively large differences between the simulated and experimental ammonia conversion ratio, it is taken as a good agreement for adsorption kinetic models. The reason for the differences is the expansion during adsorption process. The average value of the difference between calculated and actual global conversion ratios is 0.038 for $MnCl_2$-EG or 0.027 for $MnCl_2$-EG-Ni@C.

7.3 AD-ORC using $MnCl_2$-EG-Ni@C

The kinetic models are used in AD-ORC to compare the enhancement by adding Ni@C into the conventional adsorbent. As ORC keeps a same performance during the reaction time, performance indicators including refrigeration, COP, thermal efficiency, exergy efficiency and waste heat emission are calculated and illustrated in Fig 7.17 to Fig 7.21. Due to the limitation in the design of the experimental test rig, the kinetic adsorption or desorption in Section 6.4 is not as fast as the kinetic models proposed by the previous researchers. Thus, Section 6.5 only compares between the cogenerations using the kinetic models found in the experiments.

7.3.1 Refrigeration

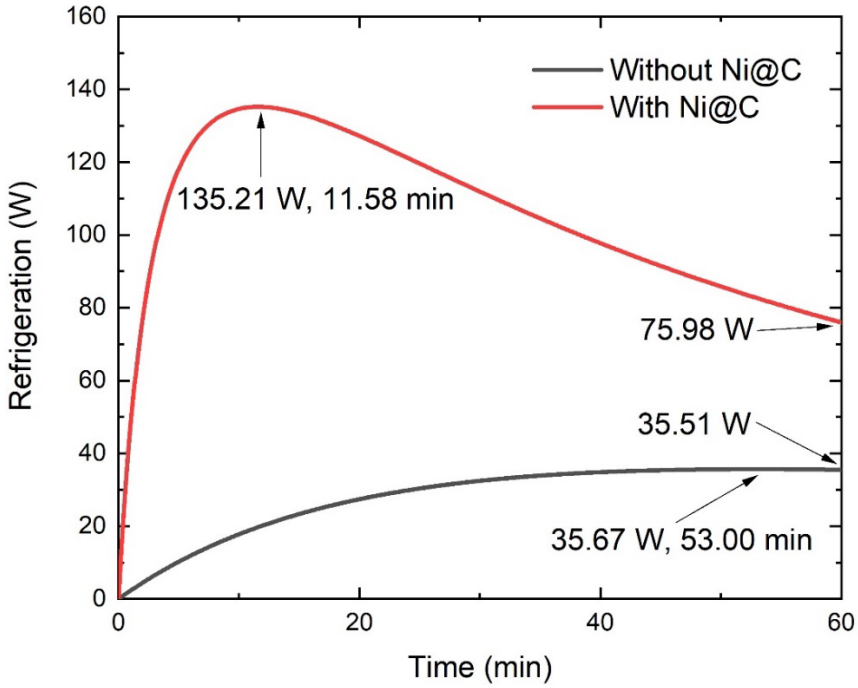

Figure 7.17 Comparison of refrigeration production in AD-ORC versus time

Fig 7.17 displays the refrigeration power generated by AD-ORC system using $MnCl_2$-EG and $MnCl_2$-EG-Ni@C.

The results show that using $MnCl_2$-EG-Ni@C can largely improve the refrigeration generated from AD-ORC system. The peak of the red line shows at 11.58 min with a refrigeration value of 135.21 W, obtained in the system using sorbents with Ni@C additives. Speculated by the acknowledge of the previous sections, there should be a peak for system applying conventional sorbents. The peak is not obvious in this illustration but found at 53.00 min through the data, with a value of 35.67 W. At the end of the time axis, the refrigeration of the system with Ni@C is 75.98 W, and the refrigeration of the system without Ni@C is 35.51 W. At the peak time of using $MnCl_2$-EG-Ni@C, the advancement made by the novel sorbents is 115.48 W while at 60 min, the improvement is 40.47 W.

7.3.2 COP

Fig 7.18 presents COP calculated from the models of AD-ORC system using the sorbents with or without Ni@C.

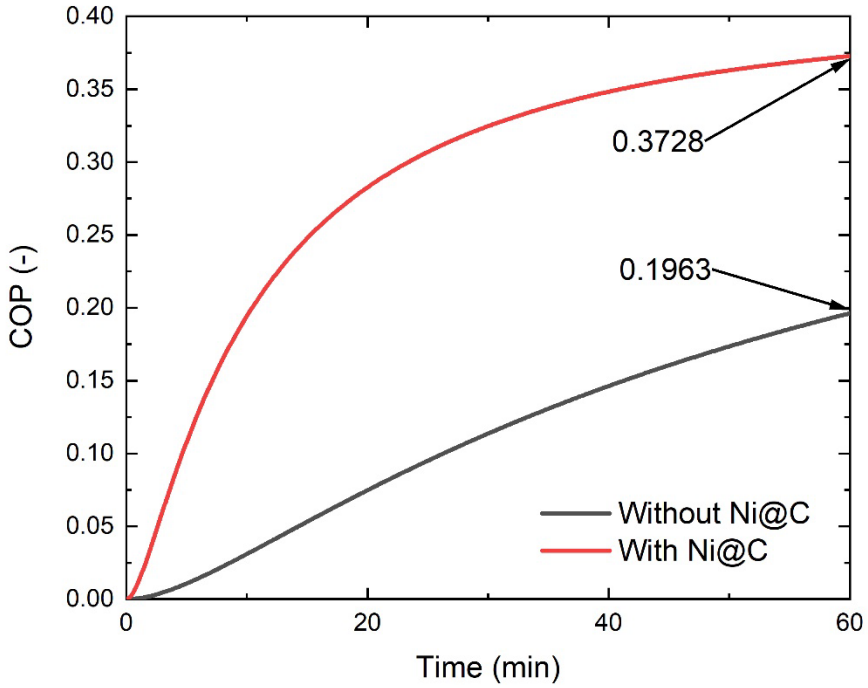

Figure 7.18 Comparison of COP in AD-ORC versus time

The result shows that COP of the cogeneration system is largely improved by adding Ni@C into conventional $MnCl_2$-EG sorbents. At the reaction time of 60 min, COP of the system using $MnCl_2$-EG is 0.1963, while COP of the system using $MnCl_2$-EG-Ni@C is 0.3728. The difference between the two values is 0.1765, which means the almost twice COP made by system using novel sorbents.

7.3.3 Thermal efficiency

Fig 7.19 shows the thermal efficiencies of AD-ORC system applying conventional or novel HTS.

The result shows that the thermal efficiency of the integrated AD-ORC system is largely enhanced by applying the novel sorbents with Ni@C. The peak of the system using $MnCl_2$-EG-Ni@C is 7.04 %, found at the reaction time of 11.58 min. The peak of AD-ORC utilising $MnCl_2$-EG is not apparent, compared with that of the red curve. However, referring to the calculated results, it is at the time of 53.00 min, with the value of 6.87 %. When the reaction time is 60 min, the thermal efficiency of the system using $MnCl_2$-EG-Ni@C is 6.94 %, while that of the system applying $MnCl_2$-EG is 6.87 %. The improvement at 60 min is 1.02 % of the original thermal efficiency, while the advancement at 11.58 min is 2.92 % of the thermal efficiency using the traditional sorbents.

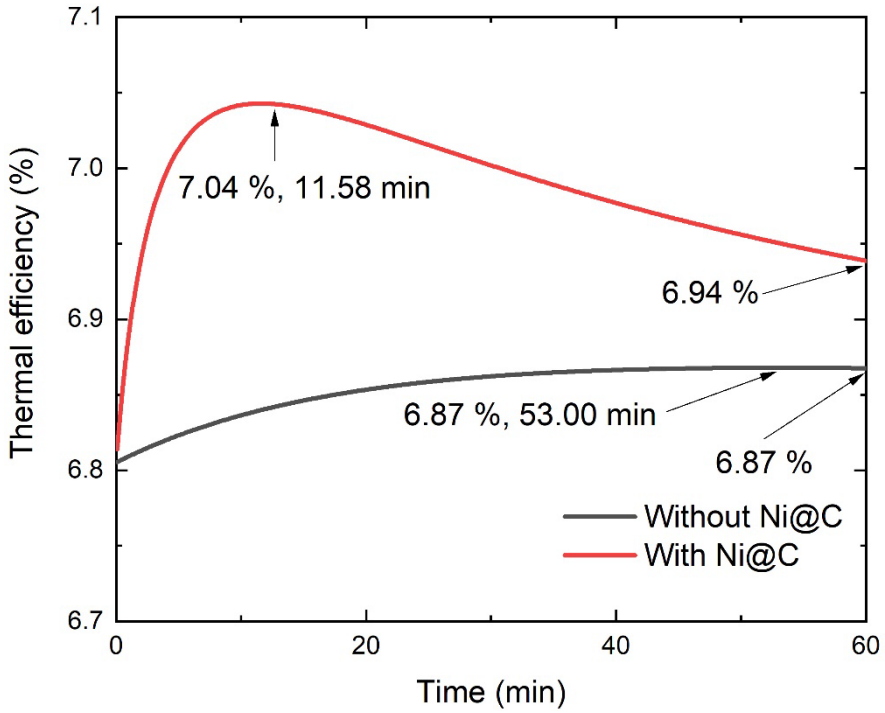

Figure 7.19 Comparison of thermal efficiency in AD-ORC versus time

7.3.4 Exergy efficiency

Fig 7.20 illustrates the exergy efficiency of AD-ORC utilising $MnCl_2$-EG and $MnCl_2$-EG-Ni@C.

The result shows that AD-ORC system with the novel sorbents has the improvement on the exergy efficiency. The red curve lies at the top of the figure, presenting a higher exergy efficiency among the illustrated time range. The peak of using Ni@C additives is 10.50 % at 11.58 min, while the peak of black curve is 10.24 % at the reaction time of 53.00 min. When the time is at 60 min, the exergy efficiency of the system using the novel sorbents is 10.35 %, while that of AD-ORC system utilising the conventional sorbents is 10.24 %. The enhancement made by the novel sorbents at 11.58 min is 2.94 % while that at 60 min is 1.07 %, compared with the original exergy efficiency.

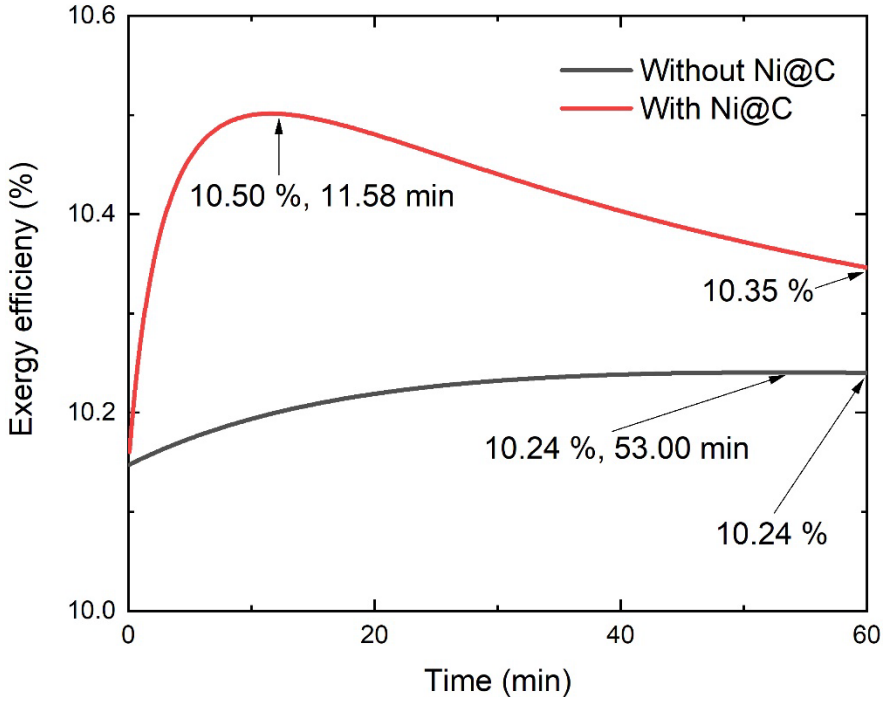

Figure 7.20 Comparison of exergy efficiency in AD-ORC versus time

7.3.5 Dump heat

Fig 7.21 is the comparison of the dump heat in AD-ORC systems using the sorbent with or without Ni@C.

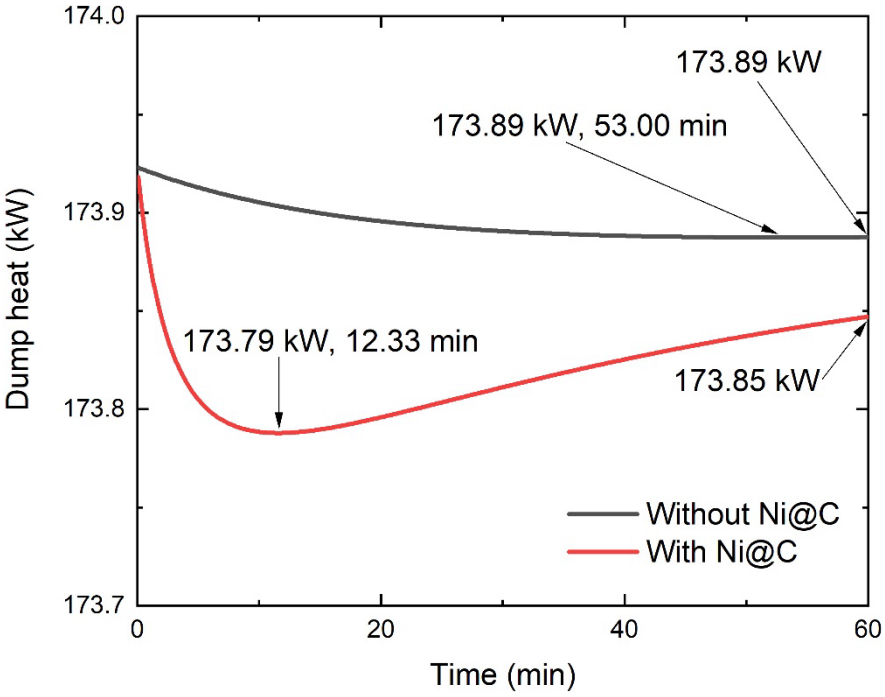

Figure 7.21 Comparison of the waste heat of AD-ORC versus time

The results demonstrate that AD-ORC system using the sorbent with Ni@C can reduce the dump heat of the system. The waste heat of AD-ORC has a lowest value of 173.79 kW at the reaction time of 12.33 min, applying $MnCl_2$-EG-Ni@C. Referring to the calculation results,

the minimum waste heat of the conventional sorbents is 173.89 kW, at 53.00 min. When the reaction has taken 60 min, the waste heat of AD-ORC is 173.89 kW utilising the conventional $MnCl_2$-EG, while that is 173.85 kW applying the novel sorbents. At 12.33 min, the advancement made by the novel sorbent is 0.11 kW, and at 60 min, the improvement is 0.04 kW.

7.4 Resorption-ORC using $MnCl_2$-EG-Ni@C

The two kinetic models are also used in resorption-ORC system to evaluate the improvement using the novel sorbents into the cogeneration systems.

7.4.1 Refrigeration

Fig 7.22 presents the refrigeration generated by resorption-ORC system, applying different adsorbents into the adsorption bed.

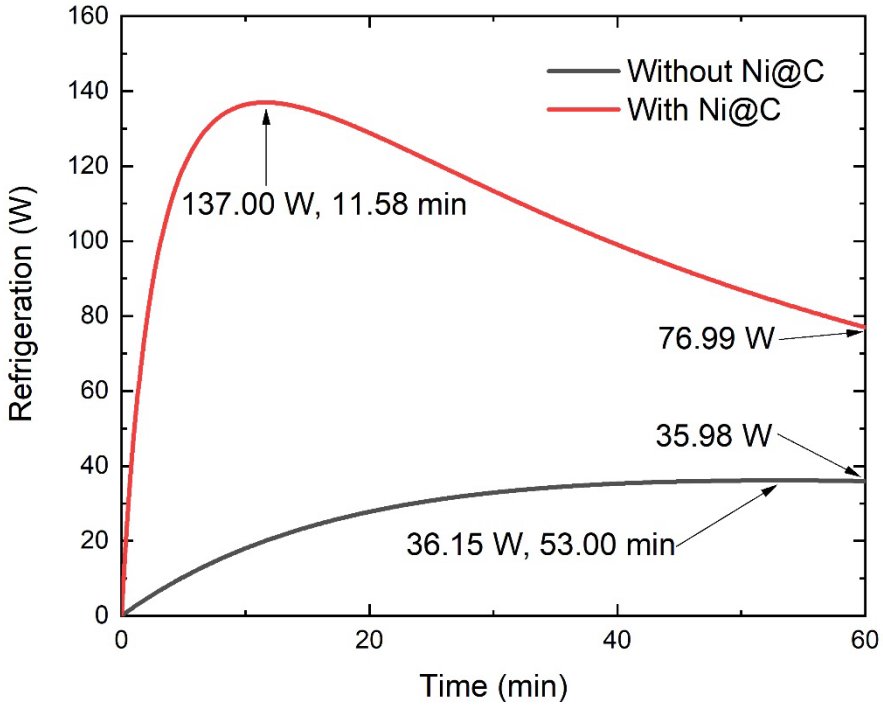

Figure 7.22 Refrigeration production versus time

The result shows that applying $MnCl_2$-EG-Ni@C can increase the refrigeration production of the system. A peak is found at 11.58 min, with the value of 137.00 W using the sorbent with Ni@C. The peak of black curve is 36.15 kW at 53.00 min, using the conventional HTS. When the reaction has taken 60 min, the refrigeration is 76.99 W of the red curve and 35.98 W of the black curve, respectively. The enhancement by adding Ni@C into $MnCl_2$-EG is 100.85 W at 11.58 min and 41.01 W at the reaction time of 60 min.

7.4.2 COP

Fig 7.23 illustrates COP of resorption-ORC system applying various sorbents.

The result reveals that COP of the cooling and power system is enhanced by applying the novel HTS. The red curve locates at the top of the figure, displaying a higher COP obtained from the simulation results. At the end of 60 min, COP of resorption-ORC system using $MnCl_2$-EG-Ni@C is 50.04 % while that of the system utilising $MnCl_2$-EG is 25.91 %. The result demonstrates the COP enhancement made by adding Ni@C into $MnCl_2$-EG is 24.13 %, when the sorbents react for 60 min.

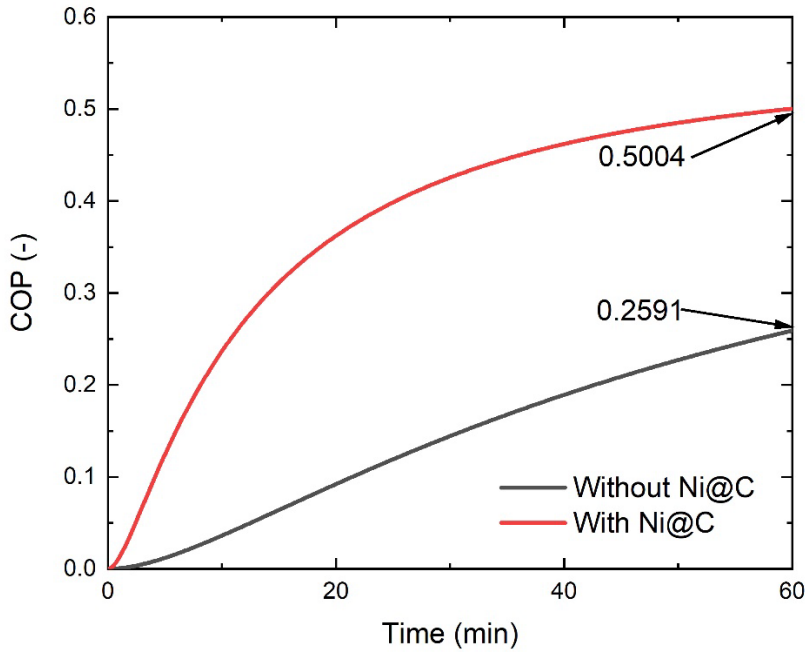

Figure 7.23 COP versus time

7.4.3 Thermal efficiency

Fig 7.24 displays the thermal efficiency of resorption-ORC system utilising sorbents with or without the additives of Ni@C.

The result demonstrates that the thermal efficiency of the system is improved by using the novel HTS. The red curve has a peak at 11.58 min with the value of 7.00 %. Meanwhile, the thermal efficiency of the black line is 6.84 %, which shows the improvement of 2.34 % of the original value, using the novel sorbents. The highest thermal efficiency of the black curve is 6.87 %, found at the reaction time of 53.00 min. At 60 min, the thermal efficiency is 6.94 % of the system using $MnCl_2$-EG-Ni@C, while that of resorption-ORC utilising $MnCl_2$-EG is 6.87 %, revealing the advancement made by the nanoparticles is 1.02 % of the original thermal efficiency.

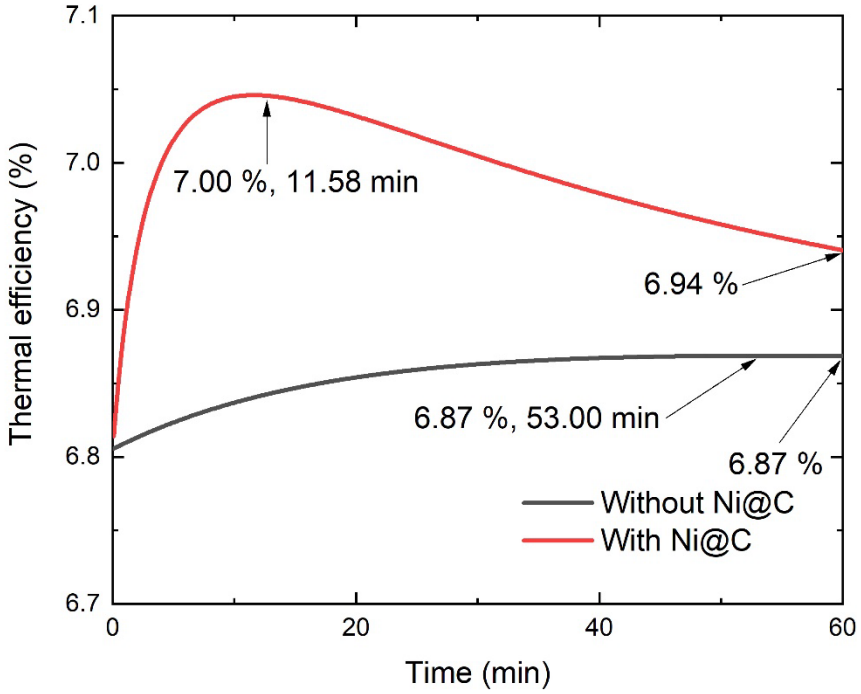

Figure 7.24 Thermal efficiency of cogeneration versus time

7.4.4 Exergy efficiency

Fig 7.25 shows the exergy efficiency of the resorption-ORC cogeneration system, applying $MnCl_2$-EG and $MnCl_2$-EG-Ni@C.

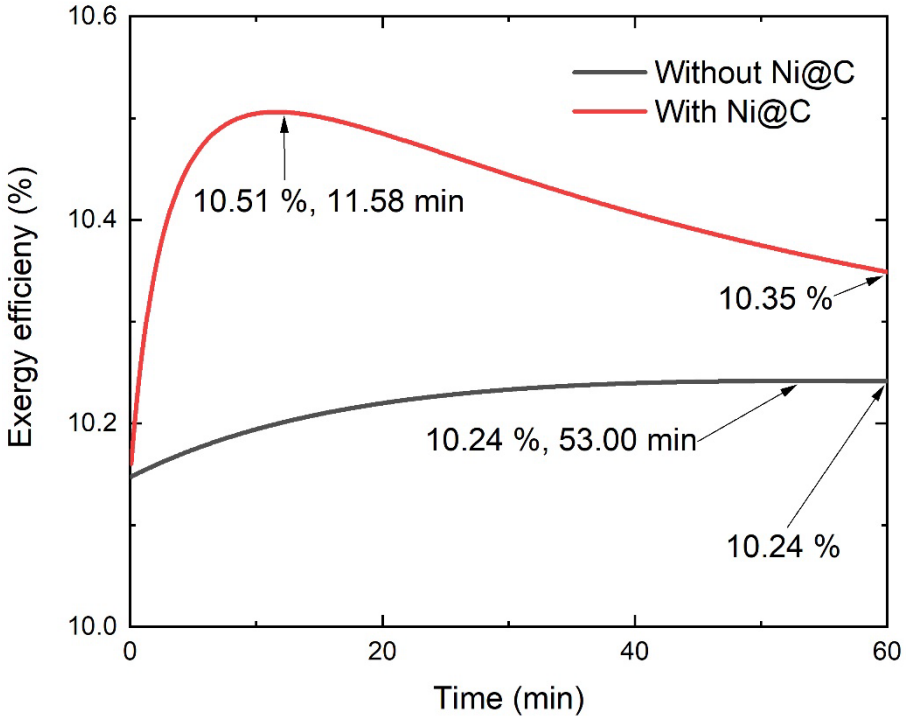

Figure 7.25 Exergy efficiency of cogeneration versus time

The results reveal that the exergy efficiency of the cogeneration system is largely improved using $MnCl_2$-EG-Ni@C in resorption-ORC system. The maximum exergy efficiency of resorption-ORC is 10.51 % at 11.58 min using the novel sorbents, while that of the cooling

and power system applying conventional HTS is 10.24 %, at the reaction time of 53.00 min. When the reaction takes 60 min, the exergy efficiency of the red curve is 10.35 %, while that of the black curve is 10.24 %, revealing the joint of Ni@C could improve 1.07 % of the thermal efficiency. The enhancement made by mixing Ni@C with the conventional MnCl2-EG is 3.04 % of the original value, at 11.58 min.

7.4.5 Dump heat

Fig 7.26 draws the dump heat of resorption-ORC cogeneration system utilising different sorbents with or without the additives of Ni@C.

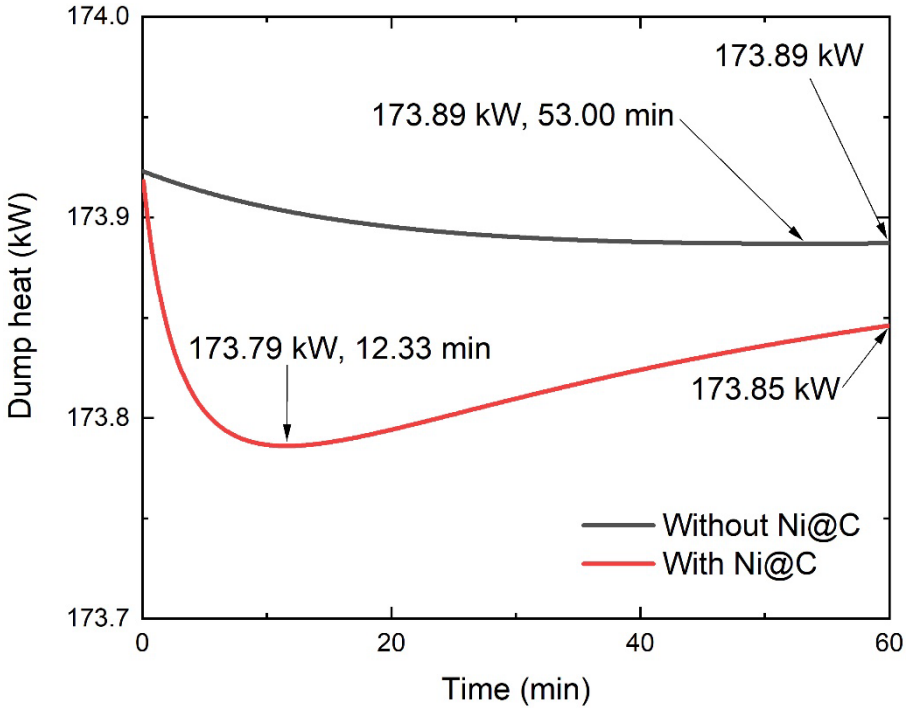

Figure 7.26 Waste heat of cogeneration versus time

The result shows that using $MnCl_2$-EG-Ni@C can reduce the dump heat of the system, compared with the result applying conventional HTS. The minimum dump heat is found at 12.33 min, with the value of 173.79 kW, using the novel sorbents. At the reaction time of 60 min, the dump heat is 173.89 kW of the system embedded with $MnCl_2$-EG, while that is 173.85 kW of resorption-ORC integrated with $MnCl_2$-EG-Ni@C. Moreover, the reduction of the dump heat is 0.04 kW while at 12.33 min, the reduction is 0.11 kW, by adding Ni@C into $MnCl_2$-EG. The reduction of the dump heat could be improved by using more adsorbents in the system.

7.5 Summary

Four variations of integrated ORC and adsorption/resorption cooling and power systems are simulated to evaluate and compare the performance of low-grade heat utilisation. A physical

model of the sorption unit based on the experiments results in Chapter 6 is applied in the simulation. Kinetic models are fitted and applied in the optimal systems to assess the influence of using the optimal novel sorbents.

- Using adsorption/resorption cycle as the first user of low-grade heat is preferred. It could increase the refrigeration production, thermal efficiency, and exergy efficiency of the cogeneration systems. At the peaks of the refrigeration, AD-ORC increases the refrigeration by 6.76 % at a 9.89 % earlier peak time, compared to ORC-AD. Resorption-ORC system increases the peak refrigeration by 8.76 % at a 58.04 % earlier time. The improvements of the other assessments are tiny. Besides, AD-ORC and resorption-ORC reduce the dump heat released to the environment. The operation timing is significant to optimise the system productions. However, COP of the system is slightly decreased in AD-ORC and resorption-ORC cooling and power systems.
- Substituting the adsorption units with the resorption units could improve the cogeneration performance of the system. The peak refrigeration production is increased by 74.40 % at a 65.27 % earlier peak time. COP of the system is enhanced by 91.71 % at 60 min. The peak thermal efficiency is improved by 3.10 %. The peak exergy efficiency is improved by 3.02 %. The dump heat of resorption-composed systems is also less than that from the systems contains the adsorption units, even the difference is tiny. The performance of ORC module is not influenced by the substitution of resorption.
- Using $MnCl_2$-EG-Ni@C can largely improve the cogeneration performance. The kinetic model found in the experiments are used in the simulation of AD-ORC and resorption ORC systems. At 60 min, the refrigeration and COP of the systems applying the novel sorbents could be about twice of the original one. A maximum improvement of the thermal efficiency can be made by 2.92 % and 2.34 % at 11.58 min in AD-ORC and resorption-ORC system, respectively. The reduction of the dump heat is up to 0.11 kW for both cogeneration systems. Besides, the cycle time is better to be controlled in 20 min for the system optimisation.

In summary, integrated resorption-ORC cooling and system using $MnCl_2$-EG-Ni@C is the optimal system found in the PhD project among all candidates. For a fixed heat source, adsorption or resorption units are preferred to be the first user instead of ORC. Besides, resorption is superior over adsorption cycles in the concept of being integrated with ORC to form a cogeneration system. Applying the novel sorbents of $MnCl_2$-EG-Ni@C can further improve the cogeneration performance based on the original resorption-ORC system.

The result indicates that it is feasible to using the resorption-ORC system to enhance the utilisation of low-grade heat. By the application of the novel sorbent, the conversion of low-grade thermal energy is largely enhanced. It is potential to apply the novel sorbent into other sorption-composed system for the improvement of the cogeneration or trigeneration performance.

Chapter 8 Conclusions and future working plans

The thesis has reported an investigation of the cascaded ORC and chemisorption cogeneration systems driven by low-grade heat. Literatures about the thermal driven power generation or cooling cycles have been reviewed and summarised. Chapter 3 reports a study of thermodynamic analysis of ORC-AD cooling and power system. In Chapter 4, the thermal-physical characteristics of the manufactured novel sorbents are tested and discussed. Chapter 5 is the experimental investigation on the sorption performance of the prepared sorbents. In Chapter 6, the comparison between ORC-AD, AD-ORC, ORC-resorption and resorption-ORC has been done using the physical model based on the experiments in Chapter 5. Moreover, the kinetic models found in the experiments are used in the simulation of AD-ORC and resorption-ORC system. In Chapter 7, chapters mentioned above are recapped to evaluate the feasibility of the combined system using the novel sorbents, and the recommendations for future researches are displayed as well.

8.1 Summary of the results

- A detailed background study has been done, reviewing existed heat conversion applications for power generation and refrigeration. The thermal-driven power generation systems have been studied from Carnot Cycle to various configuration of ORC. ORC with IHX and DLORC are two superior systems found by the author, as they are altered with simple but reasonable modifications based on the conventional ORC. However, ORC is a relatively mature technology after the long time explporations, which means that the potential to enhance ORC is quite limited. Integrating ORC with chemisorption technology to build the cogeneration systems remains attractive to the scientists. Apart from ORC, heat-dirven sorption refrigeration is a high-efficiency technology in converting low-grade heat into cooling power. To conquer the low working perfromance of chemical or physical sorption, composite sorbents are researched. Many studies have been done to improve the composite sorption performance, from the configuration, equipment and the sorbent materials. Inspired by the excellent thermal properties of the carbon coated metals, the author selects Ni/Al/Fe@C as the additional components to be mixed with conventional composite sorbents. LTS of $SrCl_2$-EG and HTS of $MnCl_2$-EG are selected from the background study of the conventional composite sorbents for their desirable properties.
- After the background study, the author is inspired by the idea of integrating ORC with chemisorption technologies to form a cascaded system which could meet the

requirement of power and cooling demanded at the same time by utilising the low-grade heat sources. Therefore, a system integrating ORC with adsorption system is built in Chapter 3 to assess whether the idea can be realised. ORC is the first user of low-grade heat. The simulation is written in MATLAB using the data base of REFPROP. The thermal analysis results include net power produced by ORC, refrigeration, SCP and COP of adsorption module, thermal and exergy efficiency and the dump heat of ORC and the cogeneration system. It is revealed that the increase of $\dot{m}_w$ and Δp_{pump} could improve the net power, the thermal and exergy efficiency, COP and the reduction of the sump heat. However, to enhance the refrigeration and COP, $\dot{m}_w$ and Δp_{pump} are advised to be reduced. For an optimisation of the performance, $\dot{m}_w$ and Δp_{pump} are 0.45 kg/s and 3200 kPa. In this case, the maximum net power, refrigeration, thermal efficiency, and exergy efficiency up is 13.21 kW, 95.7 W, 11.27 %, and 34.87 %, respectively. The minimum dump heat is 164.49 kW. The maximum COP is 0.5190. Therefore, the analysis proves the integrated ORC-chemisorption system improves the performance of ORC, given a fixed heat source. It is feasible to enhance the recovery of low-grade heat by the cascaded cogeneration system.

- As the concept of the integration has been proved to be feasible, more improvements are desired for a further enhancement of the low-grade thermal energy utilisation. According to the literature review, ORC is a relative mature technology with limited development potentials, so that chemisorption becomes the point to break through. Even the composite sorbents inherent the advantages of the chemical and physical sorbents, they still have the drawbacks of conglomeration and aggregation, which could result in the negative influence of the sorption performance. To conquer the disadvantage mentioned above, Chapter 4 reports the developed methodology of manufacturing sorbents with Ni/Al/Fe@C by inducing an extra ultrasonic bath and the different mixing medium in the mixing process. The manufactured sorbents are tested by SEM and EDX to observe the surface morphology. The SEM and EDX photos are analysed to justify the distribution and appearance of various substances. It is demonstrated that the innovative preparation procedures are useful for the uniformity of the sorbent. Later, the sorbents are sent to LFA, and the thermal diffusivity and conductivity are tested. The results reveal that the influence of the testing temperature, the salt mass ratio, the sample density and the additives of Ni/Al/Fe@C. The maximum thermal conductivity among the testing range is 2.90 W/(m·K) found in $MnCl_2$-EG-Al@C samples. The result demonstrates that the improvements of the thermal conductivities are made by all carbon coated metals, which also the shows

potential of the novel sorbents to enhance the comprehensive heat and mass transfer processes of the sorption performance.

- The thermal-physical tests in Chapter 4 proves the developed methodology a useful way to alleviate the problem of sorbent conglomeration and improve the uniformity and thermal property of the sorbents, which is potential to have positive influence on the heat and mass transfer processes of the sorption performance. Thus, the yielded sorbents are compressed into the adsorption reactor for the experimental investigation of the real sorption performance in Chapter 5. The relationship between the global conversion ratio and time is found and reported. Ni@C is found to be the optimal additive for both HTS and LTS, as it can make the maximum improvement of the sorption performance. The adsorption test of $SrCl_2$-EG-Ni@C could retrieve a maximum SCP of 5.35 kW/kg at 0.42 min, while that for $MnCl_2$-EG is 15.41 kW with Ni@C at 0.33 min when the evaporator is 20 ^oC. The result points out that the sorbents benefit from the nanoparticles, as the novel sorbents react faster than the conventional sorbents in most conditions. Chapter 5 shows the feasibility of applying the novel sorbents into integrated chemisorption systems to improve the overall energy efficiency.
- As the sorption performance is proved to be enhanced by the novel sorbents, Chapter 6 aims to use the experimental data to assess cogeneration performance of the optimal combination of the ORC and chemisorption systems. The dimensional data from the real rig in Chapter 5 is applied in the simulation models to build the physical model of adsorption units. The kinetic models found in Chapter 5 is then utilised into AD-ORC and resorption-ORC system to justify the influence made by the novel sorbents of $MnCl_2$-EG-Ni@C. The results indicate that AD/resorption-ORC system has a higher refrigeration production, thermal efficiency, and exergy efficiency of the cogeneration systems, compared with ORC-AD/resorption, respectively. Substituting adsorption module by resorption units improves the cogeneration performance of the system. Besides, using adsorption/resorption as the first heat source user reduces the waste of the heat source released. The waste heat from resorption-composed systems is also less than that from the systems contains the adsorption unit. The result also reflects that the operation timing is essential to optimise the system performance. At the end of Chapter 6, the enhancement using $SrCl_2$/$MnCl_2$-EG-Ni@C in resorption module is evaluated. The results show that the novel sorbents could largely enhance the different performance indicators. At 60 min, the refrigeration and COP of the systems applying the novel sorbents could be about twice of the original one. A maximum improvement

of the thermal efficiency can be achieved by 2.92 % and 2.34 % in AD-ORC and resorption-ORC system, respectively. The reduction of the dump heat is up to 0.11 kW for both cogeneration systems. Resorption-ORC system using $MnCl_2$-EG-Ni@C is the optimal system among all candidates. It is feasible to use it improve the utilisation of low-grade heat.

8.2 Recommendations for further work

Although resorption-ORC system using the novel sorbents appears to be a promising solution for cooling and power system driven by low-grade heat, further explorations and more efforts of the development are still required for it to become a realistic substitute to the conventional heat-driven energy technologies. The advantages and the challenges of the integrated ORC-chemisorption systems need to be studied further in detail. Some fundamental investigations of the operational characteristics and system performance of the integrated cogeneration cycles have been done in this PhD project. It is suggested that the further exploration could include three main directions:

- Configurations of integrated ORC-chemisorption system;
- Material used in sorption and ORC;
- Improvement of the experimental procedures and equipment.

8.2.1 Configurations of the integrated ORC-chemisorption system

The configuration of the integrated ORC-chemisorption system could be improved from the following aspects.

The simple ORC module studied in the thesis could be replaced by the developed variations as reported in the literature review, to increase the power generation efficiencies. For example, it could be added with an IHX to recover the heat bears in the expanded working fluid. Besides, the basic ORC could also be replaced by DLORC to fit the condition which provides two heat sources.

More connections between ORC and chemisorption cycles could be made rather than only cascaded utilisation of the heat source. For instance, the adsorption heat of LTS in the refrigeration mode could be recovered to ORC. One more example, in a dual source condition, resorption cycles can be used to recover the high temperature source. The low temperature source can be used to pre-heat ORC working fluid, and the rest heat of the high temperature source could be applied to evaporate the working fluid of ORC

Some enhancement could be made in the simulation of the cogeneration system. Reducing the ideal hypothesis in the simulation and improving the precision of the parameters could decrease the deviations between the reality and the simulation.

The economic evaluation based on various system configurations and the operational characteristics is also crucial to assess the feasibility of the cogeneration system, rather than just compare the system performance listed in the thesis.

8.2.2 Material used in sorption and ORC

While paying attention to the material, both the sorbent in sorption cycles and the working fluid in ORC could be explored for optimising the system performance.

The exploration of the sorbent could be divided by three areas, the chemical salt, the porous media and the additives. The chemical salts could be replaced by other chlorides such as $MgCl_2$ and $CaCl_2$. Even the chemical salts are limited in types, the porous medium could be substituted by other candidates. New porous medium could be explored by many treatments such as pre-heat treatment or acid-treatment. Recently studied materials which have been demonstrated to possess good heat and mass transfer properties can be utilised as the additives, such as other carbon coated metals or graphene.

The improvement could also be made by the working fluid selection. Referring to the different system configurations and operational conditions, exploring types of ORC fluid and select an optimal one can enhance the performance of ORC.

8.2.3 Improvement of the experiments

Some suggestions are given based on the experience of the experiments.

The equipment used in the experiments could be improved. The bottles used for ultrasonic bath should be substituted by the wide neck bottles for the convenience of being filled with EG. The pipework of the sorption rig should be shortened to reduce the heat loss. The thermostat connected to the oil bath could be replaced by one with a large cooling capacity, rather than cool the thermal fluid by exchanging heat with tap water. It could reduce the influence caused by the adsorption heat which is not removed quickly in the PhD project.

More tests of material thermal-physical properties could be done to ensure the reason for the performance results, corresponding to the heat and mass transfer in related testing conditions. The permeability of the sorbent material could be done for the evaluation of the mass transfer process. The densities and testing conditions of the samples can vary in a larger range. Prediction models could be built based on the discovery of the thermal-physical property

tests. Moreover, the residue of the sorbent after the sorption performance tests could be tested again for the thermal-physical properties to compare the difference caused by the sorption cycles.

Experimental investigation is suggested to be done on the proposed system to verify the practical performance. A test system should be constructed based on the system configuration.

Reference

[1] D. L. Klass, "Chapter 1 - Energy Consumption, Reserves, Depletion, and Environmental Issues," in *Biomass for Renewable Energy, Fuels, and Chemicals*San Diego: Academic Press, 1998, pp. 1-27.

[2] I. Sarbu and C. Sebarchievici, "General review of solar-powered closed sorption refrigeration systems," *Energy Conversion and Management,* vol. 105, pp. 403-422, 2015/11/15/ 2015.

[3] T. Chen, W. Zhuge, Y. Zhang, and L. Zhang, "A novel cascade organic Rankine cycle (ORC) system for waste heat recovery of truck diesel engines," *Energy Conversion and Management,* vol. 138, pp. 210-223, 2017/04/15/ 2017.

[4] J. Yang, J. Li, Z. Yang, and Y. Duan, "Thermodynamic analysis and optimization of a solar organic Rankine cycle operating with stable output," *Energy Conversion and Management,* vol. 187, pp. 459-471, 2019/05/01/ 2019.

[5] J. Li, Q. Liu, Z. Ge, Y. Duan, and Z. Yang, "Thermodynamic performance analyses and optimization of subcritical and transcritical organic Rankine cycles using R1234ze(E) for 100–200°C heat sources," *Energy Conversion and Management,* vol. 149, pp. 140-154, 2017/10/01/ 2017.

[6] R. Mastrullo, A. W. Mauro, R. Revellin, and L. Viscito, "Modeling and optimization of a shell and louvered fin mini-tubes heat exchanger in an ORC powered by an internal combustion engine," *Energy Conversion and Management,* vol. 101, pp. 697-712, 2015/09/01/ 2015.

[7] W. Xu, J. Zhang, L. Zhao, S. Deng, and Y. Zhang, "Novel experimental research on the compression process in organic Rankine cycle (ORC)," *Energy Conversion and Management,* vol. 137, pp. 1-11, 2017/04/01/ 2017.

[8] B. A. Landry, " Utilization of Waste Heat " *Science,* vol. 117, p. 3, 1953.

[9] P. Taylor, "Energy Technology Perspectives 2010," *Scenarios & strategies to,* vol. 2050, 2010.

[10] J. Deng, R. Z. Wang, and G. Y. Han, "A review of thermally activated cooling technologies for combined cooling, heating and power systems," *Progress in Energy and Combustion Science,* vol. 37, no. 2, pp. 172-203, 4// 2011.

[11] G. Grossman and A. Johannsen, "Solar cooling and air conditioning," *Progress in Energy and Combustion Science,* vol. 7, no. 3, pp. 185-228, 1981/01/01 1981.

[12] K. Sumathy, K. H. Yeung, and L. Yong, "Technology development in the solar adsorption refrigeration systems," *Progress in Energy and Combustion Science,* vol. 29, no. 4, pp. 301-327, // 2003.

[13] Y. A. Cengel and M. A. Boles, "Thermodynamics: an engineering approach," *Sea,* vol. 1000, p. 8862, 2002.

[14] Y. Lu, L. Wang, G. Tian, and T. Roskilly, "Study on a small scale solar powered organic Rankine cycle utilizing Scroll expander," 2012.

[15] T.-C. Hung, T. Y. Shai, and S. K. Wang, "A review of organic Rankine cycles (ORCs) for the recovery of low-grade waste heat," *Energy,* vol. 22, no. 7, pp. 661-667, 1997.

[16] D. S. L. Cardwell, *From Watt to Clausius: The rise of thermodynamics in the early industrial age*. Cornell University Press, 1971.

[17] J. W. Jameson, "ON THE PERFORMANCE OF THE SCREW STEAM SHIPSAHEL', FITTED WITH DU TREMBLEY'S COMBINED-VAPOUR ENGINE, AND OF THE SISTER SHIPOASIS'FITTED WITH STEAM-ENGINES WORKED EXPANSIVELY, AND PROVIDED WITH PARTIAL SURFACE CONDENSATION.(INCLUDING APPENDICES AND PLATE)," in *Minutes of the Proceedings of the Institution of Civil Engineers,* 1859, vol. 18, pp. 233-252: Thomas Telford-ICE Virtual Library.

[18] A. Parsad, "Field testing of a 600kW organic Rankine cycle waste recovery," *Energy Technology: Proceedings of the Energy Technology Conference*, vol. 1, pp. 462-494, 1980.
[19] E. Macchi and M. Astolfi, Organic Rankine Cycle (ORC) Power Systems : Technologies and Applications: Elsevier Science, 2016. [Online]. Available: http://ncl.eblib.com/patron/FullRecord.aspx?p=4659388.
[20] Y. Lu, "A resorption cogeneration cycle for power and refrigeration," Ph. D. Ph. D., Sir Joseph Swan Centre for Energy Research, University of Newcastle upon Tyne, 2016.
[21] A. I. Kalina, "Combined-cycle system with novel bottoming cycle," *Journal of engineering for gas turbines and power*, vol. 106, no. 4, pp. 737-742, 1984.
[22] X. Zhang, M. He, and Y. Zhang, "A review of research on the Kalina cycle," *Renewable and sustainable energy reviews*, vol. 16, no. 7, pp. 5309-5318, 2012.
[23] H. Chen, D. Y. Goswami, and E. K. Stefanakos, "A review of thermodynamic cycles and working fluids for the conversion of low-grade heat," *Renewable and sustainable energy reviews*, vol. 14, no. 9, pp. 3059-3067, 2010.
[24] P. Bombarda, C. M. Invernizzi, and C. Pietra, "Heat recovery from Diesel engines: A thermodynamic comparison between Kalina and ORC cycles," *Applied Thermal Engineering*, vol. 30, no. 2–3, pp. 212-219, 2// 2010.
[25] H. M. Leibowitz and H. A. Micak, "Design of a 2MW Kalina cycle binary module for installation in Husavik, Iceland," *Transactions-Geothermal Resources Council*, pp. 75-80, 1999.
[26] D. Y. Goswami and F. Xu, "Analysis of a new thermodynamic cycle for combined power and cooling using low and mid temperature solar collectors," *Journal of Solar Energy Engineering*, vol. 121, no. 2, pp. 91-97, 1999.
[27] F. Xu, D. Y. Goswami, and S. S. Bhagwat, "A combined power/cooling cycle," *Energy*, vol. 25, no. 3, pp. 233-246, 2000.
[28] A. A. Hasan, D. Y. Goswami, and S. Vijayaraghavan, "First and second law analysis of a new power and refrigeration thermodynamic cycle using a solar heat source," *Solar Energy*, vol. 73, no. 5, pp. 385-393, 11// 2002.
[29] S. Lu and D. Y. Goswami, "Optimization of a novel combined power/refrigeration thermodynamic cycle," in *ASME Solar 2002: International Solar Energy Conference*, 2002, pp. 75-82: American Society of Mechanical Engineers.
[30] A. A. Hasan and D. Y. Goswami, "Exergy analysis of a combined power and refrigeration thermodynamic cycle driven by a solar heat source," *Journal of Solar Energy Engineering*, vol. 125, no. 1, pp. 55-60, 2003.
[31] H. Xi, M.-J. Li, C. Xu, and Y.-L. He, "Parametric optimization of regenerative organic Rankine cycle (ORC) for low grade waste heat recovery using genetic algorithm," *Energy*, vol. 58, pp. 473-482, 2013/09/01/ 2013.
[32] G. Li, "Organic Rankine cycle performance evaluation and thermoeconomic assessment with various applications part I: Energy and exergy performance evaluation," *Renewable and Sustainable Energy Reviews*, vol. 53, pp. 477-499, 2016/01/01/ 2016.
[33] Y. Zhou, Y. Wu, F. Li, and L. Yu, "Performance analysis of zeotropic mixtures for the dual-loop system combined with internal combustion engine," *Energy Conversion and Management*, vol. 118, pp. 406-414, 2016/06/15/ 2016.
[34] N. Nazari, P. Heidarnejad, and S. Porkhial, "Multi-objective optimization of a combined steam-organic Rankine cycle based on exergy and exergo-economic analysis for waste heat recovery application," *Energy Conversion and Management*, vol. 127, pp. 366-379, 2016/11/01/ 2016.
[35] G. Shu, G. Yu, H. Tian, H. Wei, X. Liang, and Z. Huang, "Multi-approach evaluations of a cascade-Organic Rankine Cycle (C-ORC) system driven by diesel engine waste

heat: Part A – Thermodynamic evaluations," *Energy Conversion and Management,* vol. 108, pp. 579-595, 2016/01/15/ 2016.
[36] B. F. Tchanche, G. Papadakis, G. Lambrinos, and A. Frangoudakis, "Fluid selection for a low-temperature solar organic Rankine cycle," *Applied Thermal Engineering,* vol. 29, no. 11-12, pp. 2468-2476, 2009.
[37] F. Heberle and D. Brüggemann, "Exergy based fluid selection for a geothermal Organic Rankine Cycle for combined heat and power generation," *Applied Thermal Engineering,* vol. 30, no. 11-12, pp. 1326-1332, 2010.
[38] D. Wei, X. Lu, Z. Lu, and J. Gu, "Performance analysis and optimization of organic Rankine cycle (ORC) for waste heat recovery," *Energy conversion and Management,* vol. 48, no. 4, pp. 1113-1119, 2007.
[39] M. Pons and J. J. Guilleminot, "Design of an Experimental Solar-Powered, Solid-Adsorption Ice Maker," *Journal of Solar Energy Engineering,* vol. 108, no. 4, pp. 332-337, 1986.
[40] G. Cacciola and G. Restuccia, "Progress on adsorption heat pumps," *Heat Recovery Systems and CHP,* vol. 14, no. 4, pp. 409-420, 1994/07/01 1994.
[41] M. Pons *et al.*, "Thermodynamic based comparison of sorption systems for cooling and heat pumping: Comparaison des performances thermodynamique des systèmes de pompes à chaleur à sorption dans des applications de refroidissement et de chauffage," *International Journal of Refrigeration,* vol. 22, no. 1, pp. 5-17, 1// 1999.
[42] S. Mauran, P. Prades, and F. L'Haridon, "Special Issue Solid Sorption Refrigeration and Heat Pumps Heat and mass transfer in consolidated reacting beds for thermochemical systems," *Heat Recovery Systems and CHP,* vol. 13, no. 4, pp. 315-319, 1993/07/01 1993.
[43] R. Z. Wang, "Adsorption refrigeration research in Shanghai Jiao Tong University," *Renewable and Sustainable Energy Reviews,* vol. 5, no. 1, pp. 1-37, 3// 2001.
[44] B. B. Saha, I. I. El-Sharkawy, S. Koyama, J. B. Lee, and K. Kuwahara, "Waste heat driven multi-bed adsorption chiller: heat exchangers overall thermal conductance on chiller performance," *Heat Transfer Engineering,* vol. 27, no. 5, pp. 80-87, 2006.
[45] R. E. Critoph, "Proceedings of the Conference on Porosity and Carbon materials: Measurements and applications Activated carbon adsorption cycles for refrigeration and heat pumping," *Carbon,* vol. 27, no. 1, pp. 63-70, 1989/01/01 1989.
[46] K. Wang, J. Y. Wu, R. Z. Wang, and L. W. Wang, "Composite adsorbent of CaCl 2 and expanded graphite for adsorption ice maker on fishing boats," *International Journal of Refrigeration,* vol. 29, no. 2, pp. 199-210, 2006.
[47] D. C. Wang, "Development of a silica gel–water adsorption chiller and study of the characteristics of adsorption systems driven by variable heat source," *Shanghai Jiao Tong University,* 2005.
[48] R. G. Oliveira and R. Z. Wang, "A consolidated calcium chloride-expanded graphite compound for use in sorption refrigeration systems," *Carbon,* vol. 45, no. 2, pp. 390-396, 2007.
[49] H. Bao *et al.*, "Chemisorption cooling and electric power cogeneration system driven by low grade heat," *Energy,* vol. 72, pp. 590-598, 2014.
[50] R. Wang, L. Wang, and J. Wu, *Adsorption Refrigeration Technology: Theory and Application*. 2014.
[51] R. E. Critoph and R. Vogel, "Possible adsorption pairs for use in solar cooling," *International Journal of Ambient Energy,* vol. 7, no. 4, pp. 183-190, 1986.
[52] M. Ron, "A hydrogen heat pump as a bus air conditioner," *Journal of the Less Common Metals,* vol. 104, no. 2, pp. 259-278, 1984/12/17 1984.
[53] M. Pons and P. Grenier, "Experimental Data on a Solar-Powered Ice Maker Using Activated Carbon and Methanol Adsorption Pair," *Journal of Solar Energy Engineering,* vol. 109, no. 4, pp. 303-310, 1987.

[54] N. Douss and F. Meunier, "Effect of operating temperatures on the coefficient of performance of active carbon-methanol systems," *Heat Recovery Systems and CHP,* vol. 8, no. 5, pp. 383-392, 1988/01/01 1988.
[55] G. Restuccia, V. Recupero, G. Cacciola, and M. Rothmeyer, "Zeolite heat pump for domestic heating," *Energy,* vol. 13, no. 4, pp. 333-342, 1988/04/01 1988.
[56] A. Hajji, W. M. Worek, and Z. Lavan, "Dynamic Analysis of a Closed-Cycle Solar Adsorption Refrigerator Using Two Adsorbent-Adsorbate Pairs," *Journal of Solar Energy Engineering,* vol. 113, no. 2, pp. 73-79, 1991.
[57] Y. Zhong, R. E. Critoph, and R. Thorpe, "Evaluation of the performance of solid sorption refrigeration systems using carbon dioxide as refrigerant," *Applied Thermal Engineering,* vol. 26, no. 16, pp. 1807-1811, 11// 2006.
[58] Z. Tamainot-Telto and R. E. Critoph, "Adsorption refrigerator using monolithic carbon-ammonia pair," *International Journal of Refrigeration,* vol. 20, no. 2, pp. 146-155, 3// 1997.
[59] O. C. Iloeje, A. N. Ndili, and S. O. Enibe, "Computer simulation of a CaCl2 solid-adsorption solar refrigerator," *Energy,* vol. 20, no. 11, pp. 1141-1151, // 1995.
[60] N. C. Srivastava and I. W. Eames, "A review of adsorbents and adsorbates in solid–vapour adsorption heat pump systems," *Applied Thermal Engineering,* vol. 18, no. 9–10, pp. 707-714, 9/1/ 1998.
[61] Y. Kato, M. Yamada, T. Kanie, and Y. Yoshizawa, "Calcium oxide/carbon dioxide reactivity in a packed bed reactor of a chemical heat pump for high-temperature gas reactors," *Nuclear Engineering and Design,* vol. 210, no. 1–3, pp. 1-8, 12// 2001.
[62] J. J. Guilleminot, F. Meunier, and J. Pakleza, "Heat and mass transfer in a non-isothermal fixed bed solid adsorbent reactor: a uniform pressure-non-uniform temperature case," *International Journal of Heat and Mass Transfer,* vol. 30, no. 8, pp. 1595-1606, 1987/08/01 1987.
[63] J. J. Guilleminot, A. Choisier, J. B. Chalfen, S. Nicolas, and J. L. Reymoney, "Special Issue Solid Sorption Refrigeration and Heat Pumps Heat transfer intensification in fixed bed adsorbers," *Heat Recovery Systems and CHP,* vol. 13, no. 4, pp. 297-300, 1993/07/01 1993.
[64] N. Mazet, M. Amouroux, and B. Spinner, "Analysis and experimental study of the transformation of a non-isothermal solid/gas reacting medium," *Chemical Engineering Communications,* vol. 99, no. 1, pp. 155-174, 1991.
[65] L. Marletta, G. Maggio, A. Freni, M. Ingrasciotta, and G. Restuccia, "A non-uniform temperature non-uniform pressure dynamic model of heat and mass transfer in compact adsorbent beds," *International Journal of Heat and Mass Transfer,* vol. 45, no. 16, pp. 3321-3330, 7// 2002.
[66] L. L. Vasiliev, D. A. Mishkinis, and L. L. Vasiliev Jr, "Multi-effect complex compound/ammonia sorption machines," in *Proceedings of the International Sorption Heat Pump Conferences, Montreal, Canada*, 1996, pp. 3-8.
[67] T. Li, R. Wang, and L. Wang, "High-efficient thermochemical sorption refrigeration driven by low-grade thermal energy," *Chinese Science Bulletin,* vol. 54, no. 6, pp. 885-905, 2009.
[68] B. Cerkvenik, A. Poredoš, and F. Ziegler, "Influence of adsorption cycle limitations on the system performance," *International Journal of Refrigeration,* vol. 24, no. 6, pp. 475-485, 9// 2001.
[69] F. Ziegler, "Recent developments and future prospects of sorption heat pump systems," *International Journal of Thermal Sciences,* vol. 38, no. 3, pp. 191-208, 3// 1999.
[70] E. E. Anyanwu, "Review of solid adsorption solar refrigerator I: an overview of the refrigeration cycle," *Energy Conversion and Management,* vol. 44, no. 2, pp. 301-312, 1// 2003.

[71] L. Luo and M. Feidt, "Thermodynamics of adsorption cycles: a theoretical study," *Heat transfer engineering*, vol. 13, no. 4, pp. 19-31, 1992.
[72] Y. Teng, R. Z. Wang, and J. Y. Wu, "Study of the fundamentals of adsorption systems," *Applied Thermal Engineering*, vol. 17, no. 4, pp. 327-338, 1997.
[73] W. Wongsuwan, S. Kumar, P. Neveu, and F. Meunier, "A review of chemical heat pump technology and applications," *Applied Thermal Engineering*, vol. 21, no. 15, pp. 1489-1519, 2001.
[74] C. Duenas, I. Pilatowsky, R. J. Romero, and A. Oskam, "Dynamic study of the thermal behaviour of solar thermochemical refrigerator: barium chloride-ammonia for ice production," *Solar energy materials and solar cells*, vol. 70, no. 3, pp. 401-413, 2001.
[75] A. Hajji and S. Khalloufi, "Improving the performance of adsorption heat exchangers using a finned structure," *International journal of heat and mass transfer*, vol. 39, no. 8, pp. 1677-1686, 1996.
[76] Q. Wang, X. Gao, J. Y. Xu, A. S. Maiga, and G. M. Chen, "Experimental investigation on a fluidized-bed adsorber/desorber for the adsorption refrigeration system," *International Journal of Refrigeration*, vol. 35, no. 3, pp. 694-700, 2012.
[77] R. Z. Wang, J. Y. Wu, Y. X. Xu, Y. Teng, and W. Shi, "Experiment on a continuous heat regenerative adsorption refrigerator using spiral plate heat exchanger as adsorbers," *Applied thermal engineering*, vol. 18, no. 1, pp. 13-23, 1998.
[78] F. Ziegler and P. Satzger, "Increase of the efficiency of the heat transfer phase in solid sorption or reaction systems," *International journal of thermal sciences*, vol. 44, no. 12, pp. 1115-1122, 2005.
[79] L. L. Vasiliev, "Heat pipes in modern heat exchangers," *Applied thermal engineering*, vol. 25, no. 1, pp. 1-19, 2005.
[80] R. Z. Wang, "Efficient adsorption refrigerators integrated with heat pipes," *Applied Thermal Engineering*, vol. 28, no. 4, pp. 317-326, 2008.
[81] L. L. Vasiliev, D. A. Mishkinis, and A. A. Antukh, "Solar–gas solid sorption heat pump," *Applied Thermal Engineering*, vol. 21, no. 5, pp. 573-583, 2001.
[82] L. L. Vasiliev, "Sorption refrigerators with heat pipe thermal control," in *Proceedings of ICCR*, 2003, pp. 405-415.
[83] L. W. Wang, R. Z. Wang, Z. Z. Xia, and J. Y. Wu, "Studies on heat pipe type adsorption ice maker for fishing boats," *international journal of refrigeration*, vol. 31, no. 6, pp. 989-997, 2008.
[84] T. X. Li, R. Z. Wang, L. W. Wang, and Z. S. Lu, "Experimental investigation of an innovative dual-mode chemisorption refrigeration system based on multifunction heat pipes," *international journal of refrigeration*, vol. 31, no. 6, pp. 1104-1112, 2008.
[85] K. Wang, "Performance and Application of CaCl 2/Expanded Graphite Adsorbent for Double Heat Pipes Type Refrigeration," *Shanghai Jiao Tong University, Shanghai*, 2007.
[86] R. Wang and L. Wang, "Adsorption refrigeration-green cooling driven by low grade thermal energy," *Chinese Science Bulletin*, vol. 50, no. 3, pp. 193-204, 2005.
[87] S. He, R. Z. Wang, Z. Z. Xia, B. Tian, and L. W. Wang, "An innovative falling film evaporative cooling with recirculation driven by low-grade heat," *Journal of Thermal Science and Engineering Applications*, vol. 1, no. 4, p. 045001, 2009.
[88] B. Choudhury, B. B. Saha, P. K. Chatterjee, and J. P. Sarkar, "An overview of developments in adsorption refrigeration systems towards a sustainable way of cooling," *Applied Energy*, vol. 104, pp. 554-567, 2013.
[89] T. X. Li, R. Z. Wang, J. K. Kiplagat, L. W. Wang, and R. G. Oliveira, "Thermodynamic study of a combined double-way solid–gas thermochemical sorption refrigeration cycle," *International journal of refrigeration*, vol. 32, no. 7, pp. 1570-1578, 2009.

[90] F. Meunier, "Solid sorption heat powered cycles for cooling and heat pumping applications," *Applied Thermal Engineering,* vol. 18, no. 9–10, pp. 715-729, 9/1/ 1998.
[91] A. B. Dai, "Coordination Chemistry," *Volume 12 of series of inorganic Chemistry,* 1987.
[92] R. P. H. Gasser and G. Ehrlich, "An introduction to chemisorption and catalysis by metals," *Physics Today,* vol. 40, p. 128, 1987.
[93] E. Willers and M. Groll, "Evaluation of metal hydride machines for heat pumping and cooling applications: Evaluation des machines à hydrure métallique dans les applications de pompes à chaleur et de refroidissement," *International Journal of Refrigeration,* vol. 22, no. 1, pp. 47-58, 1999.
[94] T. Li, R. Wang, and J. K. Kiplagat, "A target‐oriented solid‐gas thermochemical sorption heat transformer for integrated energy storage and energy upgrade," *AIChE Journal,* vol. 59, no. 4, pp. 1334-1347, 2013.
[95] M. Lebrun and P. Neveu, "Conception, simulation, dimensioning and testing of an experimental chemical heat pump," *ASHRAE Trans,* vol. 98, no. 1, pp. 3483-3495, 1992.
[96] B. Spinner, "Special Issue Solid Sorption Refrigeration and Heat Pumps Ammonia-based thermochemical transformers," *Heat Recovery Systems and CHP,* vol. 13, no. 4, pp. 301-307, 1993/07/01 1993.
[97] E. Lepinasse, V. Goetz, and G. Crosat, "Modelling and experimental investigation of a new type of thermochemical transformer based on the coupling of two solid-gas reactions," *Chemical Engineering and Processing: Process Intensification,* vol. 33, no. 3, pp. 125-134, 1994/07/01 1994.
[98] H. K. Choi, P. Neveu, and B. Spinner, "System modeling and parameter effects on design and performance of ammonia based thermochemical transformer," in *Proceeding of International Absorption Heat Pump Conference, Montreal, Canada,* 1996, pp. 505-512.
[99] V. Goetz, B. Spinner, and E. Lepinasse, "A solid-gas thermochemical cooling system using BaCl2 and NiCl2," *Energy,* vol. 22, no. 1, pp. 49-58, 1// 1997.
[100] J. Castaing-Lasvignottes and P. Neveu, "Equivalent Carnot cycle concept applied to a thermochemical solid/gas resorption system," *Applied Thermal Engineering,* vol. 18, no. 9–10, pp. 745-754, 9/1/ 1998.
[101] E. Lépinasse, M. Marion, and V. Goetz, "Cooling storage with a resorption process. Application to a box temperature control," *Applied Thermal Engineering,* vol. 21, no. 12, pp. 1251-1263, 8// 2001.
[102] L. L. Vasiliev, D. A. Mishkinis, A. A. Antukh, and A. G. Kulakov, "Resorption heat pump," *Applied thermal engineering,* vol. 24, no. 13, pp. 1893-1903, 2004.
[103] T. X. Li, R. Z. Wang, J. K. Kiplagat, and H. Chen, "Experimental study and comparison of thermochemical resorption refrigeration cycle and adsorption refrigeration cycle," *Chemical Engineering Science,* vol. 65, no. 14, pp. 4222-4230, 7/15/ 2010.
[104] H. Demir, M. Mobedi, and S. Ülkü, "A review on adsorption heat pump: Problems and solutions," *Renewable and Sustainable Energy Reviews,* vol. 12, no. 9, pp. 2381-2403, 12// 2008.
[105] J. H. Han, K.-H. Lee, D. H. Kim, and H. Kim, "Transformation analysis of thermochemical reactor based on thermophysical properties of graphite-MnCl2 complex," *Industrial & engineering chemistry research,* vol. 39, no. 11, pp. 4127-4139, 2000.
[106] T. X. Li, R. Z. Wang, J. K. Kiplagat, and L. W. Wang, "Performance study of a consolidated manganese chloride–expanded graphite compound for sorption deep-freezing processes," *Applied Energy,* vol. 86, no. 7–8, pp. 1201-1209, 7// 2009.

[107] T. Dellero, D. Sarmeo, and P. Touzain, "A chemical heat pump using carbon fibers as additive. Part I: enhancement of thermal conduction," *Applied Thermal Engineering,* vol. 19, no. 9, pp. 991-1000, 1999.
[108] Z. Tamainot-Telto and R. E. Critoph, "Monolithic carbon for sorption refrigeration and heat pump applications," *Applied Thermal Engineering,* vol. 21, no. 1, pp. 37-52, 2001.
[109] Z. Aidoun and M. Ternan, "Salt impregnated carbon fibres as the reactive medium in a chemical heat pump: the NH 3–CoCl 2 system," *Applied thermal engineering,* vol. 22, no. 10, pp. 1163-1173, 2002.
[110] L. Zhenyan, L. Yunzhuang, and Z. Jiaxin, "Zeolite-active carbon compound adsorbent and its use in adsorption solar cooling tube," *Solar Energy Materials and solar cells,* vol. 52, no. 1, pp. 45-53, 1998.
[111] L. Vasil'ev, D. Nikanpour, A. Antukh, K. Snelson, L. Vasil'ev, and A. Lebru, "Multisalt-carbon chemical cooler for space applications," *Journal of Engineering Physics and Thermophysics,* vol. 72, no. 3, pp. 572-577, 1999.
[112] L. W. Wang, R. Z. Wang, J. Y. Wu, and K. Wang, "Compound adsorbent for adsorption ice maker on fishing boats," *International Journal of Refrigeration,* vol. 27, no. 4, pp. 401-408, 2004.
[113] B. Dawoud and Y. Aristov, "Experimental study on the kinetics of water vapor sorption on selective water sorbents, silica gel and alumina under typical operating conditions of sorption heat pumps," *International Journal of Heat and Mass Transfer,* vol. 46, no. 2, pp. 273-281, 2003.
[114] A. Freni, M. M. Tokarev, G. Restuccia, A. G. Okunev, and Y. I. Aristov, "Thermal conductivity of selective water sorbents under the working conditions of a sorption chiller," *Applied thermal engineering,* vol. 22, no. 14, pp. 1631-1642, 2002.
[115] K. Daou, R. Z. Wang, G. Z. Yang, and Z. Z. Xia, "Theoretical comparison of the refrigerating performances of a CaCl 2 impregnated composite adsorbent to those of the host silica gel," *International Journal of Thermal Sciences,* vol. 47, no. 1, pp. 68-75, 2008.
[116] M. Jagtoyen and F. Derbyshire, "Some considerations of the origins of porosity in carbons from chemically activated wood," *Carbon,* vol. 31, no. 7, pp. 1185-1192, 1993/01/01/ 1993.
[117] Y. H. Zhang, "Adsorption function," *Shanghai: Shanghai Publishing House of Science and Technology Document,* 1989.
[118] R. T. Yang, "Gas separation by adsorption methods," *Publishing House of Chemical Industry, Beijing, China,* 1991.
[119] P. J. M. Carrott, M. M. L. Ribeiro Carrott, and P. F. M. M. Correia, "Evolution of porosity of activated carbon fibres prepared from pre-oxidized acrylic fibres," *Microporous and Mesoporous Materials,* vol. 264, pp. 176-180, 2018/07/01/ 2018.
[120] B. B. Saha, El-Sharkawy, II, A. Chakraborty, and S. Koyama, "Study on an activated carbon fiber–ethanol adsorption chiller: Part I–system description and modelling," *International Journal of Refrigeration,* vol. 30, no. 1, pp. 86-95, 2007.
[121] Z. Yue and J. Economy, "4 - Carbonization and activation for production of activated carbon fibers," in *Activated Carbon Fiber and Textiles,* J. Y. Chen, Ed. Oxford: Woodhead Publishing, 2017, pp. 61-139.
[122] T. Dellero and P. Touzain, "A chemical heat pump using carbon fibers as additive. Part II: study of constraint parameters," *Applied thermal engineering,* vol. 19, no. 9, pp. 1001-1011, 1999.
[123] J. H. Han, K. W. Cho, K. H. Lee, and H. Kim, "Characterization of graphite-salt blocks in chemical heat pumps," in *Ab-sorption Heat Pump Conference, Quebec: Montreal*, 1996, vol. 6773.

[124] S. Mauran, M. Lebrun, P. Prades, M. Moreau, B. Spinner, and C. Drapier, "Active composite and its use as reaction medium," ed: Google Patents, 1994.
[125] S. Mauran, O. Coudevylle, and H. B. Lu, "Optimization of porous reactive media for solid sorption heat pumps," in *Proceedings of the international sorption heat pump conference, Montreal, Canada*, 1996, vol. 38.
[126] S. Mauran, P. Prades, and F. L'Haridon, "Heat and mass transfer in consolidated reacting beds for thermochemical systems," *Heat Recovery Systems and CHP*, vol. 13, no. 4, pp. 315-319, 1993.
[127] T.-H. Eun, H.-K. Song, J. Hun Han, K.-H. Lee, and J.-N. Kim, "Enhancement of heat and mass transfer in silica-expanded graphite composite blocks for adsorption heat pumps: Part I. Characterization of the composite blocks," *International Journal of Refrigeration*, vol. 23, no. 1, pp. 64-73, 2000/01/01/ 2000.
[128] R. G. Oliveira, R. Z. Wang, and C. Wang, "Evaluation of the cooling performance of a consolidated expanded graphite–calcium chloride reactive bed for chemisorption icemaker," *International journal of refrigeration*, vol. 30, no. 1, pp. 103-112, 2007.
[129] K. Wang, J. Y. Wu, R. Z. Wang, and L. W. Wang, "Composite adsorbent of CaCl2 and expanded graphite for adsorption ice maker on fishing boats," *International Journal of Refrigeration*, vol. 29, no. 2, pp. 199-210, 2006/03/01/ 2006.
[130] L. W. Wang, Z. Tamainot-Telto, S. J. Metcalf, R. E. Critoph, and R. Z. Wang, "Anisotropic thermal conductivity and permeability of compacted expanded natural graphite," *Applied Thermal Engineering*, vol. 30, no. 13, pp. 1805-1811, 2010.
[131] L. W. Wang, Z. Tamainot-Telto, R. Thorpe, R. E. Critoph, S. J. Metcalf, and R. Z. Wang, "Study of thermal conductivity, permeability, and adsorption performance of consolidated composite activated carbon adsorbent for refrigeration," *Renewable energy*, vol. 36, no. 8, pp. 2062-2066, 2011.
[132] L. W. Wang, S. J. Metcalf, R. E. Critoph, Z. Tamainot-Telto, and R. Thorpe, "Two types of natural graphite host matrix for composite activated carbon adsorbents," *Applied Thermal Engineering*, vol. 50, no. 2, pp. 1652-1657, 2013.
[133] B. Tian, Z. Q. Jin, L. W. Wang, and R. Z. Wang, "Permeability and thermal conductivity of compact chemical and physical adsorbents with expanded natural graphite as host matrix," *International Journal of Heat and Mass Transfer*, vol. 55, no. 15, pp. 4453-4459, 2012.
[134] R. G. Oliveira, R. Z. Wang, J. K. Kiplagat, and C. Y. Wang, "Novel composite sorbent for resorption systems and for chemisorption air conditioners driven by low generation temperature," *Renewable Energy*, vol. 34, no. 12, pp. 2757-2764, 2009.
[135] Z. E. BHAT P, GHAMSRI A K, et al, "Improved Thermal Conductivity in Carbon Nanotubes-Reinforced Syntactic Foam Achieved by a New Dispersing Technique," *JOM*, pp. 2848-2854, 2015.
[136] J. Lin, H. Zhang, M. Tang, W. Tu, and X. Zhang, "Improved Thermal Property of a Multilayered Graphite Nanoplatelets Filled Silicone Resin Composite," *Journal of Materials Engineering and Performance*, vol. 24, no. 2, pp. 920-929, 2015.
[137] P. Kumar, S. Yu, F. Shahzad, S. M. Hong, Y.-H. Kim, and C. M. Koo, "Ultrahigh electrically and thermally conductive self-aligned graphene/polymer composites using large-area reduced graphene oxides," *Carbon*, vol. 101, pp. 120-128, 2016.
[138] J. Lin, H. Zhang, H. Hong, H. Liu, and X. Zhang, "A thermally conductive composite with a silica gel matrix and carbon-encapsulated copper nanoparticles as filler," *Journal of Electronic Materials*, vol. 43, no. 7, pp. 2759-2769, 2014.
[139] T. Yan, T. X. Li, H. Li, and R. Z. Wang, "Experimental study of the ammonia adsorption characteristics on the composite sorbent of CaCl2 and multi-walled carbon nanotubes," *International Journal of Refrigeration*, vol. 46, pp. 165-172, 2014/10/01/ 2014.

[140] T. Yan, T. X. Li, H. Li, and R. Z. Wang, "Experimental study of the ammonia adsorption characteristics on the composite sorbent of CaCl 2 and multi-walled carbon nanotubes," *International Journal of Refrigeration,* vol. 46, pp. 165-172, 2014.
[141] T. Yan, T. X. Li, R. Z. Wang, and R. Jia, "Experimental investigation on the ammonia adsorption and heat transfer characteristics of the packed multi-walled carbon nanotubes," *Applied Thermal Engineering,* vol. 77, pp. 20-29, 2015.
[142] H. Zhang, Q. Wu, J. Lin, J. Chen, and Z. Xu, "Thermal conductivity of polyethylene glycol nanofluids containing carbon coated metal nanoparticles," *Journal of Applied Physics,* vol. 108, no. 12, p. 124304, 2010.
[143] C. Vales-Pinzon, R. A. Medina-Esquivel, J. Ordonez-Miranda, and J. J. Alvarado-Gil, "Thermal transfer in mixtures of ethylene glicol with carbon coated iron nanoparticles under the influence of a uniform magnetic field," *Journal of Alloys and Compounds,* vol. 643, pp. S71-S74, 2015.
[144] Q. Wu *et al.*, "Preparation of carbon‐coated iron nanofluid and its application in radiofrequency ablation," *Journal of Biomedical Materials Research Part B: Applied Biomaterials,* vol. 103, no. 4, pp. 908-914, 2015.
[145] D. Goswami, "Solar thermal power: status of technologies and opportunities for research," *Heat and Mass Transfer,* vol. 95, pp. 57-60, 1995.
[146] S. Vijayaraghavan and D. Y. Goswami, "A combined power and cooling cycle modified to improve resource utilization efficiency using a distillation stage," *Energy,* vol. 31, no. 8-9, pp. 1177-1196, 2006.
[147] D. Zheng, B. Chen, Y. Qi, and H. Jin, "Thermodynamic analysis of a novel absorption power/cooling combined-cycle," *Applied Energy,* vol. 83, no. 4, pp. 311-323, 2006.
[148] M. Liu and N. Zhang, "Proposal and analysis of a novel ammonia–water cycle for power and refrigeration cogeneration," *Energy,* vol. 32, no. 6, pp. 961-970, 2007.
[149] N. Zhang and N. Lior, "Development of a novel combined absorption cycle for power generation and refrigeration," *Journal of Energy Resources Technology,* vol. 129, no. 3, pp. 254-265, 2007.
[150] H. T. Chua, K. C. Ng, A. Malek, T. Kashiwagi, A. Akisawa, and B. B. Saha, "Multi-bed regenerative adsorption chiller—improving the utilization of waste heat and reducing the chilled water outlet temperature fluctuation," *International Journal of refrigeration,* vol. 24, no. 2, pp. 124-136, 2001.
[151] L. Jiang, L. W. Wang, A. P. Roskilly, and R. Z. Wang, "Design and performance analysis of a resorption cogeneration system," *International Journal of Low-Carbon Technologies,* vol. 8, no. suppl_1, pp. i85-i91, 2013.
[152] L. Wang, F. Ziegler, A. P. Roskilly, R. Wang, and Y. Wang, "A resorption cycle for the cogeneration of electricity and refrigeration," *Applied energy,* vol. 106, pp. 56-64, 2013.
[153] H. Bao, Y. Wang, and A. P. Roskilly, "Modelling of a chemisorption refrigeration and power cogeneration system," *Applied energy,* vol. 119, pp. 351-362, 2014.
[154] L. Jiang, L. W. Wang, X. F. Zhang, C. Z. Liu, and R. Z. Wang, "Performance prediction on a resorption cogeneration cycle for power and refrigeration with energy storage," *Renewable energy,* vol. 83, pp. 1250-1259, 2015.
[155] Y. Lu, Y. Wang, H. Bao, Y. Yuan, L. Wang, and A. P. Roskilly, "Analysis of an optimal resorption cogeneration using mass and heat recovery processes," *Applied Energy,* vol. 160, pp. 892-901, 2015.
[156] F. N. Al-Mousawi, R. Al-Dadah, and S. Mahmoud, "Low grade heat driven adsorption system for cooling and power generation using advanced adsorbent materials," *Energy conversion and management,* vol. 126, pp. 373-384, 2016.
[157] F. N. Al-Mousawi, R. Al-Dadah, and S. Mahmoud, "Low grade heat driven adsorption system for cooling and power generation with small-scale radial inflow turbine," *Applied Energy,* vol. 183, pp. 1302-1316, 2016/12/01/ 2016.

[158] L. Jiang, L. Wang, R. Wang, P. Gao, and F. Song, "Investigation on cascading cogeneration system of ORC (Organic Rankine Cycle) and CaCl2/BaCl2 two-stage adsorption freezer," *Energy,* vol. 71, pp. 377-387, 2014.
[159] F. N. Al-Mousawi, R. Al-Dadah, and S. Mahmoud, "Novel system for cooling and electricity: Four different integrated adsorption-ORC configurations with two expanders," *Energy conversion and management,* vol. 152, pp. 72-87, 2017.
[160] F. N. Al-Mousawi, R. Al-Dadah, and S. Mahmoud, "Integrated adsorption-ORC system: Comparative study of four scenarios to generate cooling and power simultaneously," *Applied Thermal Engineering,* vol. 114, pp. 1038-1052, 2017.
[161] R. G. Oliveira and R. Z. Wang, "Study of a non-isothermal, non-isobaric consolidated reactive bed for chemisorption icemakers," *Chemical Engineering Journal,* vol. 138, no. 1-3, pp. 416-424, 2008.
[162] H.-J. Huang, G.-B. Wu, J. Yang, Y.-C. Dai, W.-K. Yuan, and H.-B. Lu, "Modeling of gas–solid chemisorption in chemical heat pumps," *Separation and Purification Technology,* vol. 34, no. 1-3, pp. 191-200, 2004.
[163] S. H. Choi, "Ph. D Dissertation," *Korea University,* vol. Seoul, Korea, no. 1995.
[164] L. Wang, L. Chen, H. L. Wang, and D. L. Liao, "The adsorption refrigeration characteristics of alkaline-earth metal chlorides and its composite adsorbents," *Renewable Energy,* vol. 34, no. 4, pp. 1016-1023, 2009/04/01/ 2009.
[165] T. Li, J.-H. Lee, R. Wang, and Y. T. Kang, "Enhancement of heat transfer for thermal energy storage application using stearic acid nanocomposite with multi-walled carbon nanotubes," *Energy,* vol. 55, no. Supplement C, pp. 752-761, 2013/06/15/ 2013.
[166] K. Tang *et al.*, "Investigation of thermal characteristics of strontium chloride composite sorbent for sorption refrigeration," *Thermal Science and Engineering Progress,* vol. 10, pp. 179-185, 2019/05/01/ 2019.
[167] Q. Wu, Y. Lu, K. Tang, Y. Wang, A. P. Roskilly, and H. Zhang, "Experimental Exploration of a Novel Chemisorption Composite of SrCl2-NEG Adding with Carbon Coated Ni," *Energy Procedia,* vol. 105, pp. 4655-4660, 2017/05/01/ 2017.
[168] E. Suzuki, "High‐resolution scanning electron microscopy of immunogold‐labelled cells by the use of thin plasma coating of osmium," *Journal of microscopy,* vol. 208, no. 3, pp. 153-157, 2002.
[169] J. I. Goldstein, D. E. Newbury, J. R. Michael, N. W. M. Ritchie, J. H. J. Scott, and D. C. Joy, *Scanning electron microscopy and X-ray microanalysis*. Springer, 2017.
[170] D. Stokes, *Principles and practice of variable pressure/environmental scanning electron microscopy (VP-ESEM)*. John Wiley & Sons, 2008.
[171] S. J. Metcalf, Z. Tamainot-Telto, and R. E. Critoph, "Application of a compact sorption generator to solar refrigeration: Case study of Dakar (Senegal)," *Applied Thermal Engineering,* vol. 31, no. 14-15, pp. 2197-2204, 2011.
[172] Z. Zeleny, V. Vodicka, V. Novotny, and J. Mascuch, "Gear pump for low power output ORC – an efficiency analysis," *Energy Procedia,* vol. 129, pp. 1002-1009, 2017/09/01/ 2017.
[173] A. K. Narasimhan, C. Wickramaratne, R. Kamal, D. Y. Goswami, and P. Singh, "Mapping scroll expander performance for organic working fluids using dimensionless parameters in Ns-Ds diagram," *Energy,* vol. 182, pp. 739-752, 2019/09/01/ 2019.
[174] D. Li, Z. Zuo, H. Wang, S. Liu, X. Wei, and D. Qin, "Review of positive slopes on pump performance characteristics of pump-turbines," *Renewable and Sustainable Energy Reviews,* vol. 112, pp. 901-916, 2019/09/01/ 2019.
[175] C. Liu and T. Gao, "Off-design performance analysis of basic ORC, ORC using zeotropic mixtures and composition-adjustable ORC under optimal control strategy," *Energy,* vol. 171, pp. 95-108, 2019/03/15/ 2019.

[176] S. Lecompte, H. Huisseune, M. van den Broek, S. De Schampheleire, and M. De Paepe, "Part load based thermo-economic optimization of the Organic Rankine Cycle (ORC) applied to a combined heat and power (CHP) system," *Applied Energy,* vol. 111, pp. 871-881, 2013/11/01/ 2013.
[177] Z. Ge *et al.*, "Main parameters optimization of regenerative organic Rankine cycle driven by low-temperature flue gas waste heat," *Energy,* vol. 93, pp. 1886-1895, 2015/12/15/ 2015.
[178] S. H. A. Bakar, M. K. A. Hamid, S. R. W. Alwi, and Z. A. Manan, "Selection of minimum temperature difference (ΔTmin) for heat exchanger network synthesis based on trade-off plot," *Applied Energy,* vol. 162, pp. 1259-1271, 2016/01/15/ 2016.
[179] E. H. Wang, H. G. Zhang, B. Y. Fan, M. G. Ouyang, Y. Zhao, and Q. H. Mu, "Study of working fluid selection of organic Rankine cycle (ORC) for engine waste heat recovery," *Energy,* vol. 36, no. 5, pp. 3406-3418, 2011/05/01/ 2011.

Appendix A. Meanings of various characters in REFPROP

Character (unit)	Property
P (kPa)	Pressure
T (K)	Temperature
D ($kg \cdot m^{-3}$)	Density
H ($J \cdot kg^{-1}$)	Enthalpy
S ($J \cdot kg^{-1} \cdot K^{-1}$)	Entropy
U ($J \cdot kg^{-1}$)	Internal energy
C ($J \cdot kg^{-1} \cdot K^{-1}$)	Specific heat capacity at the same pressure, C_p
O ($J \cdot kg^{-1} \cdot K^{-1}$)	Specific heat capacity at the same volume, C_v
K (-)	Ratio of the specific heats, C_p/C_v
A (m/s)	Speed of sound
X (-)	Liquid phase and gas phase composition (mass fractions)
V (Pa·s)	Dynamic viscosity
L ($W \cdot m^{-1} \cdot K^{-1}$)	Thermal conductivity
Q ($kg \cdot kg^{-1}$)	Quality (vapour fraction)
I ($N \cdot m^{-1}$)	Surface tension

Table A. Meanings of various characters in REFPROP

Appendix B. Temperature evolution of $MnCl_2$-EG-Ni/Al/Fe@C in desorption versus time

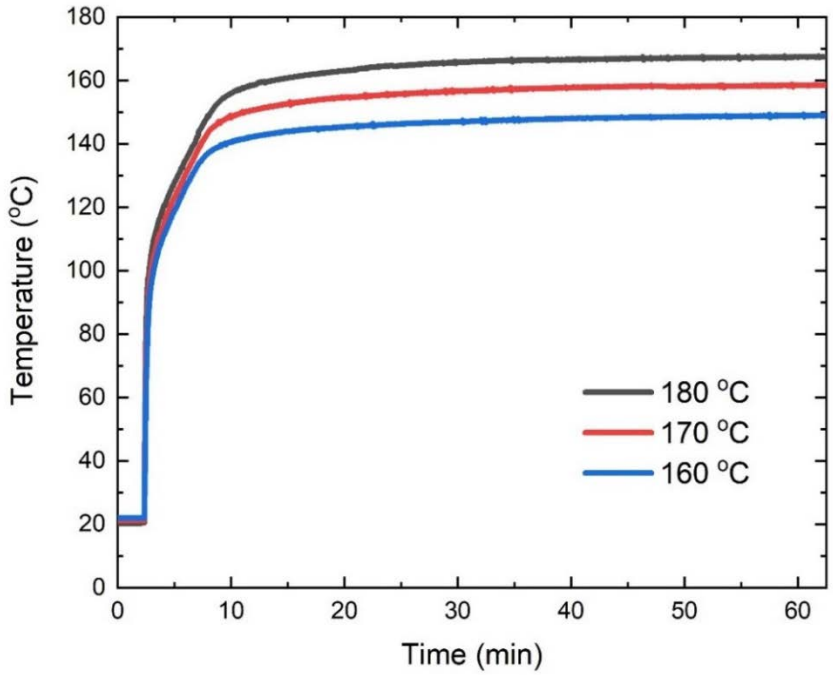

Figure B.1 Temperature evolution of $MnCl_2$-EG-Ni@C in desorption versus time

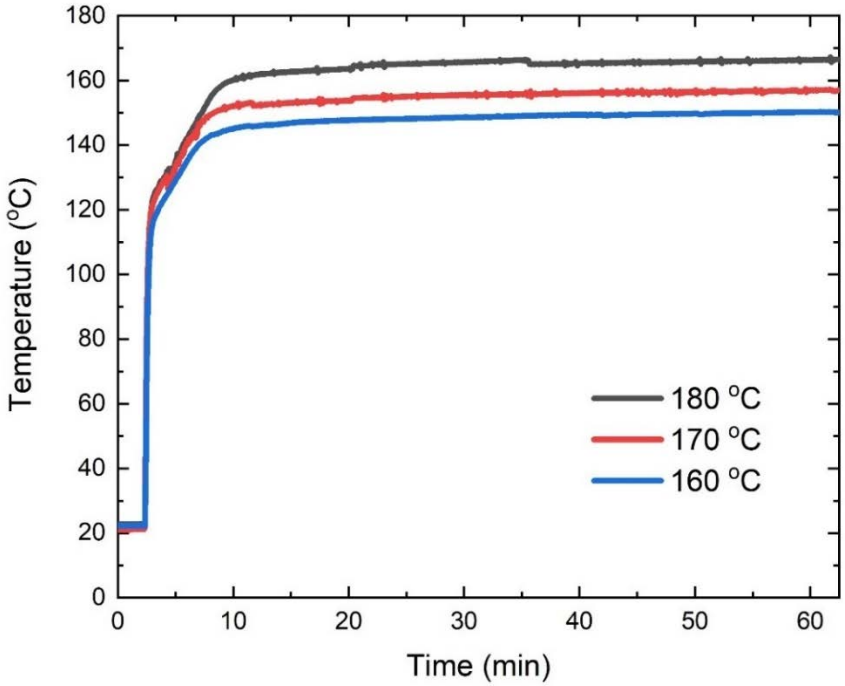

Figure B.2 Temperature evolution of $MnCl_2$-EG-Al@C in desorption versus time

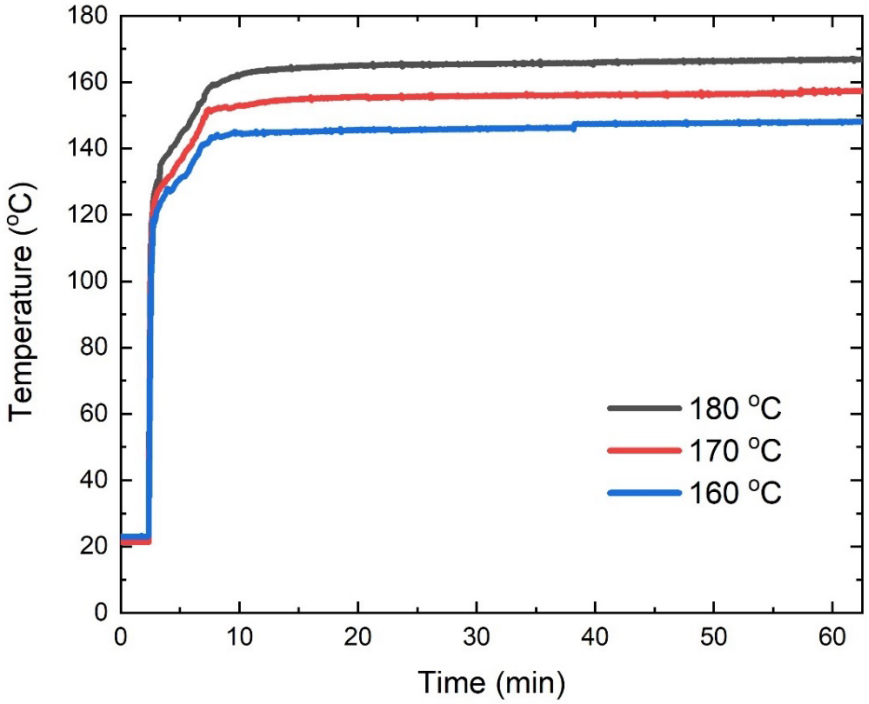

Figure B.3 Temperature evolution of $MnCl_2$-EG-Fe@C in desorption versus time